

IDŐJÁRÁS

QUARTERLY JOURNAL OF THE HUNGARIAN METEOROLOGICAL SERVICE

CONTENTS

<i>Karolina Szabóné André, Judit Bartholy, Rita Pongrácz, and József Bór: Local identification of persistent cold air pool conditions in the Great Hungarian Plain.....</i>	167
<i>Seyed Mostafa Tabatabaei, Mohammad Nazeri Tahroudi, and Bahareh Sadat Hamraz: A Comparison the performance of GEP, ANFIS and SVM models for simulating rainfall</i>	195
<i>János Tóth and István Farkas: Predictive control of a solar thermal system via on-line communication with a meteorological database server</i>	211
<i>Nikola R. Bačević, Nikola M. Milentijević, Aleksandar Valjarević, Ajša Gicić, Dušan Kićović, Milica G. Radaković, Milena Nikolić, and Milana Pantelić: Spatio-temporal variability of fair temperatures in Central Serbia from 1949 to 2018</i>	229
<i>Hristo Chervenkov and Kiril Slavov: Assessment of Agro-meteorological Indices over Southeast Europe in the Context of Climate Change (1961–2018)</i>	255
<i>Mykhailo Savenets: Air pollution in Ukraine: the view from Sentinel-5P.....</i>	271
<i>Amirhosein Aghakhani Afshar and Yousef Hassanzadeh: A hydrological toolkit to delineate patterns of blue and green water in a regional semi-arid climate in Iran via CMIP5 models.....</i>	291
<i>Elena Vyshkvarkova: Changes in extreme precipitation over the North Caucasus and the Crimean Peninsula during 1961–2018.....</i>	321

IDŐJÁRÁS

Quarterly Journal of the Hungarian Meteorological Service

Editor-in-Chief
LÁSZLÓ BOZÓ

Executive Editor
MÁRTA T. PUSKÁS

EDITORIAL BOARD

ANTAL, E. (Budapest, Hungary)	MIKA, J. (Eger, Hungary)
BARTHOLY, J. (Budapest, Hungary)	MERSICH, I. (Budapest, Hungary)
BATCHVAROVA, E. (Sofia, Bulgaria)	MÖLLER, D. (Berlin, Germany)
BRIMBLECOMBE, P. (Hong Kong, SAR)	PINTO, J. (Res. Triangle Park, NC, U.S.A.)
CZELNAI, R. (Dörgicse, Hungary)	PRÁGER, T. (Budapest, Hungary)
DUNKEL, Z. (Budapest, Hungary)	PROBÁLD, F. (Budapest, Hungary)
FERENCZI, Z. (Budapest, Hungary)	RADNÓTI, G. (Reading, U.K.)
GERESDI, I. (Pécs, Hungary)	S. BURÁNSZKI, M. (Budapest, Hungary)
HASZPRA, L. (Budapest, Hungary)	SZALAI, S. (Budapest, Hungary)
HORVÁTH, Á. (Siófok, Hungary)	SZEIDL, L. (Budapest, Hungary)
HORVÁTH, L. (Budapest, Hungary)	SZUNYOGH, I. (College Station, TX, U.S.A.)
HUNKÁR, M. (Keszthely, Hungary)	TAR, K. (Debrecen, Hungary)
LASZLO, I. (Camp Springs, MD, U.S.A.)	TÁNCZER, T. (Budapest, Hungary)
MAJOR, G. (Budapest, Hungary)	TOTH, Z. (Camp Springs, MD, U.S.A.)
MÉSZÁROS, E. (Veszprém, Hungary)	VALI, G. (Laramie, WY, U.S.A.)
MÉSZÁROS, R. (Budapest, Hungary)	WEIDINGER, T. (Budapest, Hungary)

Editorial Office: Kitaibel P.u. 1, H-1024 Budapest, Hungary

P.O. Box 38, H-1525 Budapest, Hungary

E-mail: journal.idojaras@met.hu

Fax: (36-1) 346-4669

**Indexed and abstracted in Science Citation Index Expanded™ and
Journal Citation Reports/Science Edition**

Covered in the abstract and citation database SCOPUS®

Included in EBSCO's databases

Subscription by mail:

IDŐJÁRÁS, P.O. Box 38, H-1525 Budapest, Hungary

E-mail: journal.idojaras@met.hu

IDŐJÁRÁS

Quarterly Journal of the Hungarian Meteorological Service
Vol. 125, No. 2, April – June, 2021, pp. 167–192

Local identification of persistent cold air pool conditions in the Great Hungarian Plain

Karolina Szabóné André^{1,2,*}, Judit Bartholy¹, Rita Pongrácz¹,
and József Bór²

¹ *Department of Meteorology*
Eötvös Loránd University
Pázmány Péter st. 1/A, H-1117, Budapest, Hungary

² *Institute of Earth Physics and Space Science (ELKH EPSS)*
Csatkai Endre st. 6-8, H-9400, Sopron, Hungary

**Corresponding author E-mail: karol@nimbus.elte.hu*

(Manuscript received in final form April 28, 2020)

Abstract— Cold air pool (CAP) is a winter-time, anticyclonic weather event: a cold air layer confined by the topography and warm air aloft. If its duration is more than one day, then it is called persistent cold air pool (PCAP). CAPs are mainly examined in small basins and valleys. Fewer studies pay attention to PCAPs in much larger basins (with an area of more than 50 000 km²), and it is not evident how effective the existing numerical definitions are in cases of extensive PCAP events. A possible method of identifying PCAPs in a large basin is to identify PCAP weather conditions at different measuring sites across the basin. If there are PCAP weather conditions at most of the sites, then it is likely to be an extensive PCAP.

In this work, we examine which of the documented CAP definitions can be used for reliable local detection of CAP conditions. Daily weather reports and meteorological data from two locations in the 52 000 km² sized Great Hungarian Plain have been used to obtain a reference set of days with PCAP weather conditions during two consecutive winter months. Several numerical CAP definitions were compared for their performance in recognizing the presence of PCAP weather conditions using radiosonde measurements and reanalysis data. The lowest error was produced by using the heat deficit (HD) method. So this is considered the most suitable method for local identification of PCAPs in the Great Hungarian Plain.

Key-words: persistent cold air pool; temperature inversion; heat deficit; Carpathian Basin; radiosonde; reanalysis

1. Introduction

Two very different meteorological phenomena are named cold air pool (CAP) in the literature. One of them is a synoptic scale weather formation, when there is a cold air mass above warmer air causing heavy precipitation (e.g., *Llasat and Puigcerver, 1990*). The subject of our study is the second one, which is a stagnant cold air layer in a basin or valley below a warmer air layer (*Whiteman et al., 2001*). This latter phenomenon is anticyclone-related and favorable to fog formation due to the weak near-surface wind and the strong temperature inversion causing limited vertical motion (*Chachere and Pu, 2016*). The subsidence in anticyclone plays a key role in the formation of the inversion.

CAPs can be classified into two subgroups based on the height of the base of the inversion: simple or complex (*Tóth, 1984*). In the simple case, the inversion layer starts directly from the surface, and if the level of relative humidity is sufficiently high then fog forms. This stratification can lead to severe smog events in populated areas, where various pollutants are emitted from traffic, industry, and households (e.g., *Deng et al., 2019*). In the complex case, an unstable layer forms near the surface below the temperature inversion. This leads to the formation of elevated fog or stratus cloud if the atmosphere is wet enough. CAPs can transform from simple to complex type and vice versa over time.

CAPs can be classified into two other subtypes according to their duration: nocturnal only or persistent event. Nocturnal CAP usually forms during the night and dissipates after sunrise due to the substantial change in energy budget elements associated to incoming solar radiation. It can occur throughout the year mainly in small valleys or basins (usually in the range of a few 10–100 km²). Persistent cold air pools (PCAPs) remain longer than a single diurnal cycle and can last several days or even for weeks. More specifically, this weather event typically occurs in winter, because the solar elevation angle is smaller and the daytime is shorter than in summer. These conditions lead to less incoming solar radiation that cannot destroy the inversion layer. The snow cover is also favorable for the inversion development.

PCAPs may result in different socio-economic hazards: temperature inversion in the surface layers together with weak wind may lead to severe air pollution in cities causing health problems for many people, especially, elderly and children even in smaller settlements. For instance, *Largeron and Staquet (2016a)* examined the connection between persistent inversions and wintertime PM₁₀ pollution in the valleys surrounding Grenoble, France. Their study concluded that polluted episodes are primarily driven by persistent inversions. Fog and/or smog during chilly weather conditions often results in freezing drizzle and rime accretion. These weather conditions can cause problems in transportation and electricity supply. Therefore, CAPs have a significant impact on the daily lives of the population. Unfortunately, simulating CAPs is difficult that causes a large forecasting error in

numerical weather forecasting models near the surface. That is why it is important to find a metric that adequately describes CAPs.

To study the different stages of the life cycle of CAPs in more detail, numerous experiments and field measurement campaigns were performed. In the Stable Atmospheric Boundary-Layer Experiment (SABLES 98), *Cuxart et al.* (2000) examined dynamical processes including winds in the nocturnal stable boundary layers in Spain. They observed low-level jets during every nocturnal CAP. In the Meteor Crater Experiment (METCRAX), *Whiteman et al.* (2008), the effect of solar radiation and winds on CAP evolution was investigated in Arizona, USA. Their preliminary results show that nocturnal CAP forms frequently in the crater, and internal wave motions are common in CAP. During the Cold-Air Pooling Experiment (COLPEX), the formation of CAP and fog was examined within valleys in the United Kingdom (*Price et al.*, 2011). According to the results, the temperature and turbulence during CAPs is generally greater in the Burfield valley than in the less open Duffryn valley. Initial results indicate that when clouds advected over the valley, the stability is greatly reduced. When sky becomes clear, CAP forms again. Numerical modeling of CAPs was also addressed in COLPEX using the data measured during the experiment. The initial results show that some of the successfully simulated CAPs are slightly too cold. The Persistent Cold-Air Pool Study (PCAPS) was performed to get more measurements and better understanding of PCAPS in Utah, USA (*Lareau et al.*, 2013). They showed that there is a connection between strong, long lasting PCAPS and high concentration of fine particulate matter.

The wide variety of field campaigns and perspectives led to the use of different numerical definitions. Several definitions are reviewed here only briefly and are described in detail later in Section 3. The earliest study to describe and define CAPs in the intermountain western USA was performed by *Wolyn and McKee* (1989). They introduced the concept of deep stable layer (DSL). Later, *Chachere and Pu* (2016) also used this definition and referred to the DSL as CAP. *Yu et al.* (2017) also used this method but considered the wind speed at 10 m, too.

Other methods are based on the identification of inversion over a valley or basin. There are different techniques for this purpose, for example the temperature difference between the mountain ridge and the valley base (*Iijima and Shinoda*, 2000; *Vitasse et al.*, 2017; *Conangla et al.*, 2018), or the vertical temperature profile can also be used (*Kahl et al.*, 1992). Some authors also include an upper threshold for wind speed because of the typical weak wind conditions during CAP episodes (*Whiteman et al.*, 2001; *Reeves and Stensrud*, 2009; *Reeves et al.*, 2011).

Another group of methods is based on the so-called heat deficit (e.g., *Whiteman et al.*, 1999, 2014; *Chemel et al.*, 2016; *Largerion and Staquet*, 2016a, 2016b; *Baasandorj et al.*, 2017). This measure describes the atmospheric stability of an air column.

Lareau et al. (2013) introduced a method based on the potential temperature deficit (PTD) to define CAPs.

CAPs are usually investigated in small basins (few 10–100 km²), where the approximation of horizontal temperature homogeneity can be used (*Largeron and Staquet, 2016a*). In this case, even a single measurement site that monitors the vertical temperature profile is sufficient to identify PCAPs. Fewer studies pay attention to PCAPs in much larger basins with an area of more than 50 000 km², like, e.g., the Colorado Plateau Basin of size 225 000 km² (*Whiteman et al., 1999*). Consequently, it is not evident how effective the existing numerical definitions are in cases of extensive CAP events. A possible method for identifying PCAPs in a large basin is to identify PCAP weather conditions at different measuring sites across the basin. If there are PCAP weather conditions at most of the sites, then it is likely an extended PCAP. The extension of the event can be estimated considering the areal coverage of stations.

In our study, weather conditions are analyzed in the 52 000 km² sized Great Hungarian Plain, and two locations (Budapest and Szeged, Hungary) with radiosonde measurements are considered to test local identification of PCAP weather conditions during two consecutive winter months (December 2015 and January 2016). The above-mentioned numerical CAP definitions are compared for their performance in recognizing the presence of PCAP weather conditions near these two cities.

A suitable numerical definition could be utilized possibly in synoptic-climatological research and air quality studies (e.g., *Haszpra et al., 2019*) as well as by weather forecasters during post-processing of numerical weather prediction models.

2. Data

The two considered measuring stations (Budapest and Szeged) can be found in the Carpathian Basin, which is located in Central Europe (*Fig. 1*) surrounded by the Alps (from west), the Carpathian Mountains (from north, east, and south) and the Dinarides (from south). The general altitude of the Carpathian Mountains is around 1500 m, with several peaks above 2000 m. The average height of 850 hPa pressure level is 1500 m, therefore, this level has a prominent role in this study.

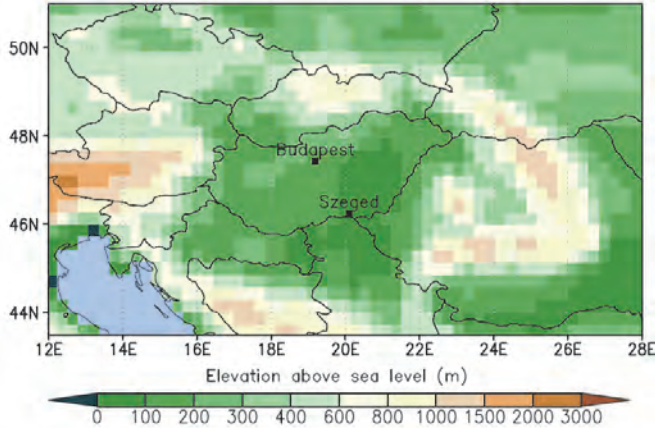


Fig. 1. Topography of the Carpathian Basin and its surroundings from the ERA5 reanalysis dataset with a horizontal resolution of 0.28125° (~ 31 km). The examined locations are indicated with black dots: Budapest and Szeged in Hungary.

The Integrated Global Radiosonde Archive (IGRA) database (Durre *et al.*, 2006; IGRA dataset) was used to examine PCAPs. There were two measurements in a day during the examined period of two months. Only one measurement is missing at Budapest, namely, on December 11, 2015 at 12 UTC.

Surface synoptic reports from the Integrated Surface Dataset (ISD) (Smith *et al.*, 2011; ISD dataset) were used for describing the weather conditions of the examined months at Budapest and Szeged. The following variables are used from the reports: hourly atmospheric pressure at station level, temperature and dew point temperature at 2 m, and wind speed at 10 m. There are 28 and 50 missing measurements at Budapest and Szeged, respectively. Out of them, 8 and 20 correspond to 00 UTC or 12 UTC, when radiosonde measurements are regularly available.

To obtain finer temporal resolution, two global gridded reanalysis datasets were used: the ERA-Interim (with ~ 79 km horizontal resolution, Dee *et al.*, 2011; ERA-Interim dataset) and the ERA5 (with ~ 31 km horizontal resolution, Hersbach *et al.*, 2019; ERA5 dataset). These datasets are available with temporal resolutions of 6 h and 1 h, respectively. Main technical details of the databases used in this study are summarized in Table 1. For the present analysis, we used only the data from the two grid cells containing the measuring sites.

Table 1. Technical details of databases used in this study to examine PCAPs

	IGRA	ISD	ERA-Interim	ERA5	
Data type	measurements	measurements	reanalysis	reanalysis	
Horizontal resolution	station data	station data	~79×79 km ²	~31×31 km ²	
Temporal resolution (h)	12	1	6	1	
Stations/grid cell center coordinates and elevation above mean sea level	Budapest, Hungary	47.4333°N 19.1833°E 138 m	47.4333°N 19.1833°E 138 m	47.25°N 19.5°E 126 m	47.53156°N 19.12533°E 168 m
	Szeged, Hungary	46.25°N 20.1°E 82 m	46.25°N 20.1°E 82 m	46.5°N 20.25°E 80 m	46.1254°N 19.9688°E 90 m
Number of vertical pressure levels below 850 hPa (including 850 hPa)	variable (min.: 3, max.: 11, average: 7)	surface data	7	7	
Missing data	Szeged: 0 Budapest: 1 (12 UTC 11th December 2015)	Szeged: 50 Budapest: 28	None	None	

3. Methods

3.1. Producing the reference set of PCAP days

The Daily Weather Reports (DWR website) is a regular product of the Hungarian Meteorological Service (HMS) prepared by experienced synoptic meteorologists. This document describes the European and Hungarian weather situation every day. It contains a map with weather fronts and cloud cover over Europe and some maps with measured data from several locations in Hungary (e.g., daily maximum and minimum temperature, calculated sunshine duration, amount and type of precipitation, maximum wind gust).

In addition to DWR, radiosonde measurements were also used to create a reference set of PCAP days. The main criterion for a PCAP day was the presence of a strong, low level inversion above the measuring station throughout the day (from 00 UTC to the subsequent 00 UTC) according to the radiosonde data.

Major steps in determining local reference PCAP days are shown in Fig. 2. The presence of mid-latitude cyclone was recognized from the front maps of the

DWR. The presence of the following conditions was examined using the textual report: (1) cumulus clouds, (2) cloudy, foggy weather, and (3) European synoptic situation (warm air advection). The expression “cold air pool” is rarely used in the textual report, but when it is used it always refers to a PCAP. Areas of the stations are identified from context. For example „near the capital”, or „central part of Hungary” correspond to Budapest, while „southern part of the country, next to the river Tisza” refers to Szeged.

Producing reference PCAP days data series is a rather time and energy consuming task, and sometimes it is subjective. The benefit of using numerical methods is that objective examinations can be made and they facilitate long-term examinations of PCAPs.

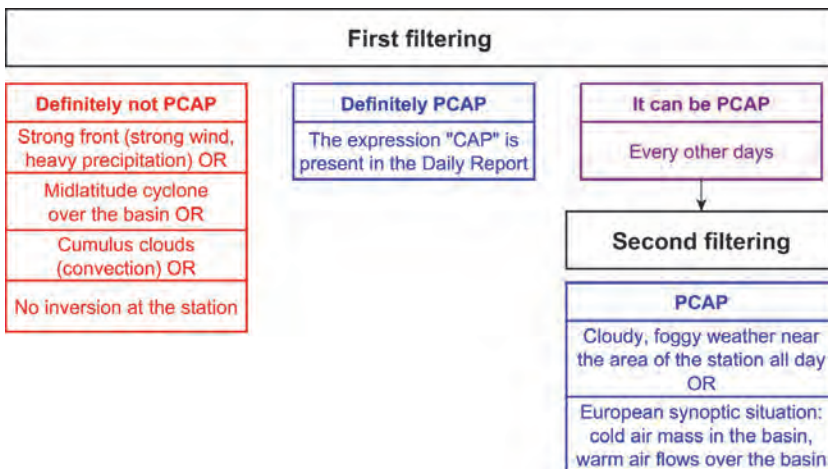


Fig. 2. Major steps in determining local reference PCAP days.

3.2. Persistent temperature inversion

The first numerical method to identify possible PCAP days is based only on atmospheric temperature inversions. To locate the inversion layers, the method designed by *Kahl* (1990) is used. The vertical temperature profile is evaluated from the surface upwards at each location and each time step. The base of a specific inversion is that vertical level where the temperature begins to increase with height for the first time (starting from the surface), while the top of this inversion is that level where temperature begins to decrease with height. If there are more than one inversion layers above each other separated by thin (less than

100 m thick) unstable layer(s), then it is considered as one inversion with embedded unstable layer(s). Inversions thinner than 20 m and inversions with a base above 850 hPa pressure level (i.e., at the general altitude of the Carpathian Mountains) are excluded from the further analysis. If the identified inversion is present all day (i.e., from 00 UTC to the following 00 UTC) according to the available data, then that particular day was taken as a day of persistent inversion. This definition is abbreviated and called INV hereafter.

3.3. Temperature inversion with low wind speed

The second applied definition is the same as INV, but it also considers wind speed at 10 m. If there is inversion and the instantaneous wind speed is lower than 3.1 ms^{-1} (Whiteman *et al.*, 2001) during the whole day (from 00 UTC to the subsequent 00 UTC), then it is defined as a PCAP day. This method is called INV+WSPD.

Wind speed of the lowest level from radiosonde data was used as “10 m wind speed” because of the large number of missing data in ISD (see Section 2). Namely, calculating PCAP days using IGRA combined with ISD data results in 35% missing data in the time series, which would make the comparison with other methods and databases difficult. That is why we used only IGRA data with this method.

3.4. Heat deficit

The third definition is based on the heat deficit (HD, Eq. (1)). HD indicates the energy that is needed for the lapse rate to change to dry adiabatic within an atmospheric column with a 1 m^2 base from the surface to a specific height (Whiteman *et al.*, 2014). The height of the 850 hPa pressure level (see Section 2) was used as a reference. The following formula was used to calculate HD as a function of time:

$$HD(t) = \frac{c_{pd}}{g} \int_{850 \text{ hPa}}^{p_0} [\theta_{850 \text{ hPa}}(t) - \theta(p, t)] dp \quad [J \text{ m}^{-2}], \quad (1)$$

where c_{pd} is the specific heat capacity at constant pressure for dry air ($1005 \text{ J kg}^{-1} \text{ K}^{-1}$), g is the gravitational acceleration (9.81 ms^{-2}), p_0 is the pressure at the lowest level (e.g., surface), $\theta_{850 \text{ hPa}}(t)$ and $\theta(p, t)$ are the potential temperatures at 850 hPa and at a given p level, respectively. The integral part in Eq. (1) is equivalent to the shaded area between the potential temperature profile and the dry adiabatic curve in *Fig. 3*.

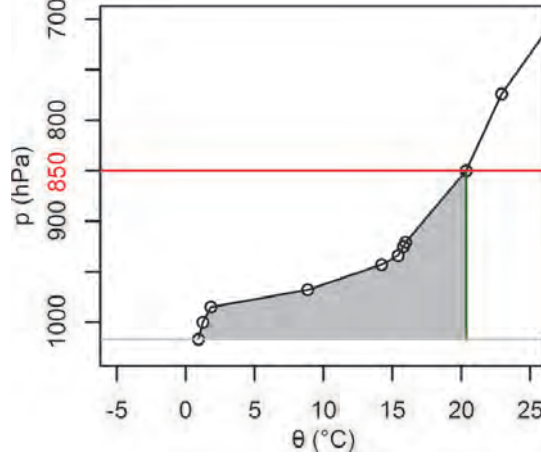


Fig. 3. Illustration of heat deficit using the potential temperature profile (line with circle symbols) at Budapest, 12 UTC, December 26, 2015. The dry adiabatic curve (vertical line) used for HD calculation is also indicated. $HD = c_p/g \times \text{shaded area} = 13.9 \text{ MJm}^{-2}$.

If the value of HD exceeds 6.56 MJm^{-2} during the whole day (from 00 UTC to the subsequent 00 UTC), then it is considered as a PCAP-like day at the given location. The threshold is defined heuristically by minimizing the total error (see Section 3.7, Fig. 5). The short name of this definition is HD6.56.

3.5. Potential temperature deficit

Besides inversion-based and HD-based definitions, potential temperature deficit (PTD; Lareau *et al.*, 2013) is also used to identify PCAP-like weather situations. Potential temperature is calculated at all vertical levels using atmospheric temperature (Eq. (2)):

$$\theta_i(t) = T_i(t) \left(\frac{1000 \text{ hPa}}{p_i(t)} \right)^{\frac{R_d}{c_{pd}}}, \quad (2)$$

where $p_i(t)$ is the pressure at a given level i , $T_i(t)$ and $\theta_i(t)$ are the temperature and the potential temperature, respectively, at the given pressure level in kelvin (K). R_d is the specific gas constant of dry air ($287 \text{ Jkg}^{-1}\text{K}^{-1}$), and c_{pd} is the specific heat of dry air under constant pressure ($1005 \text{ Jkg}^{-1}\text{K}^{-1}$).

The potential temperature of the 850 hPa pressure level (see Section 2) is subtracted from the potential temperature of each level to get the PTD at any given level (Fig. 4):

$$PTD_i(t) = \theta_i(t) - \theta_{850\text{hPa}}(t), \quad (3)$$

where CAP is assumed for vertical levels with $PTD_i < -8.58$ K. If this condition is fulfilled all day long (from 00 UTC to the subsequent 00 UTC) at least at one vertical level, then it is also considered to be a PCAP-like day at the given location. The threshold is defined heuristically by minimizing total error (see Section 3.8, Fig. 6). This definition is called $PTD_{8.58}$ hereafter.

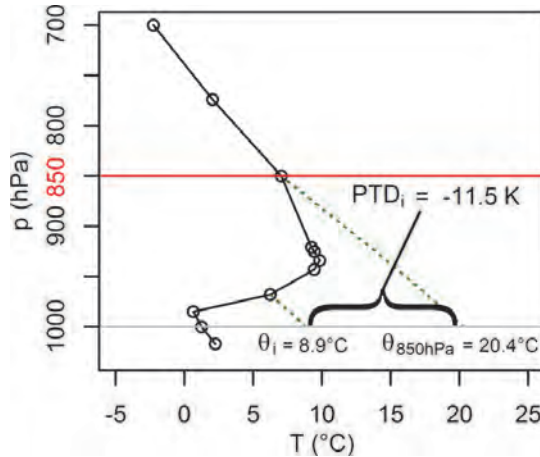


Fig. 4. Illustration of the PTD calculation using the temperature profile (the line with circles indicates the pressure levels of available measurements) at Budapest, 12 UTC, December 26, 2015. Dashed lines indicate dry adiabatic curves used to calculate potential temperatures.

3.6. Evaluating the performance of numerical PCAP identification methods

To compare different numerical PCAP identification methods, three measures derived from the contingency table (Nurmi, 2003, Section 4.1) are examined for all of the methods and databases at both stations. The first measure is the probability of false detection (POFD, Eq. (4)) calculated using false alarms and correct rejections (Table 2):

$$POFD = \frac{\text{False alarms}}{\text{False alarms} + \text{Correct rejections}}, \quad (4)$$

The second measure is called probability of misses (POM) and calculated as follows (Eq. (5)):

$$POM = \frac{\text{Misses}}{\text{Misses} + \text{Hits}}. \quad (5)$$

Furthermore, the sum of POFD and POM defined as total error (ERR) is evaluated.

Table 2. Contingency table

PCAP-like day according to the numerical method?	PCAP-like day according to the reference?	
	Yes	No
Yes	Hits (Correct alarms)	False alarms
No	Misses (False rejections)	Correct rejections

3.7. Threshold for the HD-based method

The threshold of HD-based method (see Section 3.4) was determined by calculating ERR with three databases using different thresholds for Budapest and Szeged. Fig. 5 shows the average ERR (averaging is performed over the databases). The HD threshold values that resulted in the lowest average ERR values are 6.28 MJm^{-2} and 6.84 MJm^{-2} for Budapest and Szeged, respectively. The difference of these values ($\sim 8\%$) is due to the 56 m/46 m/78 m difference in altitude between the two locations using IGRA, ERA-Interim, and ERA5, respectively. The average of the best-performing thresholds for the two cities (6.56 MJm^{-2}) was chosen as a general threshold to identify PCAP days.

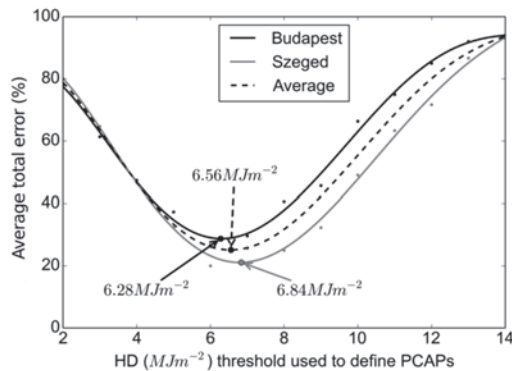


Fig. 5. Determining HD threshold by minimizing the average total error.

3.8. Threshold for the PTD-based method

The threshold of PTD-based method (see Section 3.5) was determined in the same way as in case of HD-based method. The PTD threshold values that resulted in the lowest average ERR values are 8.39 K and 8.86 K for Budapest and Szeged, respectively (Fig. 6). The difference of these values (~5%) is due to the 56 m/46 m/78 m difference in altitude between the two locations using IGRA, ERA-Interim, and ERA5, respectively. The average of the best-performing thresholds for the two cities (8.58 K) was chosen as a general threshold to identify PCAP days.

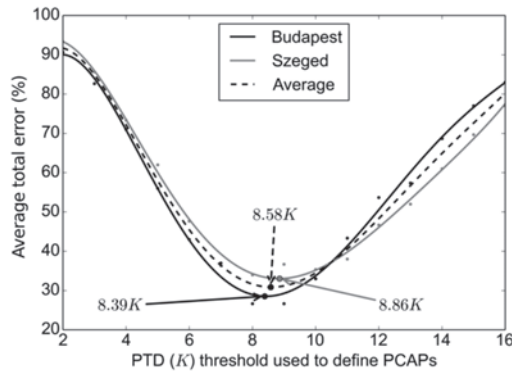


Fig. 6. Determining PTD threshold by minimizing the average total error.

4. Results and discussion

4.1. Weather conditions

Altogether four PCAP events with a duration of 5–17 days occurred over the Carpathian Basin between December 2015 and January 2016 (Table 3). The exact dates for the two examined locations were identified (see Section 3.1) and will be used as reference while comparing the definitions described earlier.

Table 3. List of PCAP events between December 2015 and January 2016 over the Carpathian Basin on the basis of Daily Weather Reports of HMS and radiosonde measurements. Non-continuous event means that PCAP conditions were not present within the period up to maximum 1 day

	First day	Last day	Duration (days)	Continuous?
PCAP1	Budapest: December 4, 2015 Szeged: December 5, 2015	December 9, 2015	Budapest: 6 Szeged: 5	yes
PCAP2	December 12, 2015	December 28, 2015	17	yes
PCAP3	January 1, 2016	January 5, 2016	5	yes
PCAP4	January 25, 2016	January 30, 2016	6	no

At the beginning of December 2015, a cold front followed by a warm front passed over the Carpathian Basin. Then, a high-pressure system formed over the basin (Fig. 7), and warm air was advected to the area aloft resulting in the formation of PCAP1 on December 4. From that day, anticyclones governed weather across the southern part of Europe, while cyclones were found at the northern part. The Carpathian Basin was located near the border of these areas within the high-pressure part. A cold front brought cold air mass with strong wind on December 10 mixing the air of the basin and destroying the PCAP.

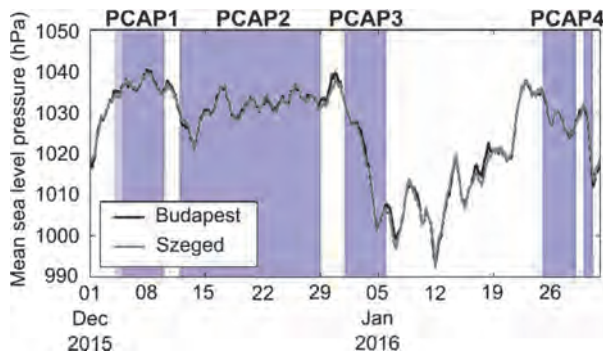


Fig. 7. Mean sea level pressure in Budapest (black) and Szeged (grey) between December 2015 and January 2016. Hourly data are from ISD dataset. Reference PCAP days are also indicated (shaded areas; darker: PCAP present at both stations, light: it is present only at Budapest).

Two days later, the southern anticyclones reached the Carpathian Basin again and PCAP2 formed. The strong westerly wind over Western Europe weakened on

December 27, and the air pressure started to increase over Scandinavia and the Baltic region forming an extended anticyclone. Frosty, dry air mass advected from Siberia at the front side of the high pressure system. It reached the Carpathian Basin on December 29 leading to the dissipation of this PCAP. The temperature decreased by about 10 °C during the following three days (*Fig. 8*).

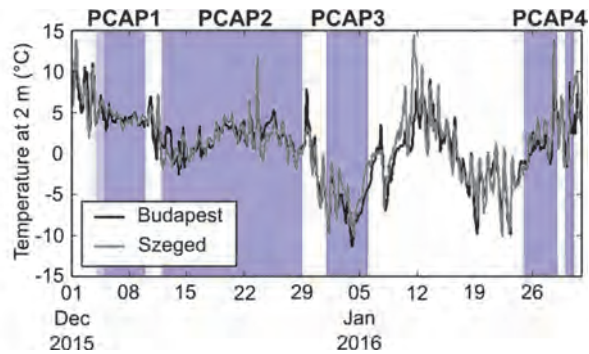


Fig. 8. Temperature at 2 m in Budapest (black) and Szeged (grey) between December 2015 and January 2016. Hourly data are from ISD dataset. Reference PCAP days are also indicated (shaded areas; darker: PCAP present at both stations, light: it is present only at Budapest).

Siberian air filled the Carpathian Basin after the PCAP2 period. Warmer and humid air mass advected over the basin from Western Europe leading to the formation of PCAP3. This event was different from other typical PCAPs. Fog did not occur at the beginning of this event because of the low relative humidity (*Fig. 9*) of the arriving Siberian air mass. In addition to that, the daily maximum speed of wind gusts was below 8 ms⁻¹ during PCAP1 and PCAP2, but in this case, it was higher: 8–10 ms⁻¹ wind gusts occurred (*Fig. 10*). Also, the air pressure decreased by 30 hPa during PCAP3 to about 1000 hPa (*Fig. 7*). However, PCAPs are usually anticyclonic weather events, so the mean sea level air pressure should be higher than 1013 hPa. According to the maps of the DWR, there was a pressure ridge over the Carpathian Basin during the PCAP3. It means that the pressure was higher in the basin than over some of the neighboring areas. Additionally, the inversion was thick (sometimes more than 1 km) during PCAP3, so the weather inside the basin was quasi-independent from the synoptic weather formations. Considering this situation, the pressure decrease can be understood, if the Mediterranean cyclone passed from west to east near the Carpathian Basin on January 3 is taken into account. Another Mediterranean cyclone with a quite strong warm front passed over the Carpathian Basin on January 6 and led to the dissipation of PCAP3.

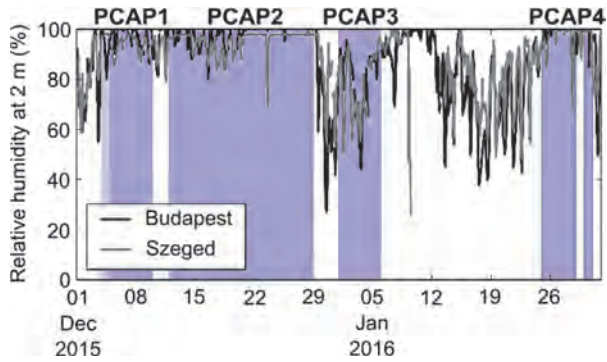


Fig. 9. Relative humidity at 2 m in Budapest (black) and Szeged (grey) between December 2015 and January 2016. Hourly data are from ISD dataset. Reference PCAP days are also indicated (shaded areas; darker: PCAP present at both of the stations, light: it is present only at Budapest).

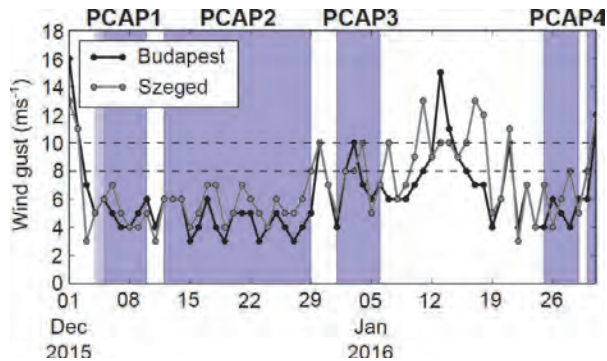


Fig. 10. Daily maximum wind gusts in Budapest (black) and Szeged (grey) between December 2015 and January 2016. Data source: Daily Weather Reports. Reference PCAP days are also indicated (shaded areas; darker: PCAP present at both stations, light: it is present only at Budapest).

A warm front approached the Carpathian Basin on January 8, and the basin was located in the warm sector of a mid-latitude cyclone from 9th to 11th of January. The warm advection caused temperature inversion, which was similar to the inversion during PCAPs. However, this event was definitely not a PCAP but a warm front.

Finally, PCAP4 was formed gradually after a warm front that had passed over the basin on January 23. The inversion strengthened day by day and became a typical PCAP inversion by January 25. Warm air mass advected from west aloft resulting in the changes of the inversion on January 27. It became a lower level inversion and the temperature difference between its base and top strongly increased. A cold front destroyed the PCAP for one day on January 29. Behind the front, the sky was clear and it led to fog formation over large areas during the night of January 29. It means that the PCAP returned within one day. The cold front that passed over the basin on January 31 destroyed this PCAP of short duration.

4.2. Numerical prediction and the reference set of PCAP days

The reference PCAP days between December 1, 2015 and January 31, 2016 summarized for Budapest and Szeged are indicated in the first line of *Fig. 11*. There is some uncertainty in the set of reference PCAP days. On one hand, the names of the cities (Budapest and Szeged) are rarely mentioned in the DWR, so the areas of the stations are identified from context (see Section 3.1). The exact location of the evaluated sites cannot be determined using the DWR. On the other hand, data of the gridded datasets correspond to an exact grid cell. This difference could lead to different results. Furthermore, there are some weather situations that are very complex, e.g., PCAP3 when it is quite challenging to decide whether or not it is a PCAP. In addition to these, it is difficult to determine the exact time of PCAP creation and dissipation, because the DWR is descriptive and the time resolution of IGRA is 12 h. If the inversion is dissipated for 4–7 hours in the afternoon, it cannot be recognized using the radiosonde measurements unlike using reanalyses with 3 h or 6 h temporal resolution. Therefore, it will be defined as PCAP-like day using IGRA, but it will not be defined as PCAP-like day using reanalyses. Note, that thin (< 20 m) inversions can be unambiguously excluded using the radiosonde measurements.

The results for the four numerical PCAP identification methods are also shown in *Fig. 11*. Each method was applied to three databases, which are also indicated at the beginning of the lines. This complex figure can be examined from several points of view. It is possible to compare 1) various numerical methods to the reference, 2) measurement-based results to reanalysis-based results, 3) the two reanalyses, 4) results from individual stations to each other.

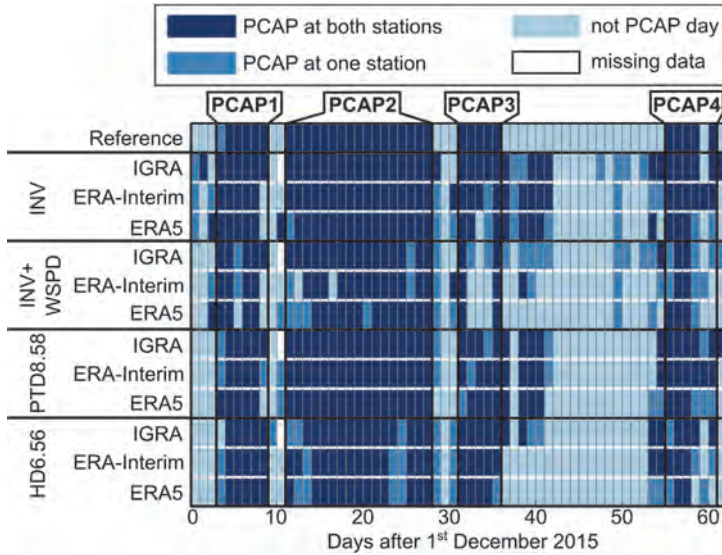


Fig. 11. The temporal distribution of PCAP days according to different definitions using different databases for two stations (Budapest and Szeged, Hungary) between December 1, 2015 and January 31, 2016. The reference is based on the Daily Weather Reports of the HMS and the vertical distribution of air temperature.

4.2.1. Numerical methods vs. reference

In general, the four PCAP periods can be identified using any of the methods (Fig. 11). During PCAP conditions, the values of HD usually exceed the determined threshold (Fig. 12) even during the special PCAP3 period. Some PCAP days were indicated falsely before PCAP4 using INV and INV+WSPD method. These are caused by thin inversion layers (~80-90 m thick), not PCAP-like inversions. PCAP3 period is almost fully or partly missing when the INV+WSPD method is used. The explanation for INV+WSPD's underperformance is the unusual high wind speeds during this period (Fig. 10). This suggests that wind affects PCAPs less in large basins than in smaller valleys. This emphasizes the need for careful consideration of the method and meteorological parameters to be used over different terrains.

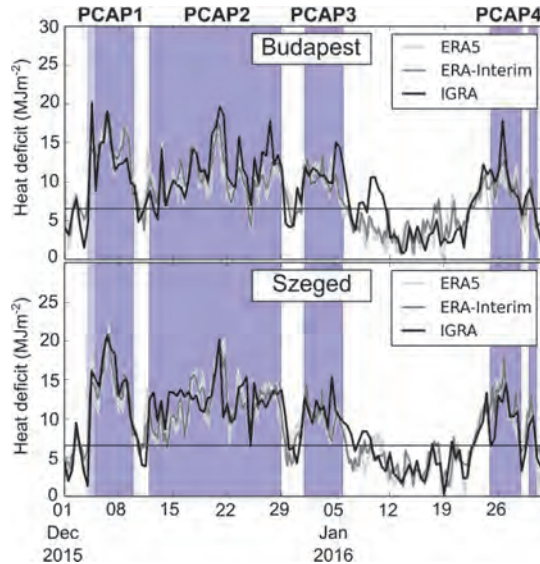


Fig. 12. Heat deficit in Budapest (top) and Szeged (bottom) between December 2015 and January 2016. The threshold used to define PCAP conditions is indicated by a horizontal line. The reference PCAP days are also indicated (shaded areas; darker: PCAP present at both stations, light: it is present only at Budapest).

PCAP3 is extended when INV or PTD8.58 methods are used with any of the databases. The inversion caused by a warm front described in Section 4.1 was indicated by PTD, but the values of the HD were below the given threshold. This situation is particularly apparent when reanalysis data was used.

4.2.2. Measurements vs. reanalyses

The most obvious difference between measurements and reanalyses can be observed in case of PCAP3 using HD6.56 method (Fig. 11). The extension of PCAP3 is present when IGRA measurements are used. These false detections are not found with reanalysis data. This difference probably comes from the difference between the databases: measurements are station data (representing single point-like location), but reanalyses contain gridded data (the values are averaged over entire grid cells). The size of the grid cells of ERA-Interim and ERA5 is approximately 6000 km² and 1000 km², respectively. The vertical resolutions also differ: reanalyses offer data on fixed pressure levels with coarser vertical resolution than the measurements. Therefore, strong local inversions may be missing from reanalyses. This leads to a decrease in HD. The days of the extension after PCAP3 were not PCAP days according to the reference. However, they were PCAP days at least over one station according to the measurements.

Besides the differences in spatial resolution, the temporal resolution also affects the results. For instance, the end of PCAP1 can illustrate this well. When only two measurements are used daily (with a difference of 12 h between them), the PCAP dissipates later than in the case of 6 hourly or 1 hourly reanalyses data. In this case, the IGRA measurements are more similar to the reference than reanalyses. Note that the reference data series was created using IGRA in addition to the DWR. The reference data series has some uncertainty in dissipation time of PCAPs due to the temporal resolution of IGRA and DWR. It means that the reanalyses can be more representative than the measurements because of their finer temporal resolution.

The radiosonde measurements are used in the reanalyses through data assimilation, therefore, the vertical temperature profiles of the three databases at 00 and 12 UTC (when radiosonde measurements are performed) should be similar to each other. However, large differences can be seen in *Fig. 13* between the vertical temperature profiles of measurements and reanalyses. The data assimilation method and the spatial resolution could result in this difference. High correlations between the time series of HD are also expected. The Spearman's correlation coefficients of the two-month-long HD time series between ERA-Interim and IGRA are slightly higher (0.86 and 0.87 at Budapest and Szeged, respectively) than between ERA5 and IGRA (0.81 and 0.84 at Budapest and Szeged, respectively).

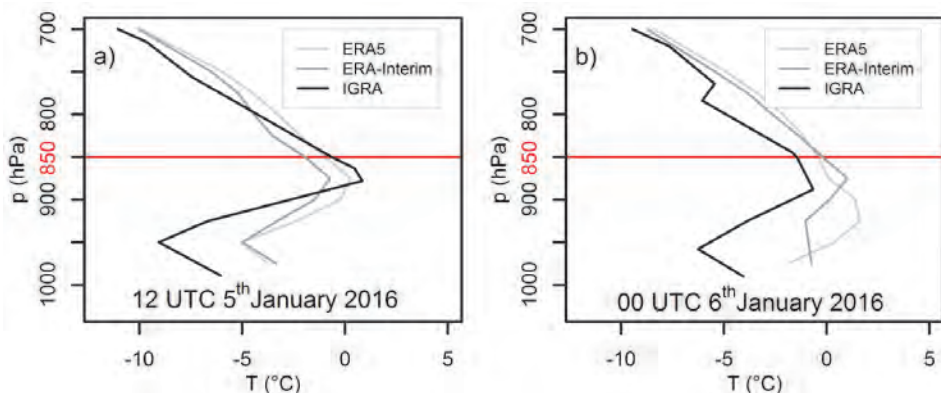


Fig. 13. Vertical distribution of atmospheric temperature at Budapest at a) 12 UTC, January 5, 2016 and b) 00 UTC, January 6, 2016 according to radiosonde measurements (black), ERA-Interim (dark grey), and ERA5 (light grey) databases.

4.2.3. ERA-Interim vs. ERA5

The different temporal resolution causes differences between the results of the two reanalyses, too. In general, the results of ERA-Interim and ERA5 are similar to each other when using PTD8.58 and HD6.56 method (*Fig. 11*). In general, the vertical distributions of atmospheric temperature based on ERA-Interim and ERA5 are also more similar to each other than the radiosonde measurements (e.g., 12 UTC, January 5, 2016, *Fig. 13a*). The Spearman's correlation coefficient of the two-month-long HD time series between ERA-Interim and ERA5 is 0.93 and 0.95 at Budapest and Szeged, respectively. Despite the high values, there are differences between the results of the two reanalyses. For example, the dissipation of PCAP3 is predicted one day earlier at Budapest when using HD6.56 method with ERA5 data (the value of HD fell below the threshold at 20 UTC, January 5). The top of the inversion was higher in ERA-Interim than in ERA5 at 00 UTC, January 6 (*Fig. 13b*). Therefore, HD was lower in ERA5 (5.8 MJm^{-2}) than in ERA-Interim (7.1 MJm^{-2}) and fell below the 6.56 MJm^{-2} threshold.

Additionally, there are differences between the two reanalyses during PCAP4. The results of ERA-Interim are closer to the IGRA measurements and are more similar to the reference than ERA5 results. This is probably caused by the different spatial resolution: ERA-Interim has coarser spatial resolution than ERA5, so it is more representative for a larger area and it fits better to the reference (it is difficult to delimit the exact location of the station using DWR, see Section 3.1).

4.2.4. Comparing the identifications at the two test locations

There is just one day (December 4, 2015) when the PCAP was present only at Budapest according to the reference database. However, the results of numerical PCAP identification differ at the two stations on several (5–18) days (*Fig. 11*). Most of the differences (10–18 days) are present using the INV+WSPD method because, in general, the daily maximum wind gusts were greater at Szeged than in Budapest (*Fig. 10*). The least differences (5–7 days) are present using the PTD8.58 method. Therefore, this method seems to be the most location-independent. Besides, numerical methods are applied to well-defined areas (e.g., precise location, grid cell) in contrast to the reference, in which the areas around the stations are identified from context. Because of the distance between the two stations, different results can be expected. This emphasizes the importance of involving more stations and using data covering larger area to determine CAPs extended to large basins. The method of defining the reference PCAP days data series is also suitable to describe extended PCAPs.

4.3. Evaluation of errors

POM, POFD, and ERR are shown in Fig. 14. In general, the values of POFD are higher than POM almost in all cases. It means that the methods rather overestimate the number of PCAP-like days. High values of POM are present when the INV+WSPD method was used, because wind speeds were high during PCAP3 and towards the end of PCAP4 (Fig. 10). An outstanding value of POFD is found in case of INV method because of thin inversion layers. PTD8.58 is the other method, which substantially overestimates the number of PCAP days.

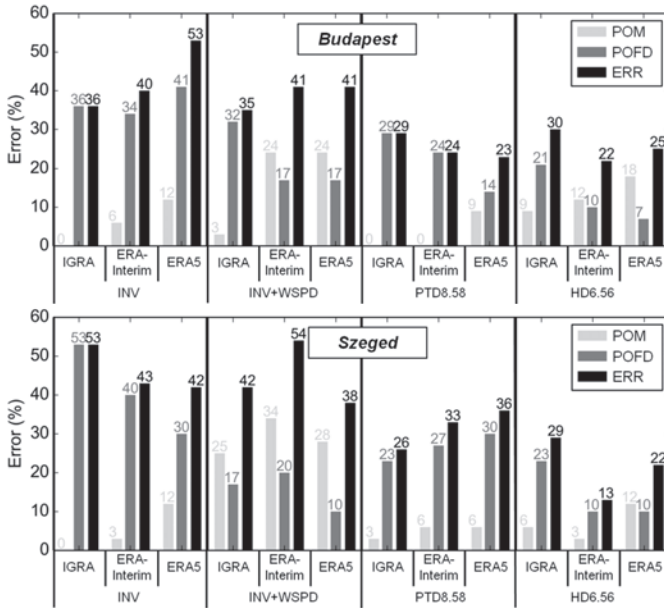


Fig. 14. Probability of miss (POM) and probability of false detection (POFD), and sum of them (ERR) at Budapest (top) and Szeged (bottom).

4.3.1. Differences in the errors of the different numerical methods

In general, the results are similar at Budapest and Szeged, when the PTD8.58 or the HD6.56 methods were used to identify PCAPs (Fig. 14). Additionally, POM values are similar also when using the INV method. There are larger differences between the results of the two stations when applying INV or INV+WSPD method. Consequently, it is recommended to use the PTD8.58 or (more preferably) the HD6.56 method to identify PCAPs over large basins rather than inversion-based methods.

4.3.2. Evaluation of average total error

The value of ERR averaged over the stations is shown in *Fig. 15* for the different methods. The lowest average ERR is produced by using HD6.56 method (24%), and the PTD8.58 method results in the second lowest value (29%). When the two gridded databases are compared, the use of ERA-Interim as source data results in lower average ERR (18%) than the use of ERA5 (24%) in case of HD6.56 method. According to these results, HD6.56 definition is preferred for the local identification of PCAPs using ERA-Interim data.

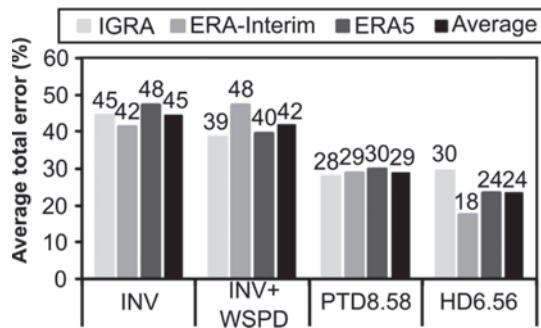


Fig. 15. Value of average total error for different numerical methods.

5. Summary and conclusions

In this study, it was examined how effective the existing numerical CAP definitions are in cases of PCAP events in the Great Hungarian Plain. Four different methods were compared to the reference and to each other during two consecutive winter months (December 2015 and January 2016). The considered methods have been adapted from other authors who examined CAPs in small valleys and basins. In order to determine which method performs better, a reference PCAP days data series was created using the regular DWRs of the HMS and radiosonde measurements. After applying the numerical methods to the various datasets, the probability of misses and false detections and the sum of them (total error) were calculated.

On the basis of the presented analysis, the following conclusions can be drawn:

- (1) Wind affects PCAPs less in large basins than in smaller valleys.

- (2) The lowest value of total error is produced by using the HD6.56 method (heat deficit below 850 hPa is larger than 6.56 MJm^{-2}), which highlights the potential further use of this method in numerical-based objective definition of PCAP.
- (3) From the three examined databases, the use of ERA-Interim data yielded the lowest value of total error when it was used with the HD6.56 method.

Overall, HD6.56 definition is preferred for the local identification of PCAPs using gridded analyses dataset providing that the reference PCAP days is selected according to the description in Section 3.1. Results obtained by using PTD method are also promising, because the errors are only slightly higher than in case of HD6.56.

The present study is not exhaustive and has limitations: (i) textual Daily Weather Reports were (also) used to determine the reference PCAP days data series, making the study partly subjective; (ii) we examined only a two-month-period; (iii) we processed the data of only 2 stations, because there are only two radio sounding stations in Hungary; (iv) the measures used do not take into account cloud formation (or at least the value of relative humidity). One possibility to improve the predictions can be if the measures used in this study were combined with other variables (e.g., relative humidity, tendency of mean sea level pressure, etc.) so that, for example, the inversion caused by the warm front and the inversion present in the PCAPs could be distinguished (see days after PCAP3, Section 4.2.1). Automation of the procedure of obtaining the reference set of PCAP days is possible and is planned using, e.g., SYNOP telegrams and radiosonde data. This would serve either as an alternative method for determining PCAP conditions objectively, and would also make it possible to extend this study in time and space (i.e., to more locations) in order to refine the numerical definitions examined in this work. The numerical definition(s) could be used in synoptic-climatological research and air quality studies (e.g., *Haszpra et al.*, 2019) as well as by weather forecasters during post-processing of numerical weather prediction models. Another possible utilization of the suggested numerical method is forecasting the outages in the production of green energy. Solar and wind energy production is heavily influenced by the weather. Having a foggy or cloudy PCAP for several days, or even weeks, with windless weather can prevent the use of these renewable sources. This is why it is important to know the frequency over time and average length of PCAPs, and how these features are likely to change in the future.

Acknowledgements: This work was supported by the Széchenyi 2020 programme, the European Regional Development Fund and the Hungarian Government via the AgroMo project [grant number GINOP-2.3.2-15-2016-00028]; the ELTE Institutional Excellence Program [grant number TKP2020-IKA-05] financed by the Hungarian Ministry of Human Capacities; and the Hungarian National Research, Development and Innovation Fund [grant numbers K-120605 and K-129162]. This study is a contribution to the PannEx Regional Hydroclimate Project of the World Climate Research Programme (WCRP) Global Energy and Water Exchanges (GEWEX) Project.

The analysis used modified Copernicus Climate Change Service information (ERA-Interim and ERA5 data) [2019].

The first author of this paper would like to say thank to *András Zénó Gyöngyösi* for his help and guidance in the world of cold air pools.

References

- Baasandorj, M., Hoch, S.W., Bares, R., Lin, J.C., Brown, S.S., Millet, D.B., Martin, R., Kelly, K., Zarzana, K.J., Whiteman, C.D., Dube, W.P., Tonnesen, G., Jaramillo, I.C., and Sohl, J.*, 2017: Coupling between Chemical and Meteorological Processes under Persistent Cold-Air Pool Conditions: Evolution of Wintertime PM_{2.5} Pollution Events and N₂O₅ Observations in Utah's Salt Lake Valley. *Environ. Sci. Technol.* 51, 5941–5950. <https://doi.org/10.1021/acs.est.6b06603>
- Chachere, C.N. and Pu, Z.*, 2016: Connections Between Cold Air Pools and Mountain Valley Fog Events in Salt Lake City. *Pure Appl. Geophys.* 173, 3187–3196. <https://doi.org/10.1007/s00024-016-1316-x>
- Chemel, C., Arduini, G., Staquet, C., Largeron, Y., Legain, D., Tzanos, D., and Paci, A.*, 2016: Valley heat deficit as a bulk measure of wintertime particulate air pollution in the Arve River Valley. *Atmos. Environ.* 128, 208–215. <https://doi.org/10.1016/j.atmosenv.2015.12.058>
- Conangla, L., Cuxart, J., Jiménez Maria, A., Martínez-Villagrasa, D., Miró Josep, R., Tabarelli, D., and Zardi, D.*, 2018: Cold-air pool evolution in a wide Pyrenean valley. *Int. J. Climatol.* 38, 2852–2865. <https://doi.org/10.1002/joc.5467>
- Cuxart, J., Yagüe, C., Morales, G., Terradellas, E., Orbe, J., Calvo, J., Fernández, A., Soler, M.R., Infante, C., Buenestado, P., Espinalt, A., Joergensen, H.E., Rees, J.M., Vilá, J., Redondo, J.M., Cantalapedra, I.R., and Conangla, L.*, 2000: Stable Atmospheric Boundary-Layer Experiment in Spain (SABLES 98): A Report. *Bound.-Layer Meteorol.* 96, 337–370. <https://doi.org/10.1023/A:1002609509707>
- Dee, D.P., Uppala, S.M., Simmons, A.J., Berrisford, P., Poli, P., Kobayashi, S., Andrae, U., Balmaseda, M.A., Balsamo, G., Bauer, P., Bechtold, P., Beljaars, A.C.M., van de Berg, L., Bidlot, J., Bormann, N., Delsol, C., Dragani, R., Fuentes, M., Geer, A.J., Haimberger, L., Healy, S.B., Hersbach, H., Hólm, E.V., Isaksen, L., Kållberg, P., Köhler, M., Matricardi, M., McNally, A.P., Monge-Sanz, B.M., Morcrette, J.-J., Park, B.-K., Peubey, C., de Rosnay, P., Tavolato, C., Thépaut, J.-N., and Vitart, F.*, 2011: The ERA-Interim reanalysis: configuration and performance of the data assimilation system. *Quart. J. Roy. Meteorol. Soc.* 137, 553–597. <https://doi.org/10.1002/qj.828>
- Deng, X., Cao, W., Huo, Y., Yang, G., Yu, C., He, D., Deng, W., Fu, W., Ding, H., Zhai, J., Cheng, L., and Zhao, X.*, 2019: Meteorological conditions during a severe, prolonged regional heavy air pollution episode in eastern China from December 2016 to January 2017. *Theor. Appl. Climatol.* 135, 1105–1122. <https://doi.org/10.1007/s00704-018-2426-4>
- Durre, I., Vose, R.S., and Wuertz, D.B.*, 2006: Overview of the Integrated Global Radiosonde Archive. *J. Climat.* 19, 53–68. <https://doi.org/10.1175/JCLI3594.1>
- DWR website: Daily Weather Reports of the Hungarian Meteorological Service. (in Hungarian) https://www.met.hu/idojaras/aktualis_idojaras/napijelentes/ (accessed 4 April 2019)
- ERA5 dataset: Copernicus Climate Change Service (C3S), 2017: ERA5: Fifth generation of ECMWF atmospheric reanalyses of the global climate. Copernicus Climate Change Service Climate Data Store (CDS), accessed 18 February 2019, available from <https://cds.climate.copernicus.eu/cdsapp#!/home>
- ERA-Interim dataset: European Centre for Medium-range Weather Forecast (ECMWF), 2011: The ERA-Interim reanalysis dataset, Copernicus Climate Change Service (C3S), accessed 18 February 2019, available from <https://www.ecmwf.int/en/forecasts/datasets/archive-datasets/reanalysis-datasets/era-interim>

- Haszpra, L., Ferenczi, Z., and Barcza, Z., 2019: Estimation of Greenhouse Gas Emission Factors Based on Observed Covariance of CO₂, CH₄, N₂O and CO Mole Fractions. *Environ. Sci. Eur.* 31, 95. <https://doi.org/10.1186/s12302-019-0277-y>
- Hersbach, H., Bell, W., Berrisford, P., Horányi, A., Muñoz Sabater, J., Nicolas, J., Radu, R., Schepers, D., Simmons, A., Soci, C., and Dee, D., 2019. Global reanalysis: goodbye ERA-Interim, hello ERA5. *ECMWF Newsl.* 159, 17–24. <https://doi.org/10.21957/vf291hehd7>
- IGRA dataset: Durre, I.; Xungang, Y.; Vose, R. S.; Applequist, S.; and Arnfield, J., 2016: Integrated Global Radiosonde Archive (IGRA), Version 2. [Derived]. NOAA National Centers for Environmental Information. <http://doi.org/10.7289/V5X63K0Q> (accessed 14 October 2018).
- Iijima, Y. and Shinoda, M., 2000: Seasonal changes in the cold-air pool formation in a subalpine hollow, central Japan. *Int. J. Climatol.* 20, 1471–1483. [https://doi.org/10.1002/1097-0088\(200010\)20:12<1471::AID-JOC554>3.0.CO;2-6](https://doi.org/10.1002/1097-0088(200010)20:12<1471::AID-JOC554>3.0.CO;2-6)
- ISD dataset: NOAA National Centers for Environmental Information, 2001: Global Surface Hourly [Integrated Surface Global Hourly data]. NOAA National Centers for Environmental Information, accessed 26 July 2019, available from <https://data.nodc.noaa.gov/cgi-bin/iso?id=gov.noaa.ncdc:C00532>
- Kahl, J.D., 1990: Characteristics of the low-level temperature inversion along the Alaskan Arctic coast. *Int. J. Climatol.* 10, 537–548. <https://doi.org/10.1002/joc.3370100509>
- Kahl, J.D., Serreze, M.C., and Schnell, R.C., 1992. Tropospheric low-level temperature inversions in the Canadian Arctic. *Atmosphere-Ocean* 30, 511–529. <https://doi.org/10.1080/07055900.1992.9649453>
- Lareau, N.P., Crosman, E., Whiteman, C.D., Horel, J.D., Hoch, S.W., Brown, W.O.J., and Horst, T.W., 2013. The Persistent Cold-Air Pool Study. *Bull. Amer. Meteorol. Soc.* 94, 51–63. <https://doi.org/10.1175/BAMS-D-11-00255.1>
- Largerón, Y. and Staquet, C., 2016a: Persistent inversion dynamics and wintertime PM10 air pollution in Alpine valleys. *Atmos. Environ.* 135, 92–108. <https://doi.org/10.1016/j.atmosenv.2016.03.045>
- Largerón, Y. and Staquet, C., 2016b: The Atmospheric Boundary Layer during Wintertime Persistent Inversions in the Grenoble Valleys. *Front. Earth Sci.* 4, e40. <https://doi.org/10.3389/feart.2016.00070>
- Llasat, M.C. and Puigcerver, M., 1990: Cold air pools over Europe. *Meteorol. Atmospheric Phys.* 42, 171–177. <https://doi.org/10.1007/BF01314823>
- Nurmi, P., 2003: Recommendations on the verification of local weather forecasts. *ECMWF Tech. Memo.* 430, 19. <https://doi.org/10.21957/y1z1thg5l>
- Price, J.D., Vosper, S., Brown, A., Ross, A., Clark, P., Davies, F., Horlacher, V., Claxton, B., McGregor, J.R., Hoare, J.S., Jemmett-Smith, B., and Sheridan, P., 2011: COLPEX: Field and Numerical Studies of a Region of Small Hills. *Bull. Amer. Meteorol. Soc.* 92, 1636–1650. <https://doi.org/10.1175/2011BAMS3032.1>
- Reeves, H.D., Elmore, K.L., Manikin, G.S., and Stensrud, D.J., 2011: Assessment of Forecasts during Persistent Valley Cold Pools in the Bonneville Basin by the North American Mesoscale Model. *Weather Forecast* 26, 447–467. <https://doi.org/10.1175/WAF-D-10-05014.1>
- Reeves, H.D. and Stensrud, D.J., 2009: Synoptic-Scale Flow and Valley Cold Pool Evolution in the Western United States. *Weather Forecast* 24, 1625–1643. <https://doi.org/10.1175/2009WAF2222234.1>
- Smith, A., Lott, N., and Vose, R., 2011: The Integrated Surface Database: Recent Developments and Partnerships. *Bull. Amer. Meteorol. Soc.* 92, 704–708. <https://doi.org/10.1175/2011BAMS3015.1>
- Tóth, P., 1984: Parametrizáció bevezetése hideg légpárnák keletkezésének és feloszlásának analízise céljából. Országos Meteorológiai Szolgálat, Meteorológiai Tanulmányok, 51. (In Hungarian)
- Vitasse, Y., Klein, G., Kirchner, J.W., and Rebetez, M., 2017: Intensity, frequency and spatial configuration of winter temperature inversions in the closed La Brevine valley, Switzerland. *Theor. Appl. Climatol.* 130, 1073–1083. <https://doi.org/10.1007/s00704-016-1944-1>
- Whiteman, C.D., Bian, X., and Zhong, S., 1999: Wintertime Evolution of the Temperature Inversion in the Colorado Plateau Basin. *J. Appl. Meteorol.* 38, 1103–1117. [https://doi.org/10.1175/1520-0450\(1999\)038<1103:WEOTTI>2.0.CO;2](https://doi.org/10.1175/1520-0450(1999)038<1103:WEOTTI>2.0.CO;2)

- Whiteman, C.D., Hoch, S.W., Horel, J.D., and Charland, A., 2014: Relationship between particulate air pollution and meteorological variables in Utah's Salt Lake Valley. *Atmos. Environ.* 94, 742–753. <https://doi.org/10.1016/j.atmosenv.2014.06.012>
- Whiteman, C.D., Muschinski, A., Zhong, S., Fritts, D., Hoch, S.W., Hahnenberger, M., Yao, W., Hohreiter, V., Behn, M., Cheon, Y., Clements, C.B., Horst, T.W., Brown, W.O.J., and Oncley, S.P., 2008: Metcrax 2006: Meteorological Experiments in Arizona's Meteor Crater. *Bull. Amer. Meteorol. Soc.* 89, 1665–1680. <https://doi.org/10.1175/2008BAMS2574.1>
- Whiteman, C.D., Zhong, S., Shaw, W.J., Hubbe, J.M., Bian, X., and Mittelstadt, J., 2001: Cold Pools in the Columbia Basin. *Weather Forecast* 16, 432–447. [https://doi.org/10.1175/1520-0434\(2001\)016<0432:CPITCB>2.0.CO;2](https://doi.org/10.1175/1520-0434(2001)016<0432:CPITCB>2.0.CO;2)
- Wolyn, P.G. and McKee, T.B., 1989: Deep Stable Layers in the Intermountain Western United States. *Mon. Weather Rev.* 117, 461–472. [https://doi.org/10.1175/1520-0493\(1989\)117<0461:DSLITI>2.0.CO;2](https://doi.org/10.1175/1520-0493(1989)117<0461:DSLITI>2.0.CO;2)
- Yu, L., Zhong, S., and Bian, X., 2017: Multi-day valley cold-air pools in the western United States as derived from NARR. *Int. J. Climatol.* 37, 2466–2476. <https://doi.org/10.1002/joc.4858>

IDŐJÁRÁS

Quarterly Journal of the Hungarian Meteorological Service
Vol. 125, No. 2, April – June, 2021, pp. 195–209

Comparison of the performances of GEP, ANFIS, and SVM artificial intelligence models in rainfall simulation

Seyed Mostafa Tabatabaei*, Mohammad Nazeri Tahroudi, and
Bahareh Sadat Hamraz

Department of Water Engineering
University of Birjand, Birjand, Iran

**Corresponding author E-mail: tabatabaei1984@yahoo.com*

(Manuscript received in final form June 15, 2020)

Abstract—In this paper, evaluation the performances of GEP (gene expression programming), ANFIS (adaptive fuzzy interference system), and SVM (support vector machine) artificial intelligence models in two scales of daily and monthly rainfall data from Urmia meteorological station (Iran) and monthly rainfall data from Diata meteorological station (India) was used in rainfall simulation. The correlation coefficient of observed and simulated values was evaluated by the R^2 criterion, simulation error was evaluated by the root mean square error (RMSE), and MB criteria and model efficiency were evaluated by the Nash-Sutcliffe method. The results show that the correlation coefficients in the GEP model based on daily data from Urmia station and monthly data from Diata station are 23 and 58%, respectively, and R^2 in simulation with GEP is estimated to be 55% lower than with the other two models. The R^2 range in both ANFIS and SVM models varies from 91 to 93%. On average, the RMSE values in the GEP simulation are 50% and 55% higher than the ANFIS ratio for daily and monthly data at the two stations, respectively, and the RMSE values of ANFIS model are 1% and 3% higher than those of the SVM at Urmia and Diata stations, respectively. The bias values of the GEP model are 72% and 60% higher than those of ANFIS at Urmia and Diata stations, respectively. The GEP efficiency factors are 56% and 61% lower than those of ANFIS at Urmia and Diata stations, respectively. And the ANFIS efficiency ratio is 1 and 2% lower than SVM in Urmia and Diata stations, respectively. Therefore, rainfall simulation with the SVM model is associated with a lower error rate and better efficiency, the ANFIS model is close to the efficiency of SVM, and the GEP model is not suitable for rainfall simulation.

Key-words: artificial intelligence models, gene expression programming, rainfall simulation, support vector machine

1. Introduction

One way to study hydrological systems and water resources to predict the behavior of its components is to use a model, or in other words, to simulate its processes (Refsgaard and Knudsen, 1996). Rainfall is an important factor that is directly involved in the hydrological cycle. Simulation and forecasting of this factor play an important role in hydrological planning and water and agricultural resources. (Refsgaard et al., 2005) Water science experts pay special attention to modeling and forecasting effective strategies in rainfall analysis and its effect on agricultural activities (Hoogenboom, 2000). Moreover, the results of a simulation model can be used to verify or correct the data (Sentelhas et al., 2001). Intelligent models, meanwhile, have shown a relatively high ability to simulate and predict nonlinear hydrological time series (Nourani and Komasi, 2013). These models include the gene expression programming (GEP), the adaptive fuzzy inference system (ANFIS), and the support vector machine (SVM) (Dibike, 2006; Jang, 1993; Ferreira, 2001).

The GEP model, developed by Ferreira (2001), is an evolutionary method based on Darwin's theory of evolution and on the ability to simulate completely nonlinear and dynamic processes (Alvisi et al., 2005). The ANFIS structure is equivalent to a post-diffusion network that uses the neural network learning algorithm in combination with fuzzy reasoning to create a mapping between the input and output space (Jang, 1993). The SVM method is also one of the supervised learning methods that can be used for both classification and regression. This method is based on the Vapnik's method of statistical learning theory (Vapnik, 1998), and it is a method for binary classification in the space of desired properties. The SVM is essentially a two-class binder that separates classes by a linear boundary. In this method, the closest samples to the decision boundary are called support vectors (Hamel, 2011). The mentioned models have been used in water engineering so far, the following are some of the researches conducted on them. Ustoorikar and Deo (2008) used GEP to estimate incomplete data on wave heights in the Gulf of Mexico, and they found that the structure was accurate in predicting time series data. AYTEK and Kisi (2008) used ANN (artificial neural network) and GEP methods to rainfall-runoff modeling in the Juniata River Basin in Pennsylvania, USA. Comparing their results showed that GEP performed better than ANN. The results of a study by Shiri and Kisi (2011) showed that, in comparing the predictive performance of short-term static level fluctuations using two models, GEP and ANFIS, both models perform well in predicting static level fluctuations, but the GEP model has a simpler structure than ANFIS. Kavehkar et al. (2013) simulated the water level fluctuations of Urmia Lake using GEP and ANN. The results showed the optimal GEP accuracy in simulating water level fluctuations. Comparing the performance of the Bayesian network and GEP models in daily river flow forecasting, Baba Ali and Dehghani (2016) showed that GEP forecasts are associated with lower error estimation. Chang and Chang (2001) used

ANFIS to predict reservoir inflow. According to their results, the predictions of the ANFIS model are more accurate than the classical models. *Choubey et al.* (2014) used the SVM model to predict and analyze the inflow of Narmada Reservoir Dam in the Indian state of Pradesh showing that this method has a very good ability to simulate and predict the average monthly flow. *He et al.* (2014) used the SVM model to predict river flow in mountainous and semi-arid regions in the northwestern part of China, and they found that SVM has better performance than ANN and ANFIS, to predict river flow in the semi-arid mountainous areas. *Tabari et al.* (2013) used SVM, ANFIS, regression, and meteorological models to simulate reference evapotranspiration using climate data. Their results showed the superiority of the SVM model over other methods. *Ahmadi et al.* (2014) used GP (genetic programming) and SVM to predict the monthly reference crop evapotranspiration. Their results showed that SVM was superior to GP. *Dehghani et al.* (2016) compared the performance of SVM, GEP, and Bayesian network models in predicting river flow. Their results showed that the SVM performed better with the least amount of error than the other models. *Mehdizadeh et al.* (2017) investigated the performance of empirical equations and soft computing approaches including GEP, SVM, as well as multivariate adaptive regression splines (MARS) in estimating monthly mean reference evapotranspiration. The performance of the SVM was better than the used empirical equations. *Hong et al.* (2018) coupled ANFIS with a genetic algorithm and differential evolution for flood spatial modeling. They combined two data mining techniques with the ANFIS model, including the ANFIS-Genetic Algorithm and the ANFIS-Differential Evolution. The result showed, the ANFIS-Differential Evolution hybrid model is more suitable for flood susceptibility mapping in their study area. *Kalantar et al.* (2018) assessed the training landslides random selection effects on support vector machine (SVM) accuracy, logistic regression (LR), and artificial neural network (ANN) models for landslide susceptibility mapping. Results showed that SVM and LR models performed better than ANN model. *Pashazadeh and Javan* (2020) compared the performance of GEP and ANN models with the equivalent Muskingum inflow model. Their results showed that the obtained outflow hydrograph by the GEP model had an excellent performance compared with ANN and equivalent Muskingum inflow models.

Due to the importance of rainfall simulation to analyze, verify, correct, and complete data and forecasts in future periods as well as the impact of long-term memory data on the performance of certain models, the aim of this study was to evaluate the efficacy and accuracy of the three models (GEP, ANFIS, and SVM) in rainfall simulation.

For this purpose, the monthly data of the 110-year-long time series of Diata station in India and the daily data of the 44-year-long time series of Urmia station have been used and the simulation performance has been evaluated using different criteria.

2. Materials and method

In this study, two series of monthly rainfall records (1900–2010) of Diata meteorological station (Shivapouri Region of Madhya State of India) and daily rainfall records (1961–2005) of Urmia synoptic station (Iran) were used. To perform the simulation, 90% of the data was used to train (learning phase) and the remaining 10% of the data was used to test (testing phase) the models, followed by running the SVM, ANFIS, and GEP algorithms and the evaluation criteria. *Fig. 1* shows the location of the Urmia and Diata meteorological stations in Iran and India, respectively.

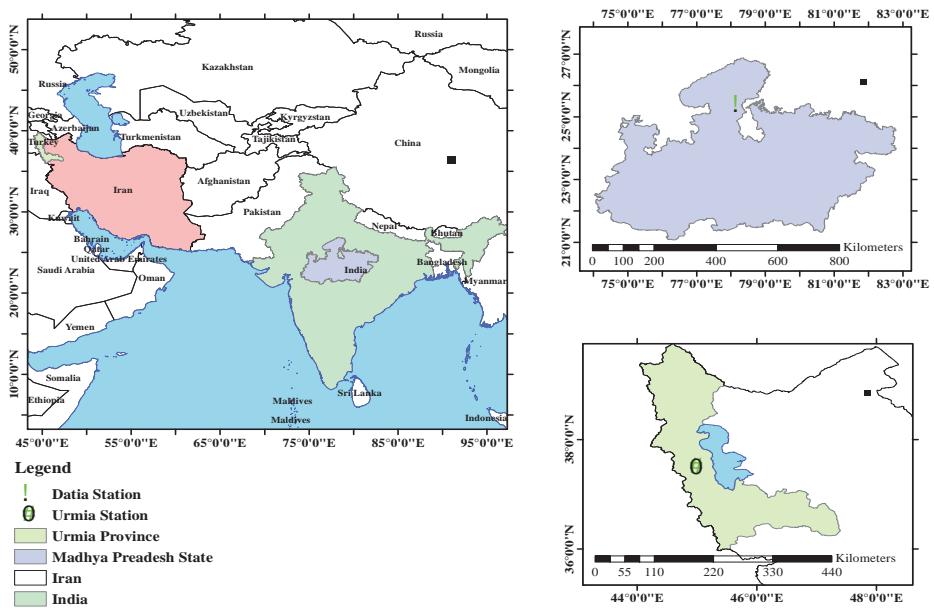


Fig. 1. Location map of the selected stations in Iran and India.

2.1. Gene expression programming (GEP)

This method is a combination of methods such as genetic programming (GP) and genetic algorithm (GA). In GEP, similarly to genetic algorithm, the individuals are encoded as linear strings of fixed length (the genome or chromosomes), and similarly to genetic programming, they are expressed as nonlinear entities of different sizes and shapes. In GEP, the genome or chromosome consists of a linear, symbolic string of fixed length composed of

one or more genes. It will be shown that despite their fixed length, GEP chromosomes can code expression trees (ETs) with different sizes and shapes. One of the strengths of GEP over GA and GP is that genetic operators' works at the chromosome level, which makes genetic diversity creation extremely simplified. The other strong point of GEP is its unique, multigeneric nature, which allows the evolution of more complex programs composed of several sub-programs (Ferreira, 2001). Further details on this method are provided by Shoaib et al. (2015). In this study, GEP simulation was performed using GeneXpro Tools (v5) software.

2.2. Adaptive-network-based fuzzy inference system (ANFIS)

The method of adaptive fuzzy-neural inference system is a combination method, in which the fuzzy part establishes the relationship between the input and output variables, and the characteristics related to the membership functions of the fuzzy part are determined by the neural network. This method has five layers according to Fig. 2, which are described in the following steps:

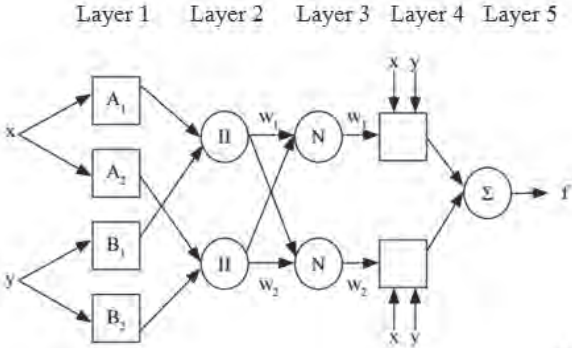


Fig 2. ANFIS network structure.

Layer 1, the input nodes: Every node in this layer acts as a member function that is assigned to each of the input variables of the model (x and y). Member amounts are determined based on the inputs belonging to each of the fuzzy sets A_1 and B_1 . In other words, the output of each node in this layer is the degree of members assigned to the input variables in the fuzzy sets, which are expressed as follows:

$$i = 1,2 \quad O_{1,i} = \mu_{A_i}(x), \quad (1)$$

$$l = 3,4 \quad O_{2,i} = \mu_{B_{i-2}}(x), \quad (2)$$

where x and y are the non-fuzzy inputs of node i , A_i , and B_i are fuzzy membership functions, and $O_{1,i}$ and $O_{2,i}$ represents the outputs of the first layer.

Layer 2, the rules nodes: Each node in this layer calculates the degree of activity of a rule. In this layer, the operator "and" is used to calculate the degree of participation of each rule. $O_{2,k}$ represents the output of the k -node in the second layer, and it is the product of the degrees of membership of each entry:

$$O_{2,k} = \mu_{A_i}(x) \cdot \mu_{B_j}(y). \quad (3)$$

Layer 3, the normalized nodes: This step calculates the ratio of the degree of participation of each rule to the total degree of participation of all the rules. As a result, this layer is defined as

$$O_{3,i} = \bar{w}_i = \frac{w_i}{\sum_{k=1}^4 w_k}, \quad (4)$$

where w_i is the i th output node of the previous layer.

Layer 4, the adaptive nodes: This step uses the result parameters to calculate the output of each node:

$$O_{4,i} = \bar{w}_i f_i = \bar{w}_i (p_i x + q_i y + r_i), \quad (5)$$

where w_i is i th output node of the previous layer and $\{p_i, r_i, q_i\}$ are linear adaptive parameters.

Layer 5, the output node: This step expresses the final output value as the sum of the output nodes of the previous layer:

$$O_{5,i} = \bar{w}_i f_i = \frac{\sum_{i=1}^4 w_i f_i}{\sum_{i=1}^4 w_i}. \quad (6)$$

The ANFIS network learning algorithm is a hybrid learning algorithm consisting of a descending gradient algorithm and a minimum squared return method. The descending algorithm is used to update the network's nonlinear

parameters and the estimate of the minimum return square is used to adjust the network weights. Network training error is defined as:

$$E = \sum_{i=1}^N (f_i - \hat{f}_i)^2, \quad (7)$$

where f_i and \hat{f}_i are the optimal and estimated outputs of the network for the i th input, respectively, and N is the total number of input-output data pairs (training data) of the network (Jang, 1993).

2.3. Support vector machine (SVM)

SVM is a supervised learning model that is based on the constrained optimization theory and the method of structural risk minimization. In this model, the function related to the dependent variable Y , which is itself a function of several independent variables of x , is estimated. Similarly to other regression issues, it is assumed that the relationship between independent and dependent variables are specified with an algebraic function $f(x)$ plus an acceptable error ε .

$$f(x) = W^T \cdot \phi(x) + b, \quad (8)$$

$$y = f(x) + \varepsilon, \quad (9)$$

where the W (vector of the equations) and b (constant) are the characteristics of the regression, and ϕ is Kernel function. The purpose is to find the function of $f(x)$. This is achieved by using the SVM training phase. Therefore, to calculate W and b , it is necessary to optimize the error function (Eq. (10)) in the ε -SVM model by considering the conditions in Eq. (11):

$$\frac{1}{2} W^T W + C \sum_{i=1}^N \xi_i + C \sum_{i=1}^N \xi_i^*, \quad (10)$$

$$\begin{aligned} W^T \cdot \phi(x_i) + b - y_i &\leq \varepsilon + \xi_i^* \\ y_i - W^T \cdot \phi(x_i) - b &\leq \varepsilon + \xi_i \\ \xi_i, \xi_i^* &\geq 0 \quad , \quad i = 1, \dots, N \end{aligned}, \quad (11)$$

where C is a positive integer that determines the penalty when the model training error occurs, ϕ is the Kernel function, N is the number of samples, and

the two characters ξ_i and ξ_i^* are slack variables determining the upper and lower limits of the training error associated with the allowable error value ε . In the case of predictions, the data are placed within the ε -boundary range. But, if the data is out of range, then there is an equivalent error ξ_i and ξ_i^* (Eskandari et al., 2012). After defining the Lagrangian coefficients, the characteristics of W and b in the regression SVM model are calculated using Crash-Cohen-Tucker theory, in which W is consistent with Eq. (12), and as a result, for SVM model, we will calculate Eq. (13):

$$W = \sum_{j=1}^N (a_j + a_j^*) \phi(x_j), \quad (12)$$

$$W = \sum_{i=1}^N (a_i + a_i^*) \phi(x_i)^T \phi(x) + b, \quad (13)$$

where a_i and a_i^* are Lagrangian terms and $(a_i + a_i^*)$ can be zero or non-zero. Therefore, only the data sets whose coefficients a_i^* are assumed to be non-zero, are entered into the final regression equation. These data sets are known as the support vectors. Finally, the regression SVM function can be rewritten as

$$f(x) = \sum_{i=1}^N a_i \phi(x_i)^T \phi(x_j) + b. \quad (14)$$

In Eq.(14), the calculation of $\phi(x)$ in the specified space may be very complex. To solve this problem, a kernel function is selected in the regression SVM model. Different kernel functions can be used to construct different types of ε -SVM models (Hofmann, 2002):

$$K(x_i, x) = \phi(x_i)^T \phi(\sqrt{b^2 - 4ac}) \quad (15)$$

2.4. Performance criteria

The correlation coefficient R2 (Eq. (16)), root mean square error (RMSE) (Eq. (17)), Nash-Sutcliffe efficiency coefficient NSE (Eq. (18)), and the bias or model bias MB (Eq. (19)) were used as performance criteria to evaluate the accuracy and efficiency of the used models.

$$R^2 = \left(\frac{\text{COV}(P_i, P'_i)}{\sigma_{P_i} \sigma_{P'_i}} \right)^2, \quad (16)$$

$$RMSE = \sqrt{\frac{\sum_{i=1}^n (P_i - P'_i)^2}{S}}, \quad (17)$$

$$NSE = 1 - \frac{\sum_{i=1}^T (P_i - P'_i)^2}{\sum_{i=1}^T (P_i - \bar{P}_i)^2}, \quad (18)$$

$$MB = \frac{\sum_{i=1}^n (P'_i - P_i)}{P_i}, \quad (19)$$

where P_i are the observed values, P'_i are the simulated values, \bar{P}_i are the mean observed values, S is the number of data, σ_{P_i} is the variance of observed values, $\sigma_{P'_i}$ is the variance of simulated values (Nash and Sutcliffe, 1970; Swinnow and Campbell, 2013; Salas et al., 1980). The flowchart of the proposed methodology is presented in Fig. 2.

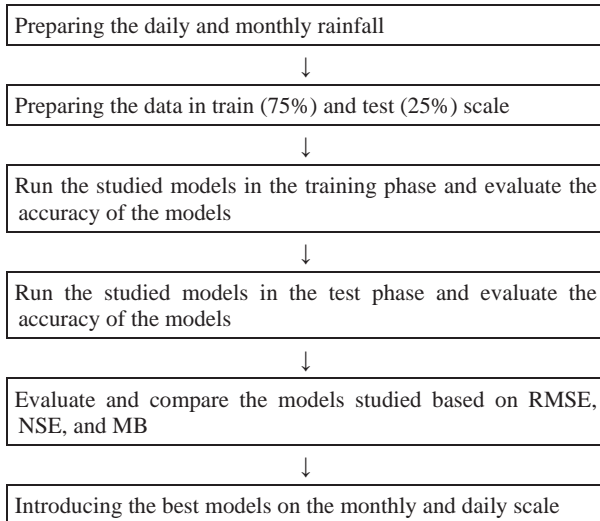


Fig 2. Flowchart of the proposed methodology

3. Results and discussion

Rainfall simulation has been demonstrated by GEP, ANFIS, and SVM models along with the correlation between observed and simulated value. The results are shown in *Figs. 4, 5, and 6*. According to these figures, in simulation with GEP, simulated rainfall is less than the observed values, and the correlation diagram of this simulation shows the relative scattering of simulated data, and the simulated values by ANFIS and SVM are more consistent with observational data. The correlation between the observed and simulated values of these two models is high and slightly different from each other. The data correlation in the ANFIS model is slightly higher than in the SVM. The correlation coefficient in simulation with GEP is estimated to be 55% lower than the other two models, and the R^2 range in both ANFIS and SVM models varies from 91 to 93%.

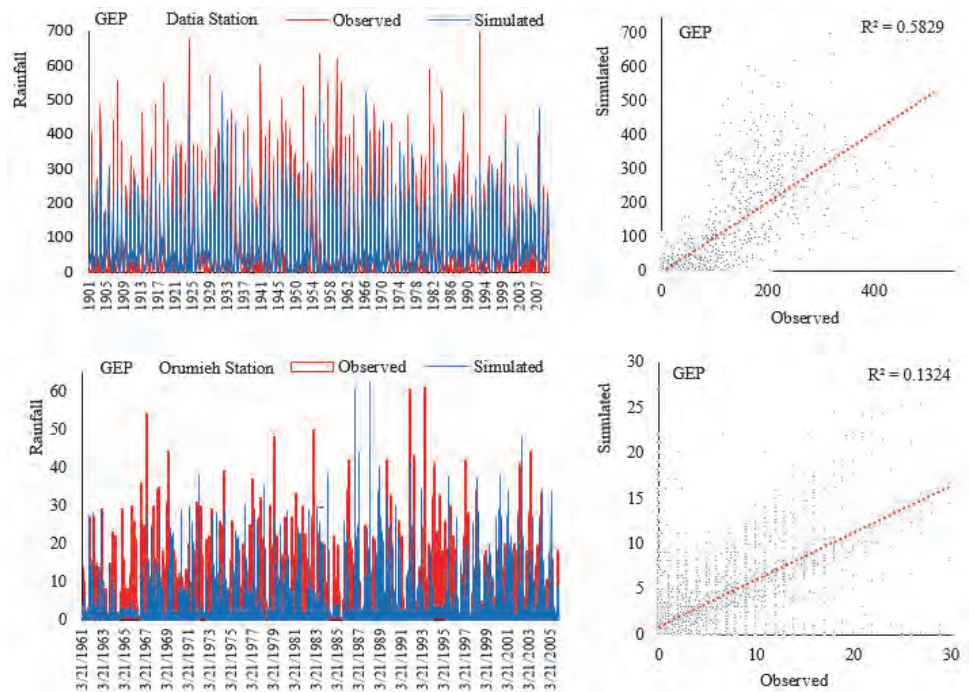


Fig 4. Rainfall simulation and the correlation between observational data and simulation in the GEP model (mm).

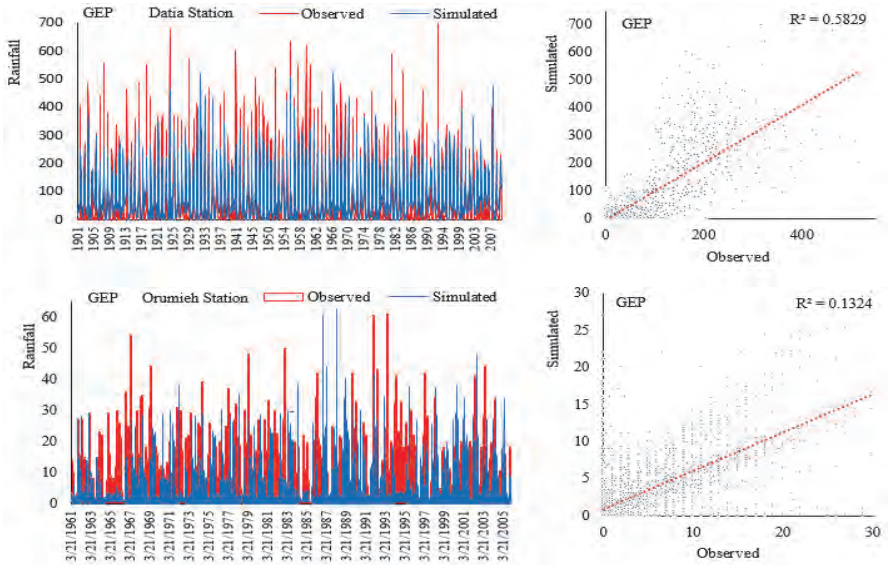


Fig 5. Rainfall simulation and the correlation between observational data and simulation in the ANFIS model (mm)

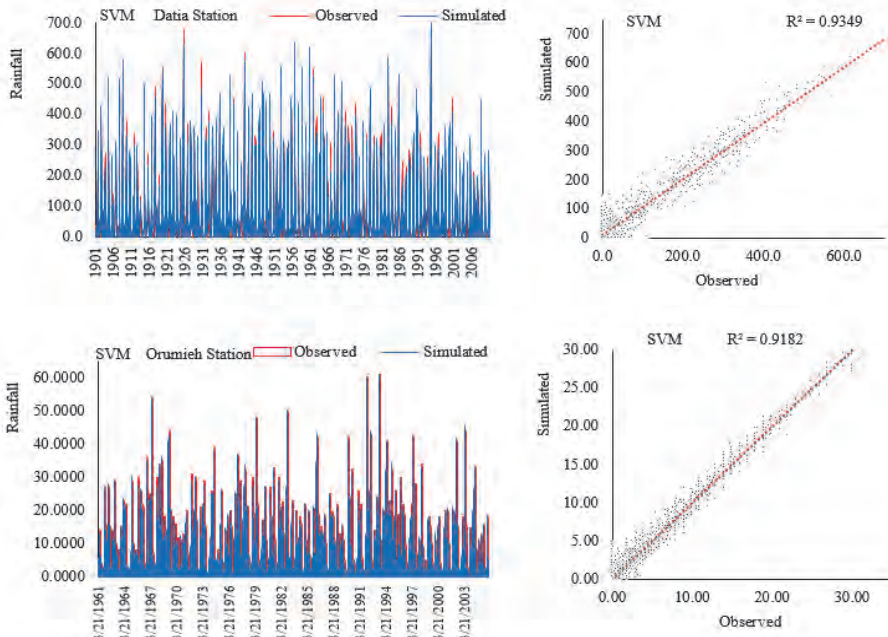


Fig 6. Rainfall simulation and the correlation between observational data and simulation in the SVM model (mm)

3.1. Evaluation of the performance of simulation models

The evaluation of GEP, ANFIS, and SVM models using RMSE, MB, and NSE criteria are presented in *Table 1*. The comparison of simulations based on daily and monthly rainfall data shows that the root mean square error (RMSE) in simulation with daily data is less than with monthly data and the model bias (MB) is more in daily data compared to monthly. The Nash-Sutcliffe efficiency (NSE) criteria of models with daily data are higher than monthly, the details of which can be examined in the table. On average, the root mean square error (RMSE) in the GEP simulation is 50 and 55% higher than that of the ANFIS for Urmia and Diata stations, respectively. However, ANFIS is superior to SVM in the training phase and performs worse in the test phase. But on average, the RMSE of the ANFIS model is 1 and 3% higher than that of the SVM at Urmia and Diata stations, respectively. The bias model of GEP is 72 and 60% higher than that of ANFIS at Urmia and Diata stations, respectively. The ANFIS bias is 62 and 15% higher than the SVM bias at Urmia and Diata stations, respectively. The GEP's Nash-Sutcliffe efficiency (NSE) criteria are 56 percent and 61% lower than the NSE of ANFIS at Urmia and Diata stations, respectively. The NSE of ANFIS is 1 and 2% lower than the NSE of SVM in Urmia and Diata stations, respectively.

Table 1. Evaluating the performance of simulation models GEP, ANFIS, and SVM

Model	Station	Index					
		NSE (%)		MB (mm)		RMSE (mm)	
		Test	Train	Test	Train	Test	Train
GEP	Urmia	27	31	0.672	2.13	2.647	3.389
	Diata	21	24	0.605	0.0276	70.558	81.327
ANFIS	Urmia	88	92	0.662	0.111	0.998	0.997
	Diata	83	93	0.145	0.106	35.592	32.453
SVM	Urmia	90	92	0.291	0.358	0.952	1.007
	Diata	88	93	0.099	0.189	32.702	33.002

By comparing the results of this study with the result of other researchers, it can be shown that the result is consistent with the results of *Ahmadi et al.* (2014) in the superiority of the SVM model over GEP to estimate reference evapotranspiration over a 37-year-long period. Results are consistent also with the results of *Tabari et al.* (2013), that they simulated the reference crop transpiration by using SVM and ANFIS, and showed the relative superiority of SVM. On the other hand, results of *Shiri et al.* (2013), which used ANN, ANFIS, SVM, and GEP

methods to predict rainfall and evaporation parameters to predict groundwater level fluctuations, are inconsistent with the research results of the present study showing better GEP efficiency. The reason for the inefficiency of ANFIS and SVM in this study is related to the limited groundwater data due to their nature. Also, they used eight-year time series data in their research. Therefore, if the data used is limited, other models may be as efficient as ANFIS and SVM, which require an evaluation through different indicators.

4. Conclusion

Based on the performance criteria, evaluating efficiency, and accuracy of three models, GEP, ANFIS, and SVM in daily and monthly rainfall simulation, the correlation coefficient of rainfall simulation with daily data is higher than that of the simulations with monthly data in all three models. The correlation in GEP simulation is significantly lower than in the other two models, and ANFIS performs 1% better than SVM with daily and monthly data. According to the RMSE criterion, the use of daily data performs better than the use of monthly data in all three models, GEP simulation performs worse than the other two models, and ANFIS has a slight superiority over SVM, which requires further research. In all three simulations, the model bias (MB) with daily data is higher than monthly, and the simulation bias in GEP is 76% and 83% higher than the bias in ANFIS and SVM, respectively. The efficiency of all three models performs better in simulation with daily data than with monthly data, and the efficiency of the GEP model is 27% better on average according to this criterion, and SVM has about 4% better performance than that of ANFIS. Therefore, the SVM rain simulation is associated with a lower error rate and better efficiency, the ANFIS model has the same capability as the SVM, and the GEP model is not suitable for simulating rainfall. Therefore, the higher MB and RMSE, as well as less R^2 and NSE of GEP model than the other two models show poor GEP performance compared to ANFIS and SVM. Due to the slight advantage of ANFIS over SVM based on R^2 and RMSE criteria and the relative superiority of SVM over ANFIS based on MB and NSE criteria, SVM can be introduced as the superior model.

References

- Ahmadi, F., Radmanesh, F., MirAbbasi, R., and Aishm, S., 2014: Prediction of Monthly Evaporation and Transpiration of Reference Plant in the Northwest of the Country Using Genetic Programming and Support Vector Machine. *J. Iranian Irrigation Drainage* 1, 65–54.
- Alvisi, S., Mascellani, G., Franchini, M., and Bardossy, A., 2005: Water Level Forecasting Through Fuzzy Logic and Artificial Neural Network Approaches. *J. Hydrol. Earth Syst. Sci.* 2, 1107–1145. <https://doi.org/10.5194/hessd-2-1107-2005>

- Aytek, A. and Kisi, O., 2008: A Genetic Programming Approach to Suspended Sediment Modeling. *J. Hydrology* 351, 288–298. <https://doi.org/10.1016/j.jhydrol.2007.12.005>
- Babaali, H.R. and Dehghani, R., 2016: Comparison of the Performance of Business Network Models and Gene Expression Programming in Predicting Daily River Flow (Case Study: Marbara River). *J. Environ. Sci. Technol.* 2(2), 96–108.
- Chang, L.C. and Chang, F.J., 2001: Intelligent Control for Modelling of Real-Time Reservoir Operation. *J. Hydrolog. Proc.* 15, 1621–1634. <https://doi.org/10.1002/hyp.226>
- Choubey, V., Mishra, S., and Pandey, S.K., 2014: Time Series Data Mining in Real Time Surface Runoff Forecasting Through SVM. *Int. J. Comput. Appl.* 98(3), 23–30. <https://doi.org/10.5120/17163-7223>
- Dehghani, R., Younesi, H., and Torabi Poodeh, H., 2016: Comparison of the Performance of Support Vector Machine Models, Gene Expression Programming and Business Network in Predicting River Flow (Case Study: Kashkan River). *J. Water Soil Conserv. Res.* 24(4), 161–177.
- Dibike, B.Y. and Coulbaly, P., 2006: Temporal Neural Networks for Downscaling Climate Variability and Extremes. *J. Neural Networks* 19, 135–144. <https://doi.org/10.1016/j.neunet.2006.01.003>
- Eskandari, A.S., Ruhollah, N., Mearaji, H., and Kiaqadari, A., 2012: Development of an Appropriate Model Based on Artificial Neural Network and SVM for Predicting 5-day Biochemical Biochemistry. *J. Environ.* 38, 71–82.
- Ferreira, C., 2001: Gene Expression Program-Ming a New Adaptive Algorithm for Solving Problems. *J. Complex Syst.* 13(2), 87–129.
- Hamel, L.H., 2009: Knowledge Discovery with Support Vector Machines. Wiley and Sons. <https://doi.org/10.1002/9780470503065>
- He, Z., Wen, X., Liu, H., and Du, J., 2014: A Comparative Study of Artificial Neural Network, Adaptive Neuro Fuzzy Inference System and SVM for Forecasting River Flow in the Semiarid Mountain Region. *J. Hydrology* 509, 379–386. <https://doi.org/10.1016/j.jhydrol.2013.11.054>
- Hofmann, T., Tsochantaridis, I., and Altun, Y., 2002: Learning Over Structured Output Spaces Via Joint Kernel Functions. Sixth Kernel Workshop.
- Hong, H., Panahi, M., Shirzadi, A., Ma, T., Liu, J., Zhu, A.X., Chen, W., Kougiaris, L., and Kazakis, N., 2018: Flood Susceptibility Assessment in Hengfeng Area Coupling Adaptive Neuro-Fuzzy Inference System With Genetic Algorithm and Differential Evolution. *Sci. Total Environ.* 621, 1124–1141. <https://doi.org/10.1016/j.scitotenv.2017.10.114>
- Hoogenboom, G. 2000: Contribution of Agrometeorology to the Simulation of Crop Production and Its Applications. *J. Agricult. Forest Meteorol.* 103, 137–157. [https://doi.org/10.1016/S0168-1923\(00\)00108-8](https://doi.org/10.1016/S0168-1923(00)00108-8)
- Jang, J.S.R., 1993: ANFIS: Adaptive- Network- Based Fuzzy Inference Systems. IEEE Transactions on Systems. *Man Cybernetics* 23, 665–685. <https://doi.org/10.1109/21.256541>
- Kalantar, B., Pradhan, B., Naghibi, S.A., Motevalli, A., and Mansor, S., 2018: Assessment of the Effects of Training Data Selection on the Landslide Susceptibility Mapping: A Comparison Between Support Vector Machine (SVM), Logistic Regression (LR) and Artificial Neural Networks (ANN). *J. Geomat. Nat. Hazards Risk* 9, 49–69. <https://doi.org/10.1080/19475705.2017.1407368>
- Kavehkar sh, Ghorbani, M., Ashrafzadeh, A., and Darbandi, P., 2013: Simulation of Water Level Fluctuations Using Gene Expression Programming. *J. Civil Engin. Environ.* 43(3), 72–75.
- Mehdizadeh, S., Behmanesh, J., and Khalili, K., 2017: Using MARS, SVM, GEP and Empirical Equations for Estimation of Monthly Mean Reference Evapotranspiration. *Comput. Electronics Agricult.* 139, 103–114. <https://doi.org/10.1016/j.compag.2017.05.002>
- Nash, J.E. and Sutcliffe, J.V., 1970: River flow forecasting through conceptual models part I-A discussion of principles. *J. Hydrology* 10, 282–290. [https://doi.org/10.1016/0022-1694\(70\)90255-6](https://doi.org/10.1016/0022-1694(70)90255-6)
- Nourani, V. and Komasi, M., 2013: A geomorphology-based ANFIS model for multistation modeling of rainfall–runoff process. *J. Hydrology* 490, 41–55. <https://doi.org/10.1016/j.jhydrol.2013.03.024>
- Pashazadeh, A., and Javan, M., 2020: Comparison of the gene expression programming, artificial neural network (ANN), and equivalent Muskingum inflow models in the flood routing of multiple branched rivers. *Theor. Appl. Climatol.* 139, 1349–1362. <https://doi.org/10.1007/s00704-019-03032-2>

- Refsgaard, J.C., Henriksen, H.J., Harrar, W.G., and Scholten Kassahun, A., 2005: Quality assurance in model based water management - review of existing practice and outline of new approaches. *J. Environ. Modell. Software*. 20, 1201–1215. <https://doi.org/10.1016/j.envsoft.2004.07.006>
- Refsgaard, J.C. and Knudsen, J., 1996: Operational validation and intercomparison of different types of hydrological models. *J. Water Resour. Res.* 32, 2189–2202. <https://doi.org/10.1029/96WR00896>
- Salas, J.D., Delleur, J.W., Yevjevich, V., and Lane, W.L., 1980: Applied Modeling of Hydrologic Time Series. Water resource Publications. Littleton, Colorado . U.S.A.
- Sentelhas, P.C., deFaria, R.T., Chaves, M.O., and Hoogenboom, G., 2001: Evaluation of the WGEN and SIMMETEO weather generators for the Brazilian tropics and subtropics, using crop simulation models. *Revista Brasileira de Agrometeorologia. Santa Maria.*; 9, 357–376.
- Shiri, J., Kisi, O., Yoon, H., Lee, K.K., and Hossein Nazemi, A., 2013: Predicting groundwater level fluctuations with meteorological effect implications . A comparative study among soft computing techniques. *J. Comput. Geosci.* 56, 32–44. <https://doi.org/10.1016/j.cageo.2013.01.007>
- Shiri, J. and Kisi, O., 2011: Comparison of genetic programming with neuro-fuzzy systems for predicting short-term water table depth fluctuations. *J. Comput. Geosci.* 37, 1692–1701. <https://doi.org/10.1016/j.cageo.2010.11.010>
- Shoaib, M., Shamseldin, A.Y., Melville, B.W., and Khan, M.M., 2015: Runoff Forecasting using Hybrid Wavelet Gene Expression Programming(WGEP) Approach. *J. Hydrology.* 527, 326–344. <https://doi.org/10.1016/j.jhydrol.2015.04.072>
- Swinscow, T.D.V. and Campbell, M.J., 2013: Statistics at Square One. London: BMJ Publication.
- Tabari, H., Martinez, C., Ezani, A., and Hosseinzadeh Talaei, P., 2013: Applicability of SVMs and adaptive neuro- fuzzy inference system for modeling potato crop evapotranspiration. *J. Irrigat. Sci.* 31, 575–588. <https://doi.org/10.1007/s00271-012-0332-6>
- Ustoorkar, K. and Deo, M.C., 2008: Filling up Gaps in Wave Data with Genetic Programming. *J. Marine Struct.* 21, 177–195. <https://doi.org/10.1016/j.marstruc.2007.12.001>
- Vapnik, V.N., 1998: Statistical Learning Theory. Wiley, New York.

IDŐJÁRÁS

Quarterly Journal of the Hungarian Meteorological Service
Vol. 125, No. 2, April – June, 2021, pp. 211–227

Predictive control of a solar thermal system via on-line communication with a meteorological database server

János Tóth and István Farkas*

*Institute of Technology
Hungarian University of Agriculture and Life Sciences,
Páter K. u. 1, 2100 Gödöllő, Hungary*

**Corresponding author E-mail: farkas.istvan@uni-mate.hu*

(Manuscript received in final form July 8, 2020)

Abstract— In this paper, the mathematical models of a solar thermal system which governs the solar thermal collector, the heat storage system, and the pump are presented. It has been shown that it is possible to connect a Simulink-based model to a meteorological database server using standard communication protocols by a C language-based component in order to import real-life weather information into the simulation. The setup of the model predictive control of this solar thermal system and the results of the simulation are also presented. This computationally heavy control method is possible to use on today's personal computers, and it can be expanded.

Key-words: SimSolar, Simulink, TCP/IP, JSON

1. Introduction

The need for renewable energy solutions has grown over the years, and the growth has continuously been rising. The technologies that utilize solar energy are solar thermal and photovoltaic systems. The process of design and optimization of these systems involves a huge number of calculations based on various types of mathematical models describing the system.

The block-oriented modeling technique is a technique where a complex mathematical model can be abstracted into a block-relation model. The “block” can be interpreted as a function with inputs and outputs, and it can be visualized as a rectangle. In this way, the mathematical model transforms into a “wiring diagram”, where the underlying principles of the model can be seen easier, and

the linking of the blocks represent the relationships among the parts of the physical model (Parrino *et al.*, 2005).

The block-oriented modeling technique can be combined with the model-based design (Qu *et al.*, 2010). This design method focuses on the mathematical models of a system and uses the data of its simulations to reduce the cost of the prototyping phase of the product to optimize the already existing systems.

The hardware-in-the-loop (HIL) simulation is the extension of the block-oriented modeling. This method can connect the real-time world to the simulation by creating a block in the simulation that can read measurement data using dedicated measurement hardware (Tóth *et al.*, 2019).

Another way to connect real-world data to the simulation is by using a database, especially a meteorological source database. These databases can be accessed directly (Tóth and Farkas, 2018), but there is a security risk for public databases, so this method is common for local networks. A more acceptable way to access data from a public online database is to go through a TCP/IP (Transmission Control Protocol/Internet Protocol) API (Application Programming Interface). The API provides a way to the developer to interface with the application in a controlled manner. The most common format of these server-client messages (APIs) are JOSN (JavaScript Object Notation) and XML (Extensible Markup Language) (Wang, 2011). The advantage of this method is that the database is not directly accessible, and the messages can be viewed in a regular web browser in a human-readable format. This approach can greatly improve the productivity of the simulation, because it skips the step of the manual exchange of the data, and the request of a different data set is just a change of a few parameters of the model.

The operation of a dynamical system usually requires a kind of control unit; in this case, the unit is a predictive control unit, which is a sophisticated solution in time-delayed solar systems. The predictive controlling algorithms provide a way to handle the systems with a slow response time. Such algorithms usually are neural network-based (Shuzhi *et al.*, 2008) or mathematical model-based (Qin and Badgwell, 2003). The model predictive control (MPC) can be used if the mathematical model of the system and its inverse are known. This approach is a natural choice for solar thermal systems, because these types of systems are well known in the mathematical modeling perspective, and they have slow response time, especially if a solar thermal farm is considered.

The aim of this paper is to present the block-oriented mathematical model of a solar thermal system and to show its model predictive control based on the data stored server and accessed through a TCP/IP API. The simulations were done using the Simulink framework. The mathematical models of the operational units of the solar thermal system are parts of a Simulink library, called SimSolar (Tóth and Farkas, 2017).

2. Materials and methods

In this session the applied mathematical models for the main components of the solar thermal system are presented. The components are composed as blocks in the Simulink simulation.

2.1. Model of the solar collector

The solar thermal collector converts the radiant energy from the Sun into heat. The mathematical model of the solar collector, the Hottel-Whillier model (Farkas, 1999), is interpreted as shown in Fig. 1.

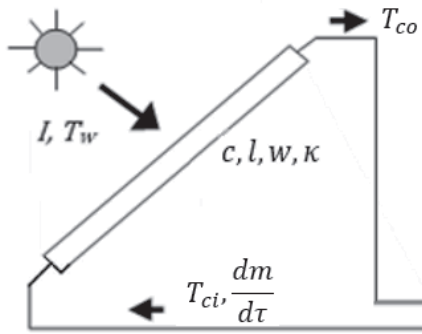


Fig. 1. Schematic diagram of the solar collector.

The governing equation of the Hottel-Whillier model can be written as

$$T_{co}(\tau) = T_w(\tau) + \frac{I(\tau)}{\kappa_{aw}} + \left(T_{ci}(\tau) - T_w(\tau) - \frac{I(\tau)}{\kappa_{aw}} \right) \exp \left(-\frac{\kappa_{mw}wl}{c_c \frac{dm_c}{d\tau}} \right), \quad (1)$$

where

- τ - time (s),
- T_{co} - outlet temperature of the solar collector (°C),
- T_w - ambient temperature (°C),
- I - solar radiation (W m^{-2}),
- κ_{aw} - heat transfer coefficient (absorber – environment) ($\text{W m}^{-2} \text{K}^{-1}$),
- T_{ci} - inlet temperature of the solar collector (°C),
- κ_{mw} - heat transfer coefficient (working fluid – environment) ($\text{W m}^{-2} \text{K}^{-1}$),
- w - width of the solar collector (m),
- l - length of the solar collector (m),

c_c - specific heat of the working fluid ($\text{J kg}^{-1} \text{K}^{-1}$),
 $dm_c/d\tau$ - mass flow-rate of the working fluid (kg s^{-1}).

The implementation and the parameters of the applied model can be seen in Figs. 2 and 3.

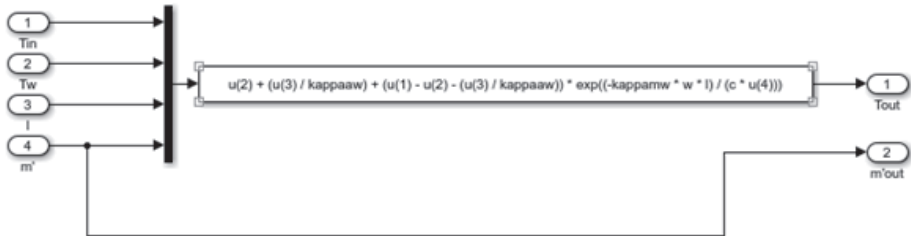


Fig. 2. Simulink implementation of the solar collector model.

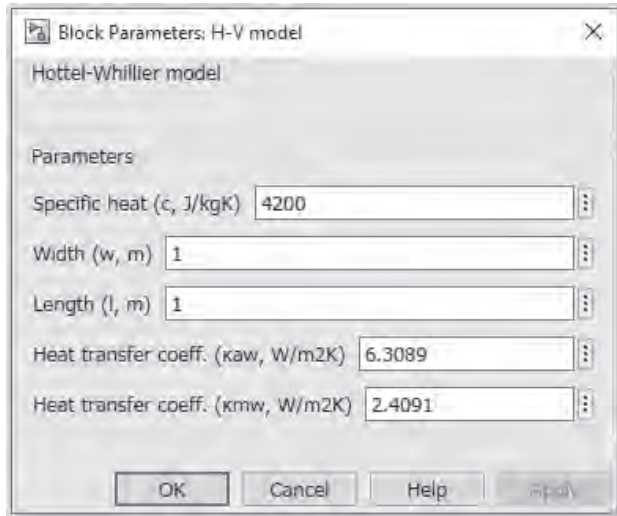


Fig. 3. Parameter window of the solar collector model.

In order to use the block in the simulation, the following parameters have to be set in the parameter window:

- specific heat of the containing fluid ($\text{J kg}^{-1} \text{K}^{-1}$),

- width of the solar collector (m),
- length of the solar collector (m),
- heat transfer coefficient (absorber - working fluid) ($\text{W m}^{-2} \text{K}^{-1}$),
- heat transfer coefficient (environment - working fluid) ($\text{W m}^{-2} \text{K}^{-1}$).

2.2. Model of the heat storage

In most cases, the period of the consumption of the collected solar energy is not necessarily the same as the time of the collection, so this energy must be stored for later use. The storage of the heat is taken care of by this unit. The interpretation of the heat storage model (Farkas, 1999) can be seen in Fig. 4. The heat storage could provide hot water for additional technological purposes.

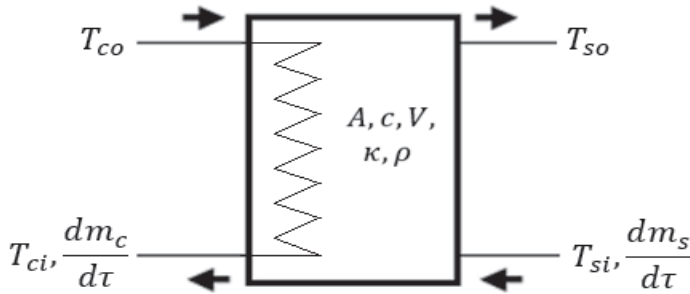


Fig. 4. Schematic diagram of the heat storage.

The related governing equations are as follows:

$$T_{ci}(\tau) = (T_{co}(\tau) - T_{so}(\tau)) \exp\left(-\frac{\kappa_s A_s}{c_s \frac{dm_c}{d\tau}}\right) + T_{so}(\tau), \quad (2a)$$

$$c_s V_s \rho_s \frac{dT_{so}}{d\tau} = c_s \frac{dm_s}{d\tau} (T_{si}(\tau) - T_{so}(\tau)) + c_s \frac{dm_c}{d\tau} (T_{co}(\tau) - T_{ci}(\tau)), \quad (2b)$$

where

- τ - time (s),
- T_{ci} - inlet temperature of the solar collector ($^{\circ}\text{C}$),
- T_{co} - outlet temperature of the solar collector ($^{\circ}\text{C}$),
- T_{so} - outlet temperature of the storage ($^{\circ}\text{C}$),
- κ_s - heat transfer coefficient in the heat storage ($\text{W m}^{-2} \text{K}^{-1}$),

- A_S - surface of the heat storage (m^2),
- c_s - specific heat of the working fluid in the heat storage ($J\ kg^{-1}\ K^{-1}$),
- m_s - mass of the working fluid in the heat storage (kg),
- V_s - volume of the heat storage (m^3),
- ρ_s - density of the working fluid in the heat storage ($kg\ m^{-3}$),
- T_{Si} - inlet temperature of the heat storage ($^{\circ}C$),
- c_c - specific heat of the working fluid in the solar collector ($J\ kg^{-1}\ K^{-1}$),
- $dm_c/d\tau$ - mass flow-rate of the working fluid in the solar collector ($kg\ s^{-1}$).

The implementation and the parameters of the applied model are shown in Figs. 5 and 6.

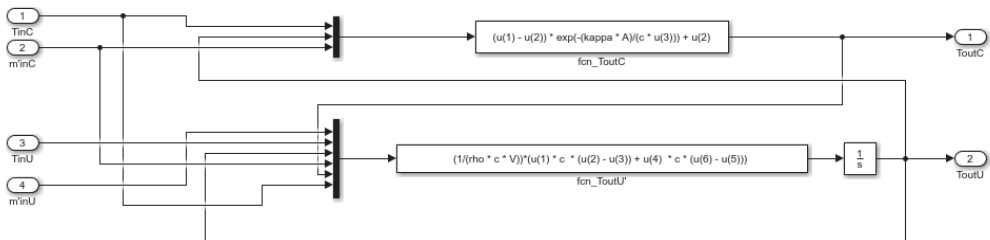


Fig. 5. Simulink implementation of the heat storage model.

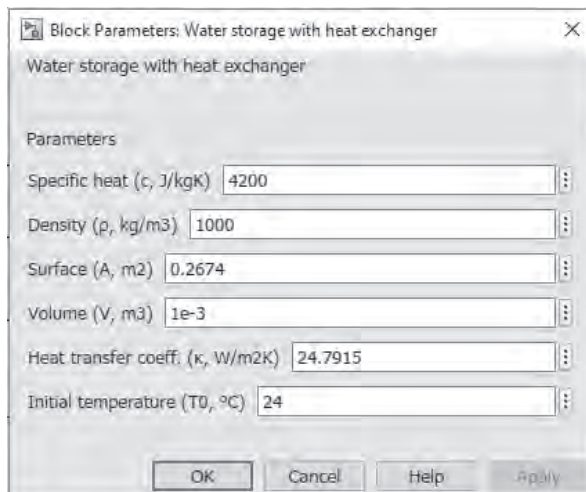


Fig. 6. Parameter window of the heat storage model.

In order to use the block in the simulation, the following parameters have to be set in the parameter window of the block:

- specific heat of the containing fluid ($\text{J kg}^{-1} \text{K}^{-1}$),
- density of the containing fluid (kg m^{-3}),
- surface of the heat storage (m^2),
- volume of the heat storage (m^3),
- heat transfer coefficient (storage, environment) ($\text{W m}^{-2} \text{K}^{-1}$),
- initial temperature ($^{\circ}\text{C}$).

2.3. Model of the pump

The pump circulates the working fluid in the system, which allows the flow of the liquid through the collector circuit to be controlled. The current model of the pump is linear. It describes a linear characteristic, i.e., the output mass flow rate is the product of the maximum mass flow rate and the control signal:

$$\frac{dm}{d\tau} = \frac{dm}{d\tau}_{max} u(\tau). \quad (3)$$

The implementation and the parameters of the applied model are presented in *Figs. 7 and 8*.

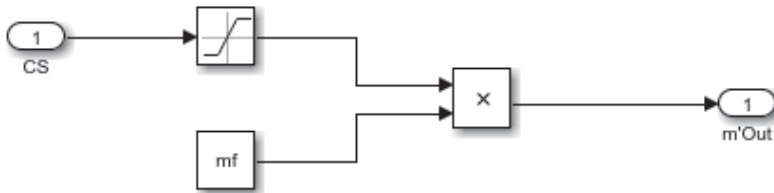


Fig. 7. Simulink implementation of the pump model.

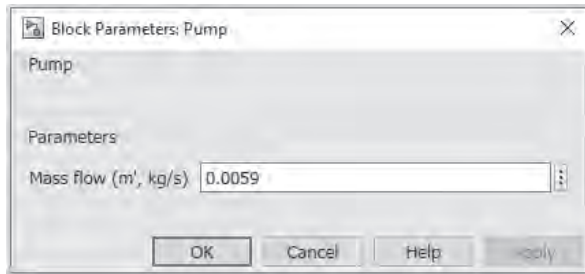


Fig. 8. Parameter window of the pump model.

In order to use the block in the simulation, the maximal mass flow-rate (kg s^{-1}) has to be set in the parameter window of the block.

2.4. Weather API

To access data from a server to run the simulation, a custom Simulink component had to be made. The Weather API block needs a server to communicate with. This server contains a database and a JSON based API. The server-client messages using TCP/IP provides the necessary information about the requested data. The server responds with a JSON formatted message containing the required data or an error message if an error occurred.

The API was designed in a way, that it can also be accessed using a web browser. For example, a request can be sent by typing into the address bar:

```
http://127.0.0.1/api/api.php?startDate=2018-04-17&startTime=06:00:00&endDate=2018-04-17&endTime=20:30:00&sensors=TW,I
```

This works only if a local server with the necessary API is up and running.

The response of this request contains the data from the sensors “TW” and “I” from the measurement interval from 06:00, April 17, 2018 to 20:30, April 17, 2018 in JSON format or an error message describing the error.

The Simulink implementation of this block contains a Level-2 MATLAB S-Function (*mathworks.com*, 2020b) written in the C programming language to handle the low-level file input/output duties and to implement the TCP/IP client. The parsing of the JSON formatted response is done using DaveGamble’s cJSON library (*github.com*, 2020).

In order to reduce the workload of the server, the block only requests for data, if updated data available. After the data arrives, the block saves it in a file, and uses the request to name this file uniquely. This mechanism allows the block to keep track of the already requested data.

The working principle of the Weather API block can be seen in *Fig. 9*.

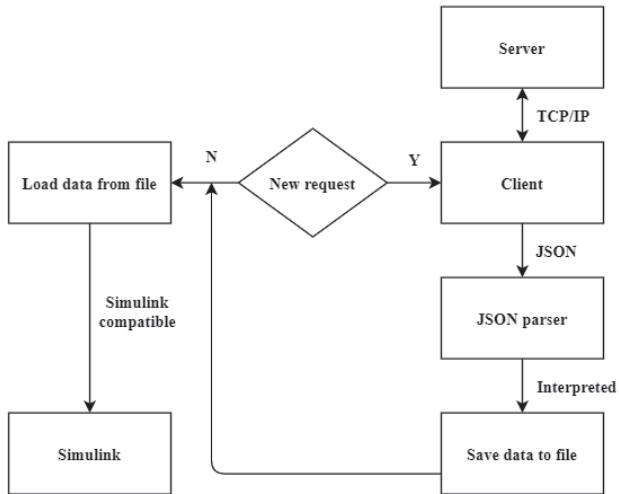


Fig. 9. Working principle of the Weather API block.

The block contains an option for linear interpolation; this is useful when the measurement frequency of the data is low compared to the accuracy of the simulation. The parameters of the related Simulink block are shown in *Fig. 10*.

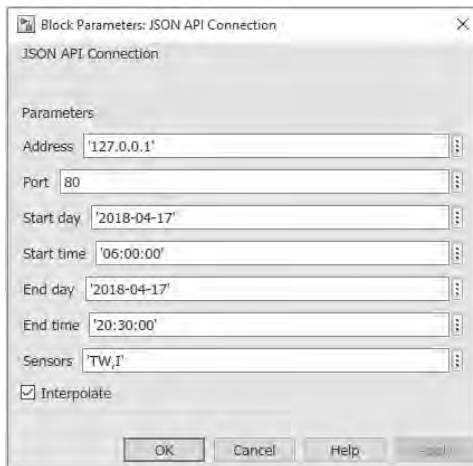


Fig. 10. Parameter window of the Weather API block.

In order to use the block in a simulation, the following parameters have to be set in the parameter window of the block:

- address of the server (IP address or URI),
- port of the server (integer value),
- the start day of the simulation (in yyyy-MM-dd format),
- the start time of the interval (in HH-mm-ss format),
- end day of the interval (in yyyy-MM-dd format),
- the end time of the interval (in HH-mm-ss format),
- name of the data fields (comma separated list),
- request for interpolation (boolean value).

2.5. Model predictive controller

In a solar thermal system, the controllers manipulate the pump operation ensuring the expected temperature of the outlet medium. In this paper, the MPC algorithm was chosen to study the behavior of the control process. This control would be an ideal choice for solar thermal systems, even for solar thermal farms, due to its ability to handle slow response times.

The controller is part of the Model Predictive Control Toolbox of Simulink (*mathworks.com*, 2020a). *Fig. 11.* shows the working principle of the model predictive controller.

The setup and tuning of the controller can be done using its graphical interface. The main parameters of the controller are:

- *Prediction horizon*: the quantity of future control intervals the controller must assess by prediction while optimizing its values at the control interval (*mathworks.com*, 2020c).
- *Control horizon*: the quantity of adjustments steps to be optimized at the control interval (*mathworks.com*, 2020c).
- *Constraints*: the minimum and maximum values that the output of the controller must obey.

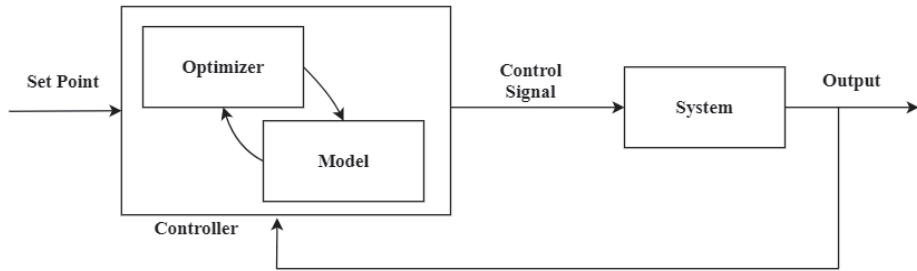


Fig. 11. Working principle of the model predictive controller.

3. Results

The examined system and the results of the simulation are presented in this section.

3.1. Examined system

The examined system consists of the models of the solar thermal collector, the heat storage, the two pumps (in the primary (collector-side) loop and in the secondary (consumer-side) loop), and the controller. The input data of the simulation comes from the database through TCP/IP protocol using the JSON format. The technical parameters were identified based on previous measurements using a physically built solar thermal system (Tóth *et al.*, 2019).

Technical parameters of the solar collector:

- width of the solar collector: 1 m,
- height of the solar collector: 1 m,
- heat transfer coefficient (absorber – working fluid): $6.31 \text{ W m}^{-2} \text{ K}^{-1}$,
- heat transfer coefficient (environment – working fluid): $4.21 \text{ W m}^{-2} \text{ K}^{-1}$,
- constant mass flow rate of the collector-side Pump1: 0.0059 kg s^{-1} ,
- working fluid: water.

Technical parameters of the water storage with heat exchanger:

- volume of the storage: 10^{-3} m^3 ,
- area of the storage: 0.2674 m^2 ,

- heat transfer coefficient in the heat storage: $24.79 \text{ W m}^{-2} \text{ K}^{-1}$,
- initial temperature: $22.9 \text{ }^\circ\text{C}$,
- maximum mass flow rate of the consumer-side Pump2: 0.0059 kg s^{-1} ,
- working fluid: water.

Parameters of the controller:

- set point temperature (SP): $50 \text{ }^\circ\text{C}$,
- prediction horizon: 3600 s ,
- control horizon: 1800 s ,
- constraint interval of control (CS): 0-1.

The block-oriented implementation of the solar thermal system can be seen in *Fig. 12*. The figure shows that the control signal of the primary loop (CS1) is set to a constant value of 1, as it is indicated in the rectangular block, which means that the mass flow rate of this loop is 0.0059 kg s^{-1} .

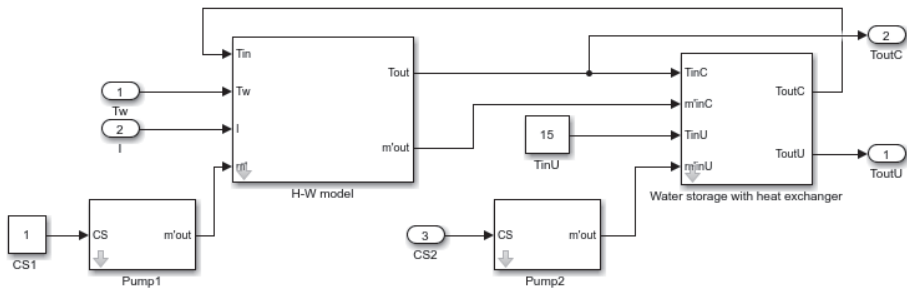


Fig. 12. Simulink implementation for the model of the solar thermal system.

The block-oriented implementation of the controlled system can be seen in *Fig 13*. During this experiment due to technical reasons, the solar thermal system was controlled at the consumer-side (CS2).

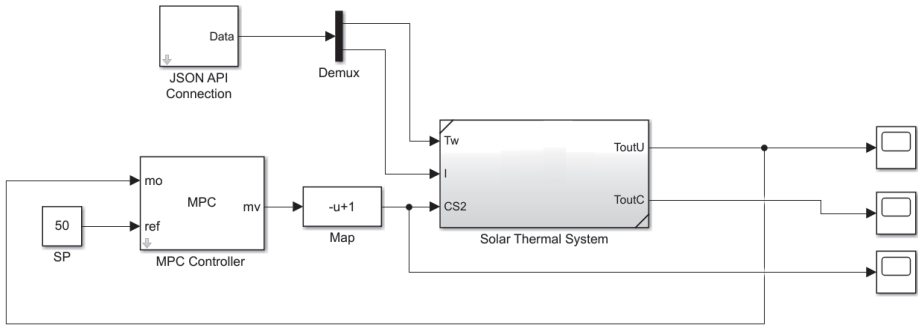


Fig. 13. Simulink implementation for the controlled solar thermal system.

The input of the simulation, the environmental temperature, and the solar irradiance comes from a verified mathematical model. The main purpose of this simulation was to study the model predictive controller and the Weather API block/server, which was easily achievable by the generation of the input data. If the simulation works with this data set, obviously it will equally work with a different data set that comes from measurements. The inputs of the simulation can be seen in Fig. 14 and 15.

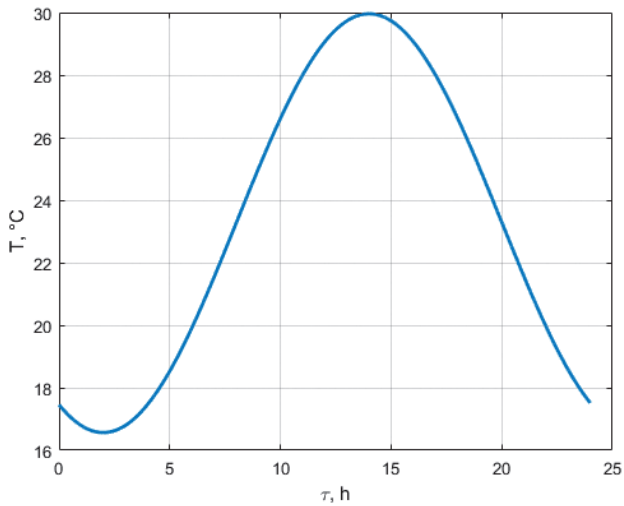


Fig. 14. Input data: ambient temperature.

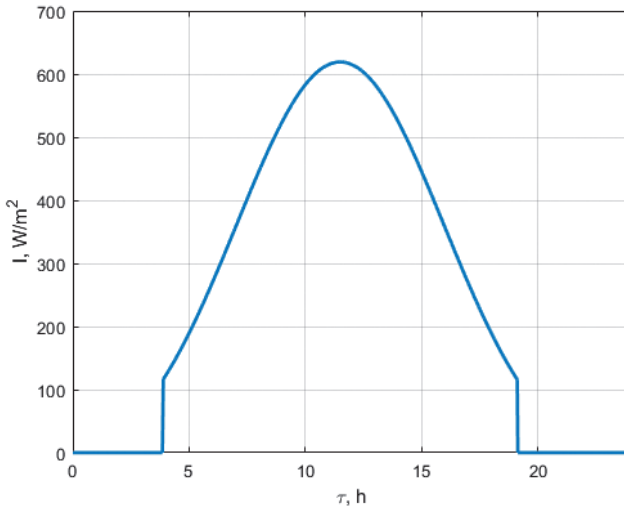


Fig. 15. Input data: solar irradiance.

3.2. Results of the simulation

The outlet temperature of the consumer-side (T_{outU}) of the heat storage and the outlet temperature of the solar collector (T_{outC}) can be seen in Fig. 16. The figure shows that the controlled heat storage temperature kept the 50 °C set point value with less than 0.2 °C dynamic error in the controlled period. Additionally, it was observed that in the non-controlled period, the solar collector outlet and the heat storage temperatures had almost the same value because of the relatively small volume of the storage tank.

Fig. 17 shows the flow rate of the consumer-side pump which is proportional to the control signal (CS2). It can be seen, that the controller solved a dynamic problem with online optimization, and the control signal reflects the characteristics of both the environmental temperature and the solar irradiance, as it was expected.

The MPC was chosen for its ability to handle dynamic systems with slow response time, and the results show that this control algorithm is capable of solving the controlling task of a solar thermal system. The study confirmed that this control approach works with the current framework, namely the SimSolar block-library and the Model Predictive Control Toolbox of Simulink, and this fact opens up a way for further expansion of this idea, e.g., the HIL implementation.

The simulation verified that the Weather API block works. This result is as important as the working of the MPC, because it proved that a generic C language-based TCP/IP client could be implemented within the Simulink framework. This

means that it can be the base of a bridge between the modern online data storage methods and the Simulink framework, because every major online system has some form of an API, either TCP/IP based or C language library. Despite the fact that the C language is mainly used as a system programming language, it is a generic programming language with nearly 50 years' worth of programmer knowledge along with the proven-to-work function libraries.

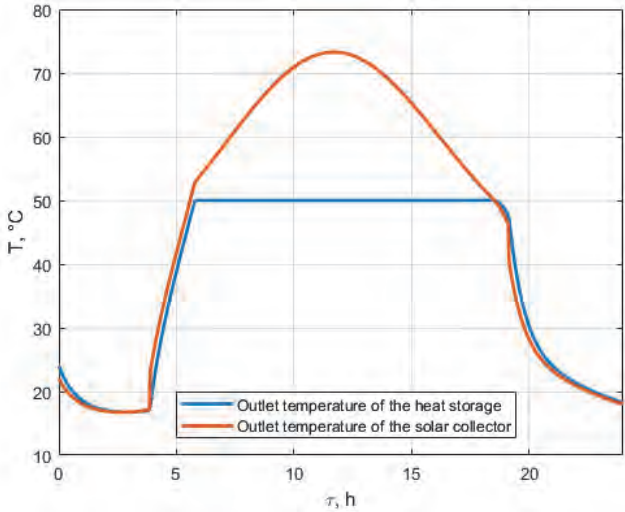


Fig. 16. Outlet temperatures of the system.

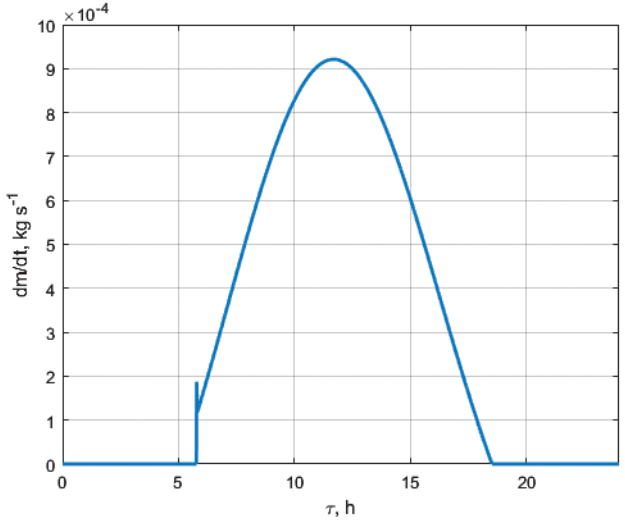


Fig. 17. Mass flow-rate of the controlled consumer-side pump.

4. Summary

A previously verified mathematical model capable of describing a solar thermal system was created in a block-oriented way. This model of the system contains the mathematical models of the solar collector, the heat storage, and the pump. These components are part of the block-oriented library for the solar thermal simulations, called SimSolar.

In order to use real-life measurement data in the simulation, a custom Simulink block was created in the C programming language that can handle the TCP/IP based communication with the server, and it can interpret the JSON formatted response of the server. This block has proven that an external source of data, especially the meteorological ones, can be integrated into the simulation workflow of the Simulink framework, and the usage of an external programming language can be beneficial to solve problems that Simulink is not designed to solve by itself.

The controlling of the model of the solar thermal system was performed by a model predictive controller to study and refine its behavior. Usually, the solar thermal systems have a slow response time, so the predictive control algorithm would be more suitable for them. The development in the IT field has paved the way to exploit such a computationally heavy control method by using an average personal computer.

The studied system had a set point of 50 °C, and the controller kept the outlet temperature within the set limits.

This research has shown that the usage of an online database server containing input data for the simulation is a quality-of-life addition; it eases the process of the import of the real-life data into the simulation. It has also shown that the model predictive control of a solar thermal system can be carried out using computers available at home, and it can be expanded with an HIL simulation in the future.

References

- Farkas, I., 1999: Computer simulation, Textbook, 45–68.
- Parrino, M., Mannoni, A., Bonisoli, E., and Sorli, M., 2005: Block-oriented models for transient HVAC simulations, *J. Passenger Car: Mech. Syst. J.* 114, No. 6.
<https://doi.org/10.4271/2005-01-2002>
- Tóth, J. and Farkas, I., 2017: A Simulink library for solar energy applications, *R&D in Mech. Engin. Lett.* 16.
- Tóth, J. and Farkas, I., 2018. Implementing database support for Simulink applied for solar thermal systems. Book of Abstracts, 24th Workshop on Energy and Environment.
- Tóth, J., Erdélyi, V., Farkas, I., and Jánosi, L., 2019. Hardware-in-the-loop control of a small-scale thermal system. Book of abstracts, BioPhys Spring 2019.
- Shuzhi, S.G., Chenguang, Y.; and Tong, H.L., 2008. Adaptive predictive control using neural network for a class of pure-feedback systems in discrete time. *IEEE Trans. Neural Netw.* 19, 1599–1614.
<https://doi.org/10.1109/TNN.2008.2000446>

- Qin, S.J. and Badgwell, T.A.*, 2003: A survey of industrial model predictive control technology. *Contr. Engin. Practicle 11*. 733–764. [https://doi.org/10.1016/S0967-0661\(02\)00186-7](https://doi.org/10.1016/S0967-0661(02)00186-7)
- Qu, M., Yin, H., and Archer, D.H.*, 2010: A solar thermal cooling and heating system for a building: Experimental and model based performance analysis and design, *Solar Energy 84*. 166–182. <https://doi.org/10.1016/j.solener.2009.10.010>
- Wang G.*, 2011: Improving data transmission in web applications via the translation between XML and JSON. Proceedings - 2011 3rd International Conference on Communications and Mobile Computing, CMC 2011. <https://doi.org/10.1109/CMC.2011.25>
<https://www.github.com/DaveGamble/cJSON>
<https://www.mathworks.com/products/mpc.html>
<https://www.mathworks.com/help/simulink/sfg/writing-level-2-matlab-s-functions.html>
<https://www.mathworks.com/help/mpc/ug/choosing-sample-time-and-horizons.html>

IDOJÁRÁS

Quarterly Journal of the Hungarian Meteorological Service
Vol. 125, No. 2, April – June, 2021, pp. 229–253

Spatiotemporal variability of air temperatures in Central Serbia from 1949 to 2018

Nikola R. Bačević*¹, **Nikola M. Milentijević**¹, **Aleksandar Valjarević**²,
Ajša Gicić¹, **Dušan Kićović**³, **Milica G. Radaković**⁴, **Milena Nikolić**¹,
and **Milana Pantelić**⁴

¹*University of Priština, Faculty of Sciences
Department of Geography
Kosovska Mitrovica, Serbia*

²*University of Belgrade, Faculty of Geography
Studentski Trg 3/III, Belgrade, Serbia*

³*The College of Tourism
Academy of Applied Studies, Belgrade, Serbia*

⁴*University of Novi Sad,
Faculty of Sciences, Department of Geography,
Tourism and Hotel Management, Novi Sad, Serbia*

**Corresponding author e-mail: nikola.bacevic@pr.ac.rs*

(Manuscript received in final form July6, 2020)

Abstract—The paper presents trends for three categories of variables: average annual, average maximum and average minimum air temperatures. Data was provided by the meteorological yearbooks of the Republic Hydrometeorological Service of Serbia. The main goal of this paper is to detect possible temperature trends in Central Serbia. The trend equation, trend magnitude, and Mann-Kendall non-parametric test were used in the analysis of climate parameters. The used statistical methods were supplemented by GIS numerical analysis, which aimed to analyze the spatial distribution of isotherms from 1949 to 2018. The obtained results indicate that out of the 72 analyzed time series, an increase in air temperature is dominant in 61 time series, while 11 time series show no changes. The highest increase was recorded in the average maximum time series (4.2 °C), followed by an increase of 3.5 °C in average maximum air temperatures. The highest increase in the average annual time-series was 3.0 °C. The lowest increases in air temperature were recorded in the average minimum time series (0.1 and 0.2 °C). In two average minimum time series a decrease in average air temperatures was identified (-0.6 and -0.4 °C). The application of GIS tools indicates the existence of interregional

differences in the arrangement of isotherms, led by the orography of the terrain. In the spatial distribution of the analyzed variables, "poles of heat" and "poles of cold" stand out, and the influence of the urban heat island is evident (especially in the case of the urban agglomeration of Belgrade). The manifested spatial patterns of air temperature need to be further examined and the correlation with possible causes need to be determined. For these reasons, the paper provides a solid basis for studying the climate of this area in the future, as it provides insight into climate dynamics over the past decades.

Key-words: variability, climate change, air temperature trends, Mann-Kendall trend test, GIS numerical analysis, isotherms, Central Serbia

1. Introduction

Climate change is referred to as large variations in climate averages which exist for decades or even longer periods. *Hansen et al.* (2013) concluded that the Pleistocene climate oscillations yield a fast-feedback climate sensitivity of $3\pm 1\text{ }^{\circ}\text{C}$ for a 4 W m^{-2} CO_2 forcing if Holocene warming relative to the Last Glacial Maximum (LGM) is used as calibration. The most of the research on climate change and climate variability was focused on analyses of the second half of the 20th century. This is highlighted by the conclusion of the 5th Assessment Report (AR5) of the Intergovernmental Panel on Climate Change (IPCC): „it is extremely likely that more than half of the observed increase in global average surface temperature from 1951 to 2010 was caused by the anthropogenic increase in greenhouse gas concentrations and other anthropogenic forcings together“ (*Bindoff et al.*, 2013). According to the IPCC (2018), a $0.87\text{ }^{\circ}\text{C}$ increase of mean air temperature on global scale during the last decade (2005–2015) was identified. A similar trend continued during this decade. Thus, the WMO (2019) identified 2015, 2016, 2017, and 2018 as the warmest years during the instrumental period.

In recent years, various studies for detecting possible trends and changes related to climate across the world's regions have been published. *Klein Tank and Können* (2003) identified changes in mean air temperatures trends for more than 100 meteorological stations across Europe. The pronounced warming was especially intensive between 1976 and 1999; it is primarily associated with an increase in warm extremes rather than with a decrease in cold extremes. *ElNesr et al.* (2010) analyzed the changes of air temperature trends over the Arabian Peninsula. A warming trend was found in cases of mean annual, mean maximum, and mean minimum air temperatures. Exceptions are the winter months (November to January), where non-significant cooling trends were observed. *Karaburun et al.* (2011) analyzed the trends of annual, seasonal, and monthly mean, minimum, and maximum temperatures in Istanbul from 1975 to 2006 by using the Mann-Kendall (MK) test and the Sen's method. Based on the air temperature measurements from 622 meteorological stations in China, *Du et al.* (2019) analyzed the temperature response to the global warming effects at

national and regional scales. They identified air temperature changes from 0.2 °C per decade from 1998 to 2012. However, the mean increase is lower in comparison to the period from 1960 to 1998 (0.4 °C per decade).

Numerous papers are dealing with air temperature changes across the regions of Southeast Europe: in Montenegro (*Luković et al.*, 2013; *Burić et al.*, 2014, 2015, 2018, 2019), Bosnia and Herzegovina (*Trbić et al.*, 2017; *Popov et al.*, 2017, 2018a, 2018b, 2019), Croatia (*Tadić et al.*, 2019; *Radilović et al.*, 2020), and Slovenia (*Milošević et al.*, 2013, 2017; *Tošić et al.*, 2016).

Observed climatological data for Serbia were analyzed and classified into a few main categories: air temperature variables (*Unkašević and Tošić*, 2013; *Gocić and Trajković*, 2013; *Bajat et al.*, 2015; *Putniković et al.*, 2018; *Vukočić et al.*, 2018) and parameters as aridity and drought (*Gocić and Trajković*, 2014a, 2014b; *Hrnjak et al.*, 2014; *Radaković et al.*, 2018; *Milentijević et al.*, 2018; *Trajković et al.*, 2020). Several papers are focused on climate change problems on regional level on the territory of Serbia: Vojvodina (*Gavrilov et al.*, 2015, 2016, 2019), Kosovo and Metohija¹ (*Bačević et al.*, 2017, 2018; *Gavrilov et al.*, 2018). However, on the territory of Central Serbia, air surface temperature trends were not examined up to now. For that reason, the purpose of this paper is to analyze the variability of selected meteorological variables at 24 meteorological stations over Central Serbia from 1949 to 2018. Thus, the main objectives of this study are: (1) to analyze and discuss the trend characteristics of meteorological variables in details; (2) to quantify the significance of changes by using the linear regression, the trend magnitude calculated from the trend equation, and by the application of MK non-parametric test; and (3) to present spatial distribution of isotherms on a defined study area using GIS numerical analysis.

2. Data and methods

2.1. Research area

Central Serbia is located on the Balkan Peninsula and is a toponym that refers to the territory of Serbia (excluding the autonomous provinces Vojvodina, and Kosovo and Metohija). The borders of Central Serbia with the neighboring regions are natural: 1) in the west the River Drina forms the border with Bosnia and Herzegovina, 2) in the north, the River Danube forms the border with Romania, while Danube and Sava rivers with Vojvodina, 3) in the east, the Carpatho-Balkans form the border with Bulgaria, 4) in the south it borders Northern Macedonia, and 5) in the southwest it borders Montenegro. The total

¹ According to the Kumanovo Agreement and United Nations Security Council Resolution 1244 (1999), Kosovo and Metohija are considered as the part of Serbian territory under the international protectorate (*Clark*, 2014).

area of Central Serbia (Fig. 1) is 55,947 km², and it makes up 63.3% of the territory of the Republic of Serbia (88,361 km²). The most important orographic units that affect the transformation of air masses and the climate of Central Serbia are the Pannonian Plain, the Dinarides, and the Carpatho-Balkans. Arctic continental air masses come to Central Serbia across the Pannonian Plain in the colder half of the year. The Dinarides and Carpatho-Balkanids represent an orographic barrier, which weakens the flow of air masses. In these parts, continental tropical air masses originating from North Africa in the warmer half of the year cause high summer temperatures (Ducić and Radovanović, 2005). As a consequence of this atmospheric circulation, absolute temperature extremes were recorded in the meteorological stations of Serbia. Thus, in Smederevska Palanka, the absolute maximum air temperature of 44.9 °C was recorded on July 24, 2007. The absolute temperature minimum of -39.0 °C was recorded on the Pešter plateau, on January 26, 2006 (Andjelković, 2007). In Central Serbia, the influence of the continental and temperate-continental climates prevail. According to the Köppen climate classification, Central Serbia belongs to the Cfa climate (average temperature above 20 °C during the warmer months and above -3 °C during the colder months), while in the high mountains (above 1500 m) the Dfa climate is present (average temperature below 20 °C during warmer months and below -3 °C during colder months (Radinović, 1981). The average annual air temperature for the time interval from 1949 to 2018 is 10.7 °C, the average maximum air temperature is 25 °C, while the average minimum temperature is -1.9 °C.

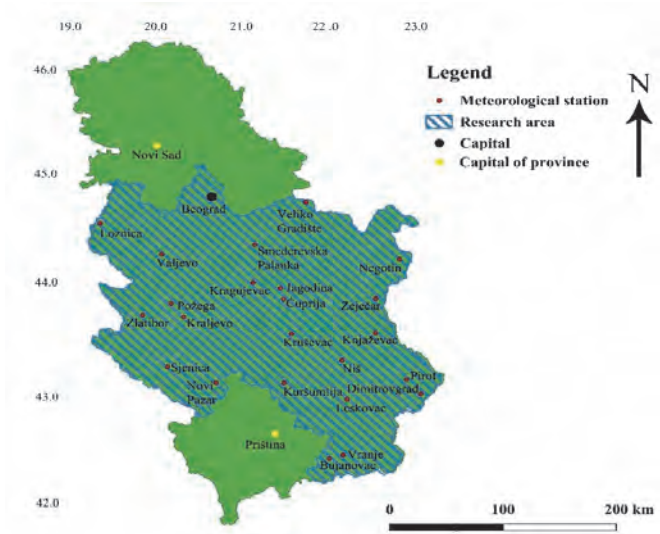


Fig. 1. Geographical position of Central Serbia with the analyzed meteorological stations.

2.2. Materials

In this study, three data sets of surface air temperatures were used: monthly mean temperatures, monthly maximum temperatures, and monthly minimum temperatures. From these three data sets, new data sets were created: mean annual air temperatures (YT), mean maximum air temperatures (YT_x), and mean minimum air temperatures (YT_n). The selected climatological datasets were collected from 24 meteorological stations from Central Serbia for the period from 1949 to 2018. For the purpose of this study, based on the mentioned meteorological stations, 72 time series were identified (Fig. 2). The data (Table 1) were obtained from the Republic Hydrometeorological Service of Serbia (RHSS, 2019). Analysis was performed on the selected stations due to three reasons: 1) each of the stations has good quality of datasets, 2) the data are reliable, 3) the data have adequate record length. Before calculation, the homogeneity of the temperature data was examined. Inhomogeneity in time series can cause the incorrect interpretation of climate time series (Rahman *et al.*, 2017), and be misleading in the interpretation of tendencies in the time series. Several methods can be used to detect abrupt changes, e.g., Alexandersson's test (Alexandersson, 1986), Pettitt's test (Kocsis *et al.*, 2020). In this paper, the homogeneity test according to Alexandersson (1986) was performed. Applying the Alexandersson's test, all series were found to be homogeneous. Heterogeneity of orography indicates different climate conditions over the defined study area. For example, the relative altitude between the highest (Sjenica) and the lowest meteorological stations (Negotin) is 996 meters of altitude.

2.3. Methods

Three main statistical procedures were used in order to analyze the temperature trends in 72 time series. In the first step, the trend equation (tendency) was calculated for each time series using the method of linear regression (Mudelsee, 2014). Second, in all cases the trend magnitude was calculated from the trend equation (Gavrilov *et al.*, 2018). Finally, the third step was to assess all trends using the MK non-parametric test (Zeleňáková *et al.*, 2018).

Table 1. Geographic features and short names of the analyzed meteorological stations used in the study.

Station No.	Station name	Latitude (N)	Longitude (E)	Altitude (m)
1.	Beograd (BG)	44°48′	20°28′	132
2.	Bujanovac (BU)	42°27′	21°46′	399
3.	Ćuprija (CU)	43°56′	21°23′	123
4.	Dimitrovgrad (DI)	43°01′	22°45′	450
5.	Jagodina (JA)	43°59′	21°23′	115
6.	Knjaževac (KŽ)	43°34′	22°15′	263
7.	Kragujevac (KG)	44°02′	20°56′	181
8.	Kraljevo (KV)	43°43′	20°42′	215
9.	Kruševac (KS)	43°37′	21°15′	404
10.	Kuršumlija (KU)	43°08′	21°16′	384
11.	Leskovac (LE)	42°59′	21°57′	231
12.	Loznica (LO)	44°32′	19°14′	121
13.	Negotin (NG)	44°14′	22°32′	42
14.	Niš (NI)	43°20′	21°54′	202
15.	Novi Pazar (NP)	43°08′	20°31′	545
16.	Pirot (PI)	43°09′	22°35′	373
17.	Požega (PŽ)	43°51′	20°02′	311
18.	Sjenica (SJ)	43°16′	20°00′	1038
19.	Smederevska Palanka (SP)	44°22′	20°57′	121
20.	Valjevo (VA)	44°17′	19°55′	174
21.	Veliko Gradište (VG)	44°45′	21°30′	80
22.	Vranje (VR)	42°33′	21°55′	433
23.	Zaječar (ZA)	43°53′	22°17′	144
24.	Zlatibor (ZL)	43°44′	19°43′	1029

2.3.1. Linear regression and trend equation

The linear regression describes X_{trend} by means of two parameters, namely the intercept, β_0 , and the slope, β_1 (Mudelsee, 2019). This method is used to estimate the trend by the following equation:

$$X(i) = \beta_0 + \beta_1 T(i) + S(i)X_{noise}(i), \quad (1)$$

where $T(i)$ is the time variable assigned to $X(i)$ and $S(i)X_{noise}(i)$ is the error term.

The trend equation has been long utilized in this type of research as an approach (Wibig and Glowicki, 2002), because it gives results which are simple to interpret; both graphically and analytically on the basis of the shape and parameters of the trend equation. For instance, the sign of the temperature trend depends on the value of the slope. There are three possible scenarios: a) if the size of slope is greater than zero, the sign of trend is *positive* (increase); b) if it is equal to zero, *there is no trend* (no changes); and c) if it is less than zero, the sign of trend is *negative* (decrease).

2.3.2. The trend magnitude

Based on the trend equation, the trend magnitude was defined and calculated as the difference in air surface temperature between the beginning and the end of the period (Gavrilov et al., 2016). The explained statistical procedure was defined as:

$$\Delta y = y(P_b) - y(P_e), \quad (2)$$

where Δy is the trend magnitude in °C, values $y(P_b)$ and $y(P_e)$ represent air surface temperatures from the trend equation in the beginning, P_b , and at the end of period, P_e . In our cases, the beginning period is defined as, $P_b=1949$, while the end of the period is $P_e=2018$.

2.3.3. The Mann-Kendall non-parametric test

In this study, the non-parametric MK test is used for the detection of the trend in a time series. This test is widely used in environmental science, because it is simple and robust and can cope with missing values and values below a detection limit. The first proposal of the test was by Mann (1945) and Kendall (1938). The MK test is a rank-based nonparametric test for assessing the significance of a trend, and it has been widely used in hydrometeorological trend detection studies: hydrological time series (Burn and Hag Elnur, 2002); air surface temperature (Karmeshu, 2012), precipitation (Ahmad et al., 2015), temperature extremes (Serra et al., 2001), aridity (Hrnjak et al., 2014), evapotranspiration (Shadmani et al., 2012). However, inconsistencies in hydroclimatical data recording may occur due to various reasons, such as: instrumentation, changes in observation procedures, or changes in gauge location or surrounding conditions (Alexander et al., 2006).

The MK test statistic S (Karmeshu, 2012) can be calculated as:

$$S = \sum_{i=1}^{n-1} \sum_{j=i+1}^n \text{sgn}(x_j - x_i), \quad (3)$$

where n is the number of data points, x_j and x_i are the data values in time series i and j ($j > i$), respectively, and $sgn(x_j - x_i)$ is the sign function as:

$$sgn(x_j - x_i) = \begin{cases} +1, & \text{if } x_j - x_i > 0 \\ 0, & \text{if } x_j - x_i = 0 \\ -1, & \text{if } x_j - x_i < 0 \end{cases} \quad (4)$$

The variance is computed as:

$$var(S) = \frac{n(n-1)(2n+5) - \sum_{i=1}^m t_i(t_i-1)(2t_i+5)}{18}, \quad (5)$$

where n is the number of data points, m represents the number of tied groups while t_i denotes the number of ties of extent i . A tied group is a set of sample data having the same value. In cases where the sample size $n > 10$, the standard normal test statistic Z_s is computed as:

$$Z_s = \begin{cases} \frac{S-1}{\sqrt{var(S)}}, & \text{if } S > 0 \\ 0, & \text{if } S = 0 \\ \frac{S+1}{\sqrt{var(S)}}, & \text{if } S < 0 \end{cases} \quad (6)$$

Positive values of Z_s indicate increasing trends, while negative Z_s values show decreasing trends. Testing trends is done at the specific α significance level. By using MK test, two hypotheses were tested: zero hypothesis (H_0) – pointing to the inexistence of trend in time series; and alternative hypothesis (H_a) – pointing to the existence of statistically significant trend in time series for the chosen level of significance (α). The main role in MK test belongs to the value of p (Razavi *et al.*, 2016). The value of p determines the accuracy of hypothesis. If the value p is lower than the chosen level of significance α (it is common that $\alpha=0.05$ or 5%), the hypothesis H_0 should be rejected and hypothesis H_a is accepted. When p is larger than the level of significance, then the hypothesis H_0 is accepted (Gavrilov *et al.*, 2016). In the paper *XLSTAT* software was used (www.xlstat.com) for calculating the probability p , and for hypothesis testing.

2.3.4. QGIS analysis

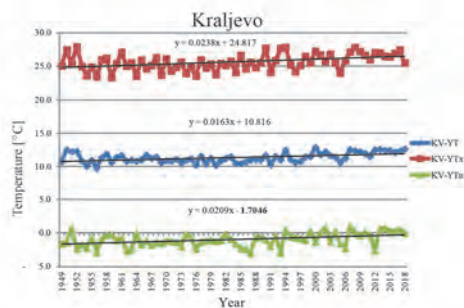
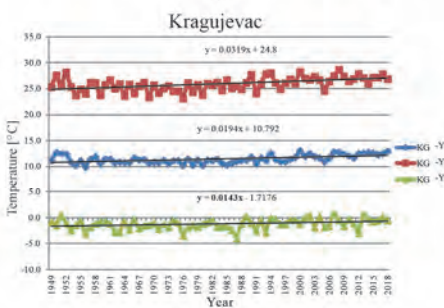
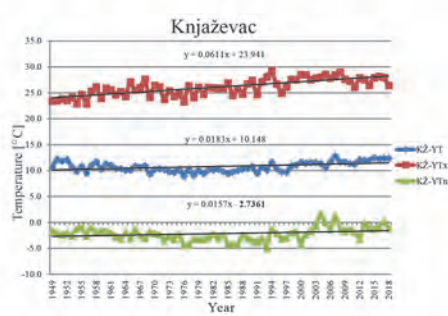
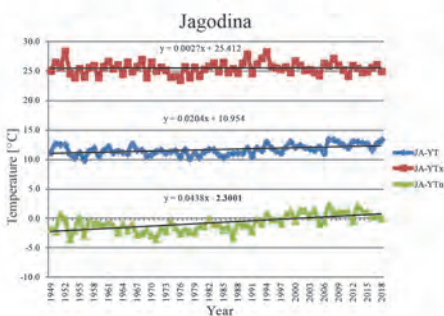
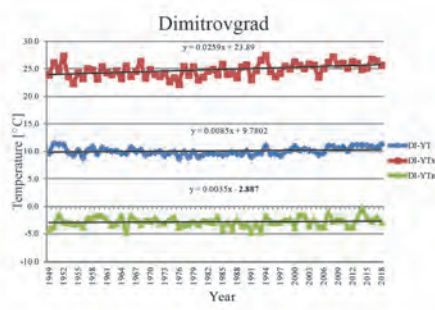
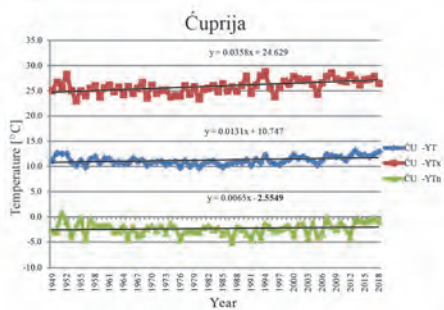
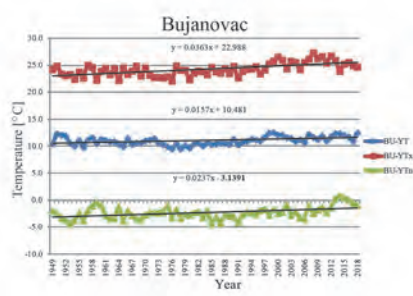
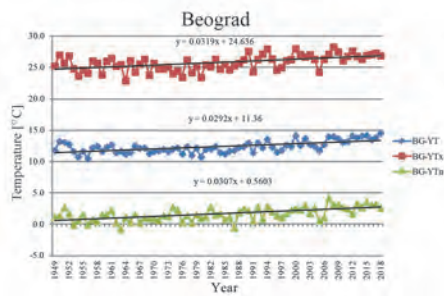
GIS and data modeling are very powerful tools for estimating and calculating data of meteorological properties within an area (Tomazos and Butler, 2009; Blake *et al.*, 2007). There are several methods for this calculation, but in this

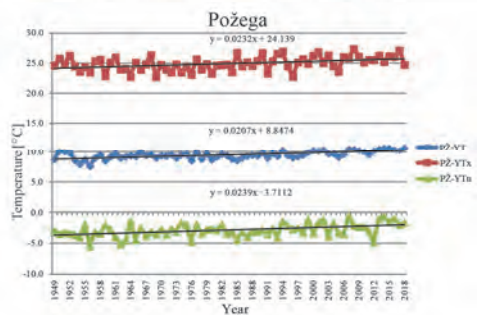
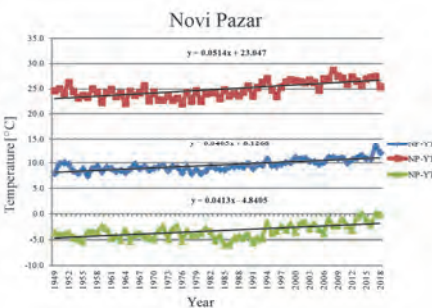
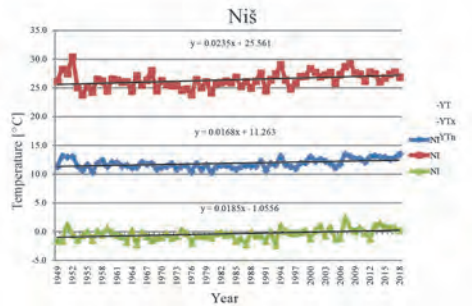
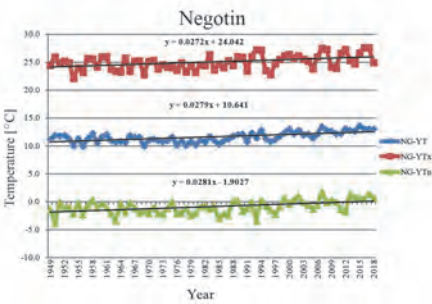
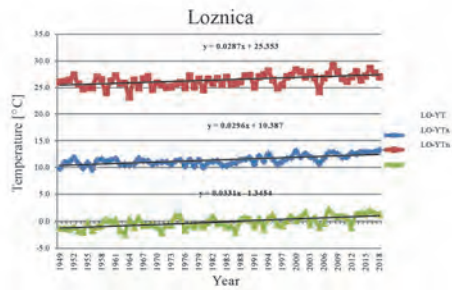
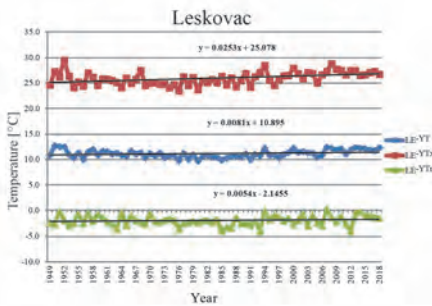
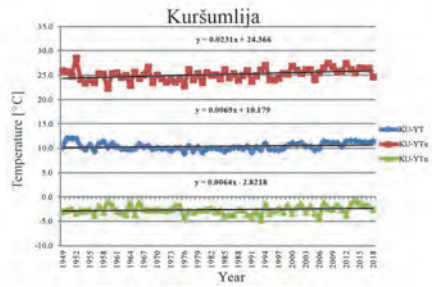
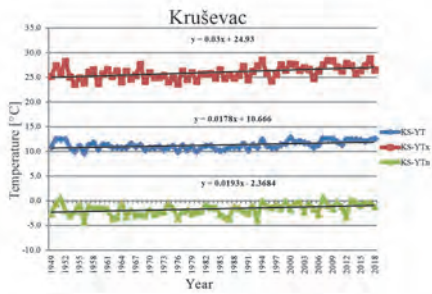
research we gave importance to the methods of kriging and interpolations. Semi-automated and ordinary kriging methods were established through the QGIS 3.12.0 (Quantum Geographical Information System) and SAGA (System for Automated Geoscientific Analysis) tools. Although there are a few other methods which can be used in spatial analysis, the priority is given to the semi-automated and ordinary krigings, because they include autocorrelation of the statistical relationship among measured points (Valjarević *et al.*, 2018). These maps show the dispersion of climate properties, temperature and precipitation on the territory of Central Serbia. GIS methods and spatial variability functions can be used along with methods of interpolation in mapping the climate properties (Wang *et al.*, 2018). The models used in the spatial research are based on the Gaussian distribution. QGIS has a wide range of spatial models, which can be successfully applied. Method of interpolation is also used in order to compare potential errors in the estimations. In this research, the data from 24 meteorological stations were used. These stations are well distributed. In that way, the created maps have a small percent of errors.

3. Results

3.1. Trend parameters

In this paper, the main results are summarized in *Table 2* and *Figs. 2* and *3*. The data for 24 meteorological stations, which are located in Central Serbia (a total of 72 time series), are analyzed. The obtained results for the analyzed climate variables are presented through the trend equation and trend magnitude in *Fig. 2* and *Table 2*. The results of the MK trend test as well as the evaluation of hypotheses are shown in *Fig. 3*. The spatial distribution of average annual (YT), average maximum (YT_x), and average minimum (YT_n) air temperatures is shown in more detail in *Fig. 4*.





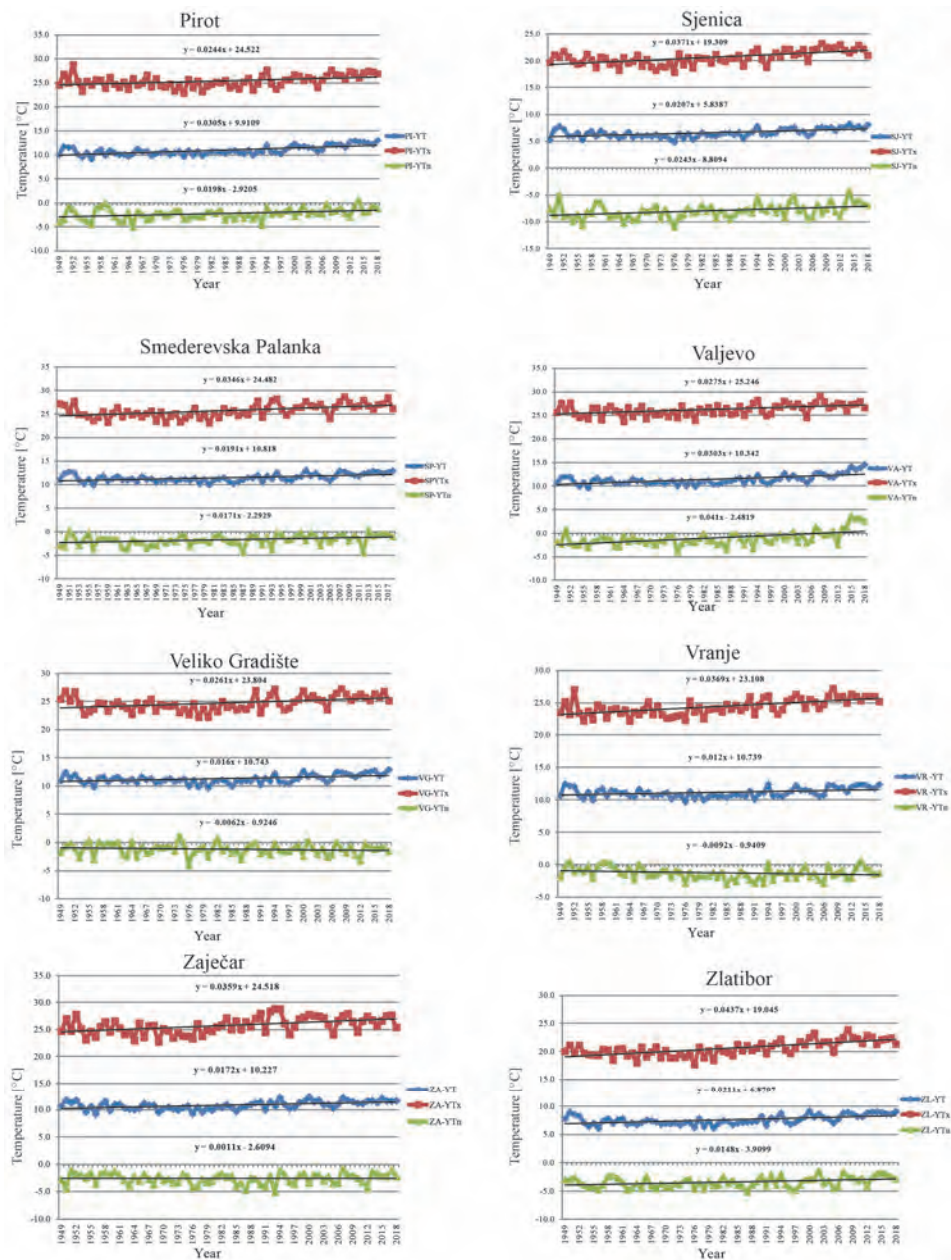


Fig. 2. Average annual (YT), average maximum (YT_x) and average minimum air temperatures (YT_n), trend equations and linear trend for selected meteorological stations in Central Serbia from 1949 to 2018.

Table 2. Trend equation, trend magnitude (Δy), and average temperature for 72 time series for average annual (YT), average maximum (YT_x) and average minimum (YT_n) temperatures for the 24 selected stations. Acronyms for stations are listed in Fig. 2.

Time series	Trend equation	Δy (°C)	Average temperature (°C)
BG-YT	$y = 0.0292x + 11.36$	2.0	12.1
BG-YT _x	$y = 0.0319x + 24.636$	2.2	25.8
BG-YT _n	$y = 0.0307x + 0.5603$	2.1	1.6
BU-YT	$y = 0.0157x + 10.481$	1.1	11.0
BU-YT _x	$y = 0.0363x + 22.988$	2.5	24.3
BU-YT _n	$y = 0.0237x - 3.1391$	1.6	-2.3
ĆU-YT	$y = 0.0131x + 10.747$	0.9	11.2
ĆU-YT _x	$y = 0.0358x + 24.629$	2.5	25.9
ĆU-YT _n	$y = 0.0065x - 2.5549$	0.5	-2.3
DI-YT	$y = 0.0085x + 9.7802$	0.6	10.1
DI-YT _x	$y = 0.0259x + 23.89$	1.8	24.8
DI-YT _n	$y = 0.0035x - 2.887$	0.2	-2.8
JA-YT	$y = 0.0204x + 10.954$	1.4	11.7
JA-YT _x	$y = 0.0027x + 25.412$	0.2	25.5
JA-YT _n	$y = 0.0438x - 2.3001$	3.0	-0.7
KŽ-YT	$y = 0.0183x + 10.148$	1.3	10.8
KŽ-YT _x	$y = 0.0611x + 23.941$	4.2	26.1
KŽ-YT _n	$y = 0.0157x - 2.7361$	1.1	-2.2
KG-YT	$y = 0.0194x + 10.792$	1.3	11.5
KG-YT _x	$y = 0.0319x + 24.8$	2.2	25.9
KG-YT _n	$y = 0.0143x - 1.7176$	1.0	-1.2
KV-YT	$y = 0.0319x + 24.8$	1.1	11.4
KV-YT _x	$y = 0.0319x + 24.8$	1.6	25.6
KV-YT _n	$y = 0.0319x + 24.8$	1.4	-1.0
KS-YT	$y = 0.0178x + 10.666$	1.2	11.3
KS-YT _x	$y = 0.03x + 24.93$	2.1	26.0
KS-YT _n	$y = 0.0193x - 2.3684$	1.3	-1.7
KU-YT	$y = 0.0069x + 10.179$	0.5	10.4
KU-YT _x	$y = 0.0231x + 24.366$	1.6	25.2
KU-YT _n	$y = 0.0064x - 2.8218$	0.4	-2.6
LE-YT	$y = 0.0081x + 10.895$	0.6	11.2
LE-YT _x	$y = 0.0253x + 25.078$	1.7	25.9
LE-YT _n	$y = 0.0054x - 2.1455$	0.4	-2.0
LO-YT	$y = 0.0296x + 10.387$	2.0	11.4
LO-YT _x	$y = 0.0287x + 25.353$	2.0	26.3
LO-YT _n	$y = 0.0331x - 1.3454$	2.3	-0.2
NG-YT	$y = 0.0279x + 10.641$	1.9	11.6

Time series	Trend equation	Δy (°C)	Average temperature (°C)
NG-YT _x	$y = 0.0272x + 24.042$	1.9	25.0
NG-YT _n	$y = 0.0281x - 1.9027$	1.9	-1.0
NI-YT	$y = 0.0168x + 11.263$	1.2	11.1
NI-YT _x	$y = 0.0235x + 25.561$	1.6	26.4
NI-YT _n	$y = 0.0185x - 1.0556$	1.3	-0.3
NP-YT	$y = 0.0405x + 8.1268$	2.8	9.5
NP-YT _x	$y = 0.0514x + 23.047$	3.5	24.9
NP-YT _n	$y = 0.0413x - 4.8405$	2.8	-3.4
PI-YT	$y = 0.0305x + 9.9109$	2.1	11.0
PI-YT _x	$y = 0.0244x + 24.522$	2.1	25.4
PI-YT _n	$y = 0.0198x - 2.9205$	1.4	-2.2
PŽ-YT	$y = 0.0207x + 8.8474$	1.4	9.6
PŽ-YT _x	$y = 0.0232x + 24.139$	1.6	24.9
PŽ-YT _n	$y = 0.0239x - 3.7112$	1.7	-2.8
SJ-YT	$y = 0.0207x + 5.8387$	1.4	6.6
SJ-YT _x	$y = 0.0371x + 19.309$	2.6	20.6
SJ-YT _n	$y = 0.0243x - 8.8094$	1.7	-8.0
SP-YT	$y = 0.0191x + 10.818$	1.3	12.0
SP-YT _x	$y = 0.0346x + 24.482$	2.4	25.7
SP-YT _n	$y = 0.0171x - 2.2929$	1.2	-1.8
VA-YT	$y = 0.0303x + 10.342$	2.1	11.4
VA-YT _x	$y = 0.0275x + 25.246$	2.0	26.2
VA-YT _n	$y = 0.041x - 2.4819$	2.8	-1.1
VG-YT	$y = 0.016x + 10.743$	1.1	11.4
VG-YT _x	$y = 0.0261x + 23.804$	1.8	24.8
VG-YT _n	$y = -0.0062x - 0.9246$	-0.4	-1.1
VR-YT	$y = 0.012x + 10.739$	0.8	11.2
VR-YT _x	$y = 0.0369x + 23.108$	2.6	24.4
VR-YT _n	$y = -0.0092x - 0.9409$	-0.6	-1.3
ZA-YT	$y = 0.0172x + 10.227$	1.2	10.8
ZA-YT _x	$y = 0.0359x + 24.518$	2.5	25.8
ZA-YT _n	$y = 0.0011x - 2.6094$	0.1	-2.6
ZL-YT	$y = 0.0211x + 6.8797$	1.5	7.6
ZL-YT _x	$y = 0.0437x + 19.045$	3.0	20.5
ZL-YT _n	$y = 0.0148x - 3.9099$	1.0	-3.4

Based on the magnitude of the trend (Δy), the character of climate change can be presented, i.e., the average increase or decrease of observed climate variables. Generally speaking, the analyzed time series show an increase in average annual (YT), average maximum (YT_x) and average minimum (YT_n) air temperatures in Central Serbia. The highest average increase was recorded in the case of average maximum air temperatures (time series KŽ-YT_x records an

average increase of 4.2 °C). Weaker intensity of changes was recorded in two time series: 3.5 °C (NP-YT_x) and 3.0 °C (JA-YT_n). The lowest increase in air temperature was recorded in the case of average minimum air temperatures (time series ZA-YT_n). In this particular case, an average increase in air temperature of only 0.1 °C was recorded. Similar results were observed in the time series DI-YT_n (Δy is 0.2 °C) and JA-YT_x (Δy is 0.2 °C). In two time series, which refer to air temperatures YT_n (VR-YT_n and VG-YT_n), a decrease in air temperature was recorded, with averages -0.6 °C and -0.4 °C, respectively.

3.2. Trend assessment

The results obtained by applying the non-parametric MK trend test, which serves to assess the hypotheses, are described in more detail in *Fig. 3*. General conclusions can be summarized in the following statements: a) out of a total of 72 time series, a statistically significant positive trend was recorded in 61 time series (the hypothesis H_a prevails, while the p value is lower than the significance level α). In these time series the risk percentage is very low and ranges from 0.01% to 5.00%, which indicates that this statement should not be rejected; b) on the other hand, in the remaining 11 time series there is no trend (and in these cases the hypothesis H_o prevails, while the p value is greater than the significance level α). In these time series, the risk of rejecting this hypothesis is significantly higher and ranges from 5.00% to 95.46%. In four time series, the risk of rejecting such a claim ranges from 5.00% to 10.00%, which indicates that there is no trend. Also, in the next four time series, the risk of rejecting this hypothesis ranges from 10.00% to 50.00%, which indicates a declining trend. In the last three time series, the value of risk ranges from 70.15% to 95.46%, which indicates a growing trend and a possible transition to a positive trend.

In most of the analyzed cases, a positive equation trend is followed by a positive significant trend from MK test (*Fig. 3*). The third case shows two deviations, when the positive trend was not recognized by the MK test in Knjaževac, as well as the negative trend was not recognized in Veliko Gradište. According to the MK test in case of Vranje, a positive significant trend was recorded together with a negative equation trend.

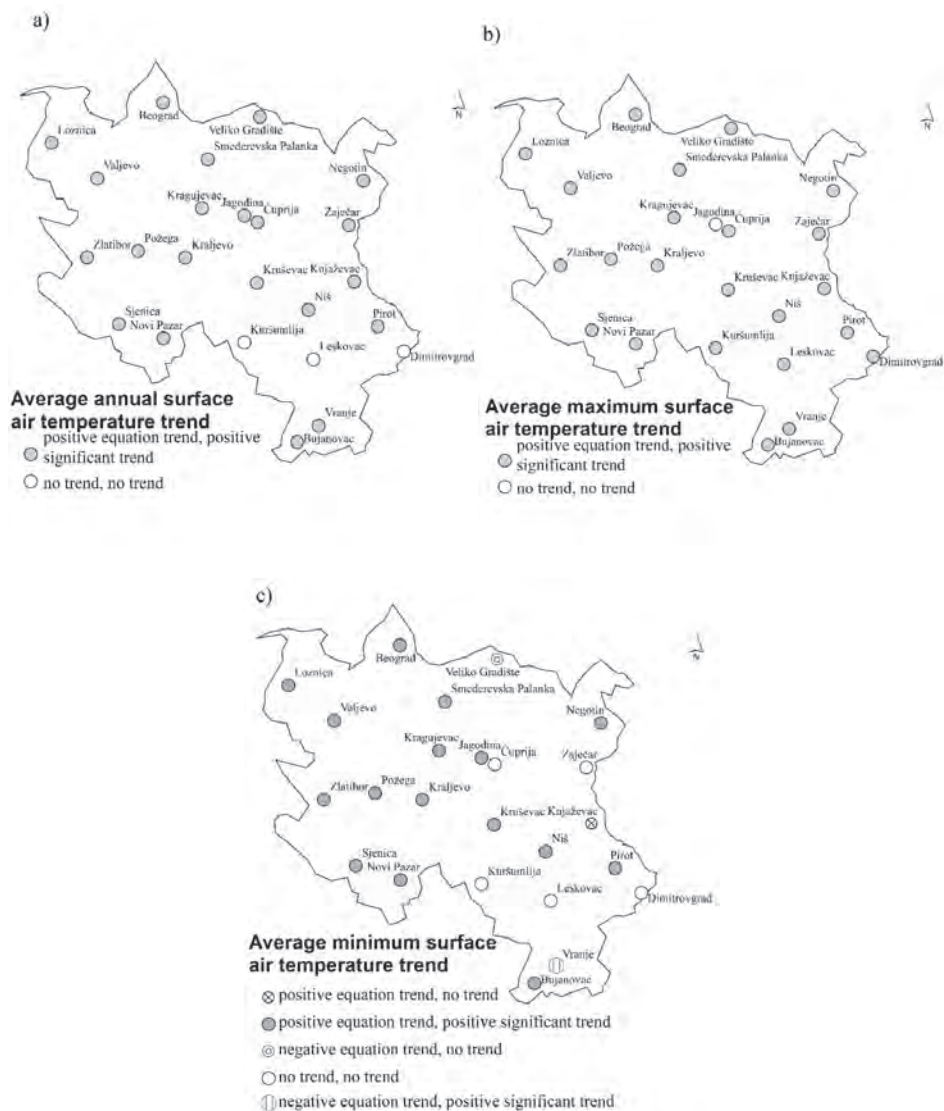


Fig. 3. The results of linear equation trends and MK test separated by a comma: a) average annual air temperature; b) average maximum air temperature; c) average minimum air temperature.

3.3. GIS numerical analysis

The spatial distribution of average annual (YT), average maximum (YT_x) and average minimum (YT_n) air temperatures from 1949 to 2018 in Central Serbia is shown in more detail in Fig. 4.

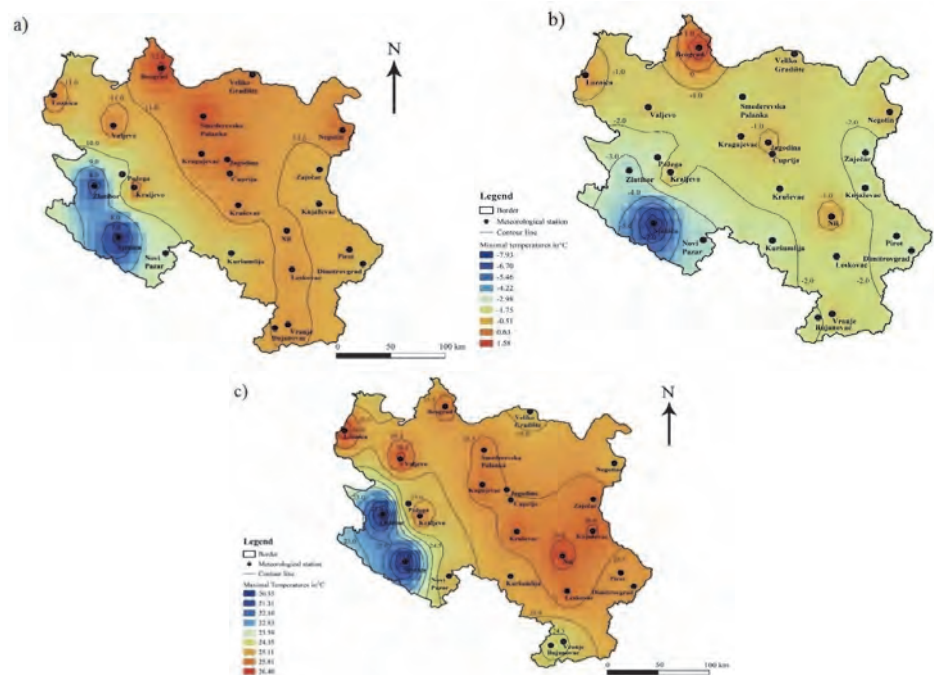


Fig. 4. Spatial distribution of a) average annual (YT), b) average maximum (YT_x), and c) average minimum (YT_n) air temperatures from 1949 to 2018 in Central Serbia.

Fig. 4 shows the distribution of average annual air temperatures (YT) in the analyzed area. Interregional differences in average air temperatures are caused by the influence of orography. Thus, the isotherms of 7 °C and 8 °C dominate in the hilly and mountainous area of the southwestern part of Central Serbia. The meteorological station at Beograd limits the isotherm to 12 °C, where the influence of the "urban heat island" is obvious. Thermal conditions in the central, eastern, and southern parts of the study area are limited by the 11 °C isotherm.

The values of average maximum air temperatures (YT_x) from 1949 to 2018 are summarized in *Fig. 4*. The patterns of behavior of average maximum air temperatures are similar in relation to average air temperatures. The valley positions of cities such as Niš, Knjaževac, Loznica, and Valjevo are the cause of the high average maximum air temperature (isotherm of 26 °C). These thermal oases are also the "poles of heat" of the analyzed area. The thermal inequalities of Zlatibor and Sjenica are even more caused by terrain hypsometry (isotherms of only 21 °C).

In the spatial distribution of average minimum air temperatures (YT_n) from 1949 to 2018, significant differences can be noticed in relation to the previously analyzed climate variables (*Fig. 4*). The effect of the "city heat island" can be partly explained by the increase in the average minimum air temperature at the meteorological station at Beograd, as a macro-proportional variation that affects the local microclimate. Here, in addition to the impact of urbanization and the increase in the population of the urban area, the intense warming in the winter months, the impact of traffic and industry come to the fore (*Unkašević, 1994*). However, additional research is needed to correlate the relationship between these parameters and the average minimum air temperature. At most meteorological stations, in the case of average minimum air temperatures, isotherms from -1.0 °C to -2.0 °C dominate. The exceptions are, as in the case of average annual (YT) and average maximum air temperatures (YT_x), the meteorological stations Sjenica (-7.0 °C) and Zlatibor (-4.0 °C), which represent the "cold poles" in Central Serbia.

4. Discussion

From the above presented results it can be concluded that the increase of the air temperature is dominant in Central Serbia. Based on the trend magnitude in *Table 2*, the increase in the temperatures was in a wide range of values from 0.1 °C to 4.2 °C. However, in two time series related to the mean minimal air temperatures, the decreases from -0.4 °C and -0.6 °C were identified. This behavior of the air temperatures in Central Serbia resembles the warming in the Northern Hemisphere (*Leroux, 2005*). Warming is expected to be enhanced and accelerated in the high latitudes of the Northern Hemisphere (the so-called "Arctic amplification" effect). The rise in Arctic near-surface air temperatures has been twice as large as the global average in recent decades (*Screen and Simmonds, 2010*). *Zheng and Wang (2019)* identified the past two summers as very hot in the Northern Hemisphere. A combination of natural internal variabilities and global warming explains summer air temperature variations in the Northern Hemisphere.

It is difficult to find identical results in regions over the world, but there are some similarities. *Türkes and Sümer (2004)* detected increasing air

temperatures in the western part of Turkey. *Kousari and Asadi Zarch* (2011) identified a significantly increasing trend for the minimum and mean temperatures while changes were not found for the maximum temperature in arid and semi-arid regions of Iran. In the mountainous part of Europe, the Swiss temperatures from 1959 to 2008 were analyzed (*Ceppi et al.*, 2012). The authors summarized: a) all trends are positive and mostly significant with an annual average warming rate of 0.35 °C/decade (~1.6 times as large as the northern hemispheric warming rate), b) altitude-dependent trends are found in autumn and early winter, where the trends are stronger at low altitudes (<800 m asl), and in spring where slightly stronger trends are found at altitudes close to the snow line. In the wider Mediterranean region, increasing trends have also been recorded. In their paper, *Gonzalez-Hidalgo et al.* (2015) suggested that the warming rate in the Spanish mainland reached a maximum between 1970 and 1990, followed by a decrease in intensity in both maximum temperatures (T_{\max}) and minimum temperatures (T_{\min}) until the present. Furthermore, the decrease in the warming rate in T_{\max} has been higher than in T_{\min} for the last three decades; therefore, recent annual warming rates appears to depend more on T_{\min} than on T_{\max} . Significant trends disappear from the middle of the 1980s at any temporal window length in both T_{\max} and T_{\min} at annual and seasonal scales except in spring T_{\min} . By analyzing data from 52 meteorological stations in Greece, a negative trend between 1960 and 1976 was found (*Mamara et al.*, 2016). A statistically significant positive trend has been reported since the period from 1977 to 2004. In the Southern Levantine Basin, *Tonbol et al.* (2018) examined the mean annual variations. The results of the study revealed that 2010 was the hottest year in the region, while 2011 was the coolest. These conclusions are in agreement with the latest *IPCC* report (2018), in which the increase in the global temperature is not homogeneously distributed on the Earth surface. Similarly, in the near region, the temperature increase is dominant in Montenegro (*Burić et al.*, 2014), Bosnia and Herzegovina (*Trbić et al.*, 2017; *Popov et al.*, 2018a, 2018b, 2019). In the territory of Serbia, in the region of Vojvodina (*Gavrilov et al.*, 2015, 2016) and in Kosovo (*Gavrilov et al.*, 2018), positive trends in air temperature were also observed. However, *Radaković et al.* (2018) did not notice any significant changes in the aridity trends over Central Serbia. Therefore, the dominant increase of air temperature is not in accordance with aridity trends in the same study area.

5. Conclusion

Based on the analyzed climate variables, certain conclusions can be drawn. In this paper, a total of 72 time series were analyzed using: a) trend equations, b) trend magnitude indicating the average increase or decrease in air temperature, c) MK non-parametric trend test, and d) GIS numerical analysis. Based on the

trend equation and the trend magnitude, the highest average increase was recorded in the case of average maximum air temperatures (4.2 °C). The lowest increase in air temperature was recorded in the case of average minimum air temperatures (0.1 °C). In two time series related to the average minimum air temperatures (VR-YT_n and VG-YT_n), a decrease in air temperature was recorded, which are -0.6 °C and -0.4 °C, respectively. Using the MK trend test, the obtained results indicate that in 61 time series, a statistically significant positive trend was recorded in the analyzed parameters. On the other hand, there are no changes in 11 time series (there is no trend). The spatial distribution of isotherms in Central Serbia is in the following intervals: from 6.6 °C to 12.1 °C for the average annual temperature, from 20.6 °C to 26.4 °C for the average maximum temperature, and from 1.6 °C to -7.9 °C for the average minimum temperature. Thermal inequalities are caused by pronounced hypsometric differences between the analyzed meteorological stations. They lead to the effect of a vertical thermal gradient - an average decrease of 0.65 °C in air temperature per 100 m altitude difference (*Oliver, 2005*). The presented climate dynamics of this area provide a solid basis for studying climate variations in the future, especially extreme climate events such as drought. Since the beginning of the 21st century, Europe has experienced a series of extremely hot and dry summers (2003, 2010, 2013, 2015) (*Fink et al., 2003; Laaha et al., 2017*). Drought causes numerous socio-economic consequences followed by water deficit, and impacts on nature and agricultural resources. These are the reasons why it is necessary to take appropriate adaptive measures before the manifestation of worse climatic conditions (*Bressers et al., 2016*). Central Serbia, as a significant agricultural region of the Republic of Serbia, requires certain measures in order to mitigate the resulting climate change, as defined in the Report of the Republic of Serbia under the UN Framework Convention on Climate Change (*Ministry of Environmental Protection, 2017*). Prominent reasons create the need for further research into the problems of climate change in Central Serbia (analysis of parameters such as absolute temperature extremes, seasonal air temperatures, and precipitation).

Acknowledgements: This paper represents the result within the projects III43007 and III044006 funded by the Serbian Ministry of Education, Science and Technological Development.

References

- Anđelković, G.*, 2007: Temperature conditions on July 2007 as extreme climatic phenomenon in Serbia. *Bull. Serbian Geograph. Soc.* 87., . 51–62. <https://doi.org/10.2298/GSGD0702051A>
- Ahmad, I., Tang, D., Wang, F.T., Wang, M. and Wagan, B.* 2015: Precipitation Trends over Time Using Mann-Kendall and Spearman's rho Tests in Swat River Basin, Pakistan. *Adv. Meteorol., 2015*, Article ID 431860. <https://doi.org/10.1155/2015/431860>
- Alexandersson, H.* 1986. A homogeneity test applied to precipitation data. *J. Climatol.* 6, 661–675. <https://doi.org/10.1002/joc.3370060607>

- Alexander, L.V., Zhang, X., Peterson, T.C., Caesar, J., and Gleason, B. 2006: Global observed changes in daily climate extremes of temperature and precipitation. *J. Geophys. Res.*, 2006, 111, D05109. <https://doi.org/10.1029/2005JD006290>
- Bajat, B., Blagojević, D., Kilibarda, M., Luković, J., and Tošić, I. 2015: Spatial Analysis of the Temperature Trends in Serbia during the Period 1961–2010. *Theor. Appl. Climatol.* 121, 289–301. <https://doi.org/10.1007/s00704-014-1243-7>
- Bačević, R.N., Vukoičić, Z.D., Nikolić, M., Janc, N., Milentijević, N., and Gavrilov B.M. 2017: Aridity in Kosovo and Metohija, Serbia. *Carpathian J. Earth Environ. Sci.* 12, 563–570.
- Bačević, R.N., Pavlović, M., and Rašljanin, I. 2018: Trend Assessing Using Mann-Kendall's Test for Priština Meteorological Station Temperature and Precipitation Data, Kosovo and Metohija, Serbia. *The University Thought – Publ. Nat. Sci.* 8(2), 39–43. <https://doi.org/10.5937/univtho8-19513>
- Bindoff, N.L., P.A. Stott, K.M. AchutaRao, M.R. Allen, N. Gillett, D. Gutzler, K. Hansingo, G. Hegerl, Y. Hu, S. Jain, I.I. Mokhov, J. Overland, J., Perlwitz, R. Sebbari, and X. Zhang, 2013: Detection and Attribution of Climate Change: from Global to Regional. In: *Climate Change 2013: The Physical Science Basis. Contribution of Working Group I to the Fifth Assessment Report of the Intergovernmental Panel on Climate Change* (eds. Stocker, T.F., D. Qin, G.-K. Plattner, M. Tignor, S.K. Allen, J. Boschung, A. Nauels, Y. Xia, V. Bex and P.M. Midgley). Cambridge University Press, Cambridge, United Kingdom and New York, NY, USA.
- Blake, A., Arbache, S.J., Sinclair, T.M., and Teles, V. 2007: Tourism and poverty relief. *Annal. Tourism Res.* 35, 107–126. <https://doi.org/10.1016/j.annals.2007.06.013>
- Burić, D., Luković, J., Ducić, V., Dragojlović, J., and Doderović, M. 2014: Recent trends in daily temperature extremes over southern Montenegro (1951–2010). *Nat. Hazards Earth Syst. Sci.* 14, 67–72. <https://doi.org/10.5194/nhess-14-67-2014>
- Burić, D., Ducić, V., Mihajlović, J., Luković, J. and Dragojlović, J. 2015: Recent extreme air temperature changes in Montenegro. *Bull. Serbian Geograph. Soc.* 95(4), 53-66. <https://doi.org/10.2298/GSGD140626002B>
- Burić, B.D., Dragojlović, M.J., Milenković, M., Popović, Z.Lj. and Doderović, M.M., 2018: Influence of variability of the East Atlantic Oscillation on the air temperature in Montenegro. *Thermal Sci.* 22(1B), 759-766. <https://doi.org/10.2298/TSCI170710211B>
- Burić D., Dragojlović J., Penjišević-Sočanac I., Luković J. and Doderović M., 2019: Relationship Between Atmospheric Circulation and Temperature Extremes in Montenegro in the Period 1951–2010. In: (eds. Leal Filho W., Trbic G., Filipovic D.) *Climate Change Adaptation in Eastern Europe. Climate Change Management*. Springer, Cham. https://doi.org/10.1007/978-3-030-03383-5_3
- Burn, D.H. and Hag Elnur, M.A. 2002: Detection of hydrologic trends and variability. *J. Hydrol.* 255, 107–122. [https://doi.org/10.1016/S0022-1694\(01\)00514-5](https://doi.org/10.1016/S0022-1694(01)00514-5)
- Bressers, J. T.A., Bressers, N., and Larrue, C., 2016: Governance for Drought Resilience: Land and Water Drought Management in Europe. Springer. <https://doi.org/10.1007/978-3-319-29671-5>
- Ceppi, P., Scherrer, S.C., Fischer, A.M. and Appenzeller, C. 2012: Revisiting Swiss temperature trends 1959–2008. *Int. J. Climatol.* 32, 203–213. <https://doi.org/10.1002/joc.2260>
- Du, Q., Zhang, M., Wang, S., Che, C., Ma, R., and Ma, Z., 2019: Changes in air temperature over China in response to the recent global warming hiatus. *J. Geograph. Sci.* 29, 496–516. <https://doi.org/10.1007/s11442-019-1612-3>
- Ducić, V. and Radovanović, M. 2005: *Klima Srbije*. Beograd: ZUNS.
- ElNesr, M.N., Abu-Zreig, M.M., and Alazba, A.A. 2010. Temperature trends and distribution in the Arabian Peninsula. *Amer. J. Environ. Sci.* 6, 191–203. <https://doi.org/10.3844/ajessp.2010.191.203>
- Fink, A.H., Brücher, T., Krüger, A., Leckebusch, G.C., Pinto, J.G., and Ulbrich, U. 2003: The 2003 European summer heatwaves and drought–synoptic diagnosis and impacts. *Weather* 59, 209–216. <https://doi.org/10.1256/wea.73.04>
- Gavrilov, M.B., Marković, S.B., Jarad, A. and Korać, V.M., 2015: The analysis of temperature trends in Vojvodina (Serbia) from 1949 to 2006. *Thermal Sci.* 19, 339–350. <https://doi.org/10.2298/TSCI150207062G>

- Gavrilov, M.B., Tošić, I., Marković, S.B., Unkašević, M., and Petrović, P. 2016: The analysis of annual and seasonal temperature trends using the Mann-Kendall test in Vojvodina, Serbia. *Időjárás* 122, 203–216.
- Gavrilov, M.B., Marković, S.B., Janc, N., Nikolić, M., Valjarević, A., Komac, B., Zorn, M., Punišić, M. and Bačević, N., 2018: Assessing average annual air temperature trends using the Mann-Kendall test in Kosovo. *Acta geographica Slovenica*, 58, 8–25. <https://doi.org/10.3986/AGS.1309>
- Gavrilov, M.B., Lukić, T., Janc, N., Basarin, B., and Marković, S.B. 2019: Forestry Aridity Index in Vojvodina, North Serbia. *Open Geosciences* 11, 367–377. <https://doi.org/10.1515/geo-2019-0029>
- Gocić, M. and Trajković, S., 2013: Analysis of changes in meteorological variables using Mann Kendall and Sen's slope estimator statistical tests in Serbia. *Glob. Planet. Change* 100, 172–182. <https://doi.org/10.1016/j.gloplacha.2012.10.014>
- Gocić, M. and Trajković, S. 2014a: Drought Characterisation Based on Water Surplus Variability Index. *Water Res. Manage.* 28, 3179–3191. <https://doi.org/10.1007/s11269-014-0665-4>
- Gocić, M. and Trajković, S. 2014b: Spatiotemporal characteristics of drought in Serbia. *J. Hydrology*, 510, 110–123. <https://doi.org/10.1016/j.jhydrol.2013.12.030>
- Gonzalez-Hidalgo, J.C., Peña-Angulo, D., Brunetti, M. and Cortesi, N., 2015: Recent trend in temperature evolution in Spanish mainland (1951–2010): from warming to hiatus. *Int. J. Climatol.* 36, 2405–2416. <https://doi.org/10.1002/joc.4519>
- Hansen, J., Sato, M., Russell, G., and Kharecha, P. 2013: Climate sensitivity, sea level and atmospheric carbon dioxide. *Philosophical transactions. Series A, Mathematical, physical, and engineering sciences*, 371(2001), 20120294. <https://doi.org/10.1098/rsta.2012.0294>
- Hrnjak, I., Lukić, T., Gavrilov, M.B., Marković, S.B., Unkašević, M. and Tošić, I. 2014. Aridity in Vojvodina, Serbia. *Theor. Appl. Climatol.* 115, 323–332. <https://doi.org/10.1007/s00704-013-0893-1>
- IPCC, 2018: Summary for Policymakers. In: Global Warming of 1.5°C. An IPCC Special Report on the impacts of global warming of 1.5°C above pre-industrial levels and related global greenhouse gas emission pathways, in the context of strengthening the global response to the threat of climate change, sustainable development, and efforts to eradicate poverty [Masson-Delmotte, V., P. Zhai, H.-O. Pörtner, D. Roberts, J. Skea, P.R. Shukla, A. Pirani, W. Moufouma-Okia, C. Péan, R. Pidcock, S. Connors, J.B.R. Matthews, Y. Chen, X. Zhou, M.I. Gomis, E. Lonnoy, T. Maycock, M. Tignor, & T. Waterfield (eds.)]. In Press.
- Karaburun, A., Demirci, A. and Kara, F. 2011: Analysis of spatially distributed annual, seasonal and monthly temperatures in Istanbul from 1975 to 2006. *World Appl. Sci. J.* 12, 1662–1675.
- Karmeshu, N. 2012: Trend Detection in Annual Temperature & Precipitation using the Mann Kendall Test – A Case Study to Assess Climate Change on Select States in the Northeastern United States. MSc Thesis, University of Pennsylvania. USA.
- Kendall, M. 1938: A new measure of rank correlation. *Biometrika* 30, 81–89. <https://doi.org/10.2307/2332226>
- Klein, T.A.M.G. and Können, G.P., 2003: Trends in indices of daily temperature and precipitation extremes in Europe, 1946-99. *J. Climate* 16, 3665–3680. [https://doi.org/10.1175/1520-0442\(2003\)016<3665:THODT>2.0.CO;2](https://doi.org/10.1175/1520-0442(2003)016<3665:THODT>2.0.CO;2)
- Kocsis, T., Kovács-Székely, I. and Anda, A., 2020: Homogeneity tests and non-parametric analyses of tendencies in precipitation time series in Keszthely, Western Hungary. *Theor. Appl. Climatol.* 139, 849–859. <https://doi.org/10.1007/s00704-019-03014-4>
- Kousari, M.R. and Asadi Zarch, M.A., 2011: Minimum, maximum, and mean annual temperatures, relative humidity, and precipitation trends in arid and semi-arid regions of Iran. *Arabian J. Geoscience*. 4, 907–914. <https://doi.org/10.1007/s12517-009-0113-6>
- Laaha, G., Gauster, T., Tallaksen, L. M., Vidal, J.-P., Stahl, K., Prudhomme, C., Heudorfer, B., Vlnas, R., Ionita, M., Van Lanen, H. A. J., Adler, M.-J., Caillouet, L., Delus, C., Fendekova, M., Gailliez, S., Hannaford, J., Kingston, D., Van Loon, A. F., Mediero, L., Osuch, M., Romanowicz, R., Sauquet, E., Stagge, J. H., and Wong, W. K. 2017: The European 2015 drought from a hydrological perspective. *Hydrol. Earth Syst. Sci.* 21, 3001–3024. <https://doi.org/10.5194/hess-21-3001-2017>

- Leroux, M. 2005: Global Warming - Myth or Reality? Berlin Heidelberg, Springer.
- Lukovic J., Buric D., Ducic V., Doderovic M. and Milevski I., 2013: Assessment on Temperature Extremes in Montenegro. In: (eds. Helmis C., Nastos P.) *Advances in Meteorology, Climatology and Atmospheric Physics. Springer Atmospheric Sciences*. Springer, Berlin, Heidelberg.
https://doi.org/10.1007/978-3-642-29172-2_82
- Mamara, A., Argiriou, A.A., and Anadranistakis, M. 2016: Recent Trend Analysis of Mean Air Temperature in Greece Based on Homogenized Data. *Theo. Appl. Climatol.* 126, 543–573.
<https://doi.org/10.1007/s00704-015-1592-x>
- Mann, H.B., 1945: Non-parametric tests against trend. *Econometrica*, 13, 245–259.
<https://doi.org/10.2307/1907187>
- Milentijević, N., Dragojlović, J., Ristić, D., Cimbaljević, M., Demirović, D. and Valjarević, A., 2018: The assessment of aridity in Leskovac Basin, Serbia (1981–2010). *J. Geograph. Inst. "Jovan Cvijić"*, 68, 249–264.
- Ministry of Environmental Protection, 2017: Second National Communication of the Republic of Serbia under the United Nations Framework Convention on Climate Change. Ministry of Environmental Protection, Belgrade.
- Milošević, D., Savić, S. and Žiberna, I., 2013: Analysis of the climate change in Slovenia: Fluctuations of meteorological parameters for the period 1961–2011 (Part I). *Bull. Serbian Geograph. Soc.* 93, 1–14.
<https://doi.org/10.2298/GSGD1301001M>
- Milošević, D., Savić, S., Stankov, U., Žiberna, I., Pantelić, M., Dolinaj, D., and Leščičen, I., 2017: Maximum temperatures over Slovenia and their relationship with atmospheric circulation patterns. *Geografije*, 122, 1–20. <https://doi.org/10.37040/geografije2017122010001>
- Mudelsee, M., 2014: *Climate Time Series Analysis: Classical Statistical and Bootstrap Methods*, 2nd edition. Cham, Switzerland: Springer.
- Mudelsee, M., 2019: Trend analysis of climate time series: A review of methods, *Earth-Sci. Rev.* 190, 310–322. <https://doi.org/10.1016/j.earscirev.2018.12.005>
- Oliver, E. J., 2005. Temperature Distribution. In (Ed. E.J. Oliver), *Encyclopedia of World Climatology*, 711–716. Springer, Dordrecht, The Netherlands.
- Popov, T., Gnjato, S. and Trbić, G., 2017: Trends in extreme temperatures indices in Bosnia and Herzegovina: A case study of Mostar. *Herald* 21, 107–132.
<https://doi.org/10.7251/HER2117107P>
- Popov, T., Gnjato, S. and Trbić, G., 2018a: Changes in temperature extremes in Bosnia and Herzegovina: A fixed thresholds-based index analysis. *J. Geograph. Inst. "Jovan Cvijić" SASA*, 68, 17–33.
<https://doi.org/10.2298/IJGI1801017P>
- Popov, T., Gnjato, S., Trbić, G., and Ivanišević, M., 2018b: Recent trends in extreme temperature indices in Bosnia and Herzegovina. *Carpathian J. Earth Environ. Sci.* 13, 211–224.
<https://doi.org/10.26471/cjees/2018/013/019>
- Popov, T., Gnjato, S. and Trbić, G., 2019: Changes in extreme temperature indices over the Peripannonian region of Bosnia and Herzegovina. *Geografije* 124, 19–40.
<https://doi.org/10.37040/geografije2019124010019>
- Putniković, S., Tošić, I., Lazić, L. and Pejanović, G., 2018: The influence of the large-scale circulation patterns on temperature in Serbia. *Atmosph. Res.* 213, 465–475.
<https://doi.org/10.1016/j.atmosres.2018.07.003>
- Radaković, G.M., Tošić, A.I., Bačević, R.N., Mladan, D., Marković S.B., and Gavrilov M.B., 2018: The analysis of aridity in Central Serbia from 1949–2015. *Theor. Appl. Climatol.* 133, 887–898.
<https://doi.org/10.1007/s00704-017-2220-8>
- Radilović, S., Koraćin, D., Denamiel, C., Belušić, D., Güttler, I. and Vilibić, I., 2020: Simulated and observed air temperature trends in the eastern Adriatic. *Atmosph. Sci. Lett.* 21, e951.
<https://doi.org/10.1002/asl.951>
- Radinović, Đ., 1981: *Vreme i klima Jugoslavije*. Beograd: IRO "Građevinska knjiga".

- Rahman, M.A., Yunsheng, L., and Sultana, N., 2017: Analysis and prediction of rainfall trends over Bangladesh using Mann–Kendall, Spearman’s rho tests and ARIMA model. *Meteorol. Atmosph. Physics* 129, 409–424. <https://doi.org/10.1007/s00703-016-0479-4>
- Razavi, T., Switzman, H., Arain, A. and Coulibaly, P., 2016: Regional climate change trends and uncertainty analysis using extreme indices: A case study of Hamilton, Canada. *Climate Risk Manage.* 13, 43–63. <https://doi.org/10.1016/j.crm.2016.06.002>
- RHSS, 2019: Meteorological Yearbook – Climatological Data (Meteorological Yearbook, http://www.hidmet.gov.rs/ciril/meteorologija/klimatologija_godisnjaci.php (accessed 30 February 2020).
- Serra, C., Burgueño, A. and Lana, X. 2001: Analysis of maximum and minimum daily temperatures recorded at Fabra Observatory (Barcelona, NE Spain) in the period 1917–1998. *Int. J. Climatol.* 21, 617–636. <https://doi.org/10.1002/joc.633>
- Screen, J.A. and Simmonds, I., 2010: The central role of diminishing sea ice in recent Arctic temperature amplification. *Nature*, 464(7293), 1334–1337. <https://doi.org/10.1038/nature09051>
- Shadmani, M., Marofi, S. and Roknian, M., 2012: Trend Analysis in Reference Evapotranspiration Using Mann-Kendall and Spearman’s Rho Tests in Arid Regions of Iran. *Water Resour. Manage.* 26, 211–224. <https://doi.org/10.1007/s11269-011-9913-z>
- Tadić, L., Brleković, T., Hajdinger, A., and Španja, S., 2019: Analysis of the Inhomogeneous Effect of Different Meteorological Trends on Drought: An Example from Continental Croatia. *Water*, 11(12), 2625. <https://doi.org/10.3390/w11122625>
- Tomazos, K. and Butler, R., 2009: Volunteer tourism: The new ecotourism? *Anatolia: An International J. Tourism Hospitality Res.* 20, 196–211. <https://doi.org/10.1080/13032917.2009.10518904>
- Tonbol, K.M., El-Geziry, T.M., and Elbessa, M., 2018: Evaluation of Changes and Trends of Air Temperature within the Southern Levantine Basin. *Weather* 73, 60–66. <https://doi.org/10.1002/wea.3186>
- Tošić, I., Zorn, M., Ortar, J., Unkašević, M., Gavrilov, M.B. and Marković, S.B., 2016: Annual and seasonal variability of precipitation and temperatures in Slovenia from 1961 to 2011. *Atmosph. Res.* 168, 220–233. <https://doi.org/10.1016/j.atmosres.2015.09.014>
- Trajković S., Gocić M., Misić D. and Milanović M., 2020: Spatio-Temporal Distribution of Hydrological and Meteorological Droughts in the South Morava Basin. In: (eds. Gocić M., Aronica G., Stavroulakis G. & Trajković S.) *Natural Risk Management and Engineering*. Springer Tracts in Civil Engineering. Springer, Cham. https://doi.org/10.1007/978-3-030-39391-5_11
- Trbić, G., Popov, T. and Gnjata, S., 2017: Analysis of air temperature trends in Bosnia and Herzegovina. *Geographica Pannonica*, 21, 68–84. <https://doi.org/10.5937/GeoPan1702068T>
- Türkes, M. and Sümer, U.M. 2004. Spatial and temporal patterns of trends and variability in diurnal temperature ranges of Turkey. *Theor. Appl. Climatol.* 77, 195–227. <https://doi.org/10.1007/s00704-003-0024-5>
- Unkašević, M. 1994. *Klima Beograda*. Beograd: Naučna knjiga. (on Serbian)
- Unkašević, M. and Tošić, I. 2013. Trends in temperature indices over Serbia: relationships to large-scale circulation patterns. *Int. J. Climatol.* 33, 3152–3161. <https://doi.org/10.1002/joc.3652>
- Valjarević, A., Djekić, T., Stevanović, V., Ivanović, R. and Jandžiković, B., 2018: GIS numerical and remote sensing analyses of forest changes in the Toplica region for the period of 1953–2013. *Applied Geography* 92, 131–139. <https://doi.org/10.1016/j.apgeog.2018.01.016>
- Vukočić, Z.D., Milosavljević, A.S., Penjišević, T.I., Bačević, R.N., Nikolić, M., Ivanović, D.R. and Jandžiković, M.B., 2018: Spatial analysis of temperature and its impact on the sustainable development of mountain in Central and Western Serbia. *Időjárás* 122, 259–283. <https://doi.org/10.28974/idojaras.2018.3.3>
- Zeleanáková, M., Purcz, P., Blišťan, P., Vranayová, Z., Hlavatá, H., Diaconu, D.C. and Portela, M.M., 2018: Trends in Precipitation and Temperatures in Eastern Slovakia (1962–2014). *Water*, 10(6), p. 727. <https://doi.org/10.3390/w10060727>
- Zheng, J. and Wang, C. 2019. Hot summers in the Northern Hemisphere. *Geophysical Research Letters*, 46, pp. 10891–10900. <https://doi.org/10.1029/2019GL084219>

- Wang, C., Puhan, M.A. and Furrer, R. 2018. Generalized spatial fusion model framework for joint analysis of point and areal data. *Spatial Statistics* 23, 72–90.
<https://doi.org/10.1016/j.spasta.2017.11.006>
- Wibig, J. and Glowicki, B. 2002. Trends of minimum and maximum temperature in Poland. *Climate Res.* 20, 123–133. <https://doi.org/10.3354/cr020123>
- WMO, 2019. Statement on the State of the Global Climate in 2018. WMO-No. 1233. World Meteorological Organization. Geneva, Switzerland.
- XLSTAT, <https://www.xlstat.com/en/> (accessed 10 March 2020).

IDŐJÁRÁS

Quarterly Journal of the Hungarian Meteorological Service
Vol. 125, No. 2, April – June, 2021, pp. 255–269

Assessment of agrometeorological indices over Southeast Europe in the context of climate change (1961–2018)

Hristo Chervenkov* and **Kiril Slavov**

National Institute of Meteorology and Hydrology
66, Tsarigradsko Shose blvd Sofia 1784, Bulgaria

**Corresponding author E-mail: hristo.tchervenkov@meteo.bg*

(Manuscript received in final form July 8, 2020)

Abstract— The regional response over Southeast (SE) Europe to the climate warming in global and continental scales has been confirmed to have essential impact on the agriculture and forestry since the middle of twentieth century. Normal variations in weather throughout a growing season cause variations in harvest and, generally, the impact could be large in terms of production amounts and economic returns. Agriculture is sensitive to the changes in weather and climate, and the occurrence of extreme events threaten the agricultural systems. Forests are particularly sensitive to climate change, because the long life-span of trees does not allow for rapid adaptation to environmental changes. This study provides an overview of the spatial patterns and the long-term temporal evolution of the following agrometeorological indices: growing season length, accumulated active temperatures and biologically effective degree days. Hence the focus is on the Growing season length, its start and end dates are analyzed separately. All indices are computed from the daily mean temperatures which, in turn, are derived from the output of the MESCAN-SURFEX system analysis of the collaborative initiative UERRA. The geographical domain of interest is Southeast Europe, and the assessment is performed at a very high spatial resolution on annual basis for the period 1961–2018. We find strong evidences of essential increase in the considered indices which dominates spatially over the low-elevated areas of the domain and is statistically significant at 5% level. Key message is also the revealed asymmetry of the increase in the most relevant index, the growing season length: its total lengthening is linked more to the shifting to earlier date of the start, rather than to its later cessation.

Key-words: UERRA MESCAN-SURFEX, daily mean temperature, agrometeorological indices, Southeast Europe, regional warming

1. Introduction

According to the high-level synthesis report of the United Nations, titled 'United In Science' (<https://public.wmo.int/en/resources/unitedinscience>), the climate change is the defining challenge of our time. The globally averaged surface temperature of the Earth increased 0.85 °C over the 1880 to 2012 period (Janković *et al.*, 2019). The climate change will exert influence on the ecosystems, on all branches of the international economy, and on the quality of life. That is why an operation plan for adaptation to climate changes has to be based on scientifically well-grounded assessments, giving an account of regional features in the climate changes and their consequences.

Food security is a fundamental precondition for human well-being, and the agricultural and food sector is of major economic importance. Agriculture is arguably the sector most dependent on climate. Crops and livestock are directly impacted by adverse local weather and climate. Indirectly, food production is affected by climate-driven fluctuations in water resources as well as in the processing, transport, and storage of agricultural products.

Associated with climate change there are several factors affecting forest ecosystems, which can act independently or in combination. As evidenced in many recent publications, the changes in climate have direct and indirect impact on biotic (frequency and consequences of pest and disease outbreaks) and abiotic (changes in occurrence and intensity of severe weather episodes) disturbances with strong implications for forest ecosystems. The comprehensive study of Lindner *et al.* (2010) compiles and summarizes the existing knowledge about observed and projected impacts of climate change on forests in Europe. Key message in this study is that the negative impacts of the climate change are very likely to outweigh positive trends (connected mainly with the increasing atmospheric CO₂ concentration and higher temperatures) in the southern and eastern parts of Europe. The impact of the climate change on the population of widespread conifer species with high economic and ecological value like silver fir and Norway spruce is considered in the local studies for Romania (Mihai G, *et al.*, 2018, 2020). The studies outline the high adaptive genetic variation of the Norway spruce in Southeast (SE) Europe and the resilience of the silver fir to climate change in the region.

Temperature is one of the major environment factors affecting the growth, development, and yields of crops, especially the rate of development. On one hand, crops have basic requirement for temperature to complete a specific phenophase or the whole life cycle. On the other hand, extremely high and low temperatures can have detrimental effects on crop growth, development, and yield, particularly at critical phenophases such as anthesis Luo (2011).

The study of near past climate provides an essential baseline, from which changes in the contemporary and future climate can be understood and contextualized. Past and future climate norms, documenting of climate change

are required to support transformational decisions, such as breeding new crop varieties, investments in irrigation, or relocation of production areas.

The global warming effects and the associated regional climatic changes over Central and Southeast (SE) Europe have been widely documented in the last decades based on in situ measurements (*Alexandrov et al.*, 2004; *Bartholy and Pongrácz*, 2006; *Pongrácz et al.*, 2009a, 2009b; *Croitoru et al.*, 2012), assimilated surface observations (*Birsan et al.*, 2014; *Chervenkov and Slavov*, 2019a; *Cheval et al.*, 2014; *Lakatos et al.*, 2013a, 2013b), reanalyses (*Malcheva et al.*, 2016; *Spinoni et al.*, 2015), global (*Sillmann et al.*, 2013), *Chervenkov and Slavov* (2020a)) and regional climate models (*Belda et al.*, 2015; *Gadzhev et al.*, 2018; *Pieczka et al.*, 2019; *Spiridonov and Valcheva*, 2019). Most of these studies are focused on the second half of the 20th and the first decade of the 21st century, clearly evidencing that, similarly to the global and continental trends, the regional temperature got warmer during the period. Investigations of the changes in annual variation patterns under current climatic conditions across SE Europe aim to increase the current knowledge of recent climate changes in this region, and also to provide the baseline for the foregoing assessments of possible responses of the regional climate to global warming (*Birsan et al.*, 2014).

Main aim of the present study is to analyze the spatial patterns and the temporal evolution of the near past and present thermal conditions over SE Europe from agrometeorological (AM) point of view using up-to-date data sources. These conditions are quantified by a set of AM indices with focus on the growing season length (*GSL*) index computed on annual basis from the daily mean temperatures. The daily mean temperatures are, in turn, derived from the output of the MESCAN-SURFEX model in the frames of the UERRA project (*Uden*, 2018) for the full 58-year-long time span of the data set (1961–2018) and in very high grid spacing of $0.05^\circ \times 0.05^\circ$.

The article is structured as follows. The used data and the considered indices are described in Section 1. The core of the article is Section 2, containing 3 subsections and performed calculations and obtained results. The concluding remarks are in Section 3.

2. Data and methods

2.1. Concise remarks on UERRA and MESCAN-SURFEX

The objective of the project-driven collaborative initiative UERRA (Uncertainties in Ensembles of Regional Reanalyses (RRA); www.uerra.eu) is to produce ensembles of European RRA of essential climate variables for several decades and to estimate the associated uncertainties in the data sets (*Ridal et al.*, 2018; *Uden*, 2018). It also includes recovery of historical (last

century) data and creation of user friendly data services. Within UERRA, three different numerical weather prediction (NWP) models have been employed to generate European RRA and subsequent surface reanalysis products.

The MESCAN-SURFEX system analysis uses the 2D-analysis system MESCAN (Soci *et al.*, 2016) and the land surface platform SURFEX (Bazile *et al.*, 2017) to generate a coherent surface and soil analysis. The UERRA-NWP HARMONIE-ALADIN at 11 km grid spacing is used as a starting point to further downscaling. Besides the other parameters, MESCAN-SURFEX produces air temperature at 2 m above the surface in 6-hour temporal resolution, i.e., at 00, 06, 12, and 18 UTC for the period 1961–2018. Based on the availability of this data, the daily minimum, mean, and maximum temperatures, noted henceforth tm , tg , and tx correspondingly, are derived in a regular $0.05^\circ \times 0.05^\circ$ grid and validated against independent data sets (Chervenkov and Slavov, 2021).

2.2. Agrometeorological indices

This study exploits part of the results of the work of Chervenkov and Slavov (2020b), namely the MESCAN-SURFEX derived data for the daily mean temperature, tg .

Identification of the effects of mean temperature on crop production under various field/controlled environmental conditions can be used to improve crop models for accurate representation of the impacts of temperature change on crop production at regional level. The impacts of tg on crop production could be quantified by various AM indices (Seemann *et al.*, 1979). Similar to other sector-oriented indicators which have no internationally agreed definitions, the computation of the most of the AM indicators can be performed in different ways, depending on the available data, region of interest, nature and scope of the study (Harding *et al.*, 2015). A certain exception is the *GSL*, which is standardized in frames of collaborative initiatives like STARDEX, European Climate Assessment & Dataset (ECA&D) project (van Engelen *et al.*, 2008), and Expert Team on Climate Change Detection and Indices (ETCCDI, Zhang *et al.*, 2011). According to the unified definition, the *GSL* is the annual count between the first span of at least 6 days with $tg > 5^\circ\text{C}$ and first span after July 1 (in Northern Hemisphere) of at least 6 days with $tg > 5^\circ\text{C}$. The units of measurement of the *GSL* are, obviously, days.

It must be emphasized that in some parts of the considered domain, mainly along the coastline of southern Greece, Italy, and Asia Minor, the daily mean temperature is over 5°C practically over the whole year. Thus the *GSL*, at least with this threshold temperature, could not be defined in the current way.

In the last decades, significant research has been done in many countries on temperatures critical to plants, and this, along with the aggregate evaluation of

thermal resources, made a substantially more accurate determination of climatic heat provision to crops possible (Luo, 2011).

The total active air temperature or accumulated active temperature (AAT) index is commonly used AM index mostly for heat assurance characteristics during the growth of some cultivars for example winter wheat (Seemann *et al.*, 1979). AAT is calculated as

$$AAT = \sum_{i=DOYB}^{i=DOYC} \max(tg(i) - tb, 0), \quad (1)$$

where *DOYB* is the day of year (*DOY*) at the start, and *DOYC* is the day of year at the end (cessation) of the growing seasons. The threshold temperature, *tb*, is 5 °C for the cold-tolerant and 10 °C for the thermophile species (Lakatos *et al.*, 2013b); we use the lower one in the current study. AAT is calculated in units called degree-days, °D (see Janković *et al.*, 2019).

The degree-day method, which expresses numerically the relationship of plant development and growth to atmospheric temperature, was developed in the United States in the first half of the twentieth century. In the degree-day method, the mean diurnal air temperatures above the minimum plant heat requirements are totaled (in essence, this is analogous to the total active temperature method). This method was used in connection with the determination of crop maturation times (Seemann *et al.*, 1979).

The biologically effective degree days (*BEDD*) index has been specifically targeted to describe grape growth (Gladstones, 1992). The *BEDD* index is based on a growing degree days measure and is calculated by:

$$BEDD = \sum_{i=01.04}^{i=30.09} \min(\max(tg_i - th, 0), tl), \quad (2)$$

where *th*=10 °C and *tl*=9 °C are the upper and lower threshold temperatures correspondingly. Similarly to the *AAT*, the unit of *BEDD* is °D.

Total active and effective temperatures, subsequently the values of *AAT* and *BEDD*, as well as ranges for *GSL* have been established for many crops. These methods of expressing crop heat requirements are widely used for agricultural climate evaluation in the former Soviet Union, Bulgaria, Poland, Romania, and a number of other countries (Seemann *et al.*, 1979), which motivates their selection in the present study.

These indices could be regarded not at least and beyond their AM scope as proxies of the cumulative thermal conditions during the warm period of the year.

3. Calculations and results

3.1. Verification of the GSL

The presented definitions on the one hand and the presence of data for the daily mean temperatures on the other give the opportunity for straightforward computation of the considered indices. They are computed with purpose-build procedures by the authors for the whole 58-year-long time span of the input data. First, the obtained results for the *GSL* are verified against independent data.

The database ClimData (Chervenkov *et al.*, 2019; Chervenkov and Slavov, 2019a, available for free at <https://repo.vi-seem.eu/handle/21.15102/VISEEM-343>.) contains the full set of STARDEX and ETCCDII climate indices (Cis) derived from CARPATCLIM and E-OBS daily temperature and precipitation data. It is intended to serve as convenient and versatile single-point access resource for any user interested in the CIs-based regional climatology. The *GSL* in the STARDEX CIs-collection is calculated with the original input data for the daily mean temperature and not with approximation using the arithmetic average from the *tn* and *tx* as in the ETCCDII-collection. Thus, it is reasonable to expect that it represents better this agrometeorological index. The *GSL* from STARDEX, based on CARPATCLIM data is compared to the one computed in this study as shown in *Fig. 1*.

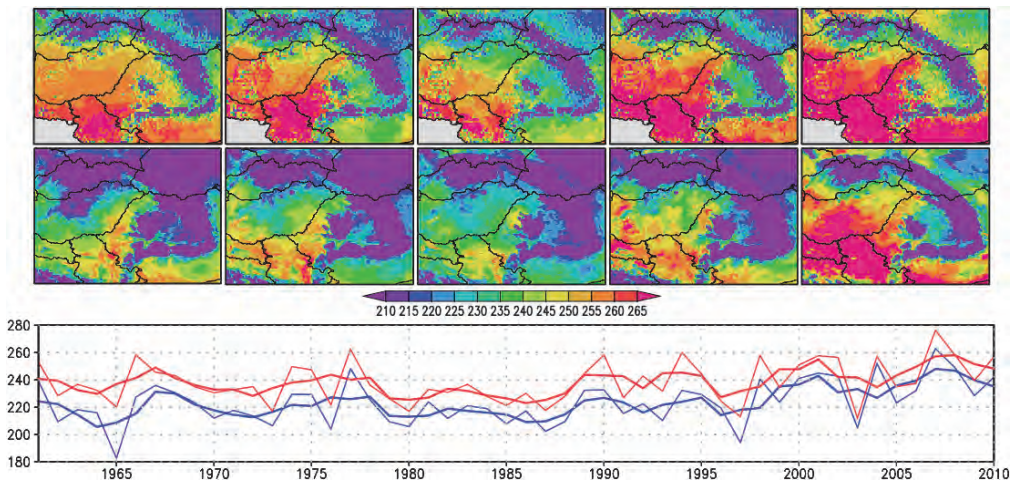


Fig. 1. Upper pane: multiyear means of the *GSL* (unit: days) for the periods [1961, 1970], [1971, 1980], [1981, 1990], [1991, 2000], and [2001, 2010] in the first, second, third, fourth, and fifth column, correspondingly, from STARDEX/CARPATCLIM (first row) and from UERRA MESCAN-SURFEX derived *tg* (second row). Lower pane: time series of the area-weighted averages (AA) of the *GSL* over the CARPATCLIM-domain from STARDEX/CARPATCLIM (red line) and from UERRA MESCAN-SURFEX derived *tg* (blue line). Fat lines are the running 3-year means.

Besides the different graphical appearance of the both sets caused by the different grid spacing ($0.1^{\circ} \times 0.1^{\circ}$ for STARDEX/CARPATCLIM and $0.05^{\circ} \times 0.05^{\circ}$ in current case), it is most obvious in the superimposition of the spatial patterns, that the *GSL* is generally underestimated in the present study compared with STARDEX/CARPATCLIM. The evolution of the AAs from both sets is coherent in time with almost constant positive shift of an 15 days of STARDEX/CARPATCLIM calculations in the present study. This fact is a direct consequence of the underestimation of the daily mean temperatures compared to the CARPATCLIM-output (Chervenkov and Slavov, 2020b). As emphasized in Chervenkov and Slavov (2020b), a part of this bias could be attributed to the principally different origin and nature of the considered data sets, which makes it practically unavoidable.

3.2. Long-term inter-annual changes

The *GSL* is certainly the most recognizable AM index and subject of many studies, considering the regional climate (Bartholy and Pongrácz, 2006; Birsan and Dumitrescu, 2014; Chervenkov and Slavov, 2019a). Most of them investigate the *GSL* solely, whereas little attention is paid on the start date (*DOYB*) of the vegetation period as well as to its end (cessation) date, *DOYC*. Part of the problem lies in the fact that the most standardized software tools for computation of CIs, like RclimDex of ETCCDI, output *GSL* only and not *DOYB/DOYC*. In some recent papers, like the study by Szyga-Pluta and Tomczyk (2019), the anomalies are analyzed in the length of the growing season in Poland in the period 1966–2015. The authors reveal statistically significant increase of the *GSL* on the east coast as well as in the central and southern parts of the country. The changes of the start date over the Carpathian Region in the period 1961–2010 are considered also in Lakatos *et al.* (2013b) evidencing significant shifting to earlier date. Experimenting with different approaches for calculation of *DOYB* and *DOYC*, Mesterházy *et al.* (2018) reveal that that the *GSL* in Hungary becomes significantly longer during the 21st century.

The present study is focusing on the *GSL*. Hence our main aim is not only to assess the impact of the climate change on the *GSL* but also to find seasonal shift in the vegetation period, *DOYB* and *DOYC* are analyzed together with *GSL* simultaneously.

First, in order to reveal long-term interannual changes for the considered indices, the spatial patterns of the multiyear means for the first 30-year-long period 1961–1990 are superimposed to the multiyear means for the second 30-year-long period, 1989–2018 as shown in Fig. 2.

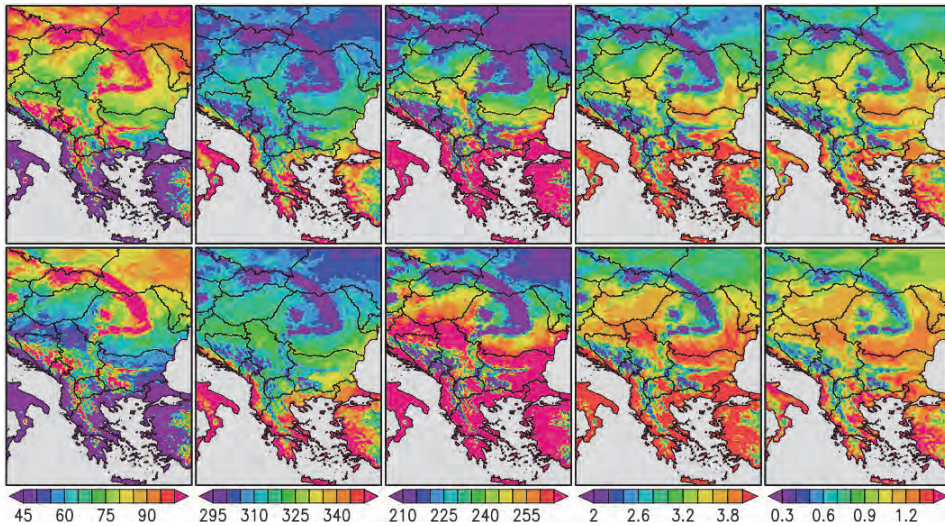


Fig. 2. Multiyear means of *DOYB*, *DOYC*, *GSL*, *AAT*, and *BEDD* in in the first, second, third, fourth, and fifth column, correspondingly, for 1961–1990 (first row) and 1989–2018 (second row). The unit of the *GSL* are days; *AAT* and *BEDD* are presented in 1000°D unit.

The spatial patterns of the considered variables are generally consistent in the both time spans. The vertical gradients, especially along the main Carpathian ridge (MCR) are better expressed than the gradients in the latitude. As expected, the analysis shows increase of all variables, except the *DOYB* which demonstrates opposite tendency.

The interannual shift of the vegetation period could be quantified simply by the middle day of the growing season, $DOYM = (DOYB + DOYC) / 2$, which is independent from the *GSL* itself. If the *DOYM* is shifted to an earlier date, independently from the absolute change of the *GSL*, the vegetation period begins earlier (negative shift); the opposite case, when the detected shift of the *DOYM* moves towards later dates (positive shift), means later occurrence of the vegetation period.

The logical next step is to assess the absolute difference between the multiyear means of both time spans as well as the relative change in respect to the earlier period. Both of these quantities, which are shown in Fig. 3, could be regarded as measures of the climate change impact on the considered variables.

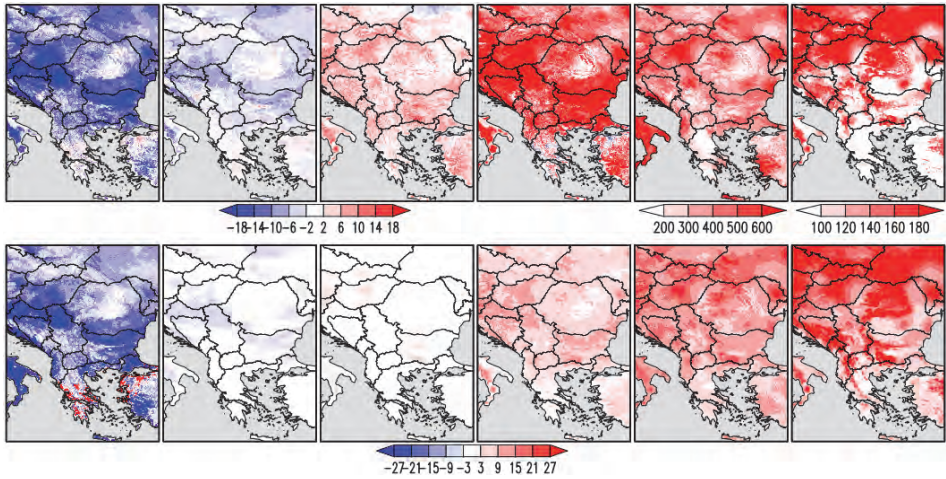


Fig. 3. First row: absolute difference between the multiyear means for 1989-2018 and 1961-1990 for *DOYB*, *DOYM*, *DOYC*, *GSL*, *AAT* and *BEDD* in in the first, second, third, fourth, fifth and sixth column, correspondingly. The units are as in Fig. 2. Second row: relative changes (in %) in the same order.

The most obvious result from the analysis of Fig. 3 is the substantial increase of *DOYC*, *GSL*, *AAT*, and *BEDD* over the entire area. The *DOYC* is shifted towards later dates up to a week, and the *GSL* is sifted latermore than two weeks over the bigger part of the domain. The increase of the *AAT*, and especially *BEDD*, is spatially more heterogeneous than the increase for the other variables. The vertical gradient of the detected changes is most clearly expressed in relative terms for the *BEDD*. It is worth noting, however, that the latter index has limited applicability in high-elevated areas.

The negative shift of the *DOYB* also appears clearly. It is spatially dominating except a few grid cells mostly along the coast lines of Greece and Turkey. In these grid cells, as emphasized before, the vegetation period begins in the first days of the year and small (less than a day) differences results in big relative changes. The decrease of the *DOYB* over the flat parts of the domain is generally in the interval of -21 to -9 days which, in absolute terms, is more than the increase of the *DOYC* over the same places. As a result, the *DOYM*, i.e., the whole vegetation period, is shifted to earlier dates with generally 2 to 10 days.

The relative share of the negative shift of the *DOYB* in the total increase of the multiyear mean of the *GSL* for 1989–2018 relative to 1961–1990 as well as the temporal evolution of the area-weighted over land averages of *DOYB*, *DOYM*, *DOYC*, *GSL* are shown in Fig. 4.

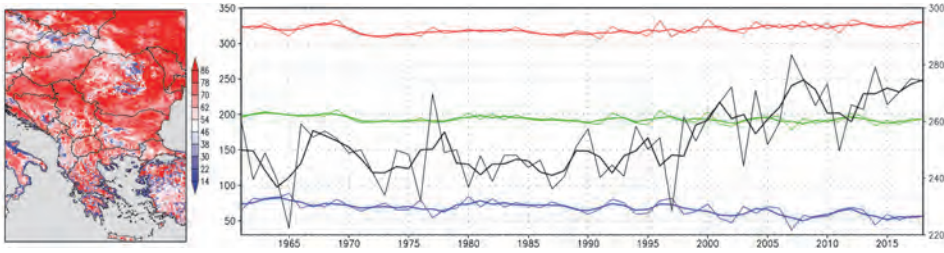


Fig. 4. Left pane: relative share (in %) of the negative shift of the *DOYB* in the total increase of the *GSL*. Right pane: temporal evolution of the *DOYB* (blue line), *DOYC* (red line), *DOYM* (green line, left ordinate) and *GSL* (black line, right ordinate, units: days). Fat lines are the running 3-year means.

In agreement with the results from the analysis of Fig. 3, the left pane of Fig. 4 shows that the total increase of the multiyear mean of the *GSL* for 1989–2018 relative to 1961–1990 is caused over the flat parts of the domain by more than 70% from the negative shift of the *DOYB*. The vertical gradients are clearly distinguishable: over the mountains this share is significantly smaller, suggesting that in these regions the negative shift of the *DOYB* has equal, even smaller contribution than that of the positive *DOYC*-shift in the total increase of the *GSL*.

The evolution of *DOYB*, *DOYC*, and especially of *GSL*, as well as in smaller degree of *DOYM* shows fairly clear tendencies, despite of some colder episodes as, for example, 1965. These episodes are distinguishable also in the lower pane of Fig. 1. The *GSL* demonstrates significant oscillations from year to year. The uprising tendency, however, especially after 1980–1985, is notable.

The temporal evolution of the AAs of the *AAT* and *BEDD* are shown in Fig. 5.

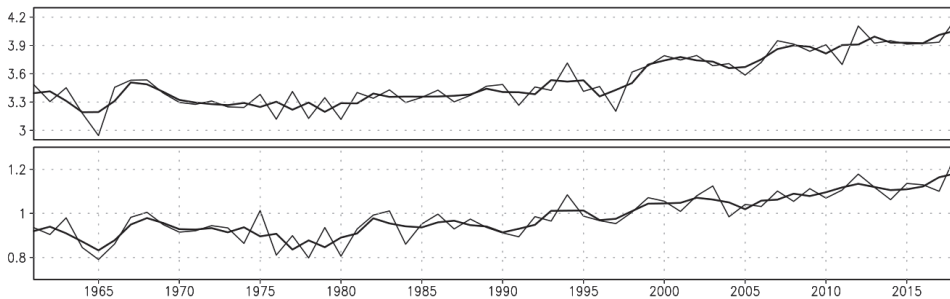


Fig. 5. Temporal evolution of the *AAT* (upper pane) and *BEDD* (lower pane) indices. The units are 1000°D . Fat lines are the running 3-year means.

Consistent with the similar results for the *GSL*, the evolution lines of the *AAT* and *BEDD* demonstrate steady increase of these values since the 1980s.

3.3. Trend analysis

The importance of assessing trends in climate extremes is often emphasized (e.g., *Chervenkov et al.*, 2019) and, consequently, the trend analysis is an essential part of the most recent studies considering either regional (*Bartholy and Pongrácz*, 2006; *Birsan et al.*, 2014; *Chervenkov and Slavov*, 2020a; *Croitoru et al.*, 2012; *Lakatos et al.*, 2013, and many others) or global (*Sillmann et al.*, 2013) long-term climate changes.

The Mann–Kendall (MK) test is a non-parametric procedure, especially suitable for non-normally distributed data, data containing outliers, and nonlinear trends (*Birsan et al.*, 2014). Subsequently, it is used as practically standard tool for estimation of the statistical significance of trends in time series of climate variables (see references above).

The estimation of the magnitude of the trend is performed with the Theil–Sen estimator (TSE), which is also a non-parametric procedure, using a linear model to estimate the slope of the trend (*Croitoru et al.*, 2012). It is increasingly applied in many geophysical branches, including climatology, as superior alternative of the ordinary least squares (see *Chervenkov and Slavov*, 2019b, and references therein). The MK test as well as the TSE were applied for each of the considered variables, on the time series of 58 annual values (from 1961 to 2018) and for all 301×321 grid cells individually. The results are presented in *Fig. 6*.

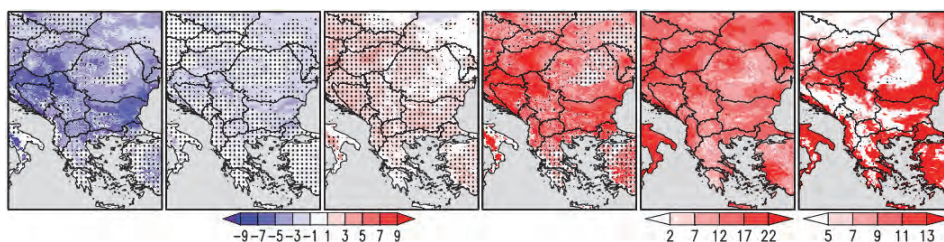


Fig. 6. Trend magnitude for *DOYB*, *DOYM*, *DOYC*, *GSL*, *AAT*, and *BEDD* in the first, second, third, fourth, fifth, and sixth column, correspondingly. The units for *DOYB*, *DOYM*, *DOYC*, and *GSL* are days/10 years; for *AAT* is °D/year, and for *BEDD* is °D/10 years. Stippling indicates grid points with changes that are not significant at the 5% significance level.

Many conclusions could be drawn from *Fig. 6*. The first and foremost conclusion is the notable increasing trend for *GSL*, *AAT*, and *BEDD*. This trend

dominates practically over the whole domain and is statistically significant at the 5% significance level over the low-elevated regions which, generally, are the biggest importance for the agriculture. As it is expected, mountains have the weakest trend for *GSL*, *AAT*, and *BEDD* without statistical significance. The vertical gradient in the spatial pattern of the trend is most notable for the *BEDD* index. *DOYB* demonstrates clear decreasing trend which, with values typically between -5 days/10 years and -1 days/10 years, is statistically significant over the flat regions. This result, in particular, confirms the finding in *Lakatos et al.* (2013b), where it is revealed that the *DOYB* shows significant change over the low-elevated areas of the Carpathian Region in 1961–2010 period. The areas experiencing decreasing trend of *DOYM* and increasing trend of *DOYC* are spatially dominating. These trends, however, are relatively weak and, generally, statistically not significant.

As noted in *Birsan et al.* (2014) in their study of the thermal extremes over the Carpathian Region, the signal of the significant trends of the considered parameters is spatially consistent as there are no areas of mixed trends within the study domain.

4. Conclusion

The present study provides an overview of the spatial patterns in very high resolution and the long-term temporal evolution on annual basis of the selected AM indices over SE Europe in the period 1961–2018. Generally, it confirms the essential impact of the ongoing climate change on the agriculture and forestry in the region. As noted in Section 2.2., however, the application of the selected indices cannot be limited to their agricultural implementations only, hence they could be treated as measures of the cumulative thermal conditions during the warm half of the year.

Consistently with the long-term changes of the mean temperatures over the domain, documented in the most recent papers, the present study reveals strong evidences for the role of the regional climate warming on the considered indices. The *GSL*, *AAT*, and *BEDD* indices experienced essential increase which dominates spatially over the low-elevated areas of the domain and is statistically significant at the 5% significance level. Key message is also the revealed asymmetry in the increase of the most relevant index, the *GSL*: its total lengthening is linked more (more than 70% as relative share over the bigger part of the domain) to the shifting to earlier date of the start, rather than to later cessation. Our proposal is to use the middle day of the *GSL*, *DOYM*, as indicator for such long-term shifts appears also novel in this regard. Our computations show that *DOYM* is shifted to earlier dates practically over the whole domain, but this shift is statistically not significant over its bigger part.

The estimated changes of the AM indices in the near past and recent climate could be also prerequisite for deep ecological and economical consequences. Longer growing seasons, as well as bigger *AAT* and *BEDD*, may allow for a greater diversity of crops (including those with long maturation periods), and the potential for multiple harvests on the same land. Conversely, both irrigation needs and the risk from invasive species, pests, and pathogens may increase (*Harding et al.*, 2015).

The study could be extended and continued in many directions. The logical next step is to accomplish the work assessing the future changes and trends based on climate simulations. Hence the temperatures in all CMIP5 scenarios are projected to rise further, it is reasonable to expect additional increase of these indicators. Our preliminary computations with the regional climate model RegCM confirm this assumption. The study could also be extended backwards in time, as far as possible, in order to capture more general and robust trends. However, as for many other efforts in the regional climatology, the necessary prerequisite for such task is the (free) availability of reliable data with proper spatial coverage and spatio-temporal resolution.

The data sets with the AM indices, as well as the trend measures (p-value and trend line slope) are in standard form (GrADS binary/descriptor files) and could be supplied from the corresponding author upon request.

Acknowledgments: This work is based on the UERRA project (EU FP7 Collaborative Project, Grant agreement 607193). Hence this study entirely exploits free available data and software, the authors would like to express their deep gratitude to the organizations and institutions (UERRA project, CARPATCLIM, MPI-M, UNI-DATA, Copernicus Data Store), which provides free of charge software and data. Without their innovative data services and tools this work would be not possible. Personal thanks to *I. Tsonevsky* from ECMWF for the cooperation. The authors also thank the anonymous reviewer for the useful comments on first version of this manuscript.

References

- Alexandrov, V., Schneider, M., Koleva, E., and Moisselin, J.-M.*, 2004: Climate variability and change in Bulgaria during the 20th century. *Theor. Appl. Climatol.* 79, 133–149.
<https://doi.org/10.1007/s00704-004-0073-4>
- Bartholy, J. and Pongrácz, R.*, 2006: Comparing tendencies of some temperature related extreme indices on global and regional scales. *Időjárás* 110, 35–48.
- Bazile, E., Abida, R., Verelle, A., Le Moigne, P., and Szczypka, C.*, 2017: MESCAN-SURFEX surface analysis, deliverable D2.8 of the UERRA project.
<http://www.uerra.eu/publications/deliverable-reports.html>
- Belda, M., Skalák, P., Farda, A., Halenka, T., Déqué, M., Csima, G., Bartholy, J., Torma, C., Boroneant, C., Caian, M., Spiridonov, V.* 2015: CECILIA Regional Climate Simulations for Future Climate: Analysis of Climate Change Signal. *Adv. Meteorology* 2015, Article ID 354727, 13 pages, 2015 <https://doi.org/10.1155/2015/354727>
- Birsan, M.-V., Dumitrescu, A., Micu, D.M., and Cheval, S.*, 2014: Changes in annual temperature extremes in the Carpathians since AD 1961. *Nat. Hazards* 74, 1899–1910.
<https://doi.org/10.1007/s11069-014-1290-5>

- Chervenkov, H., Slavov, K., and Ivanov, V., 2019: STARDEX and ETCCDI Climate Indices Based on E-OBS and CARPATCLIM; Part One: General Description. In (Eds. G. Nikolov et al.): NMA 2018, LNCS 11189, 360–367. <https://doi.org/10.1007/978-3-030-10692-840>
- Chervenkov, H. and Slavov, K., 2019a: STARDEX and ETCCDI Climate Indices Based on E-OBS and CARPATCLIM; Part Two: ClimData in Use. In (Eds. G. Nikolov et al.) NMA 2018, LNCS 11189, 368–374. <https://doi.org/10.1007/978-3-030-10692-841>
- Chervenkov, H. and Slavov, K., 2019b: Theil-Sen Estimator vs. Ordinary Least Squares — Trend Analysis for Selected ETCCDI Climate Indices. *C. R. Acad. Bulg. Sci.* 72, 47–54. <https://doi.org/10.7546/CRABS.2019.01.06>
- Chervenkov, H. and Slavov, K., 2020: Historical Climate Assessment of Temperature-based ETCCDI Climate Indices Derived from CMIP5 Simulations, *Compt. rend. Acad. bulg. Sci.* 73, 784–790. <https://doi.org/10.7546/CRABS.2020.06.05>
- Chervenkov, H. and Slavov, K., 2021: Geo-statistical Comparison of UERRA MESCAN-SURFEX Daily Temperatures Against Independent Data Sets. *Időjárás* 125, 123–135. <https://doi.org/10.28974/idojaras.2021.1.6>
- Cheval, S., Birsan, M.-V., and Dumitrescu, A., 2014: Climate variability in the Carpathian Mountains Region over 1961–2010. *Glob. Planetary Change* 118, 85–96. <https://doi.org/10.1016/j.gloplacha.2014.04.005>
- Croitoru, A.-E., Holobaca I-H., Lazar, C., Moldovan, F., and Imbroane, A., 2012 Air temperature trend and the impact on winter wheat phenology in Romania. *Climatic Change* 111, 393–410. <https://doi.org/10.1007/s10584-011-0133-6>
- van Engelen, A., Klein Tank, A., van der Schrier, G., and Klok, L., 2008: European Climate Assessment & Dataset (ECA&D), Report 2008, "Towards an operational system for assessing observed changes in climate extremes". KNMI, De Bilt, The Netherlands.
- Gadzhev, G., Georgieva, I., Ganev, K., Ivanov, V., Miloshev, N., Chervenkov, H., and Syrakov, D., 2018: Climate Applications in a Virtual Research Environment Platform. *Scalab. Comput.: Practice Exper.* 19, 107–118. <https://doi.org/10.12694/scpe.v19i2.134>
- Gladstones, J.: 1992: Viticulture and Environment. Winetitles, Adelaide.
- Harding, A.E., Rivington, M., Mineter M.J., and Tett S.F.B., 2015: Agro-meteorological indices and climate model uncertainty over the UK. *Climatic Change* 128, 113–126 <https://doi.org/10.1007/s10584-014-1296-8>
- Janković, A., Podražčanin, Z., and Djurdjevic, V., 2019: Future climate change impacts on residential heating and cooling degree days in Serbia. *Időjárás* 123, 351–370.
- Lakatos, M., Bihari, Z., Szentimrey, T., Szalai, S., and the CARPATCLIM project Team, 2013a: Climate of the Carpathian Region - summary of the CarpatClim project, 3th EMS Annual Meeting & 11th European Conference on Applications of Meteorology (ECAM) — 09–13 September 2013, Reading, United Kingdom. <http://presentations.copernicus.org/EMS2013-501presentation.pdf>
- Lakatos, M., Szentimrey, T., Bihari, Z., and Szalai, S., 2013b: Investigation of climate extremes in the Carpathian region on harmonized data, Int. Scient. Conf. on Environmental Changes and Adaptation Strategies, Sep., 2013 Temperature thresholds and crop production: a review.
- Lindner, M., Maroschek, M., Netherer, S., Kremer, A., Barbat, A., Garcia-Gonzalo, J., Seidl, R., Delzon, S., Corona, P., Kolström, M., Lexer, M. J. and Marchetti, M., 2010: Climate change impacts, adaptive capacity, and vulnerability of European forest ecosystems. *Forest Ecol. Manage.* 259, 698–709. <https://doi.org/10.1016/j.foreco.2009.09.023>
- Luo, Q., 2011: Temperature thresholds and crop production: a review. *Climatic Change* 109, 583–598. <https://doi.org/10.1007/s10584-011-0028-6>
- Malcheva, K., Chervenkov, H., and Marinova, T., 2016: Winter Severity Assessment on the Basis of Measured and Reanalysis data. In: 16th International Multidisciplinary Scientific GeoConference SGEM 2016. SGEM, 719–726.
- Mesterházy, I., Mészáros, R., Pongrácz, R., Bodor, P., and Ladányi, M., 2018: The analysis of climatic indicators using different growing season calculation methods – an application to grapevine grown in Hungary, *Időjárás* 122, 217–235. <https://doi.org/10.28974/idojaras.2018.3.1>

- Mihai, G, Birsan, M.-V. Dumitrescu, A., Alexandru, A., Mirancea, I., Ivanov, P., Stuparu, E., Teodosiu, M., Daia, M., 2018: Adaptive genetic potential of European silver fir in Romania in the context of climate change. *Ann. For. Res.* Vol. 61, No. 1, 95–108. <https://doi.org/10.15287/afr.2018.1021>
- Mihai, G., et al. ,2020: Impact of Climate Change and Adaptive Genetic Potential of Norway Spruce at the South–eastern Range of Species Distribution. *Agr. Forest Meteorol.*, 291, 108040. <https://doi.org/10.1016/j.agrformet.2020.108040>
- Pieczka, J., Bartholy, J., Pongrácz R., and André, K.S., 2019: Validation of RegCM regional and HadGEM global climate models using mean and extreme climatic variables. *Időjárás* 123, 409–433. <https://doi.org/10.28974/idojaras.2019.4.1>
- Pongrácz, R., Bartholy, J., Gelybó, G., and Szabó, P., 2009a: Detected and Expected Trends of Extreme Climate Indices for the Carpathian Basin. In: (Eds. *Strélcová K. et al.*) *Bioclimatology and Natural Hazards*. Springer, Dordrecht, https://doi.org/10.1007/978-1-4020-8876-6_2
- Pongrácz, R., Bartholy, J., Gelybó, G., and Szabó, P., 2009b: A comparison of the observed trends and simulated changes in extreme climate indices in the Carpathian Basin by the end of this century. *Int. J. Global Warming*, 1, 336–355. <https://doi.org/10.1504/IJGW.2009.027097>
- Ridal, M., Schimanke, S., and Hopsch, S., 2018: Documentation of the RRA system: UERRA, deliverable D322 Lot1.1.1.2 in the scope of the Copernicus service C3S 322 Lot1, available via Copernicus.
- Seemann, J., Chirkov, Y.I., Lomas, J., and Primault, B., 1979: *Agrometeorology*, Springer-Verlag, Berlin Heidelberg New York. <https://doi.org/10.1007/978-3-642-67288-0>
- Sillmann, J., V.V. Kharin, X. Zhang, F.W. Zwiers, and D. Bronaugh, 2013: Climate extremes indices in the CMIP5 multimodel ensemble: Part I. Model evaluation in the present climate. *J. Geophys. Res. Atmos.*, 118, 1716–1733. <https://doi.org/10.1002/jgrd.50203>
- Soci, C., Bazile, E., Besson, F., and Landelius, T., 2016: High-resolution precipitation re-analysis system for climatological purposes. *Tellus A*: 68, <https://doi.org/10.3402/tellusa.v68.29879>
- Spinoni, J., Szalai, S., Szentimrey, T., Lakatos, M., Bihari, Z., Nagy, A., Németh, Á., Kovács, T., Mihic, D., Dacic, M., Petrovic, P., Kržič, A., Hiebl, J., Auer, I., Milkovic, J., Štěpánek, P., Zahradníček, P., Kilar, P., Limanowka, D., Pyrc, R., Cheval, S., Birsan, M. V., Dumitrescu, A., Deak, G., Matei, M., Antolovic, I., Nejedlík, P., Štastný, P., Kajaba, P., Bochníček, O., Galo, D., Mikulová, K., Nabyvanets, Y., Skrynyk, O., Krakovska, S., Gnatiuk, N., Tolasz, R., Antofie, T. and Vogt, J., 2015: Climate of the Carpathian Region in the period 1961–2010: climatologies and trends of 10 variables. *Int. J. Climatol.* 35, 1322–1341. <https://doi.org/10.1002/joc.4059>
- Spiridonov, V. and Valcheva, R., 2019: A new index for climate change evaluation. An example with the ALADIN and RegCM regional models for the Balkans and the Apennines. *Időjárás* 123, 551–576, <https://doi.org/10.28974/idojaras.2019.4.9>
- Szyga-Pluta, K. and Tomczyk, A.M., 2019: Anomalies in the length of the growing season in Poland in the period 1966–2015. *Időjárás* 123, 391–408. <https://doi.org/10.28974/idojaras.2019.3.8>
- Unden, P., 2018: UERRA: Final Report, Project No.: 607193, Period number: 3rd Ref: 607193 UERRA Final Report-13 20180319 112103 CET.pdf
- Zhang, X., Alexander, L., Hegerl, G.C., Jones, P., Tank, A.K., Peterson, T.C., Trewin, B., and Zwiers, F.W., 2011: Indices for monitoring changes in extremes based on daily temperature and precipitation data. *WIREs. Climate Change* 2, 851–870. <https://doi.org/10.1002/wcc.147>

IDŐJÁRÁS

Quarterly Journal of the Hungarian Meteorological Service
Vol. 125, No. 2, April – June, 2021, pp. 271–290

Air pollution in Ukraine: a view from the Sentinel-5P satellite

Mykhailo Savenets

Ukrainian Hydrometeorological Institute
37 Nauky Prospect, 03028, Kyiv, Ukraine
savenetsm@gmail.com

(Manuscript received in final form April 6, 2020)

Abstract—The study presents analysis of current air pollution state over Ukraine including remote regions and uncontrolled Ukrainian territories; features of NO₂, SO₂, and CO spatial distribution and seasonality under the influence of local anthropogenic emissions. The research is based on Sentinel-5P satellite data for the period of November 2018 – January 2020. Despite the increasing traffic emissions, the industrial emissions still greatly influence the air pollution in Ukraine. Sentinel-5P coverage allowed detecting a number of cities with huge anthropogenic NO₂ and SO₂ emissions, where ground-based measurements are absent. Uncontrolled territories on the east part of Ukraine still negatively affect air quality in the region due to the activity of coal-fired thermal power plants. The study indicates significant air quality changes during the heating season in winter and open burning in March – April. There were found differences in NO₂ seasonal variability over clean remote regions and industrial zones. The paper analyzes features of shipping emissions during the tourist season for Ukrainian coastline of Black and Azov Seas, showing huge negative impact of chaotic movements of tourists boats near the Dzharylhach National Nature Park.

Key-words: Sentinel-5P, air pollution, seasonality, emissions, nitrogen dioxide, sulfur dioxide, carbon monoxide

1. Introduction

Open data development significantly increases the public awareness of air quality in Ukraine. Nowadays it becomes the concern of not only scientists and ecologists, but also ordinary people. Nevertheless, the state monitoring network for atmospheric air quality is still not developed well. Recently, Ukraine started the process of implementation of air quality EU Directives (*Bashtannik et al.*, 2016), and huge steps have been done by the authorities. However, the state monitoring network is the remnant of the former Soviet Union, where most sites

were set close to the location of emission sources without orientation to the territories with the highest population density. Currently, only 37 cities are carrying out ground-based measurements. Not so long ago, the air quality monitoring network covered 53 cities, but Ukraine lost a number of them on uncontrolled territories (on the Crimea and partially in the Donetsk and Luhansk regions) due to the Ukrainian – Russian conflict.

The above mentioned coverage by monitoring network gives the possibility to analyze air pollution in large cities and over industrial regions. However, a general picture of air quality over the entire country is absent. Therefore, the overwhelming majority of research in Ukraine contain the results only for cities, where state monitoring sites exist (*Bashtannik et al.*, 2014; *Savenets et al.*, 2018; *Shevchenko et al.*, 2016; *Yatsenko et al.*, 2018). Very little amount of air pollution research had been done for Ukraine using satellite data (*Dvoretzka*, 2007; *Galytska et al.*, 2018; *Milinevsky et al.*, 2014) which often were corresponded to the territory with available ground-based measurements.

Over the globe, satellite data provide great vision of air quality, pollutants' distribution, temporal variability, etc., (*Ghude et al.*, 2013; *Krotkov et al.*, 2016; *Lamsal et al.*, 2013; *Richter et al.*, 2011). Sentinel-5P launch with TROPOMI instrument on it revolutionized remote sensing of air quality and showed new opportunities for satellite data usage, allowing distinguishing air pollution of separate cities (*Ialongo et al.*, 2020; *Zheng et al.*, 2019). In 2019, Sentinel-5P data were firstly used in Ukraine for the study of main features in pollutants' spatial distribution over the country, which showed tremendous differences in our knowledge about the most polluted areas (*Savenets et al.*, 2020). Many of the polluted territories have not been mentioned before as problematic regions. The Ukrainian coastline unexpectedly appeared as rather polluted area, firstly indicating the necessity of atmospheric air pollution analysis over the Black and Azov Seas, especially since the problem of ship emissions is not new for Europe (*Aulinger et al.*, 2016).

Great challenge appeared in 2014–2015, after the interruption of measurements on uncontrolled Ukrainian territories, where real atmospheric air quality became unknown. The situation seems to be serious on the east part of Ukraine as the territory is industrially loaded and there are no official information about the current industrial activity. The uncontrolled part of the Donetsk region is highly populated, which means the high probability of that the thermal power plants and local factories continue working. Thermal power plants and coal consumption have the greatest influence on the sulfur dioxide (SO₂) anthropogenic emissions (*Jiang et al.*, 2019), thus the absence of state control and management pose a risk for air quality in the region. Moreover, numerous military equipments from both sides protect the border and influence the environment and atmospheric air quality specifically. Changes of economic development have direct effect on pollutants' emissions (*Sinha*, 2016). In these conditions, satellites become the only sources of monitoring the atmospheric

chemicals data providing vital information for the analysis of air pollution over the uncontrolled territories.

The present study aimed to define air pollution state for the entire Ukrainian territory including remote regions and uncontrolled territories, to deepen the knowledge about seasonal changes of pollutants and to better understand spatiotemporal variability over Ukraine under the local anthropogenic load.

2. Data and methods

The research was carrying out using Sentinel-5P TROPOMI data for column number density of three pollutants: nitrogen dioxide (NO₂), carbon monoxide (CO), and sulfur dioxide (SO₂). The selected pollutants are enough for describing the features of air quality in Ukraine, because all main emission sources contain at least one of these chemical species. A large amount of data needed to be processed, because the main task is dedicated to air quality analysis in Ukraine, and total period covers more than one year. In this case, one of the most suitable instruments for analysis is the Google Earth Engine. It allows quickly processed data over Ukraine for relatively long period. The first full month in the Google Earth Engine available for all selected pollutants is November 2018, therefore the total research period covers 15 months: November 2018 – January 2020. The selected period gives the opportunity to look through the ongoing air pollution situation in Ukraine and to detect main features of seasonal changes.

Data processing were implemented in Earth Engine Code Editor using JavaScript. The original data are represented as Level 2 products, whereas Google Earth Engine converts them to Level 3 products, where data is binned by latitude/longitude, not by time. Data were filtered with quality assurance index 0.5 during the conversion; however, information might be used attentively to avoid false conclusions. Overall, temporal or spatial averaging usually offset unreliable data if any of them exist after filtering.

For general air quality estimation averaging for the entire research period was used. Air pollution analysis during particular cases and seasons implemented with averaging for the periods from several days to several months depends on the research purpose and duration of impact from emission source. In case of shipping pollution, average NO₂ data significantly smooth the main patterns, therefore, maximal values better represent spatial distribution of NO₂ pollution from shipping.

Total column derived from Sentinel-5P cannot be accurately recalculated to near-ground values, which are crucial for estimation of negative air pollution influence on human health and ecosystems. Approximate near-ground values could be calculated using some assumptions about the vertical distribution of pollutants and knowing its molar mass. The overwhelming majority of NO₂, CO,

and SO₂ molecules over industrial regions and big cities gathered in the troposphere. Let us suppose, that the pollutant distributes in the lower 10 km layer (H), and its concentrations (C) are equal on each altitude for more simple calculations. [mol/m²] must be converted to [mg/m³] for comparison with national threshold standards. Therefore, the near-ground value in [mg/m³] is:

$$C = \frac{C_{col}}{H} \cdot M \cdot A,$$

where C_{col} is the pollutant column content [mol/m²], M is the molar mass [g/mol], A is a constant, equals to 1000, for conversion from [g/m³] to [mg/m³]. H is expressed in [m].

It has to be clarified that the recalculated near-ground concentrations were comparable to the usual in-situ values, however, with lower-than-expected values. It happens because of assumption about pollutants' equal vertical distribution. However, during the analysis of heating season, even recalculated values exceed national threshold standards; therefore, the author deems it necessary to describe the formulae in favor of heating season case analysis.

3. Results and discussions

3.1. General features of air pollution in Ukraine

Ukraine had been developed as the mix of an industrial and agricultural country for more than the 50 years. Such development significantly affects the current air pollution levels and features of pollutants' spatial distribution. After the Soviet Union had collapsed, the industry in Ukraine rapidly decreased due to the huge economic crisis, and many factories were closed. Nevertheless, there are five big industrial zones in Ukraine, which are located close to mines or cities with working industrial units.

The most well-known region is Donbass situated on the east part of Ukraine. Donetsk and Luhansk administrative regions comprise most factories and mines, however, Ukrainian – Russian conflict interrupted the production on the most uncontrolled territories. Another big industrial zone located near the Dnipro River in the central part of Ukraine. There are also a powerful set of factories near Kyiv city, on the northeast near Kharkiv city, and close to the Carpathians.

In the last decade the traffic continuously increased, which caused rather serious trouble in big cities like Kyiv, Kharkiv, Odesa, Dnipro, Lviv, etc. Some drivers use cars, which do not filter the exhaust properly. Roads in the city centers, bypass routes within suburbs, and roads for commuting going out from cities are the busiest with traffic during day hours. Elevated pollution levels due to traffic emissions appear in case of favorable weather conditions with slow wind speed and temperature inversions.

Despite a large number of stationary point and linear emission sources, the square under agriculture is also big. These territories are typically low-emission zones during the year. However, the practice of agricultural burning is popular in Ukraine, therefore, in early spring and autumn, short-term but huge amount of substances from biomass burning are emitted in the atmosphere.

Talking about Ukrainian territories three regions must be mentioned: Polissia (the north part of Ukraine), the Carpathian Mountains, and the Crimean Mountains. These regions are the cleanest in Ukraine, where number of natural reserves and parks are situated. In 1986, after the Chernobyl Nuclear Power Plant explosion, the population from the closest territories had been resettled, making the Polissia region even less populated.

NO₂ column number density is the most appropriate parameter for estimation of atmospheric air quality in Ukraine, which allowed distinguishing polluted zones and typical background. The highest NO₂ column number density was observed over Kyiv and number of industrial cities in the Donbass region: Sloviansk, Kramatorsk, Khartsyzk, Kostiantynivka, Kurakhove, Novyi Svit. Kyiv combines huge emissions from traffic and industry, whereas traffic is not the main problem of Donbass cities. As in European cities, traffic emissions become the greatest issue, while industrial emissions continue to prevail over the tabove mentioned regions with high NO₂ content. Average NO₂ column number density over mentioned cities exceed $1.2 \cdot 10^{-4}$ mol/m² (Fig. 1).

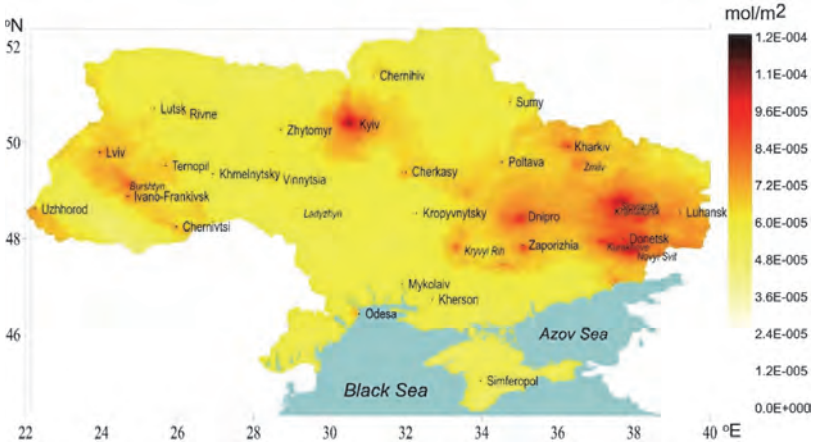


Fig. 1. Spatial distribution of average NO₂ column number density for November 2018 – January 2020.

Thermal power plants are the main pollution sources over the Donbass region. The challenge is to estimate air pollution on uncontrolled Ukrainian territories on the east, where monitoring sites stopped in-situ measurements, and industry do not provide any information about current emissions. In this situation, remote sensing became the key opportunity for air pollution monitoring over uncontrolled territories. Using Sentinel-5P data huge NO₂ emissions were detected over Novyi Svit, where Starobeshiv thermal power plant is located. It becomes clear, that power plant is operating at full capacity, and emissions might significantly exceed permissible levels.

Except for the group of cities with the highest NO₂ content, there are another two groups, where air pollution levels are high and the average NO₂ column number density reaches about $1.0\text{--}1.2\cdot 10^{-4}$ mol/m². The first group of big cities, which are the centers of administrative regions, has high NO₂ content due to traffic and industrial emissions: Kharkiv, Lviv, Odesa, Dnipro, Zaporizhzhia, Cherkassy, and others. The other group of relatively small towns, where thermal power plants emit NO₂, contains, e.g., Burshtyn, Ladyzhyn, Zmiiv.

The rest territory on the distance from industrial zones and big cities is rather clean with background NO₂ column number density of about $4.0\text{--}7.0\cdot 10^{-5}$ mol/m². Minimal NO₂ concentrations observed over Carpathians Mountains, Crimean Mountains, and Polissia on the north part of Ukraine, where average values usually do not exceed $4.0\cdot 10^{-5}$ mol/m².

The spatial distribution of average CO column number density over Ukraine is quite homogeneous. The reason of it is the longer lifetime in the atmosphere, therefore, CO can distribute on the longer distances. As a result, any significant differences in spatial distribution are smoothed. There are four cities with values exceeding $4.0\cdot 10^{-2}$ mol/m²: Mariupol (the highest CO content in Ukraine), Dnipro, Zaporizhzhia, and Kryvyi Rih. The main pollution sources in these cities are numerous factories and power plants. Average background CO column number density over Ukraine is about $3.0\cdot 10^{-2}$ mol/m². The cleanest territories are the Carpathians and Crimean Mountains, where average CO column number density do not exceed $2.0\cdot 10^{-2}$ mol/m².

The spatial distribution of SO₂ is highly heterogeneous in contract to that of CO. Therefore, analysis makes sense only for relatively large territories, not for particular point locations. Main SO₂ emission sources in Ukraine are metallurgical industry and coal-running power plants. In general, the most polluted area is southeastern Ukraine, where the most industrial sources are located. The average SO₂ column number density over these regions often exceed $3.0\cdot 10^{-4}$ mol/m². There is only one point in Ukraine, where strong SO₂ emissions are observed during the year. This point is the previously mentioned Novyi Svit with Starobeshiv thermal power plant, situated on the uncontrolled Ukrainian territory, where the average SO₂ column number density exceeds $4.6\cdot 10^{-4}$ mol/m².

3.2. Seasonal variability and meteorological impact

Ukraine is one of the largest countries in Europe with a total area of 603 628 km² having both remote clean territories and polluted industrial regions with huge anthropogenic emissions. Analysis of NO₂ column number density over Ukraine allows detecting two types of seasonal variations that significantly differ. Over clean remote regions, which are plains on the north and mountains on the west parts of the country, the summertime NO₂ content is higher than the wintertime. Industrial regions and big cities do not have clear seasonality, however, frequent elevated pollution levels during December – February disrupt the distribution, and winter average values are always higher than in other months.

NO₂ intra-annual variations in remote regions have seasonal maxima from late May to June, when column number density reach $0.7\text{--}0.8\cdot 10^{-4}$ mol/m² (Fig. 2). From March to November, NO₂ values are characterized by small variance, and concentrations form under local conditions with rarely visible impact from cities and polluted areas. In winter, the NO₂ content decreases to about $0.4\text{--}0.6\cdot 10^{-4}$ mol/m². Nevertheless, the highest NO₂ values ever observed in clean regions appeared in winter on the background of low values. It happened due to cases with polluted air advection from cities and industrial zones. These cases usually are short-term and lasts only few days, however, they disrupt the typical NO₂ seasonality. This is the reason why we could observe maximal NO₂ concentrations in the cold season, whereas, usual NO₂ content due to natural processes is the lowest. The highest NO₂ column number density exceeds $2.0\cdot 10^{-4}$ mol/m², which is typical for large, highly polluted cities.

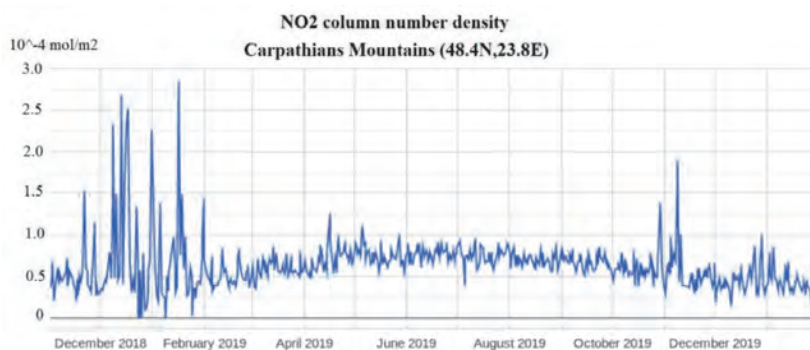


Fig. 2. NO₂ column number density over the Carpathian Mountains for November 2018 – January 2020.

NO₂ in cities and industrial regions has opposite variations with maximal content from December to February, because the weather conditions are favorable for pollutants' accumulation, car engines are running cold, and additional emissions appear from heating. NO₂ column number density in winter often exceed $3.0 \cdot 10^{-4}$ mol/m², the variance of data is high, and the polluted atmospheric air sometimes moved on long distances reaching clean regions. The most stable conditions are observed from June to August and slightly vary within $0.9\text{--}1.1 \cdot 10^{-4}$ mol/m² (Fig. 3).

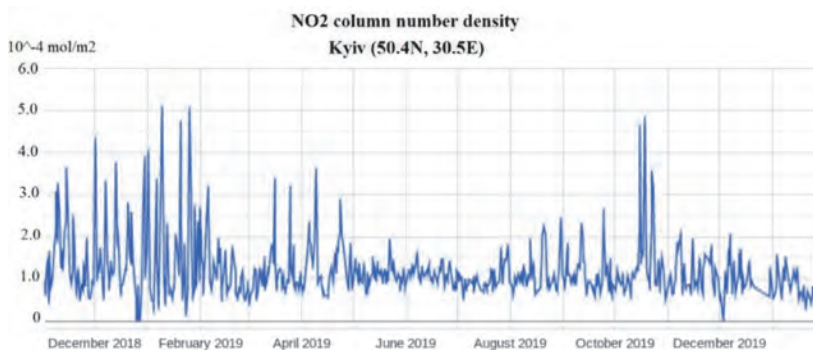


Fig. 3. NO₂ column number density over Kyiv for November 2018 – January 2020.

CO seasonal variations over Ukraine are similar for the clean and highly polluted regions. Unlike NO₂, it happens due to its longer lifetime in the atmosphere, and CO is rather equally distributed over the territory. Usually there are higher CO column number density from December to April reaching of about $3.0\text{--}4.0 \cdot 10^{-2}$ mol/m² in cities and polluted industrial zones (Fig. 4). Concentrations are lower over clean regions reaching about $2.7\text{--}3.5 \cdot 10^{-2}$ mol/m² (Fig. 5).

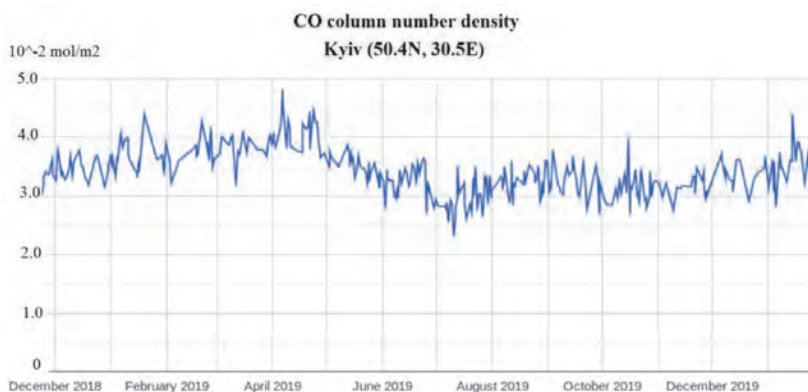


Fig. 4. CO column number density over Kyiv for November 2018 – January 2020.

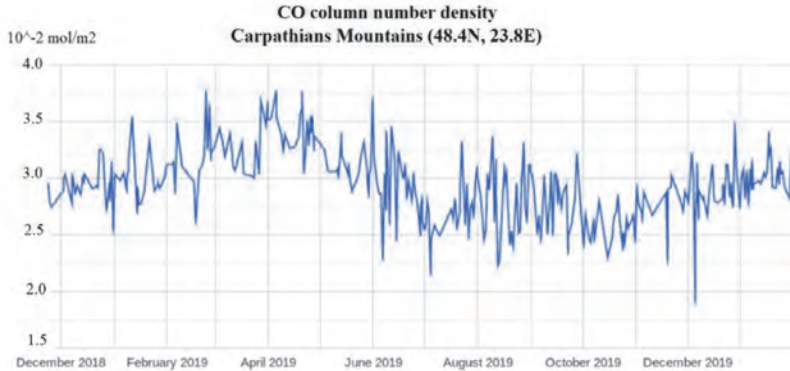


Fig. 5. CO column number density over the Carpathian Mountains for November 2018 – January 2020.

CO intra-annual changes are well explained by the intensity of anthropogenic sources. Concentrations are gradually increasing in the start of heating season, from November to March, when the CO column number density is $1.0\text{--}1.5 \cdot 10^{-2} \text{ mol/m}^2$ higher than during the warm period. However, maximal values very often appear in April, which is completely out of the ordinary distribution, because heating season usually ends by this time, and the anthropogenic load decreases from February to March due to higher air temperatures. The answer about CO maximum in April is connected to the features of agricultural land usage in Ukraine. At the end of March – beginning of April, the weather conditions become stable with constant temperature increase and absence of raining. The snow usually disappears and the land under the sunny weather gets dry enough. Open burning still is very popular among Ukrainian farmers and on the private vegetable gardens. As the result of favorable weather conditions, most fields in Ukraine are being burnt at the end of March and in April, and huge amount of combustion products including CO are emitted in the air. This is the main reason, why we observed April CO maximum instead of gradually decreasing values.

As it can be seen in Figs. 4 and 5, the CO maxima in April is detected over clean and polluted regions. Moreover, the difference between spring months and winter months is higher in clean regions, because industrial zones have more CO emission sources that smooth the temporal distribution.

The CO content accumulated in the atmosphere during February – April decreases in May and usually minimal values are observed in July – the warmest month in Ukraine. From August to November, the CO column number density varies within $2.9\text{--}3.5 \cdot 10^{-2} \text{ mol/m}^2$ over the most polluted regions; in the

Carpathian Mountains – the cleanest region in Ukraine –it varies from $2.5 \cdot 10^{-2}$ mol/m² to $2.7 \cdot 10^{-2}$ mol/m².

Through the air pollution in Ukraine mostly depends on the anthropogenic emission sources meteorological conditions also have rather big influence on pollutants' seasonality. Air mass advection with elevated pollution levels originated from the cities and industrial zones very often change the background concentrations and its spatial distribution. One of the examples is represented in *Fig. 6*, when huge amount of NO₂ was distributed from large cities to Carpathian Mountains on December 12–13, 2018. This is exactly the case, when extremely high values disrupt typical NO₂ seasonality over clean regions.

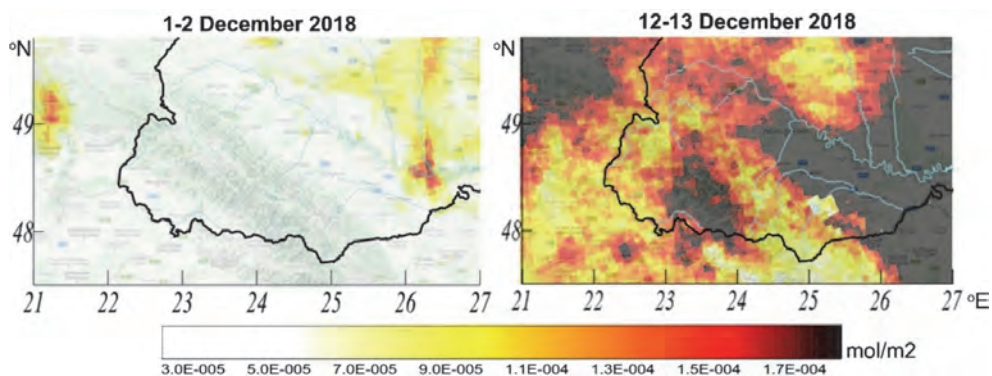


Fig. 6. NO₂ column number density over western Ukraine and the Carpathians before December 1–2, 2018 and during December 12–13, 2018 a period of polluted air advection.

Meteorological conditions significantly influence air pollution levels through the possibility for pollutants' accumulation and removal. Moreover, the intensity of emissions often depends on temperature and wind regimes because of changes in industrial exploitation. Favorable synoptic situation may decrease concentrations to background levels even over large and industrial cities. The excellent example of positive weather influence on air pollution is the difference between NO₂ column number density in January 2019 and January 2020 (*Fig. 7*).

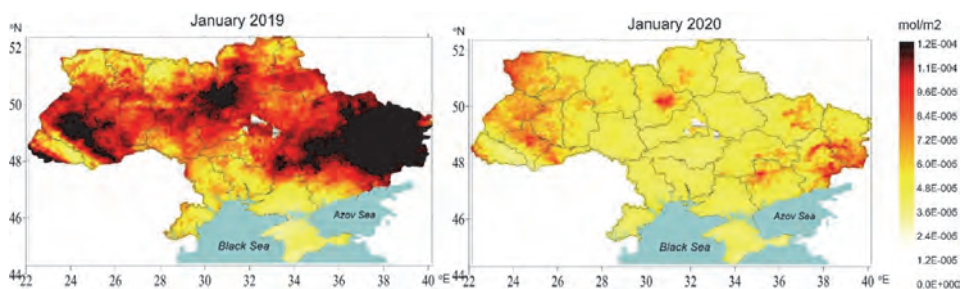


Fig. 7. Spatial distribution of average NO₂ column number density in January 2019 and January 2020.

Temperature regime is the crucial difference between the winter months of 2019 and 2020. According to the Central Geophysical Observatory named after Boris Sreznevskiy (CGO), January 2019 was a typical winter month for the Ukrainian territory (the coldest month in the year) with the average temperature of about -4 – -5 °C, which was 1 °C higher than the climate normal. In contrast, January 2020 was extremely hot with abnormal average temperature over 0.5 °C, more than 6 °C higher than the climate normal. As a result, weather affected both the decreasing of emissions and the increasing of air pollutants' removal. In January 2019, the power plants burned more fuel than in January 2020. The average NO₂ column number density in January 2019 exceeded $1.0 \cdot 10^{-4}$ mol/m² over cities and adjacent territories, while in January 2020, it was lower than $8.0 \cdot 10^{-5}$ mol/m². Moreover, higher temperatures and frequent cloudless conditions have contributed to an increase of NO_x chemical loss. Therefore, during the 2019–2020 winter, air pollution levels were low and NO₂ concentrations were close to background values over the overwhelming majority of the territory.

3.3. Tracking emissions from industrial point sources and wildfires

There are a number of towns in Ukraine with relatively small area, rather low population, absence of busy traffic, but huge pollutants' emissions from industrial point sources. These features and the well-known origin of pollutants make them excellent objects for different kind of research dedicated to air pollution analysis, to study the dependence of plume distribution on different weather conditions, and to the comparison of satellite data with modeling results. However, most of the cities do not have any in-situ measurements, therefore, Sentinel-5P data might play crucial role for air quality monitoring and emissions tracking. The best examples of such type cities in Ukraine are Ladyzhyn, Burshtyn, Kurakhove, Novyi Svit, Chuhuiv, and Slobozhanske. Except Chuhuiv, all mentioned cities has powerful thermal power plants.

Chuhuiv has several industrial emission sources close to each other. Novyi Svit is situated on the uncontrolled Ukrainian territory, therefore no information about real industrial capacities and emission inventories are available.

During favorable weather conditions, the plumes of elevated NO_2 content were distributed from industrial sources affecting air quality in the relatively clean rural areas. *Fig. 8* represents one of the cases with cloudless anticyclonic weather conditions and southwestern wind blowing for 4 days in one direction.

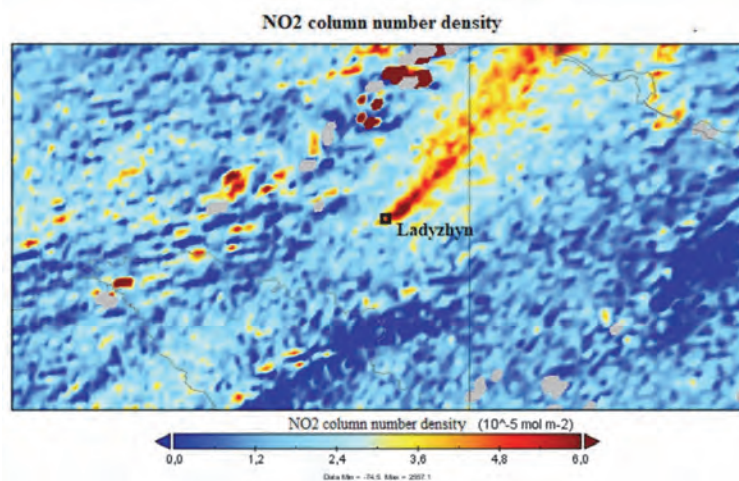


Fig. 8. NO_2 column number density and the area affected by elevated pollution levels from industrial sources (August 8, 2019).

During August 4–9, 2019, an episode of stable anticyclonic weather condition was analysed which allowed to estimate the area affected by elevated NO_2 content from thermal power plants. Total affected areas, where NO_2 column number density could be recognized as plume, cover 200 km out from cities. On large distances, other sources smooth the clarity of NO_2 plume, and it became impossible to detect the origin of the emissions.

Under the anticyclonic weather conditions with unidirectional 3–4 days wind, the affected area can be divided into 3 zones. At the distances up to 30 km, NO_2 column number density exceeds $5.0 \cdot 10^{-5} \text{ mol/m}^2$. Next zone usually covers the territory from of about 30 to 100 km out of the city, where NO_2 column number density reaches $3.7\text{--}5.0 \cdot 10^{-5} \text{ mol/m}^2$ and the plume extends like a rather narrow strip. On the distances more than 100 km, the plume is spreading, the NO_2 content decreases to $2.0\text{--}4.0 \cdot 10^{-5} \text{ mol/m}^2$, however it is still well detected. Gradually, it becomes difficult to define whether the NO_2 concentration is originated from an industrial point emission source or comes from other cities.

The heating season is one of the most remarkable periods for air pollution increase in Ukraine. Usually it starts in November and lasts to March, however some deviations of its length are possible because of its relation to the transition of daily average air temperature through 8 °C (*Krakovska et al.*, 2019). Domestic heating has some differences in comparison with thermal power supply by power plants and heating stations. The usual period of domestic heating is longer; nevertheless, there might be weaker heating intensities during the cases of warmer weather conditions in winter.

Natural gas and coal are the mostly used fuels in Ukraine during the heating season. CO and NO₂ emissions, which influence pollutants' concentrations often, cannot be tracked for this purpose by using Sentinel-5P data. CO lifetime is relatively big in comparison to the length of the heating season, therefore, it is equally distributed in different directions and no maximum appears on the average map for the winter season. NO₂ has a large number of sources, which make possible to detect emissions during the heating season only in cities with huge power plants and rather small traffic intensity. In opposite to CO and NO₂ concentrations, SO₂ column number density gives great opportunity for monitoring air pollution in Ukraine from coal-fired power plants.

There are two big regions, where SO₂ content significantly increase during the heating season due to usage of coal fuel in power plants. The first region is situated on the east part of Ukraine, where the majority of Ukrainian coal mines are located. The second region elongates from the northeast to the central regions of Ukraine. The maximum value of the SO₂ content appears in the second region only during the heating season, which indicates prevailing of coal-fired heating plants, whereas the rest of the territory mainly uses natural gas for heating purpose. The average values of total SO₂ column number density for heating season in cities with prevailing coal-burned power plants reach a level of about $2.2\text{--}4.0\cdot 10^{-3}$ mol/m². If we suppose that the SO₂ content gathered in the lower 10 km atmospheric layer, and for more easy calculations it is equally distributed within the mentioned layer, the near-ground average SO₂ concentrations for three months are comparative to the daily SO₂ threshold levels of 0.05 mg/m³ (threshold level according to the national standard (*CGO*)). Analysis showed that the mentioned two regions are highly affected by elevated SO₂ levels due to coal burning during the heating season. Moreover, the region with elevated values on the east mostly is situated on the uncontrolled Ukrainian territory, which means problems during the implementation of European standards and air quality management. The rest territory of Ukraine does not have significant elevations of SO₂ column number density with average values lower than $2.0\cdot 10^{-4}$ mol/m².

The CO datasets from Sentinel-5P allow to detect elevated pollution levels caused by wildfires, moreover, averaging for several days makes visible the plume distribution from burned areas. Forests cover more than 15% of the

Ukrainian territory, and the State Emergency Service of Ukraine (*SESU*) recorded about 96 000 wildfires in 2019. With Sentinel-5P data it is possible to detect elevated pollution levels with CO from only the minority of forest fires, nevertheless, the largest reaches were always visible. During the large forest fires in Ukraine, CO average values for the period of active fire usually reach $4.5\text{--}5.0 \cdot 10^{-2} \text{ mol/m}^2$, whereas maximal column number density of about 0.15 mol/m^2 . CO plumes from most fires usually extended to 100–150 km out from the source.

The analysis of elevated CO concentrations during wildfires showed an optimal period for appropriate disaster tracking using Sentinel-5P. Near real-time data and single data file might be good for indicating the position of maximal pollutants' concentration. However, very often it shows the plume which was transported at some distance, not the location of the exact emission source. Usage of single files, even with high quality assurance values, might cause false conclusions about the burned area. Averaging gives the opportunity to combine the plume distribution with the exact emission point using a series of the day-to-day files and to obtain a more complete picture. After averaging for different periods, it was found that 4–7 days are the optimal length for air pollution tracking. Periods of more than one week smooth the spatial values, thus plumes distribution and emission sources become less visible. Moreover, 4–7 days is the best period for staying within a single synoptic process in midlatitudes before another one appears significantly changing the direction of air advection and, consequently, the plume distribution.

3.4. Shipping pollution

Ukraine has access to the Black and Azov Seas with international seaports, active coastal shipping, numerous fishing boats and local cruise ships during the tourist season from June to September. It is worth to be noted, that the chaotic movement of fishing and tourist boats make impossible to estimate its exact amount. Big changes in Ukrainian shipping started in 2015, when the country lost control of Crimea during the Ukrainian – Russian conflict. Soon thereafter, shipping in Mariupol, Kherson, Mykolaiv, Odesa, and Chornomorsk has been increasingly congested. Tourists changed destinations, and the whole coastline of the Ukrainian mainland became a popular region for spending vacation.

All mentioned changes possibly caused the increasing of air pollution levels within the last 5 years; however, it is impossible to find any tendency due to the absence of in-situ measurements and coarse resolution of previous satellite missions. Currently, shipping pollution over sea and shoreline could be detected with Sentinel-5P data by using CO and NO₂ datasets. Air quality is affected by the different ratios of chemical compounds depending on the petrol. There are some visible elevations of background SO₂ levels over the sea;

nevertheless, observed differences are not enough large to be considered as robust. The CO content is high along the shoreline of the Azov Sea, whereas it is not clearly visible over the Black Sea.

The analysis finds three main polluted areas because of intense shipping: the main trade routes the shorelines during the tourist season, and the river mouth of Pivdennyi Buh and Dnipro rivers. Over the mentioned areas, maximal values of NO₂ column number density reach about $5.0\text{--}8.0 \cdot 10^{-4}$ mol/m² (Fig. 9).

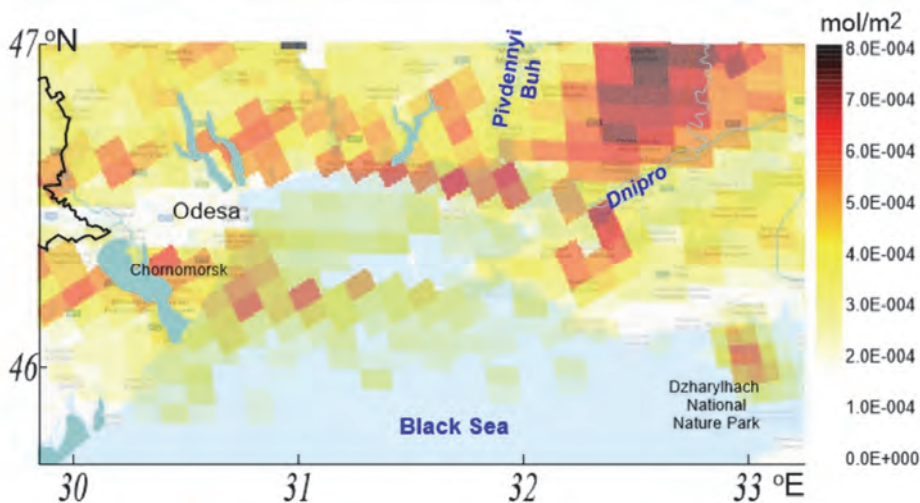


Fig. 9. Spatial distribution of maximal NO₂ column number density values over the northwestern part of the Black Sea.

NO₂ emissions is tracked by the main trade routes coming out of Odesa and Chornomorsk. Elevated NO₂ total column values can be observed during the warm season and consist of several routes. Better-detected route connects to the opposite sides of the Ukrainian mainland, whereas the less visible routes are international routes to Bulgaria, Georgia, and Turkey.

The current study finds higher NO₂ concentrations at the river mouth of Pivdennyi Buh and Dnipro, where local trade shipping prevails. The closer the sea is the higher NO₂ content can be observed, which increases also by adding emissions from tourist boats near the popular beachside resorts on the way from Kherson and Mykolaiv river ports to the sea. Maximal values in the northwestern part of the Black Sea, where number of resorts are situated, exceed the NO₂ background values: they are of about three times higher than over the

sea at some distance from the coastline and twice higher than the inland NO₂ content in that area.

The most unexpected results are obtained for the Dzharylhach National Nature Park, which is situated on the island Dzharylhach. The Park is popular among tourists, especially in its western part with two lighthouses and picturesque landscapes. During the active tourist season from June to August, NO₂ concentrations significantly increase due to the numerous boats with hundreds of tourists arrive every day (Fig. 10).

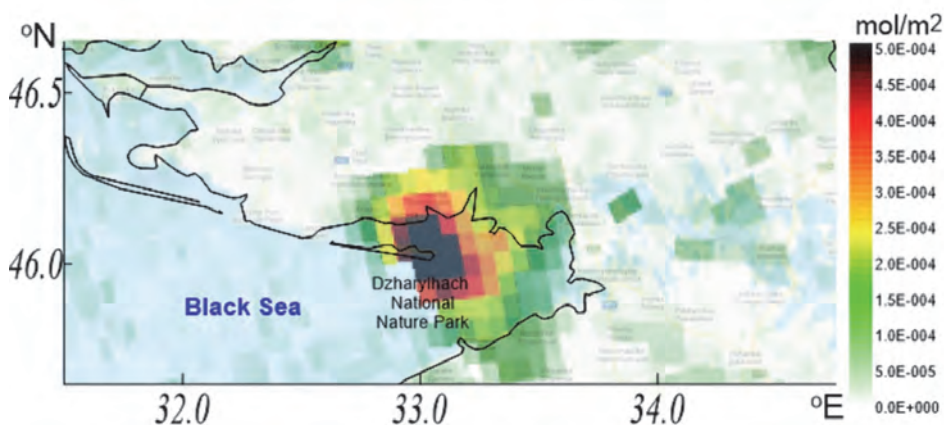


Fig. 10. Spatial distribution of maximal NO₂ column number density values over the Dzharylhach National Nature Park (June 2019).

The problem of air pollution in the Park seems to be serious, as every day the NO₂ column number density increases to $3.5\text{--}5.0\cdot 10^{-4}$ mol/m² and spreads out from the island at an average distance of about 12–15 km. The NO₂ column number density over Dzharylhach during June–August is 5 times higher than concentrations over the surrounded mainland. However, control measures to the number of boats still have not been made.

3.5. Discussions

The absence of ground-based measurements in the highly polluted industrial cities caused lack of mention in previous research papers (Bashtannik *et al.*, 2014; Savenets *et al.*, 2018; Shevchenko *et al.*, 2016; Yatsenko *et al.*, 2018). These cities are Burshtyn, Khartsyzk, Kurakhove, Ladyzhyn, Novyi Svit, with an average NO₂ column number density exceeding $1.2\cdot 10^{-4}$ mol/m², which is among the highest values in Ukraine. The mentioned cities need at least a

development of a network with indicative measurements in the future. The current study showed that the affected area around these industrial cities could cover 200 km during the favorable weather conditions with unidirectional wind. All results in this study connected with industrial sources point the need to include the mentioned cities in each plan regarding air quality management in Ukraine.

Industrial zones on uncontrolled territories on the east part of Ukraine continue to contribute negative impact on atmospheric air. Several big power plants emit huge amount of SO₂ and NO₂. The current study confirms the findings from a previous one (*Savenets et al., 2020*), that emphasized on the mismatch between different sources of official and unofficial information and news. Sentinel-5P tracked highly polluted plumes from power plants on uncontrolled territories, which are the great evidence of its work at full or close to full capacities.

The great concern is the air quality along the coastline. Very often tourists visit resorts for recreation thinking about the benefits of marine air. Actually, the whole coastline during the tourist season is highly polluted due to the numerous boats. In fact, there are no regulations of small boats' movement, moreover information about atmospheric air pollution over the sea rarely appear among scientists and ecologists in Ukraine. Chaotic tourists' activity in the Dzharylhach National Nature Park over the last few years might became a real catastrophe for local ecosystems, which need more strict protection.

The study finds that anthropogenic emissions and features of agricultural land use significantly influence the CO seasonality over Ukraine. The well-known fact is the role of CO loss due to OH concentrations decreasing in winter (*Koike et al., 2006; Rinsland et al., 2000; Zhao et al., 2002*). As a result, maximum values in the Northern Hemisphere can be observed in late winter/early spring. The open burning activities during March – April in Ukraine result in a shift of the CO maxima to April, which means that CO temporal changes could not be explained only by anthropogenic emissions in winter and CO loss because of OH. CO emissions during open burning is the main reason of that CO maximal values appear in April.

SO₂ and NO₂ seasonalities over cities depends on the location and emission sources, thus, they cannot be analyzed everywhere using similar methodology. In Ukraine, the highest SO₂ concentrations are observed during the heating season because of fossil fuels usage for heating purpose. In comparison, SO₂ seasonal changes might differ even taking into consideration European cities (*Bralic et al., 2012*).

4. Conclusions

Air pollution in Ukraine forms under the influence of traffic emissions and activity of the five biggest industrial zones. In most polluted cities, the average

NO₂ column number density exceeds $1.2 \cdot 10^{-4}$ mol/m², whereas background values are of about $4.0\text{--}7.0 \cdot 10^{-5}$ mol/m². There are three remote clean regions in Ukraine: the Carpathian Mountains, the Crimea Mountains, and Polissia with average NO₂ column number density lower than $4.0 \cdot 10^{-5}$ mol/m². CO and SO₂ contents are the highest over cities with numerous factories and coal-fired thermal power plants. Some of the most powerful emission sources are located on the uncontrolled Ukrainian territories, which are the evidence of its active work. Affected area with elevated pollution levels during the favorable weather conditions exceed 200 km out from industrial emission sources and 100–150 km during the wildfire events.

NO₂ seasonal variations differ over clean remote regions and over industrial zones and cities. NO₂ seasonal maxima can be observed in May – June over remote territories, whereas the highest values over cities occur during December – February. CO is the highest during December – March, which is the typical temporal distribution due to emissions increase and loss because of OH decreasing. However, in Ukraine the practice of open burning in late March – April makes the maximum CO concentration to shift to April. SO₂ seasonal variations depend on anthropogenic emission sources. In regions with coal-fired power plants, maximal values appear during the heating season.

During the tourist season, the coastline of Black and Azov Seas is five times more polluted than the nearest inland territories because of the uncontrolled chaotic movement of tourist and fishing boats. Maximal NO₂ column number density reaches $5\text{--}8 \cdot 10^{-4}$ mol/m², even over the territory of the Dzharylhach National Nature Park that has become a popular visit point over the last few years.

Acknowledgements: The author is grateful for the help of the organizing committee and tutors of Trans-Atlantic Training 2019 (TAT-7, Novi-Sad, Serbia, 20-24.06.2019) “Radar and optical remote sensing in the agricultural and environmental monitoring” and to the First Joint Training Course on Atmospheric Composition (Cluj-Napoka, Romania, 04-08.11.2019) for receiving valuable knowledge and skills which allow to carry out the presented study.

References

- Aulinger, A., Matthias, V., Zeretke, M., Bieser, J., Quante, M., and Backes, A., 2016: The impact of shipping emissions on air pollution in the greater North Sea region – Part 1: Current emissions and concentrations. *Atmos. Chem. Phys.* 16, 739–758. <https://doi.org/10.5194/acp-16-739-2016>
- Bashatnik, M.P., Dvoretzka, I.V., Onos, L.M., and Savenets, M.V., 2016: Osnovni zasady vydilannia zon yiakosti atmosferneho povitria na terytorii Ukrainy ta yih klasifikatsia zhidno z vymohamy dyrectyv 2004/107/EC ta 2008/50/EC. *Naukovi pratsi UkrNDGMI* 269, 123–137. (In Ukrainian)
- Багатник, М.П., Дворецька, І.В., Онос, Л.М., Савенець, М.В. 2016: Основні засади виділення зон якості атмосферного повітря на території України та їх класифікація згідно з вимогами директив 2004/107/EC та 2008/50/EC. *Наукові праці УкрНДГМІ* 269, 123-137.
- Bashatnik, M.P., Zhemera, N.S., Kiptenko, E.N., and Kozlenko, T.V., 2014: Stan zabrudnennia atmosferneho povitria nad terytorieyu Ukrainy. *Naukovi pratsi UkrNDGMI* 266, 70-93. (In Ukrainian)

- Бауманнік, М.П., Жемера, Н.С., Кінтенко, С.Н., Козленко, Т.В., 2014: Стан забруднення атмосферного повітря над територією України. *Наукові праці УкрНДДГМІ* 266, 70-93.
- Bralic, M., Buljac, M., Peris, N., Buzuk, M., Dabic, P., Brinic, S., 2012: Monthly and Seasonal Variations of NO₂, SO₂ and Black-smoke Located within the Sport District in Urban Area, City of Split, Croatia. *Croat. Chem. Acta* 85, 139–145. <https://doi.org/10.5562/cca1966>
- CGO. Central Geophysical Observatory named after Boris Sreznevskiy. <http://cgo-sreznevskiy.kiev.ua/index.php?lang=en>
- Dvoretzka, I.V., 2007: Osnovni harakterystyky polya aerosoliy nad teritoryeyu Ukrainy. *Visnyk of V. N. Karazin Kharkiv National University, Series "Geology. Geography. Ecology* 633, 120–131
- Дворецька, І.В., 2007: Основні характеристики поля аерозолу над територією України. *Visnyk of V. N. Karazin Kharkiv National University, Series "Geology. Geography. Ecology* 633, 120–131
- Galytska, E., Danylevsky V., Hommel, R., and Burrows, J.P., 2018: Increased Aerosol Content in the Atmosphere Over Ukraine During Summer 2010. *Atmos. Measure. Tech.* 11, 2101–2118. <https://doi.org/10.5194/amt-11-2101-2018>
- Ghude, S.D., Kulkarni, S.H., Jena, C., Pfister, G.G., Beig, G., Fadnavis, S., and van der A, R.J., 2013: Application of satellite observations for identifying regions of dominant sources of nitrogen oxides over the Indian Subcontinent. *J. Geophys. Res.: Atmospheres* 118, 1075–1089 <https://doi.org/10.1029/2012JD017811>.
- Ialongo, I., Virta, H., Eskes, H., Hovila, J., and Douros, J., 2020: Comparison of TROPOMI/Sentinel-5 Precursor NO₂ observations with ground-based measurements in Helsinki. *Atmos. Meas. Tech.* 13, 205–218. <https://doi.org/10.5194/amt-13-205-2020>
- Jiang, J., Zhab, Y., and Li, L., 2019: Simulation analysis of atmospheric SO₂ contributions from different regions in China. *Atmos. Pollut. Res.* 3, 913–920. <https://doi.org/10.1016/j.apr.2018.12.019>
- Koike, M., Jones, N.B., Palmer, P.I., Matsui, H., Zhao, Y., Kondo, Y., Matsumi, Y., and Tanimoto, H., 2006: Seasonal variation of carbon monoxide in northern Japan: Fourier transform IR measurements and source-labeled model calculations. *J. Geophys. Res.* 111, D15306. <https://doi.org/10.1029/2005JD006643>
- Krakovska, S.V., Palamarchuk, L.V., and Shpytal, T.M., 2019: Climatic projections of heating season in Ukraine up to the middle of the 21st century. *Geofizicheskiy Zhurnal* 6(41), 144-164. <https://doi.org/10.24028/gzh.0203-3100.v41i6.2019.190072>
- Krotkov, N.A., McLinden, C.A., Can Li, Lamsal, L.N., Celarier, E.A., Marchenko, S.V., Swartz, W.H., Bucsela, E.J., Joiner, J., Duncan, B.N., Boersma, K.F., Veefkind, P., Levelt, P.F., Fioletov, V.E., Dickerson, R.R., Hao He, Zifeng Lu, and Streets, D.G., 2016: Aura OMI observations of regional SO₂ and NO₂ pollution changes from 2005 to 2015. *Atmos. Chem. Phys.* 16, 4605–4629. <https://doi.org/10.5194/acp-16-4605-2016>
- Lamsal, L.N., Martin, R.V., Parrish, D.D., and Krotkov, N.A., 2013: Scaling Relationship for NO₂ Pollution and Urban Population Size: A Satellite Perspective. *Environ. Sci. Technol.* 47, 7855–7861. <https://doi.org/10.1021/es400744g>
- Milinevsky, G., Danylevsky, V., Bovchaliuk, V., Bovchaliuk, A., Goloub, Ph., Dubovik, O., and Kabashnikov, V., 2014: Aerosol Seasonal Variations Over Urban–Industrial Regions in Ukraine According to AERONET and POLDER Measurements. *Atmos. Meas. Tech.* 7, 1459–1474. <https://doi.org/10.5194/amt-7-1459-2014>
- Richter, A., Begoin, M., Hilboll, A., Burrows, J.P., 2011: An improved NO₂ retrieval for the GOME-2 satellite instrument. *Atmos. Meas. Tech.* 4, 1147–1159. <https://doi.org/10.5194/amt-4-1147-2011>
- Rinsland, C. P., Mahieu, E., Zander, R., Demoulin, P., Forrer, J., Buchmann, B., 2000: Free tropospheric CO, C₂H₆, and HCN above central Europe: Recent measurements from the Jungfraujoch station including the detection of elevated columns during. *J. Geophys. Res.* 105, 24235–24249. <https://doi.org/10.1029/2000JD900371>
- Savenets, M., Dvoretzka, I., and Nadochii, L. 2020: Current state of atmospheric air pollution in Ukraine based on Sentinel-5P satellite data. *Visnyk of V. N. Karazin Kharkiv National University, Series Geology. Geography. Ecology* 51, 221–233.

- Savenets, M., Nadtochii, L., and Dvovetska, I., 2018: NO₂ seasonal and interannual variability in Ukrainian industrial cities. *GeoScience Engineering*, LXIV, 4, 29–36.
<https://doi.org/10.2478/gse-2018-0019>
- Shevchenko, O., Yatsenko, Y., and Danilova, N., 2016: Osoblyvosti chasovyh zmin koncentraciy formaldehidu v atmosfernomu povitri mist Ukrainy. *Visnyk Kyivskogo Natsionalnogo Universytetu. Viiskovo-spetsialni nauky* 2, 24–29.
Шевченко, О., Яценко, Ю., Данілова, Н., 2016: Особливості часових змін концентрацій формальдегіду в атмосферному повітрі міст України. *Вісник Київського національного університету. Військово-спеціальні науки* 2, 24-29. (In Russian)
- Sinha A., 2016: Trilateral association between SO₂/NO₂ emission, inequality in energy intensity, and economic growth: A case of Indian cities. *Atmos. Pollut. Res.* 4, 647-658.
<https://doi.org/10.1016/j.apr.2016.02.010>
- SESU: State Emergency Service of Ukraine. Wildfires statistics:
<https://undicz.dsns.gov.ua/ua/STATISTIKA-POZHEZH.html>
- Yatsenko, Y., Shevchenko, O., Snizhko, S., 2018: Otsinka suchasnogo rivnia ta tendencii zabrudnennia at-mosferного povitria mist Ukrainy dioksidom azotu. *Visnyk of Taras Shevchenko National University of Kyiv: Geology* 3(82), 87–95. <https://doi.org/10.17721/1728-2713.82.11>
- Яценко, Ю., Шевченко, О., Сніжко, С. 2018: Оцінка сучасного рівня та тенденцій забруднення атмосферного повітря міст України діоксидом азоту. *Вісник Національного університету імені Тараса Шевченка: Геологія* 3(82), 87-95. (In Russian)
- Zhao, Y., Strong, K., Kondo, Y., Koike, M., Matsumi, Y., Irie, H., Rinsland, C.P., Jones, N.B., Suzuki, K., Nakajima, H., Nakane, H., and Murata, I., 2002: Spectroscopic measurements of tropospheric CO, C₂H₆, C₂H₂, and HCN, in northern Japan. *J. Geophys. Res.* 107, 4343.
<https://doi.org/10.1029/2001JD000748>
- Zheng, Z., Yang, Z., Wu, Z., and Marinello, F., 2019: Spatial Variation of NO₂ and Its Impact Factors in China: An Application of Sentinel-5P Products. *Remote Sens.* 11, 1939.
<https://doi.org/10.3390/rs11161939>

IDŐJÁRÁS

Quarterly Journal of the Hungarian Meteorological Service
Vol. 125, No. 2, April – June, 2021, pp. 291–319

A hydrological toolkit to delineate patterns of blue and green water in a regional semi-arid climate in Iran via CMIP5 models

Amirhosein Aghakhani Afshar^{1*} and Yousef Hassanzadeh^{2,3}

¹ *Department of Water Engineering
Faculty of Civil Engineering
University of Tabriz, Tabriz, Iran*

² *Department of Water Engineering
Center of Excellence in Hydroinformatics,
Faculty of Civil Engineering
University of Tabriz, Tabriz, Iran.*

³ *Farazab Co. (Consulting Engineers), PMO, Tabriz, Iran.*

**Corresponding author E-mail: a.h.aghakhani@tabrizu.ac.ir*

(Manuscript received in final form May 26, 2020)

Abstract—Water scarcity and the climate change impacts on water components will drastically alter everybody's life. The Soil and Water Assessment Tool (SWAT) has been utilized in this study in combination with Sequential Uncertainty Fitting Program (SUFI-2) to simulate precipitation (P), temperature (T), blue water (BW), green water flow (GWF), and green water storage (GWS) in Kashafrud River Basin, Iran. The outputs of two Coupled Model Intercomparison Project Phase 5 (CMIP5) models (MIROC-ESM and GFDL-ESM2G) are selected for hydrological modeling under Representative Concentration Pathways (RCPs) of 4.5 and 8.5 and for the near future (2014-2042) and far future (2043-2100) periods compared to historical period (1995-2011). The results of RCPs, in comparison with the historical period, show that P and BW are increased and in GFDL-ESM2G are better than MIROC-ESM, while T tends to increase, and MIROC-ESM is better than GFDL-ESM2G. GWF, in all future periods (except in MIROC-ESM in near future and under RCP4.5 and 8.5) and in all RCPs tend to decrease, and the results of MIROC-ESM are better than those of GFDL-ESM2G in near future and are vice versa in far future. It is anticipated that GWS continues its historical trend in the future.

Key-words: SWAT, MIROC-ESM, GFDL-ESM2G, RCPs, blue and green waters

1. Introduction

Climate change largely affects the hydrological cycle and availability of water resources (*Pachauri et al.*, 2014). Its impact is more drastic in arid and semi-arid areas, and its effect on the accessibility of water resources to human has been focused in many studies. Studies show that climate change has an adverse impact on ecosystems and causes water crisis, both in arid and semi-arid areas (*Falkenmark and Rockström*, 2006), and millions of people would be dealing with the lack of uncontaminated water all over the world (*Pereira et al.*, 2009). A comprehensive review of climate change is a necessary path for understanding and managing the limited freshwater resources in long-term. There is a dire need for climate change impact assessment in the realm of water resources to identify the changes in water usage patterns, especially in arid and semi-arid areas. Climate change is one of the main factors effecting the quantity and quality of water resources in a river basin. Climate models are developed in recent decades by scientists in order to study these effects. General Circulation Models (GCMs) are widely being applied in predicting various scenarios for the climatic change. The Intergovernmental Panel on Climate Change (IPCC) is responsible for gathering and reviewing the world wide climate models in the framework of the international climate change assessment report for policymakers and public users (*IPCC*, 1990). So far, IPCC has presented five distinct versions of GCM models including: First Assessment Report (FAR), Second Assessment Report (SAR), Third Assessment Report (TAR), Fourth Assessment Report (AR4), and Fifth Assessment Report (AR5) models. The IPCC AR5 has provided a novel approach of developing scenarios. These scenarios extend in the scope of possible radiative forcing scenarios called Representative Concentration Pathways (RCPs), whereas AR4 uses scenarios from the IPCC Special Report on Emissions Scenarios (SRES). The RCPs cover a broader extent of possibilities than the SRES marker scenarios employed in the modeling for the IPCC AR3 and AR4. Some RCPs account for mitigation and adaptation policies in opposition to SRES (see Chapter 9, *IPCC*, 2013).

The Fifth Assessment Report (AR5) emission scenarios are founded on the different specifications, including technology level, social and economic status, and future policies that can lead to greenhouse gas emission and climate change to four new different paths. Later models were developed due to the concentration of greenhouse gases by considering radiative forcing and higher model resolution (*Taylor et al.*, 2012). The Fifth Phase of the Coupled Model Intercomparison Project (CMIP5) including sixty-one climate change models, relies on the bases of new greenhouse gas concentration emission of RCP (*Moss et al.*, 2010) and has started a few years ago under the international climate change agreement for AR5. CMIP5 has supplied a necessary basis from the compilation of AR5 and coordinated to be used in AR5, and allows for simulating, comparing, and synthesizing widespread hydro-climatic outputs from various GCMs (*IPCC*, 2013; *Taylor et al.*, 2012).

Freshwater cycle is classified into two different categories by involving the hydrological process and the storage type: green water (GW) and blue water (BW). The concepts of GW and BW were initially proposed by Falkenmark in 1995 and then expanded by other researchers (*Badou et al.*, 2018; *Hoekstra*, 2017; *Veettil and Mishra*, 2016; *Zang et al.*, 2012; *Faramarzi et al.*, 2009; *Falkenmark and Rockström*, 2006). Basically, human beings use BW as an important source of water availability in daily life. BW is a summation of surface runoff (originated from rivers, lakes, etc.) and groundwater aquifer recharge and used for irrigation purposes. Globally, irrigation water includes almost 70% of total human BW consumption (about 2500 km³/year). On the other hand, 90 percent of BW consumption (about 1200 to 1800 km³/year) belongs to agricultural BW consumption that transpires via the crops or evaporates from soils, vegetation, leaves, trees, or from water bodies. It is a misconception that agricultural water consumption is largely dependent on BW withdrawals, because about 80% of global croplands are rainfed, which consume the required water from precipitation that infiltrated into the unsaturated soil or stored in the soil texture (so-called green water, GW) (*Mekonnen and Hoekstra*, 2016). Food production and global ecosystems mainly depend on GW (a significant water source for terrestrial ecosystems), and an amount of about 5000 km³/year uses these water components as the only resource that supports rainfed agriculture on a global scale (*Lathuillière et al.*, 2016; *Zang et al.*, 2012; *Falkenmark and Rockström*, 2006). GW includes green water flow (GWF), which is the actual evapotranspiration of soil, water, and plants released into the atmosphere; and green water storage (GWS), which is the water volume stored in different soil layers at the end of a time period (*Cuceloglu et al.*, 2017; *Rodrigues et al.*, 2014; *Falkenmark and Rockström*, 2006). Although, BW is essential in irrigation water, but GWF and GWS resources are more than three times as large as BW consumption, and they play an essential role in crop production as well as in the supply of ecosystem services (*Falkenmark*, 1995). Thus, paying attention to BW and GW is very important in the management of watershed basins. In the past few years, many studies in the world have concentrated on BW and GW in the field of hydrology and water resources under climate change (*Pandey et al.*, 2019; *Afshar et al.*, 2018; *Badou et al.*, 2018; *Shrestha et al.*, 2017; *Zang et al.*, 2012; *Faramarzi et al.*, 2009) and on the importance of these components in different watershed basins for strategic decision-making (*Schyms et al.*, 2019; *Veettil and Mishra*, 2016; *Zang et al.*, 2012).

Various physically-based integrated distribution models have extended for analysis and management of catchment, including: Hydrologic Simulation Program-Fortran (HSPF), Agricultural Non-Productive Source (AGNPS) model, Erosion Productivity Impact Calculator (EPIC), Hydrology Laboratory-Research Distributed Hydrologic Model (HL-RDHM), Water Erosion Prediction Project (WEPP), Chemical Runoff Erosion from Agricultural Management System (CREAMS), and Soil and Water Assessment Tools (SWAT). SWAT was

developed and employed in most studies in order to determine the effects of climate change in the quantity and spatiotemporal distribution of BW and GW, and also the impacts of human activity on agricultural yield, chemical, and stream flow in a large scale basin (Pandey *et al.*, 2019; Dadfar *et al.*, 2019; Fazeli Farsani *et al.*, 2019; Masud *et al.*, 2018; Afshar and Hassanzadeh, 2017; Veettil and Mishra, 2016; Besharat *et al.*, 2015; Faramarzi *et al.*, 2009, 2013;). The Calibration and Uncertainty Procedures (SWAT-CUP) computer program, which connects to SWAT model, is applied in order to investigate the sensitivity analysis, the model parameters, and the calibration and validation processes (Hassanzadeh *et al.*, 2019; Shivhare *et al.*, 2018; Afshar *et al.*, 2018; Uniyal *et al.*, 2015; Abbaspour *et al.*, 2007). SWAT-CUP program also contains four algorithms to perform these processes, including a Monte Carlo Markov Chain (MCMC) algorithm, Generalized Likelihood Uncertainty Estimation (GLUE), Parameter Solution (ParaSol), and Sequential Uncertainty Fitting program (SUFI-2). Among them, SUFI-2 has extensively been employed in many parts of the world to optimize the parameters of the SWAT model, and it is found to be quite efficient in large scale models in comparison with another algorithms of SWAT-CUP program (Hassanzadeh *et al.*, 2019; Shivhare *et al.*, 2018; Li *et al.*, 2017; Abbaspour *et al.*, 2007).

Most countries in the Middle East such as Iran are located in arid or semi-arid regions with low precipitation and high temperature. The climate change in Iran, like in other similar climates, is recognized as a challenging subject, and its negative impacts on water resources can also affect the environmental and socio-economic issues, and mainly the agricultural sector. The Kashafrud River Basin (KRB), in the northeast part of Iran with a wide range of climate conditions, is expected to face changes in both water quantity and quality in future time periods. On the other hand, cultivation is carried out in irrigated agricultural (28.56%) and rainfed (15.55%) forms in the majority portion of KRB (about 44.11% of the total land use). Given the strategic importance of KRB as the only water supply of northeast Iran, not much work (except for the research done by Afshar *et al.* (2017, 2018)) has been done to study the spatial and temporal changes of BW, GWF, and GWS (and even rainfall and temperature) in the basin under future climate change scenarios.

Beyond the abovementioned facts, the current study consists of the following main objectives that are considered as innovation of the article: (1) identification of sensitive parameters of the SWAT model via the Regional Sensitivity Analysis (RSA) method based on the Latin hypercube sampling (LHS) theory and the Kolmogorov-Smirnov (K-S) test, (2) survey, comparison, and discussion the spatial and temporal variations of water resources components (e.g., blue water, green water flow, and green water storage) in the KRB during a period of 106 years by using MIROC-ESM and GFDL-ESM2G models of CMIP5 under two RCPs (4.5 and 8.5). In addition, we explain the way that the water resources components have changed in the basin levels over three time periods from 1995 to 2100 (historical: 1995–2011, near future: 2014–2042, and far future: 2043–2100). The impact of

climate parameters, such as the influence of precipitation and temperature on the availability of water resources in the basin, has also been investigated, so the third main objective of this study is the investigation of hydro-climatic conditions in sub-basins that contain hydraulic structures such as dams' reservoirs (Torogh and Kardeh dams) in them by MIROC-ESM and GFDL-ESM2G models and two RCPs (4.5 and 8.5).

2. Materials and methods

2.1. Study area

The Kashafrud River Basin, KRB is located in the northeastern part of Iran with an area of 16870 square kilometers, which is the largest basin in the Khorasan Razavi Province and located between latitudes of 35° 35' to 37° 07' N and longitudes 58° 15' to 61° 13' E. The average altitude of the basin is 1846 m above the sea level, and the eastern part is geographically low, while the western part is high. The KRB has a cold and semi-arid climate with low annual rainfall and high evapotranspiration due to the topographic conditions (Afshar *et al.*, 2017). The mean annual precipitation for this basin is about 340 mm, and the highest rainfall occurs between January and May according to the recorded climate data (Afshar *et al.*, 2017). The mean annual minimum and maximum temperatures during 1992–2005 were 7.1 °C and 20.6 °C, respectively (Afshar *et al.*, 2017). Torogh and Kardeh dams lie in the south and north of Mashhad, respectively, as the most populated cities in this area, providing water for agricultural and drinking sectors (Fig. 1). The topography of KRB, and the location of gauging and meteorological stations are depicted in Fig. 1.

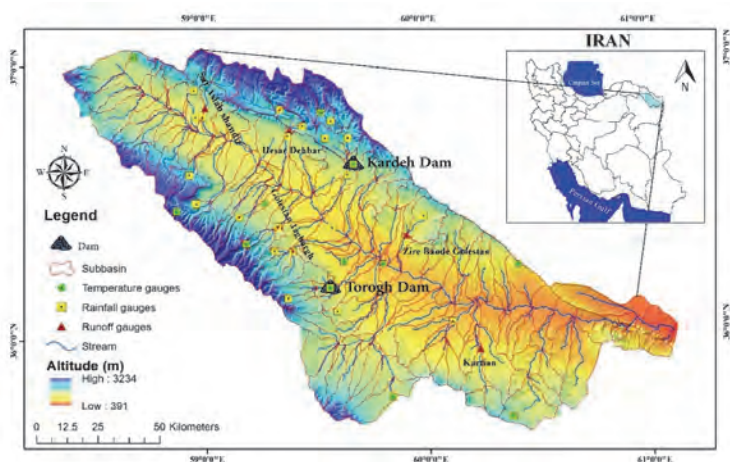


Fig. 1. DEM (digital elevation model) and the location of gauging and meteorological stations in KRB.

2.2. SWAT model, required data, and model set up

SWAT, as a continuous-term, semi-distributed, process-based model, is developed to assess alternative management strategies for short- and long-term decisions in large river basins (Arnold *et al.*, 2012) by policymakers. SWAT model has been widely applied at regional (Rahimpour *et al.*, 2020; Hassanzadeh *et al.*, 2019; Samuels *et al.*, 2018; Huang *et al.*, 2017; Rodrigues *et al.*, 2014), national (Liu *et al.*, 2017; Zhu *et al.*, 2015; Faramarzi *et al.*, 2009) and continental scales (Giles *et al.*, 2019; Faramarzi *et al.*, 2013). The basin of this model is classified into multiple sub-basins, and then the soil and topographical features are classified into hydrological response units (HRUs) according to the combination of land uses (Afshar *et al.*, 2018; Cuceloglu *et al.*, 2017; Arnold *et al.*, 2012).

The digital elevation model (DEM) for this research is extracted from topographic maps of the National Geographic Center (NGC) of Iran. The land-use map is obtained from the Indian Remote Sensing (IRS-1C) satellite images of 2002 with a spatial resolution of 23.6 meters. According to the satellite images of KRB and IRS-1C, KRB was classified into seven land-use and land-cover classes (Fig. 2a). Pasture (50.91%), generic agricultural (28.56%), and winter wheat (15.55%) lands form the majority portion of KRB and play fundamental role in the residents' economy. The studied watershed also consists of forest-evergreen (3.03%), urban (1.42%), range-brush, and water (0.5%) areas. The soil map was constructed by the Range and Watershed Department (RWD) and Agriculture Jihad Organization (AJO) of Khorasan Razavi Province (KRP), which is prepared using Landsat TM satellite with a resolution of 30 meters and classified into 19 soil types (Fig. 2b). Soil data, including rock fragment, silty sand, and clay contents, soil electrical conductivity (ECe), organic carbon content, water content, bulk density, porosity, soil hydrologic groups, and saturated hydraulic conductivity (Ks) were obtained from the soil map (which was divided into nineteen classes).

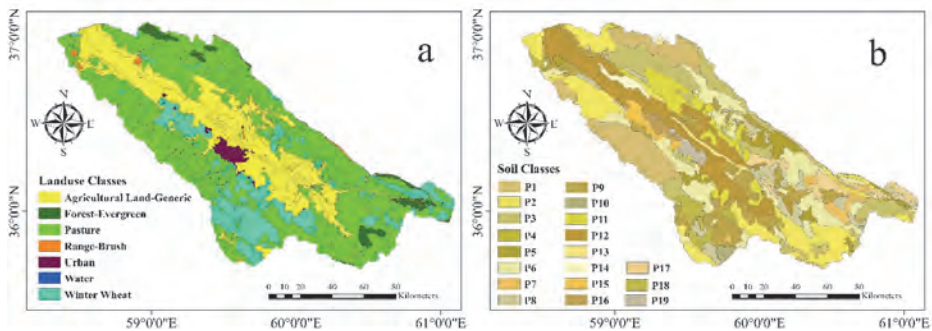


Fig. 2. Input maps to SWAT model (a. land-use and b. soil map) in KRB.

The Iran Meteorological Organization (IMO) developed the climate database of precipitation and temperature stations, located within the watershed (during 1992–2013). Monthly river discharge data of 5 stations, needed for the calibration/validation process, were received from the Iran Water Resource Management Company (IWRCM). Although, there are more flow stations located in this area, only five stations (*Table 1*) were found to be suitable in this work. The five hydrometric and rain gauge stations were established by the IWRCM in 1978, and they are already under the control of IWRCM. These stations are flood alarming stations, which are recently equipped with several instruments such as limnograph, data logger, teleferic bridge and real-time data transmitters.

Table 1. Overview of hydrometric multi-site stations in KRB

Stations	Symbol	Altitude	Latitude	Longitude	Mean monthly flow (m ³ /s)
Sar Asiab Shandiz	SARASSHA	1249 m	36.40	59.34	0.51
Zire Band Golestan	ZIRBAGOL	1164 m	36.32	59.43	0.71
Golestan Jaghargh	GOLHAGHR	1213 m	36.31	59.40	0.19
Hesar Dehbar	HESDEHB	1249 m	36.31	59.04	0.29
Kartian	KARTIAN	1232 m	36.17	59.51	0.36

The model setup in this study is carried out by the ArcSWAT 2012 interface, and the basin is divided into 217 sub-basins and subsequently divided into 635 hydrologic response units (HRUs) to evaluate the condition of GW and BW in small scales. Generally, these HRUs were determined in the model with threshold values of 20, 20, and 10 percent for land-use, soil, and slope, respectively. We concluded that small polygons with an area of less than 25 hectares could be integrated into larger polygons in the vicinity by considering the overlapping maps, based on their scale, and defining these thresholds.

2.3. Sensitivity, calibration, and uncertainty analysis

Twenty parameters were considered in the sensitivity analysis to enhance the understanding of sensitive parameters' impacts on the stream flow (*Table 2*). Predefined or prior range of SWAT parameters were mostly adopted from literature (*Zadeh et al., 2017; Nossent and Bauwens, 2012; Abbaspour et al., 2007*), which may be considered as constant ranges in the majority of cases.

Table 2. Parameters used for the sensitivity analysis

Parameters	Group process	Explanations	Prior ranges
SFTMP		Snowfall temperature	-5 to 5
SMTMP		Snow melt base temperature	-5 to 5
SMFMN	Snow	Melt factor for snow on December 21	0 to 10
SMFMX		Melt factor for snow on June 21	0 to 10
TIMP		Snow pack temperature lag factor	0.01 to 1
SOL_K		Saturated hydraulic conductivity	-0.8 to 0.8
SOL_BD	Soil water	Moist bulk density	-0.3 to 0.3
SOL_AWC		Available water capacity of the soil layer	-0.3 to 0.3
SOL_ALB		Moist soil albedo	-0.5 to 0.5
GW_DELAY		Groundwater delay time	0 to 400
GW_REVAP		Groundwater “revap” coefficient	0.02 to 0.2
GWQMN		Threshold depth of water in shallow aquifer for return flow	0 to 500
SHALLST	Groundwater	Initial depth of water in the shallow aquifer	0 to 1000
ALPHA_BF		Base-flow alpha factor	0 to 1
RCHRG_DP		Deep aquifer percolation fraction	0 to 1
REVAPMN		Threshold depth of water in shallow aquifer for “revap”	0 to 100
EPCO	Evapotranspiration	Plant uptake compensation factor	0.01 to 1
ESCO		Soil evaporation compensation factor	0.01 to 1
OV_N		Manning’s ‘n’ value for overland flow	0 to 0.08
CH_K2	Channel flow	Effective hydraulic conductivity in the main channel	0 to 150
CH_N2		Manning’s “n” value for the main channel	0 to 0.3
PCPMM		Average or mean total monthly precipitation	-0.5 to 0.5
PCPSKW	Precipitation	Skew coefficient for daily precipitation in month	-0.5 to 0.5
PCPSTD		Standard deviation for daily precipitation in month	-0.5 to 0.5
SURLAG		Surface runoff lag coefficient	1 to 24
MSK_CO1	Overland flow	Calibration coefficient used to control impact of the storage time constant for normal flow	0 to 10
MSK_CO2		Calibration coefficient used to control impact of the storage time constant for low flow	0 to 10
CN2	Runoff generation	Curve number	-0.4 to 0.4
SLSUBBSN	Geomorphology	Average slope length (m)	10 to 150

The aim of the research is to apply a comprehensive sensitivity analysis method based on the Latin hypercube sampling (LHS) theory and the Kolmogorov-Smirnov (K-S) test called generalized sensitivity analysis (GSA, also referred as regionalized sensitivity analysis, RSA) in sensitivity evaluation of SWAT model parameters. The main objective of sensitivity analysis is to understand how different components of a model (parameters) affect the outputs of the model, and its results are very effective for model calibration and model uncertainty analysis (Sobol, 2001). Additionally, sensitivity analysis also allows ranking the most important variables influencing the simulated process. One of the most widely used types of comprehensive sensitivity analysis methods is the regional sensitivity analysis (RSA) method (Freer *et al.*, 1996). The RSA method is sampled from the parametric space of model via the Latin hypercube (LH) random sampling method. Therefore, the set of different parameters is randomly generated and then the corresponding model outputs are evaluated after the execution of the model. The Latin hypercube method is in fact the same as the Monte Carlo (MC) sampling method with the difference of that sampling is done at equal distances from the logical range of each variable, which increases the accuracy of MC simulation (Mckay *et al.*, 1979). MC methods are numerical for generating random variables in such a way to maintain the properties of distribution function governing them. The set of parameters produced based on the values of their corresponding objective function (a criterion of the difference between the model output and the measured values) are arranged and divided in to two categories of good (X1) and bad (X2) parameters after being sampled from the parameter space. The cumulative distribution functions (CDFs) of the model parameters are then compared with each other via the Kolmogorov-Smirnov test:

$$KS = \max(|F1(x) - F2(x)|), \quad (1)$$

where, $F1$ and $F2$ are generalized distribution functions of the first and second parameter sets, respectively. Besides, the higher the KS in this test, the greater the probability of two distributions being different that indicates, that the corresponding parameter is more sensitive. The Nash-Sutcliffe (NS) criterion is also used as the objective function.

The SWAT model, based on monthly observed runoff at the mentioned stations, was calibrated and validated using the SUFI-2 algorithm. However, some vital details are provided below.

The SUFI-2 algorithm, as a one-at-a-time method for calibration and validation analysis in the SWAT-CUP program, provides a narrow range of measured data within 95% prediction uncertainty (95PPU) by recognizing those parameters contributing to the reduction of total uncertainty in the output data (Van Griensven *et al.*, 2006). Four indices, applied for quantifying the reliability of calibration and validation performance, are the Nash and Sutcliffe (NS) efficiency, coefficient of determination (R^2), P, and R-factor (Abbaspour *et al.*, 2007):

- The *NS* efficiency criterion, as a performance metric, demonstrates the goodness-of-fit between the simulated and observed data (*Nash and Sutcliffe, 1970*). The formula is given as follows:

$$NS = 1 - \frac{\sum_{i=1}^N (O_i - S_i)^2}{\sum_{i=1}^N (O_i - \bar{O})^2}, \quad (2)$$

where N is the number of observed data, O_i and S_i are the observed and simulated sunoff data in step i .

- The *P-factor*, indicating the observed data proportion identified by the prediction uncertainty of 95%, is frequently stated as 95PPU (*Abbaspour, 2007*). The *R-factor* corresponds to the average thickness of the 95PPU band (within the upper and lower boundaries) divided by the standard deviation of the associated measured variable (*Abbaspour, 2007*):

$$R - factor = \frac{\sum_{i=1}^N (Y_{Upper} - Y_{Lower})_i}{N \sigma_x}, \quad (3)$$

where Y_{Upper} and Y_{Lower} are the upper and lower limits of the 95PPU, σ_x is the standard deviation of the observed data, and N is the number of the observed data.

- The coefficient of determination (R^2) represents the proportion of total variance in the observed data that can be explained by the model:

$$R^2 = \left\{ \frac{\sum_{i=1}^N (O_i - \bar{O}) * (S_i - \bar{S})}{[\sum_{i=1}^N (O_i - \bar{O})^2]^{0.5} * [\sum_{i=1}^N (S_i - \bar{S})^2]^{0.5}} \right\}^2, \quad (4)$$

where N , Y_{Lower} , Y_{Upper} , and σ_x are the total number of observed data, the lower and upper limits of the 95PPU, and the standard deviation of observed data, respectively. O_i and S_i are the observed and simulated runoff data in step i , and \bar{O} and \bar{S} are the mean observed and simulated runoff data. *P-factor* and R^2 range from 0 to 100, and *R-factor* and *NS* coefficient range from 0 to ∞ and $-\infty$ to 1, respectively. When the *P-factor* and R^2 are close to 100 percent, *R-factor* is close to 0, and the *NS* coefficient is between 0.75 to 1. The best fit among simulated and observed data is obtained during calibration and uncertainty analysis.

The goodness-of-fit is calculated between the measured and simulated runoff with *NS*, R^2 , *P*, and *R* criteria in the calibration process, after each iteration (500 runs) with twenty parameters and *NS* as a likelihood function for each of the 5 runoff stations, to conduct calibration until the performance criteria were

satisfied. If these criteria are satisfied in all stations, the calibration process would be finished and parameter ranges would be applied to investigation in the validation process and to extract BW, GWF, and GWS components. Otherwise, new parameter ranges are proposed for the next iteration. The final upper and lower bounds of the parameters as well as the fitted values of parameters were obtained after one or more iterations. Time periods from 1992 to 2011 were used for calibration (2001–2011) and validation (1995–2000) processes. Also, the first three years (1992–1995) were applied to warm-up the model. The calibrated parameter ranges were used without any change with the same number of simulations as utilized for calibration in the validation process. The efficiency measures were computed during the calibration process, as well. Details of the procedures for validation, calibration, sensitivity and uncertainty analysis can be found in the study conducted by *Afshar et al.* (2018).

2.4. Climate change models and scenarios

Fourteen climate change models, among the sixty one models of CMIP5, are used frequently to simulate future climate conditions in Asia (*Afshar et al.*, 2017; *Woldemeskel et al.*, 2016; *Salzmann et al.*, 2014; *Jiang and Tian*, 2013; *Chaturvedi et al.*, 2012). Their outputs of GCMs are appropriate for simulation of climatic data at a meteorological station in a regional location using high-resolution GCMs due to the downscaling process (*Duan and Mei*, 2014). In this research, the monthly climate data (precipitation and temperature) of CMIP5 models for different time periods were extracted from the CMIP3 and CMIP5 Climate and Hydrology Projections website (<https://gdo-dcp.ucllnl.org/>). These data are downscaled using the bias-correction spatial disaggregation (BCSD) method (for more details, refer to *Afshar et al.* (2017)).

The earth system models (ESMs) are frequently applied as coupled climate models to simulate biogeochemical components. The leading institutions in the climate field also establish them. The MIROC-ESM was developed by the Japan Agency for Marine-Earth Science and Technology (JAMSTEC) in cooperation with the University of Tokyo and the National Institute for Environmental Studies (NIES) (*Nozawa et al.*, 2007). The latest version of the mentioned model has some limited functions due to the uncertainty in coupling processes, and only includes the impact of vegetation changes on dust emission and impact of deposition of dust and black carbon on snow albedo (*Watanabe et al.*, 2011). On the other hand, the Geophysical Fluid Dynamics Laboratory (GFDL) of the National Oceanic and Atmospheric Administration (NOAA) released their new ocean climate model in 2012, which is based on density layers to understand the impact of the earth's biogeochemical cycles including human activities in collaborating with the climate system (*Dunne et al.*, 2013, 2012). The GFDL also developed the Geophysical Fluid Dynamics Laboratory Earth System Model with the Generalized Ocean Layer Dynamics component (GFDL-ESM2G) model (*Dunne et al.*, 2013, 2012). The

GFDL-ESM2G model is a fully-coupled Atmosphere-Ocean General Circulation Model (AOGCM) with an interactive closed carbon cycle and does not exhibit a clear La Niña-like response. Recently, both models have been applied at different scales and locations (Samuels et al., 2018; Sylla et al., 2015). The longitude (and latitude) resolution of MIROC-ESM is about 2.8125° (and 2.796°) and in the GFDL-ESM2G model this resolution is about 2.5000° (and 2.0225°).

According to Afshar et al. (2017), MIROC-ESM and GFDL-ESM2G models were selected in this study among 14 climate models based on the evaluation criteria, i.e., the Nash-Sutcliffe (NS) efficiency coefficient, the percent of bias (PBIAS), the coefficient of determination (R^2), the ratio of the root mean square error to the standard deviation (RSR) (Table 3), and the performance rating of simulation model (Moriassi et al., 2007). Both models showed the highest agreement with observational data in KRB based on the evaluation criteria. (For more explanation about the methodology of selecting these two CMIP5 models refer to Afshar et al., 2017).

Table 3. Reported performance rating of evaluation criteria for the outputs of 14 CMIP5 models (Afshar et al., 2017)

Rating based on (Moriassi et al., 2007)	Criteria Evaluation			
	NS	PBIAS (%)	R^2	RSR
Very good (VG)	$0.75 < NS \leq 1.00$	$PBIAS \leq \pm 10.00$	$0.866 \leq R^2 < 1.00$	$0 \leq RSR \leq 0.5$
Good (G)	$0.65 < NS \leq 0.75$	$\pm 10 \leq PBIAS < \pm 15$	$0.733 \leq R^2 < 0.866$	$0.5 < RSR \leq 0.6$
Satisfactory (S)	$0.50 < NS \leq 0.65$	$\pm 15 \leq PBIAS < \pm 25$	$0.60 \leq R^2 < 0.733$	$0.6 < RSR \leq 0.7$
Unsatisfactory (US)	$NS < 0.50$	$PBIAS \geq \pm 25$	$R^2 < 0.6$	$RSR > 0.7$

Models	Criteria values			
HadGEM2-ES	0.57 (S)	-17.15 (S)	0.69 (S)	0.73 (US)
IPSL-CM5A-LR	0.71 (G)	-15.65 (S)	0.81 (G)	0.61 (S)
NorESM1-M	0.88 (VG)	-4.74 (VG)	0.92 (VG)	0.51 (G)
BCC-CSM1.1	0.62 (S)	-11.01 (G)	0.74 (G)	0.67 (S)
CCSM4	0.43 (US)	-28.15 (US)	0.52 (US)	0.79 (US)
MIROC-ESM	0.95 (VG)	-2.88 (VG)	0.97 (VG)	0.33 (VG)
CSIRO-MK3.6.0	0.51 (S)	-27.44 (US)	0.60 (S)	0.71 (US)
GFDL-ESM2M	0.66 (G)	-10.4 (G)	0.79 (G)	0.64 (S)
GFDL-ESM2G	0.92 (VG)	-2.93 (VG)	0.94 (VG)	0.37 (VG)
CESM1(CAM5)	0.55 (S)	-26.36 (US)	0.63 (S)	0.68 (S)
GFDL-CM3	0.48 (US)	-26.03 (US)	0.54 (US)	0.74 (US)
MIROC-ESM-CHEM	0.78 (VG)	-5.25 (VG)	0.71 (S)	0.66 (S)
IPSL-CM5A-MR	0.85 (VG)	-4.96 (VG)	0.85 (G)	0.46 (VG)
MIROC5	0.60 (S)	-25.75 (US)	0.71 (S)	0.68 (S)

The CMIP5 model outputs include four representative concentration pathways (RCPs) of new emission scenarios (such as RCP2.6, 4.5, 6.0, and 8.5). RCPs are based on the emission forcing level until 2100 (see Chapter 11, Sections 11.2 and 11.3, *IPCC*, 2013). The radiative forcing is the extra heat in the lower atmosphere that will be preserved by means of additional greenhouse gases.

In this study, RCP8.5 is applied as a high baseline emission scenario and the highest amount of greenhouse gas concentration by the end of the 21st century (*Van Vuuren et al.*, 2011a). The RCP8.5 radiative forcing pathway consistently rises (at a target of 8.5 W/m² in 2100), while enhancing the residual circulation furthermore and increases the level of greenhouse gases significantly (*Riahi et al.*, 2011). Consumption of oil and coal, increasing the agricultural lands, and decreasing the forest area with current trends play an essential role in providing energy, and the population of earth will reach to 12 billion until the 22 century (*Van Vuuren et al.*, 2011a). Therefore, the highest possible changes in climate will happen in this scenario.

Besides, we applied RCP4.5 as an intermediate pathway with no exceedance from the projected level of long-term radiative forcing. The emission will reach to the highest level in this scenario in the middle of the century, then decline in 30 years, then it stabilizes (*Smith and Wigley*, 2006). Renewable and nuclear powers play a greater role in this scenario, in comparison with RCP8.5 (*Van Vuuren et al.*, 2011a). The RCP6.0 is similar to RCP4.5, but is not applied in this study due to a variety of technologies and strategies employed in the greenhouse gas emissions reduction (*Hijioka et al.*, 2008).

Considering the urge for developing realistic climate change scenarios to make the planning of adaptation measures easier, we do not contribute RCP2.6 in the climate model group because it contains negative emissions of energy use in the second half of the 21st century, and one of its key assumptions is the full involvement of all countries worldwide in the short term (*Van Vuuren et al.*, 2011b). Therefore, the best selections in this research are RCP4.5 (the medium stabilization scenario) and RCP8.5 (the high emission scenario) that encompass the whole spectrum of radiative forcing arising from RCP4.5, RCP6.0, and RCP8.5.

3. Results and discussion

3.1. Sensitivity, calibration, and validation

The most sensitive parameters with their assigned rank, based on the Kolmogorov-Smirnov (K-S) test values that are illustrated in *Fig. 3*, shows that 20 parameters affect the results of runoff simulation and play an essential role in the calibration of SWAT model. Among these parameters, ESCO, GW_REVAP, SOL_AWC, and SFTMP were the most sensitive parameters for outflow. Although the RCHRG_DP, SOL_K, and SMTMP parameters seemed to be less

sensitive, as indicated by their K-S test (*Fig. 3*), these parameters have considerably contributed to increase the model calibration results for river discharges. The fitted values of parameters, as well as the final lower and upper bounds of parameters are shown after a total of 3000 runs (six iterations) in *Table 4*. Results of calibration and validation from R^2 , NS , R , and P indices are represented in *Table 5*. More than 60% of the values of runoff data at all the stations can be bracketed on average in calibration (validation) by 95PPU. NS values were greater than 0.60 (0.64) in the calibration (validation) period, and R^2 was greater than 0.63 (0.65) at all the stations. Accordingly, the calibrated model can be applied with confidence to the set of optimized parameters, and the validation period demonstrated better agreement in respect of the calibration period (*Table 5*).

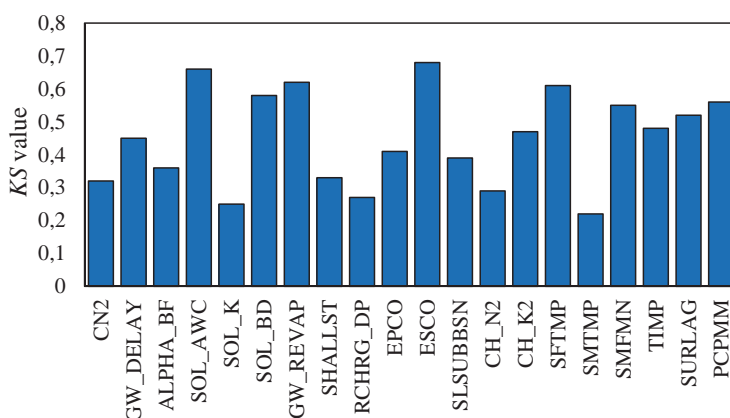


Fig. 3. Kolmogorov–Smirnov values (KS) for 20 sensitivity parameters.

Table 4. Sensitive parameters, posterior ranges, and fitted values (*Afshar et al., 2018*)

Parameters	Range of parameter		Fitted value	Parameters	Range of parameter		Fitted value
	Minimum	Maximum			Minimum	Maximum	
CN2	0.197	0.281	0.23	ESCO	0.41	0.501	0.50
GW_DELAY	132.7	159	133.55	SLSUBBSN	96.5	109.5	99.54
ALPHA_BF	0	0.08	0.042	CH_N2	0.102	0.13	0.12
SOL_AWC	0.21	0.28	0.28	CH_K2	101.5	114	101.72
SOL_K	0.15	0.32	-0.16	SFTMP	-1.0	-1.81	-1.45
SOL_BD	0.095	0.167	-0.11	SMTMP	-0.95	-1.92	-1.70
GW_REVAP	0.085	0.115	0.11	SMFMN	7.5	8.95	8.16
SHALLST	460.8	510.5	485.30	TIMP	0.50	0.70	0.51
RCHRG_DP	0.229	0.32	0.24	SURLAG	9.60	12.2	10.22
EPCO	0.29	0.41	0.29	PCPMM	-0.177	-0.325	-0.25

Table 5. Monthly runoff calibration and validation results at five stations (Afshar et al., 2018)

Stations	Calibration period				Validation period			
	R^2	NS	R -factor	P -factor	R^2	NS	R -factor	P -factor
SARASSHA	0.72	0.71	1.10	0.57	0.65	0.64	0.96	0.56
ZIRBAGOL	0.66	0.65	1.29	0.58	0.84	0.83	0.92	0.65
GOLJAGHR	0.66	0.64	0.95	0.63	0.74	0.74	0.81	0.64
HESDEHB	0.63	0.60	0.92	0.74	0.81	0.81	0.75	0.78
KARTIAN	0.68	0.63	0.90	0.66	0.87	0.87	0.58	0.67

3.2. Spatial and temporal changes of water resources components

We decided to divide future periods into two different sections, including near-term perspective (2014–2042) and far-term perspective (2043–2100) with the historical period (1992–2011) in order to have a better comparison of precipitation (P), temperature (T), blue water (BW), green water flow (GWF), and green water storage (GWS) in MIROC-ESM and GFDL-ESM2G models in this work. The concentrations of CO₂ for RCP4.5 and 8.5 are about 431 and 444 ppm in the near future and are about 533 and 811 ppm in the far future, which were used in the SWAT model.

The spatial distribution of the average values of P, T, BW, GWF, and GWS for the historical period is shown in Fig. 4 and the results show that the amounts of GWF (Fig. 4d) and BW (Fig. 4c) were higher in the upstream than those in the downstream for this time period due to the differences in precipitation patterns (Pandey et al., 2019; Fazeli Farsani et al., 2019; Zuo et al., 2015).

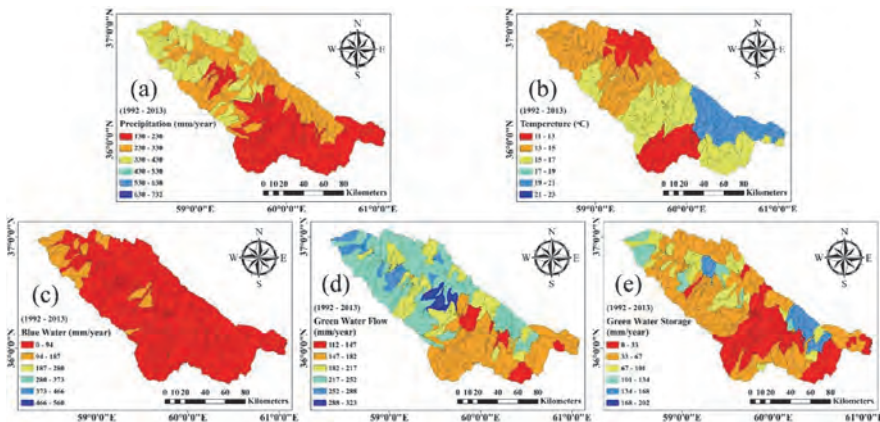


Fig. 4. Spatial pattern of mean annual water components over the KRB during the historical period.

Fig. 5 shows the simulation results of precipitation (P) in both models and scenarios. According to Fig. 5, the spatial variations of P in KRB for both RCP scenarios and periods, under the two models, show the same pattern. The highest and lowest values of this component occurred in the northern and southeastern parts of the basin, respectively. The GFDL-ESM2G model provided higher rate of P than MIROC-ESM by comparing the results of both models in the future periods. The highest value of the mentioned component was observed in the GFDL-ESM2G model in the near future period under RCP 4.5 (Fig. 5a), while the MIROC-ESM model resulted in the lowest value of mean annual P in this area in the far future period (Fig. 5f) under the same RCP.

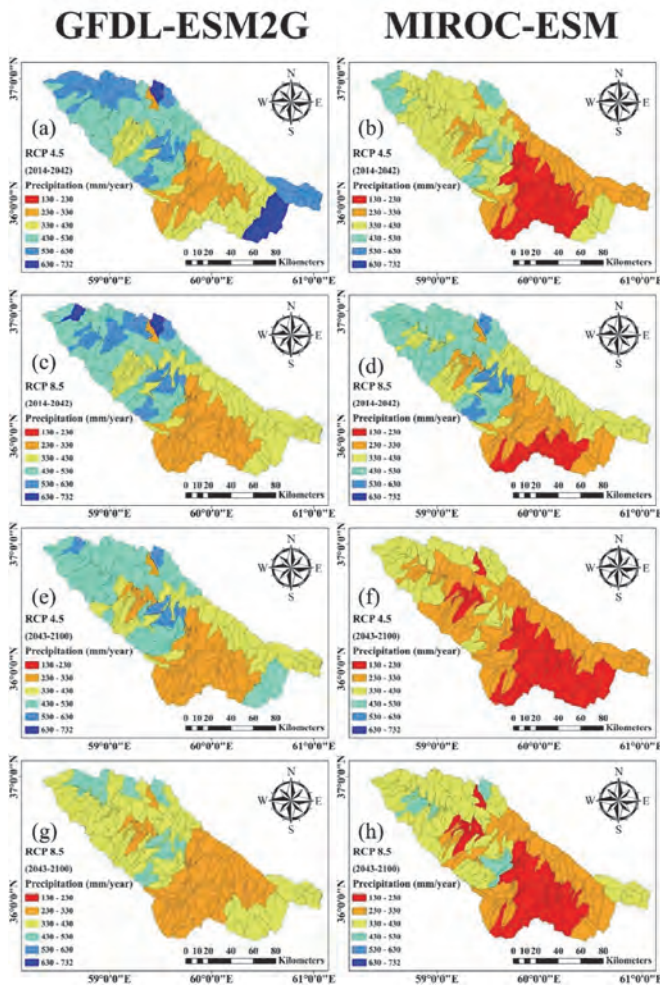


Fig. 5. Variability of precipitation, simulated under different scenarios and models for near and far future in KRB.

Fig. 6 shows the simulation results of temperature (T) in both scenarios and models. It is obvious that T will be increased by transition from near-term to far-term projection, and the spatial pattern shows that northern and high-altitude areas in the northeast and southwest would have the lowest mean annual temperature. T in RCP8.5 (Figs. 6c, d, g, and h) is higher than in RCP4.5 (Figs. 6a, b, d, and f), due to the high emission of greenhouse gases and the increase in CO₂ concentration. The MIROC-ESM model simulated higher T than the other model, and the mean annual T is estimated to increase about 3 °C in the far future period in MIROC-ESM under RCP8.5 (Fig. 6h).

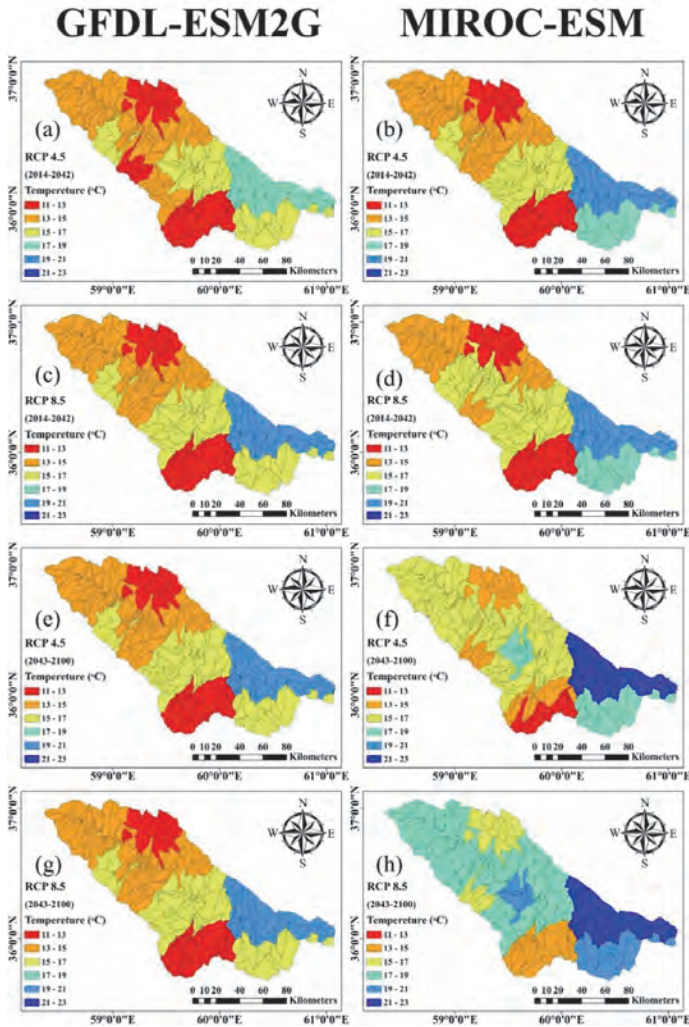


Fig. 6. Variability of temperature, simulated under different scenarios and models during the near and far future intervals in KRB.

The results of BW simulation are shown in Fig. 7 for KRB under different scenarios and models. Generally, BW decreases from northwest to southeast in the watershed. The simulations for both models and scenarios show a decreasing trend by passing from the near-term to far-term periods. The decrease of BW in the MIROC-ESM is higher than in the other model. There is no significant variation in the spatial distribution of P and BW according to the results of P (Figs. 5a-h) and the direct relationship between these two components. Furthermore, the MIROC-ESM model estimated both components higher than the GFDL-ESM2G in the future periods. The highest (lowest) mean annual BW will occur under RCP4.5 in GFDL-ESM2G in the near future (in MIROC-ESM in the far future) period (Figs. 7a, f). It should be noted that the surface runoff is a major part of BW (Pandey et al., 2019; Fazeli Farsani et al., 2019). BW is a renewable resource and potentially necessary for the agriculture sector in this area. Therefore, the climate change will have a significant impact on agricultural activities in the study area.

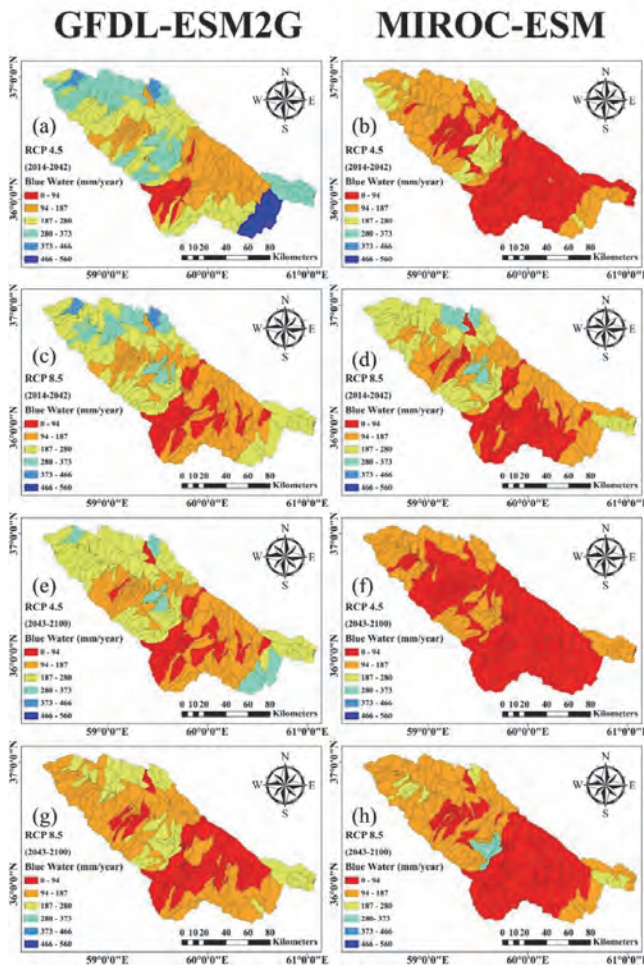


Fig. 7. Variability of BW, simulated under different scenarios and models during the near and far future intervals in KRB.

Fig. 8 shows the average values of GWF during the near and far future periods under two scenarios and models. As temperature increases in all of our calculations (Figs. 6a-h), the actual evapotranspiration expected to be increased if there is enough water. The value of GWF in the north and northwest (upstream) parts of the KRB is greater than that in the south and southeast parts of the study area. The lack of sufficient water resources in south and southeastern parts of the basin, the vegetation, and land use are the reasons of spatial distribution. The simulations show that the mean annual GWF slightly decreases under both scenarios and models by passing from the near to far period, due to the reduction of P. According to calculation results, GFDL-ESM2G simulates GWF slightly less than the other model throughout the near future. However, this parameter has been simulated higher than that by the MIROC-ESM during the far future by the mentioned model.

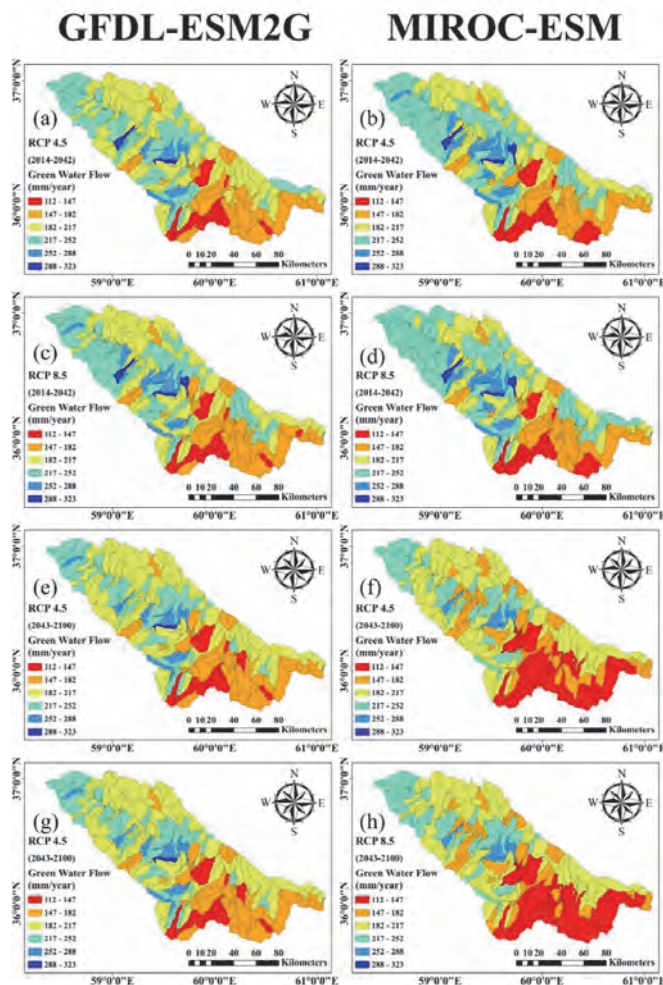


Fig. 8. Variability of GWF, simulated under different scenarios and models during the near and far future intervals in KRB.

GWS is an important water source that sustains the earth's ecosystems, especially crops, which is a vital part of human food (Schyns *et al.*, 2015). Fig. 9 shows the results of simulations for the average annual GWS in KRB by different models and under different scenarios. The highest and lowest mean annuals of this component are projected in MIROC-ESM in the near and far future periods under RCP4.5 (Figs. 9b and f). In addition, GWS by the MIROC-ESM under RCP4.5 severely reduced by transition from the near to far future (Figs. 9b and f), while it will slightly increase under RCP8.5 (Figs. 9d and h). However, GFDL-ESM2G shows a completely different trend. For instance, the value of GWS will decrease and increase by passing from the near to far future under RCP4.5 and RCP8.5, respectively. These findings are in a noble agreement with Pandey *et al.* (2019), and with Fazeli Farsani *et al.* (2019), Faramarzi *et al.* (2009), Abbaspour *et al.* (2009), that simulated P, BW, and GW values at the watershed scale.

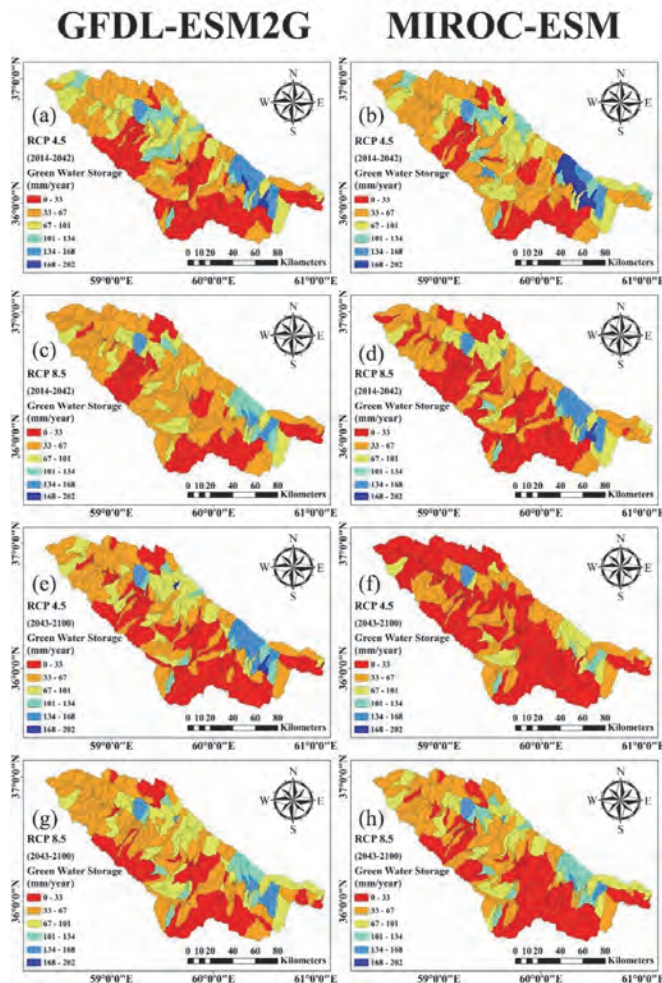


Fig. 9. Variability of GWS, simulated under different scenarios and models during the near and far future intervals in KRB.

The main reason for abrupt variations in the components of water resources (such as GWS and GWF) among the sub-basins is due to changes in the texture and soil characteristics and water holding capacity in the sub-basins (19 profiles defined in the present research) as well as to their effect on the evapotranspiration parameters in the hydrologic model (SWAT).

The mean annual water components are shown in *Table 6* in both models and RCPs and for two future periods regarding the historical period. At the same time, all the following results are compared with the historical time period. The obtained results show that BW and P increase under both scenarios, models, and future intervals compared with the historical period, and the values of BW and P, simulated by the GFDL-ESM2G model in KRB, are higher than those simulated by the other model. P and T will rise during the future intervals in both models in comparison with the historical period.

Table 6. Mean annual values of water components during historical and future intervals (mm/yr)

Hydro-climatic component	Historical period	MIROC-ESM				GFDL-ESM2G			
		Near		Far		Near		Far	
		4.5	8.5	4.5	8.5	4.5	8.5	4.5	8.5
P	250.41	319.57	372.24	269.81	297.69	442.32	402.33	390.08	348.26
T	15.30	15.72	15.83	16.70	18.32	15.44	15.61	16.60	17.67
BW	37.57	98.68	147.58	70.69	97.11	219.64	181.61	171.5	142.63
GWF	203.40	204.94	206.45	187.02	187.27	201.95	203.32	200.23	190.10
GWS	52.22	60.53	45.06	35.14	48.17	56.63	48.05	49.60	53.53

P: precipitation (mm/year), T: temperature (°C), BW: blue water (mm/year), GWF: green water flow (mm/year), GWS: green water storage (mm/year)

Calculations show that GWF only increases in the near future by the MIROC-ESM model considering the historical period. The increase of this component is about 0.75–1.49%, while it will be decreased by 8.05% under different conditions. P, BW, and GWF were higher during the near future in similar RCPs than those in the far future. However, the T component in similar RCPs shows an inverse result. GWF shows negative and positive trends by moving from the historical to near and far future, respectively. On the other hand, using two GCMs leads to differences between results. The findings of studies by *Pandey et al. (2019)*, *Xue et al. (2017)*, and *Su et al. (2016)*, also support and confirm these results. From the results of *Table 6*, it could be deduced that P will rise up by 7.2–43.4%, BW will increase by 46.9–82.9%, the T will increase by 0.9–16.5% in both RCPs and during both future periods (in comparison with historical period), while GWF will increase by 0.8–1.5% and decrease by 0.7–8.8%. Moreover, GWS tends to increase about 2.4–13.7% or decrease about 5.3–48.6% in the future intervals.

The annual P in MIROC-ESM under RCP4.5 (RCP8.5) will decrease by 15.6% (20%) in the far-term projection in comparison with that in the near-term projection. This component will decrease for both scenarios approximately by 11.8 and 13.4% in GFDL-ESM2G, respectively. However, the simulation results of the GFDL-ESM2G model in the near future under RCP4.5 (RCP8.5) is about 38.4% (8.1%) and is about 44.6% (17%) in the far future, which is more than that projected by the MIROC-ESM model. The T component under RCP4.5 and RCP8.5 in MIROC-ESM (GFDL-ESM2G) will increase approximately by 6.2 and 15.7% (7.5 and 13.2%) via moving from near-to far-term period. Furthermore, the GFDL-ESM2G under RCP4.5 (RCP8.5) simulated the annual T in the near future by 1.8% (1.4%) and in the far future by 0.6% (3.5%) less than those projected by the MIROC-ESM model, respectively. The annual BW in MIROC-ESM under RCP4.5 (RCP8.5) will decrease by 28.4% (34.2%) in the far-term projection in comparison with that in the near-term projection. This component will decrease for both scenarios approximately by 21.9 and 21.5% in GFDL-ESM2G, respectively. The amount of BW in GFDL-ESM2G in both future time periods are higher than that of MIROC-ESM. The values of GWF in the near future are higher than in the far future (between 0.9 to 8.7% under RCP4.5 and between 6.5 to 9.3% under RCP8.5) in both models and RCPs. The increasing or decreasing of GWS through the MIROC-ESM will be around 6.4% (6.6%) in comparison with GFDL-ESM2G under RCP4.5 (RCP8.5) in the near and will be around 41.1% (11.1%) in the far future intervals, respectively.

Another purpose of the study is to project the conditions of Kardeh and Torogh dam s' sub-basins for the near and far perspectives. In this study, Torogh and Kardeh dams, which are located in the southern and northern part of the KRB with different topography conditions, were selected as the two important dams located in the sub-basins 133 and 52 in order to further investigate the conditions of hydraulic structures in KRB (i.e., dams, which are the most important sources for access to water resources), respectively. The mean annual values of BW (the summation of WYLD (runoff) and DA_RCHG (aquifer discharge)), GWF (ET (evapotranspiration)), and GWS (SW (soil water content)) were extracted from the output.sub file via modeling in SWAT and SWAT-CUP software at different time periods (historical and future), and the results are presented in *Table 7*.

The GFDL-ESM2G model calculated BW higher than the MIROC-ESM in these two sub-basins in all cases in our study. The mean annual BW increases in both models and periods compared to the historical period under RCP4.5 and 8.5. The highest mean value of BW will occur in the near future, under RCP4.5, simulated by the GFDL-ESM2G in both sub-basins of the dams, while the GWS simulation shows different results. The highest mean annual GWF and GWS in both sub-basins of the dams will happen in the near future under RCP4.5, simulated by the MIROC-ESM. On the other hand, the lowest values of BW, GWF, and GWS will happen in the far future under RCP4.5 by the MIROC-ESM model. More details are represented in *Table 7*.

Table 7. Mean annual water resources components in Torogh and Kardeh dams' sub-basins (mm/year)

Dams			Torogh			Kardeh		
Water components			BW	GWF	GWS	BW	GWF	GWS
Historical period			24.9	179.7	53.9	16.9	226.2	63.2
Near future	RCP4.5	GFDL-ESM2G	285.2	161.9	46.4	267.2	198.1	164.2
		MIROC-ESM	147.5	175.0	58.1	91.2	203.6	211.1
	RCP8.5	GFDL-ESM2G	235.4	165.8	55.5	253.1	196.8	130.9
		MIROC-ESM	220.6	173.4	51.3	153.1	197.0	185.9
Far future	RCP4.5	GFDL-ESM2G	227.8	162.3	44.4	226.9	192.3	173.0
		MIROC-ESM	108.2	153.3	41.7	65.9	175.8	112.4
	RCP8.5	GFDL-ESM2G	193.5	153.9	46.0	180.4	179.2	155.8
		MIROC-ESM	170.9	158.1	44.0	117.2	178.0	161.0

4. Summary and conclusions

Potential use of MIROC-ESM and GFDL-ESM2G models under RCP4.5 and 8.5 in the historical (1995–2011), near (2014–2042), and far (2043–2100) periods to evaluate the status of water resources components (such as BW, GWF, and GWS) due to changes in climatic components (such as P and T) in KRB were simulated via the SWAT model. The SUFI-2 algorithm is applied at a monthly time step in five hydrometric stations to survey sensitivity and uncertainty analysis of the SWAT model. The main summary of the results is illustrated as follows:

- 1) Sensitivity analysis was done by the regional sensitivity analysis (RSA) method and the Kolmogorov-Smirnov (K-S) test. Results showed that 20 parameters are known as sensitive parameters. The most sensitive parameters for outflow are: ESCO, GW_REVAP, SOL_AWC, and SFTMP, while the parameters of RCHRG_DP, SOL_K, and SMTMP seemed to be less sensitive.
- 2) The model performance criteria (such as NS, R^2 , P, and R-factor) were rather satisfying for the KRB region, and the SWAT model setup is suitable for KRB to evaluate the flows of BW, GWF, and GWS.
- 3) MIROC-ESM and GFDL-ESM2G models indicated the highest compliance with the observational rainfall data in accordance with the evaluation metrics such as NS (MIROC-ESM=0.95 and GFDL-ESM2G=0.92), PBIAS

(MIROC-ESM=-2.88 and GFDL-ESM2G=-2.93), R^2 (MIROC-ESM=0.97 and GFDL-ESM2G=0.94), and RSR (MIROC-ESM=0.33 and GFDL-ESM2G=0.37), regarding the lack of information in the study area.

- 4) BW increases in all future periods and RCPs compared to the historical period due to an increase in precipitation patterns. The amount of BW in RCP8.5 was higher than in RCP4.5 in MIROC-ESM in the two future periods, but these values were vice versa in GFDL-ESM2G. BW was also higher in the near future than in the far future in both RCPs.
- 5) GWF were decreased in all future periods and RCPs in comparison with the historical period, except in the near future in both RCPs in MIROC-ESM. The amount of GWF in RCP8.5 is higher than RCP4.5 in both near and far future in MIROC-ESM, but this component was higher in RCP8.5 in GFDL-ESM2G than in RCP4.5 in the near future and conversely in the far future period. On the other hand, the values of GWF in the near future in both models and RCPs were higher than in the far future.
- 6) The GWS demonstrated positive and negative trends in different future intervals compared to the historical period. This component was more in RCP4.5 than RCP8.5 in both models and in the near future, and these results are opposite in the far future. The values of GWS in the near future were higher than in the far future in both models in RCP4.5, and these values were more in the far future than in the near future in RCP8.5.
- 7) The mean annual BW increased in both models and periods under RCP4.5 and 8.5 in the Kardeh and Torogh dam s' sub-basins, in comparison with the historical period. The highest mean annual GWS in both dam's sub-basins will happen in the near future under RCP4.5, simulated by MIROC-ESM. The lowest values of BW and GWF will occur in both sub-basins in MIROC-ESM and in the far future under RCP4.5.

Finally, it should be noted that the use of different models and scenarios identifies the range of uncertainty forecasts. The existence of differences between results of water components in the CMIP5 model limits the range of uncertainty and enlarges reliability of the projections. In addition, these models might provide decision makers and local authorities with appropriate vision for the near and long perspective condition of the region to adapt and optimize water resources in the KRB with climate change.

A complementary work to this study would be exploring the security of water resources (demand, availability, scarcity, reliability, and vulnerability) based on BW and GW trace by making an application of the mentioned models in this region and similar sub-basins with considering the changes of slope and land-use in the future time periods.

Acknowledgment: The authors would like to thank the Iran National Science Foundation (INSF) for the financial support of this study. The corresponding contract number is 96005746.

References

- Abbaspour, K.C., Faramarzi, M., Ghasemi, S.S., and Yang, H., 2009: Assessing the impact of climate change on water resources in Iran. *Water Resour. Res.* 45., 1–16. <https://doi.org/10.1029/2008WR007615>
- Abbaspour, K.C., 2007: User manual for SWAT-CUP, SWAT calibration and uncertainty analysis programs. Swiss Federal Institute of Aquatic Science and Technology, Eawag, Duebendorf, Switzerland, 93.
- Abbaspour, K.C., Yang, J., Maximov, I., Siber, R., Bogner, K., Mieleitner, J., Zobrist, J., and Srinivasan, R., 2007: Modelling hydrology and water quality in the pre-alpine/alpine Thur watershed using SWAT. *J. Hydrol.* 333, 413–430. <https://doi.org/10.1016/j.jhydrol.2006.09.014>
- Afshar, A.A., and Hassanzadeh, Y., 2017: Determination of monthly hydrological erosion severity and runoff in Torogh Dam watershed basin using SWAT and WEPP models. *Iranian J.Sci. Technol. Transact. Civil Engineer.* 41, 221–228. <https://doi.org/10.1007/s40996-017-0056-1>
- Afshar, A.A., Hasanzadeh, Y., Besalatpour, A.A., and Pourreza-Bilondi, M., 2017: Climate change forecasting in a mountainous data scarce watershed using CMIP5 models under representative concentration pathways. *Theor. Appl. Climatol.* 129, 683–699. <https://doi.org/10.1007/s00704-016-1908-5>
- Afshar, A.A., Hassanzadeh, Y., Pourreza-Bilondi, M., and Ahmadi, A., 2018: Analyzing long-term spatial variability of blue and green water footprints in a semi-arid mountainous basin with MIROC-ESM model (case study: Kashafrood River Basin, Iran). *Theor. Appl. Climatol.* 134, 885–899. <https://doi.org/10.1007/s00704-017-2309-0>
- Arnold, J.G., Moriasi, D.N., Gassman, P.W., Abbaspour, K.C., White, M.J., Srinivasan, R., Santhi, C., Harmel, R.D., Van Griensven, A., Van Liew, M.W., and Kannan, N., 2012: SWAT: Model use, calibration, and validation. *Transact. ASABE* 55, 1491–1508. <https://doi.org/10.13031/2013.42256>
- Badou, D.F., Diekkrüger, B., Kapangaziwiri, E., Mbaye, M.L., Yira, Y., Lawin, E.A., Oyerinde, G.T., and Afouda, A., 2018: Modelling blue and green water availability under climate change in the Beninese Basin of the Niger River Basin, West Africa. *Hydrol. Process.* 32, 2526–2542. <https://doi.org/10.1002/hyp.13153>
- Besharat, M., Tarinejad, R., and Ramos, H.M., 2015: The effect of water hammer on a confined air pocket towards flow energy storage system. *J. Water Supply: Res. Technol.—AQUA* 65, 116–126. <https://doi.org/10.2166/aqua.2015.081>
- Chaturvedi, R.K., Joshi, J., Jayaraman, M., Bala, G., and Ravindranath, N.H., 2012: Multi-model climate change projections for India under representative concentration pathways. *Current Sci.* 103, 791–802. <https://www.jstor.org/stable/24088836>
- Cuceloglu, G., Abbaspour, K.C., and Ozturk, I., 2017: Assessing the Water-Resources Potential of Istanbul by Using a Soil and Water Assessment Tool (SWAT) Hydrological Model. *Water*, 9(10), 1–18. <https://doi.org/10.3390/w9100814>
- Dadfar, A., Besharat, M., and Ramos, H.M., 2019: Storage ponds application for flood control, hydropower generation and water supply. *Int.l Rev. Civil Engineer.(IRECE)*, 10, 219–226. <https://doi.org/10.15866/irece.v10i4.17133>
- Duan, K., and Mei, Y., 2014: A comparison study of three statistical downscaling methods and their model-averaging ensemble for precipitation downscaling in China. *Theor. Appl. Climatol.* 116, 707–719. <https://doi.org/10.1007/s00704-013-1069-8>
- Dunne, J.P., John, J.G., Adcroft, A.J., Griffies, S. M., Hallberg, R.W., Shevliakova, E., Stouffer, R.J., Cooke, W., Dunne, K.A., Harrison, M.J., and Krasting, J.P., 2012: GFDL's ESM2 global coupled climate-carbon earth system models. Part I: Physical formulation and baseline simulation characteristics. *J. Climate*, 25, 6646–6665. <https://doi.org/10.1175/JCLI-D-11-00560.1>
- Dunne, J.P., John, J.G., Shevliakova, E., Stouffer, R.J., Krasting, J.P., Malyshev, S.L., Milly, P.C.D., Sentman, L.T., Adcroft, A.J., Cooke, W., and Dunne, K.A., 2013: GFDL's ESM2 global coupled climate-carbon earth system models. Part II: carbon system formulation and baseline simulation characteristics. *J. Climate*, 26, 2247–2267. <https://doi.org/10.1175/JCLI-D-12-00150.1>

- Falkenmark, M., 1995: Coping with water scarcity under rapid population growth. In Conference of SADC ministers, Pretoria, 23, 23-24.
- Falkenmark, M., and Rockström, J., 2006: The new blue and green water paradigm: Breaking new ground for water resources planning and management. *J. Water Res. Plan. Manage.* 132, 129–132. [https://doi.org/10.1061/\(ASCE\)0733-9496\(2006\)132:3\(129\)](https://doi.org/10.1061/(ASCE)0733-9496(2006)132:3(129))
- Faramarzi, M., Abbaspour, K.C., Schulin, R., and Yang, H., 2009: Modelling blue and green water resources availability in Iran. *Hydrol. Proc.* 23, 486–501. <https://doi.org/10.1002/hyp.7160>
- Faramarzi, M., Abbaspour, K.C., Vaghefi, S.A., Farzaneh, M.R., Zehnder, A.J., Srinivasan, R., and Yang, H., 2013: Modeling impacts of climate change on freshwater availability in Africa. *J. Hydrol* 480, 85–101. <https://doi.org/10.1016/j.jhydrol.2012.12.016>
- Fazeli Farsani, I., Farzaneh, M.R., Besalatpour, A.A., Salehi, M.H., and Faramarzi, M., 2019: Assessment of the impact of climate change on spatiotemporal variability of blue and green water resources under CMIP3 and CMIP5 models in a highly mountainous watershed. *Theor.Appl. Climatol.* 136, 169–184. <https://doi.org/10.1007/s00704-018-2474-9>
- Freer, J., Beven, K., and Ambroise, B., 1996: Bayesian estimation of uncertainty in runoff prediction and the value of data: An application of the GLUE approach. *Water Resour. Res.* 32, 2161–2173. <https://doi.org/10.1029/95WR03723>
- Giles, N.A., Babbar-Sebens, M., Srinivasan, R., Ficklin, D.L., and Barnhart, B., 2019: Optimization of linear stream temperature model parameters in the soil and water assessment tool for the continental United States. *Ecol. Engineer.* 127, 125–134. <https://doi.org/10.1016/j.ecoleng.2018.11.012>
- Hassanzadeh, Y., Afshar, A.A., Pourreza-Bilondi, M., Memarian, H., and Besalatpour, A.A., 2019: Toward a combined Bayesian frameworks to quantify parameter uncertainty in a large mountainous catchment with high spatial variability. *Environ. Monitor. Assess.* 191, 23. <https://doi.org/10.1007/s10661-018-7145-x>
- Hijioka, Y., Matsuoka, Y., Nishimoto, H., Masui, T., and Kainuma, M., 2008: Global GHG emission scenarios under GHG concentration stabilization targets. *J. Glob. Environ. Engineer.* 13, 97-108.
- Hoekstra, A.Y., 2017: Water footprint assessment: evolution of a new research field. *Water Resources Management*, 31(10), 3061–3081. <https://doi.org/10.1007/s11269-017-1618-5>
- Huang, S., Kumar, R., Flörke, M., Yang, T., Hundecha, Y., Kraft, P., Gao, C., Gelfan, A., Liersch, S., Lobanova, A, and Strauch, M., 2017: Evaluation of an ensemble of regional hydrological models in 12 large-scale river basins worldwide. *Climatic Change* 141, 381–397. <https://doi.org/10.1007/s10584-016-1841-8>
- IPCC, 1990: Climate change: the IPCC scientific assessment (1990). Cambridge University Press, London, 410p.
- IPCC, 2013: Climate change 2013: the physical science basis: Contribution of working group I to the fifth assessment report of the intergovernmental panel on climate change. (Eds. Stocker TF, Qin D, Plattner GK, Tignor M, Allen SK, Boschung J, Allen SK, Nauels A, Xia Y, Bex V, Midgley BM). Cambridge University Press, Cambridge, UK, 1535p.
- Jiang, D., and Tian, Z., 2013: East Asian monsoon change for the 21st century: Results of CMIP3 and CMIP5 models. *Chinese Sci. Bull.* 58, 1427–1435. <https://doi.org/10.1007/s11434-012-5533-0>
- Lathuillière, M.J., Coe, M.T., and Johnson, M.S., 2016: A review of green-and blue-water resources and their trade-offs for future agricultural production in the Amazon Basin: what could irrigated agriculture mean for Amazonia?. *Hydrol. Earth Syst. Sci.* 20, 2179–2194. <https://doi.org/10.5194/hess-20-2179-2016>
- Li, B., Liang, Z., He, Y., Hu, L., Zhao, W., and Acharya, K., 2017: Comparison of parameter uncertainty analysis techniques for a TOPMODEL application. *Stochast. Environ. Res. Risk Assess.* 31, 1045–1059. <https://doi.org/10.1007/s00477-016-1319-2>
- Liu, R., Wang, Q., Xu, F., Men, C., and Guo, L., 2017: Impacts of manure application on SWAT model outputs in the Xiangxi River watershed. *J. Hydrol.* 555, 479–488. <https://doi.org/10.1016/j.jhydrol.2017.10.044>
- Masud, M.B., McAllister, T., Cordeiro, M.R., and Faramarzi, M., 2018: Modeling future water footprint of barley production in Alberta, Canada: Implications for water use and yields to 2064. *Sci. Total Environ.* 616-617, 208–222. <https://doi.org/10.1016/j.scitotenv.2017.11.004>

- McKay, M.D., Beckman, R.J., and Conover, W.J., 1979: Comparison of three methods for selecting values of input variables in the analysis of output from a computer code. *Technometrics* 21, 239–245. <https://doi.org/10.1080/00401706.1979.10489755>
- Mekonnen, M.M., and Hoekstra, A.Y., 2016: Four billion people facing severe water scarcity. *Sci. Advances* 2(2), 1–6. <https://doi.org/10.1126/sciadv.1500323>
- Moriasi, D.N., Arnold, J.G., Van Liew, M.W., Bingner, R.L., Harmel, R.D., and Veith, T.L., 2007: Model evaluation guidelines for systematic quantification of accuracy in watershed simulations. *Transact. ASABE*, 50, 885–900. <https://doi.org/10.13031/2013.23153>
- Moss, R.H., Edmonds, J.A., Hibbard, K.A., Manning, M.R., Rose, S.K., Van Vuuren, D.P., Carter, T.R., Emori, S., Kainumam M., Kram, T., and Meehl, G.A., 2010: The next generation of scenarios for climate change research and assessment. *Nature* 463(7282), 747–756. <https://doi.org/10.1038/nature08823>
- Nash, J.E., and Sutcliffe, J.V., 1970: River flow forecasting through conceptual models part I—A discussion of principles. *J. Hydrol.* 10, 282–290. [https://doi.org/10.1016/0022-1694\(70\)90255-6](https://doi.org/10.1016/0022-1694(70)90255-6)
- Nossent, J., and Bauwens, W., 2012: Multi-variable sensitivity and identifiability analysis for a complex environmental model in view of integrated water quantity and water quality modeling. *Water Sci. Technology*, 65(3), 539–549. <https://doi.org/10.2166/wst.2012.884>
- Nozawa, T., Nagashima, T., Ogura, T., Yokohata, T., Okada, N., and Shiogama, H., 2007: Climate change simulations with a coupled ocean-atmosphere GCM called the model for interdisciplinary research on climate: MIROC. CGER's Supercomputer Monograph Report, 12, 73.
- Pachauri, R.K., Allen, M.R., Barros, V.R., Broome, J., Cramer, W., Christ, R., Church, J.A., Clarke, L., Dahe, Q., Dasgupta, P., Dubash, N.K., Edenhofer, O., Elgizouli, I., Field, C.B., Forster, P., Friedlingsstein, P., Fuglestvedt, J., Gomez-Echeverri, L., Hallegatte, S., Hegerl, G., Howden, M., Jiang, K., Jimenez Cisneros, B., Kattsov, V., Lee, H., Mach, K.J., Marotzke, J., Mastrandrea, M.D., Meyer, L., Minx, J., Mulugetta, Y., O'Brien, K., Oppenheimer, M., Pereira, J.J., Pichs-Madruga, R., Plattner, G.K., Pörtner, H.O., Power, S.B., Preston, B., Ravindranath, N.H., Reisinger, A., Riahi, K., Rusticucci, M., Scholes, R., Seyboth, K., Sokona, Y., Stavins, R., Stocker, T.F., Tschakert, P., van Vuuren, D., and van Ypserle, J.P., 2014: Climate Change 2014: Synthesis Report. Contribution of Working Groups I, II and III to the Fifth Assessment Report of the Intergovernmental Panel on Climate Change/R. (eds. Pachauri and Meyer), Geneva, Switzerland, IPCC, 151 p., ISBN: 978-92-9169-143-2.
- Pandey, B.K., Khare, D., Kawasaki, A., and Mishra, P.K., 2019: Climate change impact assessment on blue and green water by coupling of representative CMIP5 climate models with physical based hydrological model. *Water Res. Manage.* 33, 141–158. <https://doi.org/10.1007/s11269-018-2093-3>
- Pereira, L.S., Cordery, I., and Iacovides, I., 2009: Coping with water scarcity: Addressing the challenges. Springer Science and Business Media. <https://doi.org/10.1007/978-1-4020-9579-5>
- Rahimpour, M., Tajbakhsh, M., Memarian, H., and Aghakhani Afshar, A., 2020: Impact assessment of climate change on hydro-climatic conditions of arid and semi-arid watersheds (case study: Zoshk-Abardeh watershed, Iran). *J. Water Climate Change*. <https://doi.org/10.2166/wcc.2020.224>
- Riahi, K., Rao, S., Krey, V., Cho, C., Chirkov, V., Fischer, G., Kindermann, G., Nakicenovic, N., and Rafaj, P., 2011: RCP 8.5 – A scenario of comparatively high greenhouse gas emissions. *Climatic Change* 109, 33–57. <https://doi.org/10.1007/s10584-011-0149-y>
- Rodrigues, D.B., Gupta, H.V., and Mendiondo, E.M., 2014: A blue/green water-based accounting framework for assessment of water security. *Water Resour. Res.* 50, 7187–7205. <https://doi.org/10.1002/2013WR014274>
- Salzmann, M., Weser, H., and Cherian, R., 2014: Robust response of Asian summer monsoon to anthropogenic aerosols in CMIP5 models. *J. Geophys. Res.: Atmospheres*, 119, 11321–11337. <https://doi.org/10.1002/2014JD021783>
- Samuels, R., Hochman, A., Baharad, A., Givati, A., Levi, Y., Yosef, Y., Saaroni, H., Ziv, B., Harpaz, T., and Alpert, P., 2018: Evaluation and projection of extreme precipitation indices in the Eastern Mediterranean based on CMIP5 multi-model ensemble. *Int. J. Climatol.* 38, 2280–2297. <https://doi.org/10.1002/joc.5334>
- Schyns, J.F., Hoekstra, A.Y., Booij, M.J., Hogeboom, R.J., and Mekonnen, M.M., 2019: Limits to the world's green water resources for food, feed, fiber, timber, and bioenergy. *Proc. Nat. Acad. Sci.* 116, 4893–4898. <https://doi.org/10.1073/pnas.1817380116>

- Schyns, J.F., Hoekstra, A.Y., and Booij, M.J., 2015: Review and classification of indicators of green water availability and scarcity. *Hydrology and Earth Syst. Sci.* 19, 4581–4608. <https://doi.org/10.5194/hess-19-4581-2015>
- Shivhare, N., Dikshit, P.K.S., and Dwivedi, S.B., 2018: A Comparison of SWAT Model Calibration Techniques for Hydrological Modeling in the Ganga River Watershed. *Engineering*, 4, 643–652. <https://doi.org/10.1016/j.eng.2018.08.012>
- Shrestha, N.K., Du, X., and Wang, J., 2017: Assessing climate change impacts on fresh water resources of the Athabasca River Basin, Canada. *Sci. Total Environ.* 601, 425–440. <https://doi.org/10.1016/j.scitotenv.2017.05.013>
- Smith, S.J., and Wigley, T.M.L., 2006: Multi-gas forcing stabilization with the MiniCAM. Multi-greenhouse gas mitigation and climate policy. *Energy J.* 27, 373–391. <https://doi.org/10.5547/ISSN0195-6574-EJ-VolSI2006-NoSI3-19>
- Sobol, I.M., 2001: Global sensitivity indices for nonlinear mathematical models and their Monte Carlo estimates. *Math. Comput. Simulation*, 55, 271–280. [https://doi.org/10.1016/S0378-4754\(00\)00270-6](https://doi.org/10.1016/S0378-4754(00)00270-6)
- Su, F., Zhang, L., Ou, T., Chen, D., Yao, T., Tong, K., and Qi, Y., 2016: Hydrological response to future climate changes for the major upstream river basins in the Tibetan Plateau. *Glob. Planet. Change* 136, 82–95. <https://doi.org/10.1016/j.gloplacha.2015.10.012>
- Sylla, M.B., Giorgi, F., Pal, J.S., Gibba, P., Kebe, I., and Nikiema, M., 2015: Projected changes in the annual cycle of high-intensity precipitation events over West Africa for the late twenty-first century. *J. Climate* 28, 6475–6488. <https://doi.org/10.1175/JCLI-D-14-00854.1>
- Taylor, K.E., Stouffer, R.J., and Meehl, G.A., 2012: An overview of CMIP5 and the experiment design. *Bull. Amer. Meteorol. Soc.* 93, 485–498. <https://doi.org/10.1175/BAMS-D-11-00094.1>
- Uniyal, B., Jha, M.K., and Verma, A.K., 2015: Parameter identification and uncertainty analysis for simulating streamflow in a river basin of Eastern India. *Hydrol. Proc.*, 29, 3744–3766. <https://doi.org/10.1002/hyp.10446>
- Van Griensven, A.V., Meixner, T., Grunwald, S., Bishop, T., Diluzio, M., and Srinivasan, R., 2006: A global sensitivity analysis tool for the parameters of multi-variable catchment models. *J. Hydrology*, 324, 10–23. <https://doi.org/10.1016/j.jhydrol.2005.09.008>
- Van Vuuren, D.P., Edmonds, J., Kainuma, M., Riahi, K., Thomson, A., Hibbard, K., Hurtt, G.C., Kram, T., Krey, V., Lamarque, J.F., and Masui, T., 2011a: The representative concentration pathways: an overview. *Climatic Change*, 109, 5–31. <https://doi.org/10.1007/s10584-011-0148-z>
- Van Vuuren, D.P., Stehfest, E., den Elzen, M.G., Kram, T., van Vliet, J., Deetman, S., Isaac, M., Goldewijk, K.K., Hof, A., Beltran, A.M., and Oostenrijk, R., 2011b: RCP2. 6: exploring the possibility to keep global mean temperature increase below 2 C. *Climatic Change*, 109, 95. <https://doi.org/10.1007/s10584-011-0152-3>
- Veetil, A.V., and Mishra, A.K., 2016: Water security assessment using blue and green water footprint concepts. *J. Hydrol.* 542, 589–602. <https://doi.org/10.1016/j.jhydrol.2016.09.032>
- Watanabe, S., Hajima, T., Sudo, K., Nagashima, T., Takemura, T., Okajima, H., Nozawa, T., Kawase, H., Abe, M., Yokohata, T., and Ise, T., 2011: MIROC-ESM: model description and basic results of CMIP5-20c3m experiments. *Geosci. Model Develop. Discuss.* 4, 1063–1128. <https://doi.org/10.5194/gmdd-4-1063-2011>
- Woldemeskel, F.M., Sharma, A., Sivakumar, B., and Mehrotra, R., 2016: Quantification of precipitation and temperature uncertainties simulated by CMIP3 and CMIP5 models. *J. Geophys. Res.: Atmospheres*, 121, 3–17. <https://doi.org/10.1002/2015JD023719>
- Xue, L., Zhu, B., Yang, C., Wei, G., Meng, X., Long, A., and Yang, G., 2017: Study on the characteristics of future precipitation in response to external changes over arid and humid basins. *Sci. Rep.* 7, 1–13. <https://doi.org/10.1038/s41598-017-15511-5>
- Zadeh, F.K., Nossent, J., Sarrazin, F., Pianosi, F., van Griensven, A., Wagener, T., and Bauwens, W., 2017: Comparison of variance-based and moment-independent global sensitivity analysis approaches by application to the SWAT model. *Environ. Modell. Software* 91, 210–222. <https://doi.org/10.1016/j.envsoft.2017.02.001>

IDŐJÁRÁS

Quarterly Journal of the Hungarian Meteorological Service
Vol. 125, No. 2, April – June, 2021, pp. 321–336

Changes in extreme precipitation over the North Caucasus and the Crimean Peninsula during 1961–2018

Elena Vyshkvarkova

Institute of Natural and Technical Systems
Lenin St. 28, Sevastopol, 299011, Russian Federation
aveiro_7@mail.ru

(Manuscript received in final form June 8, 2020)

Abstract— Based on daily meteorological data, spatial and temporal distributions of extreme precipitation in 1961–2018 were examined for the North Caucasus and the Crimean Peninsula. Extreme precipitation indices recommended by the Expert Team for Climate Change Detection and Indices were calculated for 45 meteorological stations. Analysis shows that the highest values of extreme precipitation indices are on the Black Sea coast of the Caucasus, except duration of dry spell, because of the atmospheric circulation features and the complex orography of studied area. Extreme precipitation trends are spatially incoherent and mostly statistically insignificant over the studied territory. Significant upward trends on the Caspian Sea coast and Stavropol Upland and statistically significant decreasing trends in the fixed threshold-based indices and all intensity indices over the Crimean Peninsula were detected. Positive and significant correlation between precipitation indices (except consecutive dry days) and altitude was obtained.

Key-words: extreme precipitation, indices, trend, North Caucasus, Crimean Peninsula

1. Introduction

The observed trend of climate change has been particularly noticeable since the 1970s (*Hartmann et al.*, 2013). Against the backdrop of global air temperature trends, cases of extreme events associated with precipitation in the middle latitudes of the Northern Hemisphere are becoming more frequent (IPCC, 2014). Changes in extreme precipitation are of great interest around the world because of its huge potential impact on efficiency of the activities in many sectors of economy and human life (*Changnon et al.*, 2000; *Zhang et al.*, 2017).

Extremely low precipitation leads to drought, wildfires, swallowing of rivers, hindered navigation and water supply, and crop losses (Ray *et al.*, 2015). Droughts in many Russian regions and subsequent wildfires caused great disasters in 2010, 2012, and 2019. In reverse, heavy rainfall causes floods, erosion, and landslides in the mountains. A good example is the floods in Krasnodar Krai of Russia in early July 2012, when the equivalent of two–five months precipitation norm fell in short time (Meredith *et al.*, 2015, Kotlyakov *et al.*, 2013). Lack of water in reservoirs on the Crimean Peninsula, Krasnodar Krai, and other regions of Northern Caucasus in 2019 resulted from abnormally warm weather and prolonged lack of precipitation.

Unlike temperature extremes, the distribution of extreme precipitation is spatially and temporally incoherent in many regions (Frich *et al.*, 2002; Alexander *et al.*, 2006; Donat *et al.*, 2013). Precipitation extremes have been studied in many regions all over the world, e.g., in Asia (Limsakul and Singhruck, 2016; Khan *et al.*, 2019; Wang *et al.*, 2012; Liu *et al.*, 2013; Tong *et al.*, 2019; Yang *et al.*, 2019; Nie *et al.*, 2019), Europe (Klein Tank and Konnen, 2003; Mathbout *et al.*, 2018; Popov *et al.*, 2018; Bartolomeu *et al.*, 2016; Lupikasza, 2010), and North America (Brown *et al.*, 2010; Sayemuzzaman and Jha, 2014).

Previous studies in Russia have also found spatially and seasonally incoherent patterns of change in extreme precipitation. The conclusion thereof, as reflected in the Second Roshydromet Assessment Report on Climate Change and its Consequences in the Russian Federation across the European part of Russia, is that there was an increase in annual rainfall over 1936–2010 (*Second Roshydromet Assessment Report*, 2014). For the southwestern part of Siberia, no significant trends were observed over 1969–2011 in relative and absolute precipitation indices (ETCCDI indices) at the regional level (Degefie *et al.*, 2014). In the densely populated territories of Russia, the frequency of extreme winter precipitation has increased by an average of 20–40%. Rising occurrence rates of extreme summer precipitation were observed in the Central Black Earth Region of the European part of Russia over 1961–2013 (Zolotokrylin and Cherenkova, 2017). In 2000–2015, extreme winter precipitation was observed on a greater number of days per year compared to 1970–1999 in the European part and in the southern part of Russia (Titkova *et al.*, 2018). Paper Ye (2018) identifies a correlation between air temperature and wet/dry periods: higher air temperatures were consistently associated with longer dry periods and shorter wet periods in summer. Opposite tendencies in annual precipitation amount, daily precipitation maximum, and number of days with precipitation in different seasons were obtained for foothill and steppe zones in the central part of North Caucasus for 1955–2004 (Ashabokov *et al.*, 2008). Later Tashilova *et al.* (2019) found not unidirectional changes in the precipitation regime in the Caucasian region during 1961–2011.

Whether globally or specifically in Russia, there are no clear patterns of extreme precipitation. The goal, hereof, is to investigate the spatio-temporal variability of extreme precipitation over North Caucasus and the Crimean Peninsula for 1961–2018.

2. Data and methods

2.1. Study area

The studied area includes the territory of the North Caucasus and the Crimean Peninsula. The North Caucasus consists of the northern slopes of the Greater Caucasus Mountains and Ciscaucasia. The northern border of Caucasus passes through the Kuma-Manych Depression, the Sea of Azov, and the Kerch Strait. It is bounded by the Black Sea in the west. The region is located on the border of temperate and subtropical latitudes, not far from the warm Mediterranean Sea. The movement of air masses and their transformation in the territory of the North Caucasus are extremely complex and diverse. Cyclones nearly always come from the west or northwest, and as they move to the east and southeast, the air masses they bring lose moisture. The western lowlands of Ciscaucasia are more humid than their eastern part. In the west, the annual precipitation is 380–520 mm, and in the Caspian region, it is only 220–250 mm. In the foothills and the Stavropol Upland, precipitation rises to 600–650 mm. The situation is further complicated by the extreme irregularity of precipitation over time. The eastern part of the studied region (the Caspian Sea coast) shows a high precipitation concentration index (Vyshkvarkova *et al.*, 2018), which allows to detect relative contribution of rainy days to the total amount (Martin-Vide, 2004). Mountain slopes are much better moistened: in the mountains of the Western Caucasus at altitudes above 2000 m, 2500–2600 mm precipitation falls in a year; to the east, their number decreases to 900–1000 mm.

The Crimean Peninsula has a diverse climate and includes several types of it: steppe, subtropical, and mountain climate. The average annual rainfall varies from 250 mm in the steppe zone to 1000 mm and more in the Crimean Mountains.

2.2. Data source and methodology

The analysis of changes in extreme climate indices over 1961–2018 was carried out using climatological data set of daily precipitation collected at 45 meteorological stations over the North Caucasus and the Crimean Peninsula (Fig. 1). One station is located in Caspian Sea on Tyuleny Island. Data were provided by the All-Russian Research Institute of Hydrometeorological Information – World Data Centre (RIHMI-WDC) (<http://aisori-m.meteo.ru>).

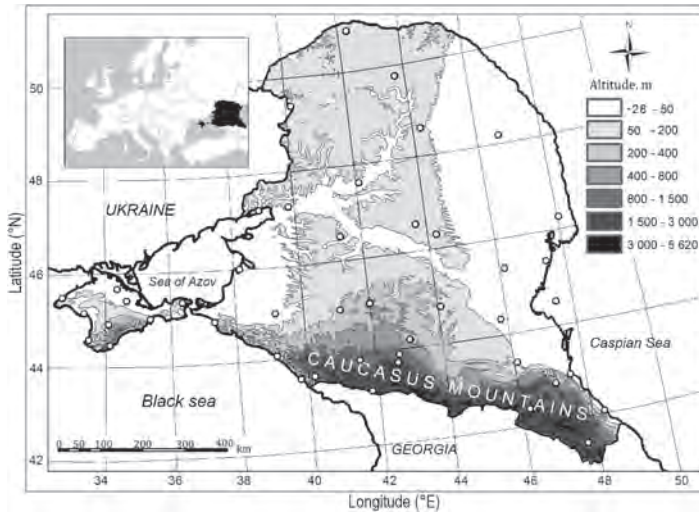


Fig. 1. Studied area and location of meteorological stations.

The input data were used for calculation of 10 extreme climate indices recommended by the CCI/CLIVAR Expert Team for Climate Change Detection and Indices (ETCCDI) for climate change assessment (<http://www.clivar.org/organization/etccdi>). Definition of extreme precipitation indices is presented in *Table 1*. Data quality control and indices calculating were done using RCLimDex software developed by *Zhang and Yang (2004)* (freely available from <http://etccdi.pacificclimate.org/software>). Extreme precipitation indices are usually divided into two groups: indices in precipitation (RX1day, RX5day, PRCPTOT, R95p, R99p) and SDII, and indices in the number of precipitation days (R10 mm, R20 mm, CDD and CWD) (*Wang et al., 2013, Liu et al., 2013*). Indices also can be divided into fixed threshold-based indices (R10 and R20), duration-based indices (CDD and CWD), absolute indices (RX1day, RX5day, PRCPTOT and SDII), and percentile-based indices (R95p and R99p) (*Alexander et al., 2006*).

The trend magnitudes were calculated using the non-parametric Sen's slope estimator (*Sen, 1968*) and the least squares method. Statistical significance of the trends was detected depending on the Mann–Kendall test with a 95% confidence level (*Mann, 1945; Hamed and Rao, 1998*). The probability density functions for each index were calculated for two subperiods: 1961–1990 and 1991–2018. The two-tailed nonparametric Kolmogorov–Smirnov test was performed to test whether the distributions changed significantly between the two specified periods and to confirm observed trends (*Dodge, 2008*). The Pearson's correlation coefficient was used to analyze the relationship between extreme precipitation indices and altitude. All tests and calculations were performed in XLSTAT Version 2014.5.03.

Table 1. Definition of extreme precipitation indices used in the study

ID	Indicator name	Definition	Units
CDD	Consecutive dry days	Maximum number of consecutive days when precipitation ≤ 1 mm	days
CWD	Consecutive wet days	Maximum number of consecutive days when precipitation ≥ 1 mm	days
PRCPTOT	Annual total wet-day precipitation	Annual total precipitation from days ≥ 1 mm	mm
R10mm	Number of heavy precipitation days	Number of days per year when precipitation ≥ 10 mm	days
R20mm	Number of very heavy precipitation days	Number of days per year when precipitation ≥ 20 mm	days
RX1day	Max 1-day precipitation amount	Annual maximum 1-day precipitation	mm
RX5day	Max 5-day precipitation amount	Annual maximum consecutive 5-day precipitation	mm
SDII	Simple daily intensity index	The ratio of annual total precipitation to the number of wet days (≥ 1 mm)	mm/day
R95p	Very wet days	Annual total precipitation from days ≥ 95 th percentile	mm
R99p	Extremely wet days	Annual total precipitation from days ≥ 99 th percentile	mm

3. Results

3.1. Spatial distribution of extreme precipitation indices

Consecutive dry days (CDD) and wet days (CWD) are duration indices based on the maximum duration of dry and wet periods. CDD values over the studied area varied from 19 to 55 days and peaked in the Caspian Sea coastal zone (Tyuleny Island). The Black Sea coast has the lowest CDD index. In the steppe part of the studied region, the index is 29–33 days. In Crimea, the index varies from 31 days on the south coast to 41 days in the north. The opposite patterns are typical for the CWD index. The lowest values are observed for the coast of the Caspian Sea (3 days), and the highest are found on the Black Sea coast of Caucasus and on high mountain stations (up to 10 days). In Crimea, the index is 5–6 days. All indices, except CDD peak on the Black Sea coast, decrease towards the north and northeast.

Spatial distribution of the PRCPTOT index values corresponds to the annual precipitation. The highest values (1600–1800 mm) are found high in the mountains. This region features the greatest total precipitation of different types (showery and compound) in Russia (*Chernokulsky et al.*, 2018 over 1966–2014). The coast of the Caspian Sea has the lowest value of the index. On the Black Sea coast of Caucasus, the annual precipitation increases southwards from 500 mm in Anapa to 1600 mm in Sochi. Over the Crimean Peninsula, PRCPTOT rises from the north (about 400 mm) to the south towards the Crimean Mountains.

Indices R10mm and R20mm are frequency indices which are based on the absolute threshold. They represent the number of days of heavy and very heavy rainfall when the daily precipitation is 10 or 20 mm higher, respectively. R10mm ranges from 4 to 63 days per year. The number of heavy precipitation days rises from NW to SE over the North Caucasus and peaks on the western slopes. In the Crimea, the index varies from 9 to 18 days.

R20mm index has an identical spatial distribution. Values range from 1 day on the Tyuleny Island to 33 days per year in the mountains. It varies from 2 to 5.5 days/year in the Crimea. The annual index RX1day (90 mm) peaks in the Kluxor Pereval (a mountain pass across the Main Caucasian Range). Large values were also observed for the Black Sea coast of the Caucasus (Sochi region) (as in *Ashabokov et al.* (2017) over 1961–2011). Eastern arid zone has low values of RX1day index (about 30 mm). The Crimean Peninsula has a fairly even distribution of the index (30–40 mm). The annual index RX5day ranges from 35 to 180 mm. It varies within 40–70 mm in the Crimea and peaks on the Black Sea coast. These indices represent the maximum single-day and consecutive five-day precipitation amounts, respectively, to provide information about the most rainy periods of the year; they are a potential flood indicator. A simple index of precipitation intensity (SDII) also peaks on the Black Sea coast of the Caucasus (14 mm/day), and it is minimal in the east of the studied region (about 5 mm/day). It varies slightly (5 – 7 mm/day) in the Crimea.

The highest value (350–450 mm) for annual total precipitation on days above the 95th percentile (R95p) is found on the Black Sea coast of the Caucasus Mountains, and the lowest value is for the north-eastern part of the studied area and the northern coast of the Caspian Sea.

The North Caucasus and the Crimean Peninsula mainly have R95p of about 30–40 mm. The eastern arid region has the lowest R99p (about 20 mm). The Black Sea coast of the Caucasus has the highest annual total precipitation on days above the 99th percentile (110–150 mm).

3.2. Trends in precipitation extremes

Table 2 shows the generalized results of trend analysis and the percentage of stations with positive and negative trends in annual precipitation indices.

Table 2. Percentage (%) of stations with positive or negative trends for extreme precipitation indices over the North Caucasus and the Crimean Peninsula 1961–2018

Index	Sig (+)	Non-sig (+)	Sig (–)	Non-sig (–)	No trend
CDD	8.89	37.78	2.22	11.11	40
CWD	13.33	–	–	–	86.67
PRCPTOT	22.22	57.78	–	20	–
R10mm	20	22.22	4.44	8.9	44.44
R20mm	11.11	4.44	11.11	4.44	68.9
RX1day	6.67	44.44	11.11	37.78	–
RX5day	8.89	55.55	6.67	28.89	–
SDII	22.22	28.9	15.55	15.55	17.78
R95p	13.3	51.2	13.3	22.2	–
R99p	8.9	4.4	–	4.4	82.3

The consecutive dry days (CDD) showed a positive (dry) trend at 47% of all stations, 9% of them exhibited a statistically significant increase. Significant upward trends were found on the Crimean Peninsula reaching 2–4 days per decade. Results showed that the negative slopes of CDD were concentrated in the Caspian lowland (Fig. 2). Most stations (about 87%) did not show any trends in wet periods (the CWD index). The stations, where CWD exhibited significant positive trends, were mainly those on the Crimean Peninsula (+0.3 to 0.6 days/decade). For annual precipitation (PRCPTOT), statistically significant increase was typically observed for the Caspian Sea coast (23 mm/decade in Astrakhan, north coast of the Caspian Sea) and in the Stavropol Upland (9 to 17 mm/decade). More than 42% of the stations showed an increase in R10mm, but only 20% of those had a statistically significant change (0.3 to 0.5 days/decade on the Caspian Sea coast and 0.9 to 1.1 in the mountains). Significant decrease was observed on the Crimean Peninsula (about –1 day/decade). About 70% of the stations did not show any change in R20mm. Stations that showed statistically significant increase were concentrated in the Stavropol Upland, where the change reached 0.5 days/decade. As for RX1day, half of the stations had a positive trend, and the rest had a negative trend, which were statistically significant for only 7% and 11% of the stations, respectively. Statistically significant decrease was mainly observed on the Crimean Peninsula (–5.5 mm/decade on the west coast of peninsula). As for RX5day, about 65% of the meteorological stations showed positive trends but only 9% showed significance, mainly those in the Stavropol Upland (4.5 mm/decade). The Stavropol Upland is the climatic border between the eastern and western part of Ciscaucasia.

The percentages of stations with positive and negative trends for SDII are 51% (22% statistically significant) and 31% (15% statistically significant), respectively. Increasing trends for intensity index were observed in the Stavropol Upland and on the coast of the Caspian Sea (0.1 mm/day per decade on average), while significant decrease was mainly found on the Crimean Peninsula (ranging from -0.1 to -0.4 mm/day per decade). For very wet days (R95p), 65% of the stations showed an upward trend, while 13% of all stations observed statistically significant changes. Most of the stations situated on the Crimean Peninsula had downward trends for R95p (ranging from -12 to -22 mm/decade). In the studied area, about 82% of meteorological stations did not show any trends in R99p.

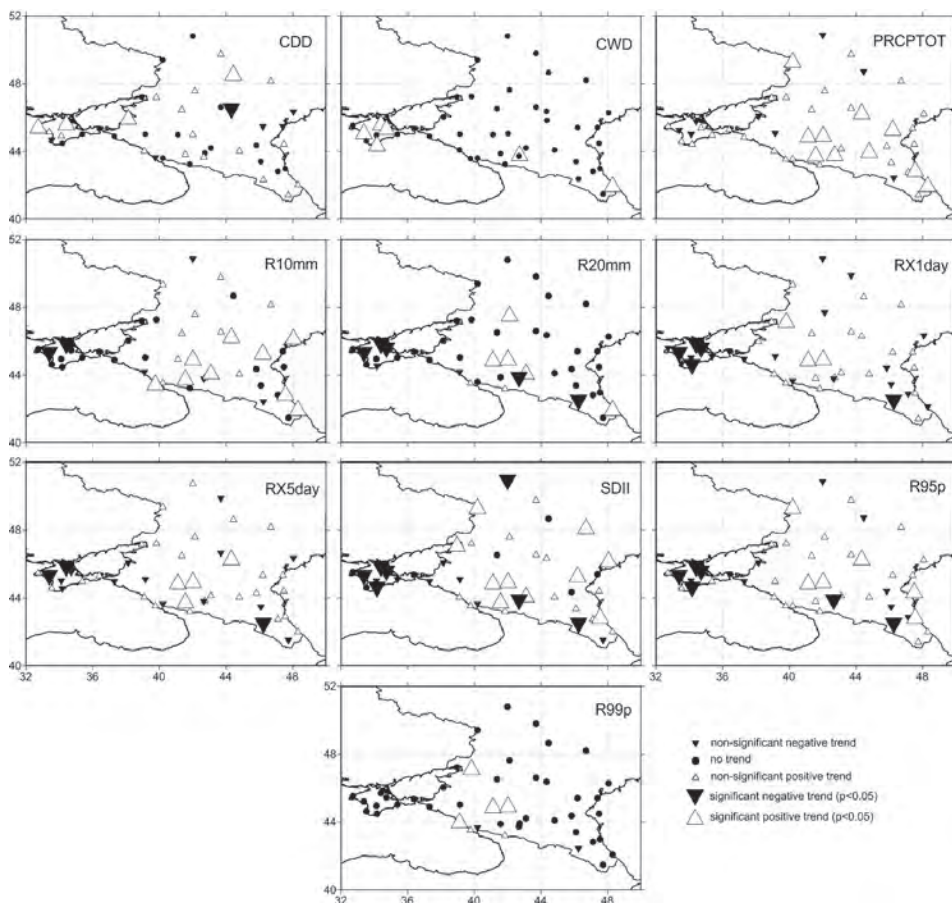


Fig. 2. Spatial distribution of trends over the North Caucasus and the Crimean Peninsula in 1961–2018.

Fig. 3 shows the regional average series of extreme precipitation indices. In 1961–2018, all extreme precipitation indices were rising in the studied region, although insignificantly. The regional trend for dry periods (CDD) over 1961–2018 was 4.5 days/decade. PRCPTOT for the studied area was rising at a rate of 5.4 mm/decade. Simple daily intensity index (SDII) showed virtually no change in the regional average (0.1 mm/day per decade). Fixed-threshold indices (R10mm, R20mm and CWD) changed only slightly (0.1 to 0.7 days/decade). Percentile-based indices (R95p and R99p) had upward trends (not significant) and reached 16 and 23 mm/decade respectively. Maximum 1-day and 5-day precipitation amount also exhibited an upward trend at 3 and 6 mm/decade, respectively.

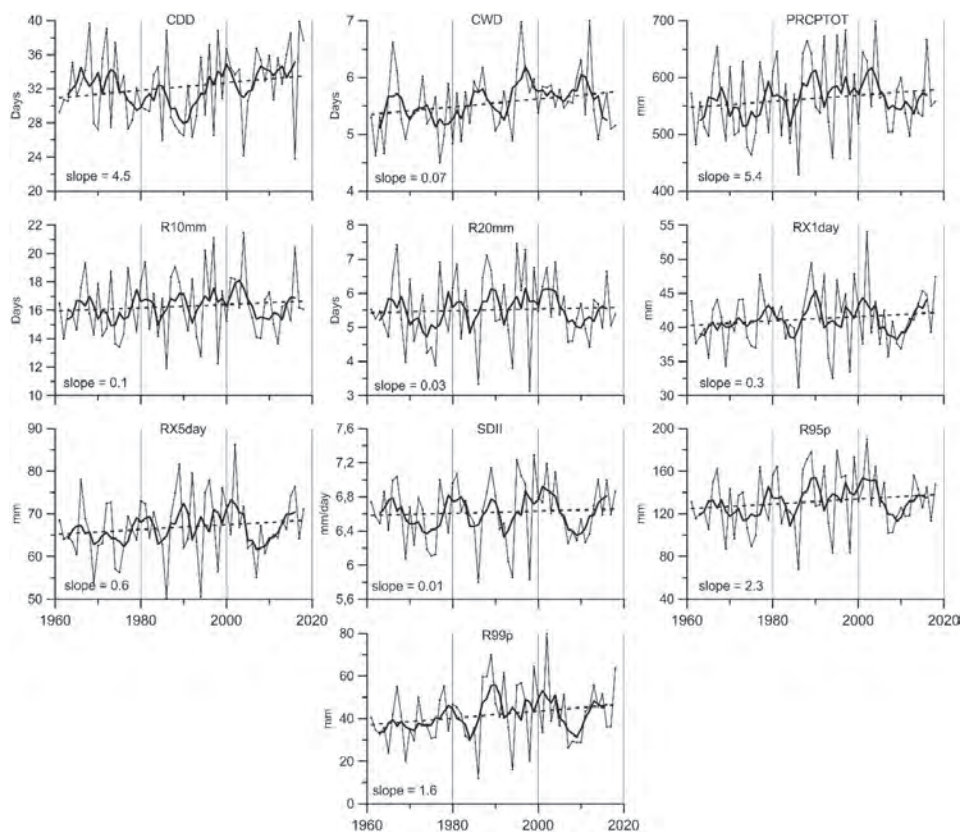


Fig. 3. The regional average series of extreme precipitation indices over 1961–2018. Thin black lines represent average values of indices, bold black lines represent the 5-year moving average, and dotted black lines show trends. The slopes of trends are represented in units per decade.

3.3. Changes in the average annual values of extreme precipitation indices

Fig. 4 shows changes in the average annual values of extreme precipitation indices for 1961–1990 and 1991–2018. In order to examine changes in extreme precipitation indices (and to confirm the observed trends), the probability density functions (PDFs) for each index were calculated for two subperiods: 1961–1990 and 1991–2018.

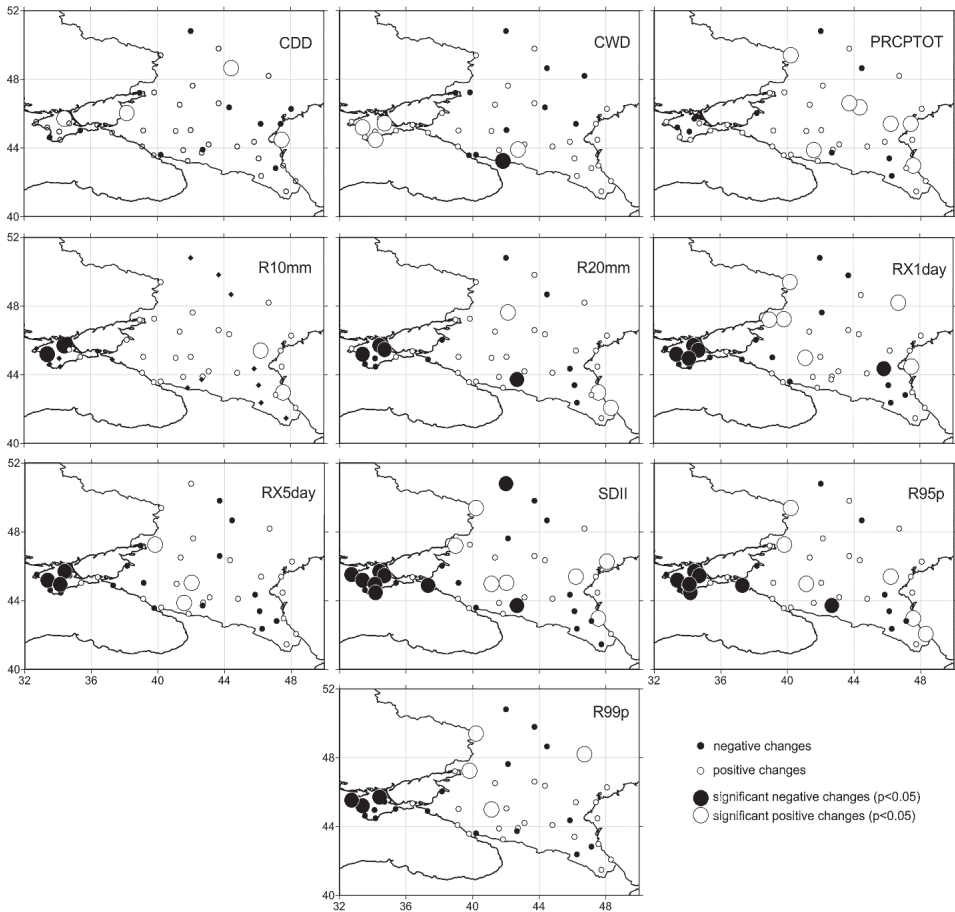


Fig. 4. Changes in average annual values of extreme precipitation indices over the North Caucasus and the Crimean Peninsula in 1991–2018 relative to 1961–1990. Negative changes mean decreasing index value in period 1991–2018 compared with period 1961–1990. Positive changes – vice versa. Significance of changes was determined by the Kolmogorov–Smirnov test on 95% confidence level.

The majority of stations did not show any statistically significant shifts (by the Kolmogorov-Smirnov test) in the index distribution between the two subperiods. The duration of dry and wet periods (CDD and CWD) as well as PRCPTOT showed positive changes in the latter period for the studied region (73–80%). PRCPTOT index exhibited statistically significant increase for the Caspian Sea coast in the latter period ($p < 0.05$).

Fixed threshold-based indices (R10mm and R20mm) and all intensity indices (RX1day, RX5day, SDII, R95p, and R99p) shifted their distributions towards smaller values for the Crimean Peninsula in the latter period compared to the reference period (statistically significant at $p < 0.05$). Number of days with precipitation above 10 and 20 mm were observed in 1991–2018 for Ciscaucasia with single significant values for the Caspian Sea coast.

3.4. Correlation between extreme precipitation indices and altitude

As it was mentioned above, the region has complex orography. *Table 3* shows the Pearson correlation coefficients (r) for extreme precipitation indices and altitude. Except for CDD, extreme precipitation indices have positive correlations with altitude, and they all are statistically significant at 95% confidence level.

Table 3. Correlation coefficients between extreme precipitation indices and altitude in 1961–2018

	CDD	CWD	PRCPTOT	R10 mm	R20 mm	RX1day	RX5day	SDII	R95p	R99p
Altitude	-0.41	0.51	0.43	0.43	0.35	0.32	0.39	0.31	0.43	0.44

The North Caucasus can be divided into several zones by the nature of its landscape: plains (0–500 m a.s.l.), foothills (500–1,000 m a.s.l.), mountains (>1,000 m a.s.l.), and high-mountain (>2,000 m a.s.l.) (*Tashilova et al.*, 2019). In addition, there are areas below sea level (the Caspian Lowland) were allocated. All Crimean stations are located in the plains (below 500 m). *Table 4* shows the average values of extreme precipitation indices by the altitudinal ranges.

As it is shown in *Table 4*, all indices (except CDD) display increase-decrease-increase tendency as the altitude increases. CDD demonstrates an opposite distribution. Decrease in indices (except CDD) is typical for the mountain stations (1000–2000 m). This range is represented by one station (Akhty), located in the southeast of the studied region. Despite its altitude, the climate of this region is temperate continental with an annual precipitation of about 400 mm. The heterogeneity in the altitudinal changes of extreme

precipitation index is made by the region of the Black Sea coast of the Caucasus, which is characterized by high average annual precipitation (about 1500 mm).

Table 4. Changes of extreme precipitation indices in altitudinal ranges

Altitudinal ranges (m)	CDD (days)	CWD (days)	PRCPTOT (mm)	R10 mm (days)	R20 mm (days)	RX1day (mm)	RX5day (mm)	SDII (mm/day)	R95p (mm)	R99p (mm)
-24 – 0	43.8	3.9	242.9	5.8	1.5	31.7	44.1	5.1	64.6	23.5
0–500	32.1	5.4	515.2	14.5	4.5	40.0	62.9	6.4	121.1	38.8
500–1000	24.7	7.5	1102.7	35.4	15.3	55.7	107.4	9.3	237.2	65.9
1000–2000	35.3	4.4	376.3	10.7	2.4	31.7	46.5	5.9	79.9	24.1
>2000	23.4	8.0	1131.0	35.2	14.3	60.2	114.2	8.9	266.7	86.2

4. Discussion and conclusions

This paper dwells upon the spatial and temporal distribution of climate extremes indices for the North Caucasus and the Crimean Peninsula. The analysis is based on the climate data for 1961–2018 from 45 meteorological stations. Climate extremes indices recommended by the World Meteorological Organization (CCL/CLIVAR/JCOMM) and the Expert Team on Climate Change Detection and Indices (ETCCDI) were used. The use of these indices enables comparison of analyses carried out in any regions and combining them in a global picture (*Zhang et al.*, 2011).

Analysis shows that all indices (except CDD) peak for the Black Sea coast of Caucasus, while the Caspian Sea coast and the Caspian Lowland have the lowest values, which is due to the features of atmospheric circulation over this region and to the complex orography. The greatest amount of precipitation is associated with westerly winds that carry moisture from the Atlantic. Their humidity is then subject to the interference from the slopes of the mountains and hills facing west, and in the east, the climate becomes drier and more continental (*Vyshkvarkova et al.*, 2018).

Extreme precipitation trends are spatially incoherent and mostly statistically insignificant in the studied territory. Statistically significant downward trends in the fixed threshold-based indices and all intensity indices were detected for the Crimean Peninsula. At the same time, the Stavropol Upland had statistically significant upward trends in these indices as well as in PRCPTOT. Both dry and wet periods have been growing longer simultaneously on the Crimean Peninsula.

A similar trend was observed for some regions of the central and southern part of European Russia in 1950–2009 (Zolina *et al.*, 2013). Statistically significant downward changes in the average annual extreme precipitation indices (except the duration of dry and wet periods and the precipitation amount) were detected for the Crimean Peninsula. Precipitation indices (except consecutive dry days) and altitude were found to correlate positively and significantly.

Neither Russia nor the Caucasus show clear signs in the changes of extreme precipitation regime. The results obtained in the article are consistent with the regional changes in extreme precipitation observed in the southern part of European Russia. Aleshina *et al.* (2018) found significant trends in precipitation intensity and total monthly precipitation for no more than two months a year on the Black Sea coast over 1984–2014. Extreme precipitation growth (R95tot index) of up to 3% per decade was observed for the southern part of European Russia in 1950–2000 (Zolina *et al.*, 2009). Bulygina *et al.* (2007) did not identify significant changes in days with extremely large daily precipitation when comparing 1951–2006 records to 1977–2006 records for Southern Russia.

According to the Second Roshydromet Assessment Report on Climate Change and its Consequences in the Russian Federation (2014) in winter, throughout the 21st century for all scenarios, there is a steady positive trend in precipitation all over Russia. Summer precipitation in the southern regions is projected to drop by up to 25% compared to the late 20th century. Maximum five-day precipitation in a year will increase by the mid-21st century; by the end of the current century, they will rise by up to 10% against the baseline. In the southern regions (including the Caucasus Mountains), the significant relative increase in the precipitation intensity maximum is expected by the middle of the 21st century according to the CMIP5 ensemble projections (Khlebnikova *et al.*, 2019). At the same time, the frequency of extreme precipitation will decrease in the southern parts of Russia by the end of the 21st century according to results obtained by Aleshina *et al.* (2019). Apparently, there is no clear signal of changes in extreme precipitation in the future

Redistribution of precipitation throughout the year, observed changes in precipitation regime, and possible changes in the intensity and frequency of extreme precipitation events in the future are becoming one of the main threats facing the region. The studied region has had to address water shortages in recent years (poor filling of reservoirs in the Crimea and Krasnodar Krai). This provides a more detailed picture of the spatially coherent trends in precipitation extremes over the territory of the North Caucasus and the Crimean Peninsula. It also calls for further research of different periods of the year (not only seasons), for example, for the vegetation periods of different crops, because Ciscaucasia is an agricultural region. Due to its complex orography, part of the studied area is flood-prone, while droughts and related problems (crop loss, reservoir underflow, etc.) are possible in other parts.

Acknowledgment: The author would like to thank Evgeniy Rybalko for his technical assistance and is grateful to the editor and anonymous reviewer, for their helpful comments on the manuscript.

Funding: The study was supported by state assignment of Institute of Natural and Technical Systems (Project Reg. No. AAAA-A19-119031490078-9). Analysis of precipitation in Sevastopol region was funded by RFBR and Sevastopol, project number 20-45-920008.

References

- Aleshina, M.A., Toropov, P.A., and Semenov, V.A., 2018: Temperature and humidity regime changes on the Black Sea coast in 1982–2014. *Rus. Meteor. Hydrol.* 4, 41–53.
<https://doi.org/10.3103/S1068373918040040>
- Aleshina, M.A., Cherenkova, E.A., Semenov, V.A., Bokuchava, D.D., Matveeva, T.A., and Turkov, D.V., 2019: Observed and expected changes in extreme precipitation frequency in Russia in the 20th–21st centuries. *Proc. SPIE* 11208. <https://doi.org/10.1117/12.2540921>
- Alexander, L., Zhang, X., Peterson, T., Caesar, J., Gleason, B., Klein Tank, A., Haylock, M., Collins, D., Trewin, B., Rahimzadeh, F., Tagipour, A., Ambenje, P., Rupa Kumar, K., Revadekar, J., Griffiths, G., Vincent, L., Stephenson, D., Burn, J., Aguilar, E., Brunet, M., Taylor, M., New, M., Zhai, P., Rusticucci, M., and Vazquez Aguirre, J., 2006: Global observed changes in daily climate extremes of temperature and precipitation. *J. Geoph. Res. Atmos.* 111, D05109. <https://doi.org/10.1029/2005JD006290>
- Ashabokov, B.A., Bishchokov, R.M., and Derkach, D.V., 2008: Study of changes in the regime of atmospheric precipitation in the Central Northern Caucasus. *Russ. Meteor. Hydrol.* 33, 125–129. <https://doi.org/10.3103/S1068373908020106>
- Ashabokov, B.A., Tashilova, A.A., Kesheva, L.A., and Taubekova, Z.A., 2017: Trends in precipitation parameters in the climate zones of Southern Russia (1961–2011). *Rus. Meteor. Hydrol.* 42, 150–158. <https://doi.org/10.3103/S1068373917030025>
- Bartolomeu, S., Carvalho, M.J., Marta-Almeida, M., Melo-Gonçalves, P., and Rocha, A., 2016: Recent trends of extreme precipitation indices in the Iberian Peninsula using observations and WRF model results. *Phys.chemistry Earth. Parts A/B/C* 94, 10–21.
<https://doi.org/10.1016/j.pce.2016.06.005>
- Brown, P.J., Bradley, R.S., and Keimig, F.T., 2010: Changes in extreme climate indices for the Northeastern United States, 1870–2005. *J. Climate* 23, 6555–6572.
<https://doi.org/10.1175/2010JCLI3363.1>
- Bulygina, O.N., Razuvaev, V.N., Korshunova, N.N., and Groisman, P.Ya., 2007: Climate variations and changes in extreme climate events in Russia. *Environ. Res. Lett.* 2, 045020.
<https://doi.org/10.1088/1748-9326/2/4/045020>
- Changnon, S.A., Pielke Jr., R.A., Changnon, D., Sylves, R.T., and Pulwarty, R., 2000: Human factors explain the increased losses from weather and climate extremes. *Bull. Am. Meteorol. Soc.* 81, 437–442. [https://doi.org/10.1175/1520-0477\(2000\)081<0437:HFETIL>2.3.CO;2](https://doi.org/10.1175/1520-0477(2000)081<0437:HFETIL>2.3.CO;2)
- Chernokulsky, A.V., Kozlov, F.A., Zolina, O.G., Bulygina, O.N., and Semenov, V.A., 2018: Climatology of precipitation of different genesis in Northern Eurasia. *Rus. Meteor. Hydrol.* 43, 425–435.
<https://doi.org/10.3103/S1068373918070014>
- Degefie, D.T., Fleischer, E., Klemm, O., Soromotina, O.V., Tolstikov, A.V., and Abramov, N.V., 2014: Climate extremes in South Western Siberia: past and future. *Stoch. Environ. Res. Risk Assess.* 28, 2161–2173. <https://doi.org/10.1007/s00477-014-0872-9>
- Dodge, Y., 2008. *The Concise Encyclopedia of Statistics*. Springer Science + Business Media, LLC.
- Donat, M.G., Alexander, L.V., Yang, H., Durre, I., Vose, R., Dunn, R.J.H., Willett, K.M., Aguilar, E., Brunet, M., Caesar, J., Hewitson, B., Jack, C., Klein Tank, A.M.G., Kruger, A.C., Marengo, J., Peterson, T.C., Renom, M., Oria Rojas, C., Rusticucci, M., Salinger, J., Elrayah, A.S., Sekele, S.S., Srivastava, A.K., Trewin, B., Villarroya, C., Vincent, L.A., Zhai, P., Zhang, X., and Kitching, S., 2013: Updated analyses of temperature and precipitation extreme indices since the beginning of the twentieth century: the HadEX2 dataset. *J. Geophys. Res. Atmos.* 118, 1–16. <https://doi.org/10.1002/jgrd.50150>

- Frich, P., Alexander, L.V., Della-Marta, P.M., Gleason, B., Haylock, M., Tank, A.K., and Peterson, T., 2002: Observed coherent changes in climatic extremes during the second half of the twentieth century. *Clim. Res.* 19, 193–212. <https://doi.org/10.3354/cr019193>
- Hamed, K. and Rao, A., 1998: A modified Mann Kendall trend test for autocorrelated data. *J. Hydrol.* 204, 182–196. [https://doi.org/10.1016/S0022-1694\(97\)00125-X](https://doi.org/10.1016/S0022-1694(97)00125-X)
- Hartmann, D.L., Klein Tank, A.M.G., Rusticucci, M., Alexander, L.V., Brönnimann, S., Charabi, Y., Dentener, F.J., Dlugokencky, E.J., Easterling, D.R., Kaplan, A., Soden, B.J., Thorne, P.W., Wild, M., and Zhai, P.M., 2013. Observations: atmosphere and surface. In: Stocker, T.F., Qin, D., Plattner, G.-K., Tignor, M., Allen, S.K., Boschung, J., Nauels, A., Xia, Y., Bex, V., and Midgley, P.M. (Eds.), *Climate Change 2013: The Physical Science Basis. Contribution of Working Group I to the Fifth Assessment Report of the Intergovernmental Panel on Climate Change*. Cambridge University Press, Cambridge, United Kingdom and New York, NY, USA. <https://doi.org/10.1017/CBO9781107415324.008>
- IPCC, 2014: *Climate change 2014: synthesis report. Contribution of Working Groups I, II and III to the Fifth Assessment Report of the Intergovernmental Panel on Climate Change* (Eds. Core Writing Team, Pachauri, R.K. and Meyer, L.A.) IPCC, Geneva.
- Khan, M.J.U., Islam, A.K.M.S., Das, M.K., Mohammed, K., Bala, S.K., and Islam, G.M.T., 2019: Observed trends in climate extremes over Bangladesh from 1981 to 2010. *Clim. Res.* 77, 45–61. <https://doi.org/10.3354/cr01539>
- Khlebnikova, E.I., Rudakova, Yu.L., and Shkolnik, I.M., 2019: Changes in precipitation regime over the territory of Russia: data of regional climate modeling and observations. *Russ. Meteor. Hydrol.* 44, 431–439. <https://doi.org/10.3103/S106837391907001X>
- Klein Tank, A.M.G., and Konnen, G.P., 2003. Trends in indices of daily temperature and precipitation extremes in Europe, 1946–1999. *J. Clim.* 16, 3665–3680. [https://doi.org/10.1175/1520-0442\(2003\)016<3665:TIIODT>2.0.CO;2](https://doi.org/10.1175/1520-0442(2003)016<3665:TIIODT>2.0.CO;2)
- Kotlyakov, V.M., Desinov, L.V., Dolgov, S.V., Koronkevich, N.I., Likhacheva, E.A., Makkaveev, A.N., Medvedev, A.A., and Rudakov, V.A., 2013: Flooding of July 6–7, 2012, in the town of Krymsk. *Regional Research of Russia* 3, 32–39. <https://doi.org/10.1134/S2079970513010061>
- Limsakul, A. and Singhruck, P., 2016. Long-term trends and variability of total and extreme precipitation in Thailand. *Atmos. Res.* 169, 301–317. <https://doi.org/10.1016/j.atmosres.2015.10.015>
- Liu, W., Zhang, M., Wang, S., Wang, B., Li, F., and Che, Y., 2013: Changes in precipitation extremes over Shaanxi Province, northwestern China, during 1960–2011. *Quat. Int.* 313–314, 118–129. <https://doi.org/10.1016/j.quaint.2013.06.033>
- Lupikasza, E., 2010: Spatial and temporal variability of extreme precipitation in Poland in the period 1951–2006. *Int. J. Climatol.* 30, 991–1007. <https://doi.org/10.1002/joc.1950>
- Mann, H.B., 1945: Nonparametric tests against trend. *Econometrica* 13, 245–259. <https://doi.org/10.2307/1907187>
- Mathbout, S., Lopez-Bustins, J.A., Roye, D., Martin-Vide, J., Bech, J., and Rodrigo, F.S., 2018: Observed changes in daily precipitation extremes at annual timescale over the Eastern Mediterranean during 1961–2012. *Pure Appl. Geophys.* 175, 3875–3890. <https://doi.org/10.1007/s00024-017-1695-7>
- Martin-Vide, J., 2004: Spatial distribution of a daily precipitation concentration index in Peninsular Spain. *Int. J. Climatol.* 24, 959–971. <https://doi.org/10.1002/joc.1030>
- Meredith, E.P., Semenov, V.A., Maraun, D., Park, W., and Chernokulsky, A.V., 2015. Crucial role of Black Sea warming in amplifying the 2012 Krymsk precipitation extreme. *Na. Geosci.* 8, 615–619. <https://doi.org/10.1038/ngeo2483>
- Nie, H., Qin, T., Yang, H., Chen, J., He, S., Lv, Z., and Shen, Z., 2019: Trend analysis of temperature and precipitation extremes during winter wheat growth period in the major winter wheat planting area of China. *Atmosphere* 10, 240. <https://doi.org/10.3390/atmos10050240>
- Popov, T., Gnjata, S., and Trbić, G., 2018: Analysis of extreme precipitation over the Peripannonian region of Bosnia Hercegovina. *Időjárás* 122, 433–452. <https://doi.org/10.28974/idojaras.2018.4.5>
- Ray, D., Gerber, J., MacDonald, G., and West, P., 2015: Climate variation explains a third of global crop yield variability. *Nat Commun.* 6, 5989. <https://doi.org/10.1038/ncomms6989>

- Sayemuzzaman, M. and Jha, M.K., 2014: Seasonal and annual precipitation time series trend analysis in North Carolina, United States. *Atmos. Res.* 137, 183–194. <https://doi.org/10.1016/j.atmosres.2013.10.012>
- Second Roshydromet Assessment Report on Climate Change and its Consequences in the Russian Federation. General summary, 2014: Moscow, Roshydromet.
- Sen, P.K., 1968: Estimates of the regression coefficient based on Kendall's tau. *J. Am. Stat. Assoc.* 63, 1379–1389. <https://doi.org/10.1080/01621459.1968.10480934>
- Tashilova, A.A., Ashabokov, B.A., Kesheva, L.A., and Teunova, N.V., 2019: Analysis of climate change in the Caucasus region: end of the 20th–beginning of the 21st century. *Climate* 7, 11. <https://doi.org/10.3390/cli7010011>
- Titkova, T.B., Cherenkova, E.A., and Semenov, V.A., 2018: Regional features of changes in winter extreme temperatures and precipitation in Russia in 1970–2015. *Ice and Snow* 58, 486–497. (In Russian). <https://doi.org/10.15356/2076-6734-2018-4-486-497>
- Tong, S., Li, X., Zhang, J., Bao, Y., Bao, Y., Na, L., and Si, A., 2019: Spatial and temporal variability in extreme temperature and precipitation events in Inner Mongolia (China) during 1960–2017. *Sci. Tot. Environ.* 649, 75–89. <https://doi.org/10.1016/j.scitotenv.2018.08.262>
- Vyshkvarkova, E., Voskresenskaya, E., and Martin-Vide, J., 2018: Spatial distribution of the daily precipitation concentration index in Southern Russia. *Atmos. Res.* 203, 36–43. <https://doi.org/10.1016/j.atmosres.2017.12.003>
- Wang, B.L., Zhang, M.J., Wei, J.L., Wang, S.J., Li, S.S., Ma, Q., Li, X.F., and Pan, S.K., 2013: Change in extreme events of temperature and precipitation over Xinjiang, northwest China, during 1960–2009. *Quat. Int.* 298, 141–151. <https://doi.org/10.1016/j.quaint.2012.09.010>
- Wang, H., Chen, Y., and Chen, Z., 2012: Spatial distribution and temporal trends of mean precipitation and extremes in the arid region, northwest of China, during 1960–2010. *Hydrol. Process.* 27, 1807–1818. <https://doi.org/10.1002/hyp.9339>
- Yang, H., Xiao, H., Guo, C., and Sun, Y., 2019: Spatial-temporal analysis of precipitation variability in Qinghai Province, China. *Atmos. Res.* 228, 242–260. <https://doi.org/10.1016/j.atmosres.2019.06.005>
- Ye H., 2018: Changes in duration of dry and wet spells associated with air temperatures in Russia. *Environ. Res. Lett.* 13, 034036. <https://doi.org/10.1088/1748-9326/aaae0d>
- Zhang, H., Wang, Y., Won Park, T., and Deng, Y., 2017: Quantifying the relationship between extreme air pollution events and extreme weather events. *Atmos. Res.* 188, 64–79. <https://doi.org/10.1016/j.atmosres.2016.11.010>
- Zhang, X. and Yang, F., 2004: RClimDex (1.0) User Guide. Climate Research Branch Environment. Canada, Downsview (Ontario, Canada).
- Zhang, X., Alexander, L., Hegerl, G.C., Jones, P., Klein Tank, A., Peterson, T.C., Trewin, B., and Zwiers, F.W., 2011: Indices for monitoring changes in extremes based on daily temperature and precipitation data. *WIREs Clim. Change* 2, 851–870. <https://doi.org/10.1002/wcc.147>
- Zolina, O., Simmer, C., Belyaev, K., Kapala, A., and Gulev, S., 2009: Improving estimates of heavy and extreme precipitation using daily records from European rain gauges. *J. Hydrometeorol.* 10, 701–716. <https://doi.org/10.1175/2008JHM1055.1>
- Zolina, O., Simmer, C., Belyaev, K., Gulev, S., and Koltermann, P., 2013: Changes in the duration of European wet and dry spells during the last 60 years. *J. Clim.* 26, 2022–2047. <https://doi.org/10.1175/JCLI-D-11-00498.1>
- Zolotokrylin, A. and Cherenkova, E., 2017: Seasonal changes in precipitation extremes in Russia for the last several decades and their impact on vital activities of the human population. *Geograp. Environ. Sustainab.* 10, 69–82. <https://doi.org/10.24057/2071-9388-2017-10-4-69-82>

INSTRUCTIONS TO AUTHORS OF *IDŐJÁRÁS*

The purpose of the journal is to publish papers in any field of meteorology and atmosphere related scientific areas. These may be

- research papers on new results of scientific investigations,
- critical review articles summarizing the current state of art of a certain topic,
- short contributions dealing with a particular question.

Some issues contain “News” and “Book review”, therefore, such contributions are also welcome. The papers must be in American English and should be checked by a native speaker if necessary.

Authors are requested to send their manuscripts to

Editor-in Chief of IDŐJÁRÁS
P.O. Box 38, H-1525 Budapest, Hungary
E-mail: journal.idojaras@met.hu

including all illustrations. MS Word format is preferred in electronic submission. Papers will then be reviewed normally by two independent referees, who remain unidentified for the author(s). The Editor-in-Chief will inform the author(s) whether or not the paper is acceptable for publication, and what modifications, if any, are necessary.

Please, follow the order given below when typing manuscripts.

Title page should consist of the title, the name(s) of the author(s), their affiliation(s) including full postal and e-mail address(es). In case of more than one author, the corresponding author must be identified.

Abstract: should contain the purpose, the applied data and methods as well as the basic conclusion(s) of the paper.

Key-words: must be included (from 5 to 10) to help to classify the topic.

Text: has to be typed in single spacing on an A4 size paper using 14 pt Times New Roman font if possible. Use of S.I.

units are expected, and the use of negative exponent is preferred to fractional sign. Mathematical formulae are expected to be as simple as possible and numbered in parentheses at the right margin.

All publications cited in the text should be presented in the *list of references*, arranged in alphabetical order. For an article: name(s) of author(s) in Italics, year, title of article, name of journal, volume, number (the latter two in Italics) and pages. E.g., *Nathan, K.K.*, 1986: A note on the relationship between photosynthetically active radiation and cloud amount. *Időjárás* 90, 10–13. For a book: name(s) of author(s), year, title of the book (all in Italics except the year), publisher and place of publication. E.g., *Junge, C.E.*, 1963: *Air Chemistry and Radioactivity*. Academic Press, New York and London. Reference in the text should contain the name(s) of the author(s) in Italics and year of publication. E.g., in the case of one author: *Miller* (1989); in the case of two authors: *Gamov* and *Cleveland* (1973); and if there are more than two authors: *Smith et al.* (1990). If the name of the author cannot be fitted into the text: (*Miller*, 1989); etc. When referring papers published in the same year by the same author, letters a, b, c, etc. should follow the year of publication. DOI numbers of references should be provided if applicable.

Tables should be marked by Arabic numbers and printed in separate sheets with their numbers and legends given below them. Avoid too lengthy or complicated tables, or tables duplicating results given in other form in the manuscript (e.g., graphs). *Figures* should also be marked with Arabic numbers and printed in black and white or color (under special arrangement) in separate sheets with their numbers and captions given below them. JPG, TIF, GIF, BMP or PNG formats should be used for electronic artwork submission.

More information for authors is available: journal.idojaras@met.hu

Published by the Hungarian Meteorological Service

Budapest, Hungary

ISSN 0324-6329 (Print)

ISSN 2677-187X (Online)